# Wideband, Multiband, Tunable, and Smart Antenna Systems for Mobile and UWB Wireless Applications 2016

Guest Editors: Renato Cicchetti, Antonio Faraone, Diego Caratelli, and Massimiliano Simeoni



# Wideband, Multiband, Tunable, and Smart Antenna Systems for Mobile and UWB Wireless Applications 2016

### Wideband, Multiband, Tunable, and Smart Antenna Systems for Mobile and UWB Wireless Applications 2016

Guest Editors: Renato Cicchetti, Antonio Faraone, Diego Caratelli, and Massimiliano Simeoni



### **Editorial Board**

Ana Alejos, Spain Mohammod Ali, USA Jaume Anguera, Spain Rodolfo Araneo, Italy Alexei Ashikhmin, USA Herve Aubert, France Paolo Baccarelli, Italy Xiulong Bao, Ireland Toni Björninen, Finland Stefania Bonafoni, Italy Djuradj S. Budimir, UK Paolo Burghignoli, Italy Shah Nawaz Burokur, France Giuseppe Castaldi, Italy Luca Catarinucci, Italy Felipe Cátedra, Spain Marta Cavagnaro, Italy Deb Chatterjee, USA Shih Yuan Chen, Taiwan Yu Jian Cheng, China Renato Cicchetti, Italy Riccardo Colella, Italy Lorenzo Crocco, Italy Claudio Curcio, Italy F. D'Agostino, Italy M. Elena de Cos Gómez, Spain Tayeb A. Denidni, Canada Giuseppe Di Massa, Italy Michele D'Urso, Italy Hala A. Elsadek, Egypt

Francisco Falcone, Spain Miguel Ferrando Bataller, Spain Flaminio Ferrara, Italy Vincenzo Galdi, Italy Claudio Gennarelli, Italy Farid Ghanem, Algeria Sotirios K. Goudos, Greece Rocco Guerriero, Italy Kerim Guney, Turkey Song Guo, Japan Mohamed Himdi, France Tamer S. Ibrahim, USA M. T. Islam, Malaysia M. R. Kamarudin, Malaysia Slawomir Koziel, Iceland Luis Landesa, Spain Ding-Bing Lin, Taiwan Angelo Liseno, Italy P. Lombardo, Italy Giampiero Lovat, Italy Lorenzo Luini, Italy Atsushi Mase, Japan Diego Masotti, Italy C. F. Mecklenbräuker, Austria Massimo Migliozzi, Italy A. T. Mobashsher, Australia Ananda S. Mohan, Australia J.-M. Molina-Garcia-Pardo, Spain Giorgio Montisci, Italy Marco Mussetta, Italy

N. Nasimuddin, Singapore Miguel Navarro-Cia, UK Mourad Nedil, Canada Symeon Nikolaou, Cyprus Giacomo Oliveri, Italy Pablo Otero, Spain A. D. Panagopoulos, Greece Ikmo Park, Republic of Korea Josep Parrón, Spain Matteo Pastorino, Italy Massimiliano Pieraccini, Italy Xianming Qing, Singapore Ahmad Safaai-Jazi, USA S. Safavi-Naeini, Canada M. Salazar-Palma, Spain Stefano Selleri, Italy Prabhakar Singh, India Raffaele Solimene, Italy Gino Sorbello, Italy Seong-Youp Suh, USA Sheng Sun, Hong Kong Larbi Talbi, Canada Luciano Tarricone, Italy Parveen Wahid, USA Wen-Qin Wang, China Shiwen Yang, China Yuan Yao, China Jingjing Zhang, Denmark

### **Contents**

### Wideband, Multiband, Tunable, and Smart Antenna Systems for Mobile and UWB Wireless Applications 2016

Renato Cicchetti, Antonio Faraone, Diego Caratelli, and Massimiliano Simeoni Volume 2017, Article ID 1425263, 3 pages

### Wideband and UWB Antennas for Wireless Applications: A Comprehensive Review

Renato Cicchetti, Emanuela Miozzi, and Orlandino Testa Volume 2017, Article ID 2390808, 45 pages

### Smart Cylindrical Dome Antenna Based on Active Frequency Selective Surface

Tongyu Ding, Shaoqing Zhang, Liang Zhang, and Yanhui Liu Volume 2017, Article ID 5901625, 14 pages

### Impact on Antijamming Performance of Channel Mismatch in GNSS Antenna Arrays Receivers

Zukun Lu, Junwei Nie, Feiqiang Chen, and Gang Ou Volume 2016, Article ID 1909708, 9 pages

### A Compact Novel Three-Port Integrated Wide and Narrow Band Antennas System for Cognitive Radio Applications

N. Anvesh Kumar and A. S. Gandhi Volume 2016, Article ID 2829357, 14 pages

#### Design and Performance Analysis of MISO-ORM-DCSK System over Rayleigh Fading Channels

Gang Zhang, Chuan gang Wang, Guo quan Li, and Jin zhao Lin Volume 2016, Article ID 8459109, 8 pages

### Wideband, Low-Profile, Dual-Polarized Slot Antenna with an AMC Surface for Wireless Communications

Wei Hu, Rui-Na Lian, Zhao-Yang Tang, and Ying-Zeng Yin Volume 2016, Article ID 7641382, 8 pages

### Dielectric Resonator Antennas: Basic Concepts, Design Guidelines, and Recent Developments at Millimeter-Wave Frequencies

S. Keyrouz and D. Caratelli Volume 2016, Article ID 6075680, 20 pages

### A Multiband Proximity-Coupled-Fed Flexible Microstrip Antenna for Wireless Systems

Giovanni Andrea Casula, Paolo Maxia, Giorgio Montisci, Giuseppe Valente, Giuseppe Mazzarella, and Tonino Pisanu

Volume 2016, Article ID 8536058, 7 pages

### On-Body Characterization of Planar Differential Antennas for Multiple, Wide, and Narrow Bands

Luigi Vallozzi, Domenico Pepe, Thijs Castel, Hendrik Rogier, and Domenico Zito Volume 2016, Article ID 7439403, 9 pages

#### Band-Notched UWB Antenna with Switchable and Tunable Performance

Wei Wu, Yun-Bo Li, Rui-Yuan Wu, Chuan-Bo Shi, and Tie-Jun Cui Volume 2016, Article ID 9612987, 6 pages

### A Wideband Antenna with Circular and Rectangular Shaped Slots for Mobile Phone Applications

Wei-Hua Zong, Xiao-Mei Yang, Xia Xiao, Shan-Dong Li, Xiang-Yang Wei, Zhe-Jun Jin, and Xiao-Yun Qu Volume 2016, Article ID 2975425, 9 pages

### A Small Planar Antenna for 4G Mobile Phone Application

Hu Jian-rong, Li Jiu-sheng, and Wu Di Volume 2016, Article ID 4791831, 7 pages

### A Novel Dual-Band Circularly Polarized Rectangular Slot Antenna

Biao Li, Yang Ding, and Ying-Zeng Yin Volume 2016, Article ID 9071610, 8 pages Hindawi International Journal of Antennas and Propagation Volume 2017, Article ID 1425263, 3 pages http://dx.doi.org/10.1155/2017/1425263

### **Editorial**

### Wideband, Multiband, Tunable, and Smart Antenna Systems for Mobile and UWB Wireless Applications 2016

### Renato Cicchetti, <sup>1</sup> Antonio Faraone, <sup>2</sup> Diego Caratelli, <sup>3,4</sup> and Massimiliano Simeoni <sup>5</sup>

Correspondence should be addressed to Renato Cicchetti; cicchetti@die.uniroma1.it

Received 14 February 2017; Accepted 14 February 2017; Published 5 March 2017

Copyright © 2017 Renato Cicchetti et al. This is an open access article distributed under the Creative Commons Attribution License, which permits unrestricted use, distribution, and reproduction in any medium, provided the original work is properly cited

### 1. Introduction

Due to exceptionally high data rates attainable with modern wireless communication systems and the app-based use paradigm, wireless connectivity through multiple and even diverse air interfaces has become a common requirement in the RF architecture of mobile communication devices. Modern wireless devices frequently incorporate five or more antennas to enable cellular voice, video and data, Wi-Fi, and GPS connectivity, across multiple bands. Multiple antenna systems are frequently designed to implement diversity or spatial multiplexing schemes, as in the case of WCDMA and LTE, to increase resiliency and capacity of wireless links, and to operate multiple voice/data links simultaneously. Carrier aggregation is demanding that multiple cellular bands are to be served simultaneously. Concurrently, ultrawideband (UWB) systems used in short-range communications, remote sensing, and through-the-wall radar imaging have introduced a new paradigm in the antenna design where the mitigation of pulse distortion is of the essence, thus requiring a shift in antenna design approach and the introduction of novel compact radiating systems. Moreover, vehicular communication systems, in order to provide safety warnings and traffic information, employ dedicated short-range communication devices that are intended to be used in vehicle-to-vehicle and vehicle-to-infrastructure communications, thereby enabling the use of cloud-based applications. Following these trends of the market, the level

of complexity in the design and implementation of antenna systems and relevant radio-frequency (RF) front-ends in wireless terminals has grown dramatically, requiring highly innovative solutions.

This special issue is intended to reflect current research trends and novel approaches in the analysis and synthesis of antenna systems and associated RF front-ends for next generations of mobile communication devices, applicable to various device forms such as smartphones, tablets, laptops, and wearable computers, as well as for UWB communication systems and radars, including the ones adopted in the automotive industry. Particular emphasis has been put in the analysis and design of broadband, multiband, and reconfigurable antennas for wireless and UWB applications, as well as in the identification of special materials and antenna integration techniques with the host platforms. Special effort has been devoted to the characterization of the radio channel and to the improvement of the quality of service. The special issue consists of 13 contributions that can be divided into the following 6 topics.

# 2. Contributions to Broad- and Multibanding Techniques

In "A Compact Novel Three-Port Integrated Wide and Narrow Band Antennas System for Cognitive Radio Applications," by N. A. Kumar and A. S. Gandhi, the authors present

<sup>&</sup>lt;sup>1</sup>Department of Information, Electronic and Telecommunication Engineering, University of Rome "La Sapienza", Rome, Italy

<sup>&</sup>lt;sup>2</sup>Chief Technology Office, Motorola Solutions Inc., Fort Lauderdale, FL, USA

<sup>&</sup>lt;sup>3</sup>The Antenna Company, Eindhoven, Netherlands

<sup>&</sup>lt;sup>4</sup>Tomsk Polytechnic University, Tomsk, Russia

<sup>&</sup>lt;sup>5</sup>European Space Agency, ESA-ESTEC, Keplerlaan, Noordwijk, Netherlands

the design and realization of a three-port radiating structure, integrating wide- and narrow-band antennas for cognitive radio applications. The radiating system consists of an UWB antenna for spectrum sensing, as well as two narrow-band antennas for wireless communication integrated on the same substrate. In particular, the first narrow-band antenna covers the frequency band between 8.78 GHz and 9.23 GHz, while the second one covers the frequency band between 7.33 GHz and 7.7 GHz and the frequency band between 9.23 GHz and 9.82 GHz, respectively.

In "A Novel Dual-Band Circularly Polarized Rectangular Slot Antenna," by B. Li et al., the authors present a dual-band circularly polarized antenna consisting of a rectangular metal frame, acting as a ground, and an S-shaped monopole working as a radiator. The circular polarization is obtained by means of a suitable design of the S-shaped monopole and of the external metallic frame. The antenna covers the frequency bands 2.39–2.81 GHz and 5.42–5.92 GHz and, therefore, can be conveniently applied in WLAN and WiMAX applications.

In "On-Body Characterization of Planar Differential Antennas for Multiple, Wide, and Narrow Bands" by L. Vallozzi at al., the authors present the results of on-body experimental tests of a set of four planar differential antennas with optimized layout of the radiating arms. It is observed that the performance of the considered antennas is acceptable when they are placed at a distance of 15 mm from the chest area of a human body. Therefore, they can be employed successfully in short-range off-body communications, as well as for the monitoring of vital signs, or body area network applications. Finally, it is observed that the proposed antennas can cover several frequency bands of interests, such as the lower portion of the UWB range from 3 to 5 GHz, the 868 MHz and 2.45 GHz ISM bands, and the 1.2 GHz band (lower L-band) for Global Positioning and Navigation Satellite System (GNSS), as well as the Ultrahigh Frequency (UHF) band at 915 MHz for Radio-Frequency Identification (RFID).

# 3. Contributions to Antennas for Wideband and UWB Applications

In "Wideband and UWB Antennas for Wireless Applications: A Comprehensive Review," by R. Cicchetti et al., the authors present a comprehensive review concerning the geometry, the manufacturing technologies, the materials, and the numerical techniques, adopted for the analysis and design of wideband and UWB antennas for wireless applications. Planar, printed, dielectric, and wearable antennas, achievable on laminate (rigid and flexible) and textile dielectric substrates, are considered. The performances of small, low-profile, and dielectric resonator antennas are illustrated paying particular attention to the application areas concerning portable devices (mobile phones, tablets, laptops, wearable computers, etc.) and radio base stations. This information provides a guidance to the selection of the different antenna types depending on required bandwidth, gain, field polarization, time-domain response, dimensions, and materials, as well as on the constraints related to the host platform.

In "Dielectric Resonator Antennas: Basic Concepts, Design Guidelines, and Recent Developments at Millimeter-Wave Frequencies," by S. Keyrouz and D. Caratelli, the authors present an up-to-date literature overview of the most effective design approaches for controlling circuital characteristics and radiation properties of dielectric resonator antennas (DRAs). The main advantages of DRAs are discussed in detail, with special emphasis put on the most advanced techniques for antenna feeding, size reduction, and gain enhancement. In this way, guidance is given to RF front-end designers in the selection of different DRA topologies useful for achieving desired performance in terms of bandwidth, radiation pattern, polarization, and ease of integration with the host platform. In particular, advances in the application of DRA technology at mm-wave frequencies have been presented, and the most recent implementation of on-chip and off-chip DRAs has been reviewed. It has been shown that silicon-based DRAs realized with standard CMOS process are characterized by good efficiency and gain, thus proving the good potential of DRAs for upcoming 5G communications, as well as high-resolution radar applications.

### 4. Contributions to Smart Antennas

In "Smart Cylindrical Dome Antenna Based on Active Frequency Selective Surface," by T. Ding et al., the authors present a highly agile, electronically steerable active smart dome antenna. The radiating structure is composed of an active dipole antenna surrounded by 16 strips with active frequency selective surfaces forming a dome. The response of the frequency selective surfaces is continuously tuned by varying the bias voltages of suitable varactors. In this way, some strips integrated in the dome can be biased in order to become reflective, while other strips are tuned so as to focus the electromagnetic energy at the boresight, thus enabling the coverage of the complete angular range.

In "Band-Notched UWB Antenna with Switchable and Tunable Performance," by W. Wu et al., the authors present a novel UWB antenna with switchable and tunable notch bands. The antenna consists of a circular UWB monopole printed on a trapezoidal ground plane. The radiating structure is integrated with two filters whose frequency behavior is electronically controlled by PIN and varactor diodes. The PIN diodes are used to control the switch between the lower (centered at about 4.5 GHz) and upper (centered at about 6 GHz) notch frequency bands, while the varactors are used to tune the filters in the individual bands.

# 5. Contributions to Antennas for Mobile Phones

In "A Small Planar Antenna for 4G Mobile Phone Application" by H. Jian-rong et al., the authors present the analysis and design of a small planar multiband antenna operating in the 4G frequency bands. The antenna consists of two horizontal-U rings, a shorting line, and a ground plane printed on a commercial FR4 substrate. The antenna satisfies the requirement of 6 dB return loss across the LTE700/LTE2300/LTE2500 and WiMAX 3500 bands.

In "A Wideband Antenna with Circular and Rectangular Shaped Slots for Mobile Phone Applications," by W.-H. Zong et al., the authors present a wideband slot antenna for mobile phone applications. The antenna is composed of two slots. The main slot, whose shape is a combination of a rectangle and a circle, presents small size, while an additional slot having rectangular shape is employed to excite a resonance at higher frequencies. The two slots are fed with a bent shape structure to obtain wideband impedance matching characteristics. The measurements performed on an antenna prototype confirm that the proposed antenna solution covers the LTE700/2300/2500, GSM850/900/1800/1900, and UMTS bands with nearly omnidirectional radiation patterns.

# 6. Contributions to Substrates, Special Materials, and Fabrication Techniques

In "Wideband, Low-Profile, Dual-Polarized Slot Antenna with an AMC Surface for Wireless Communications," by W. Hu et al., the authors present a wideband dual-polarized slot antenna loaded with an artificial magnetic conductor (AMC) for WLAN/WiMAX and LTE applications. The antenna structure consists of two pairs of arrow-shaped slots realized along the diagonals of a square patch. Two orthogonal stepped microstrip feedlines are used to excite horizontal and vertical field polarization, independently, while an AMC surface composed of  $7\times7$  unit cells is employed to achieve unidirectional radiation patterns.

In "A Multiband Proximity-Coupled-Fed Flexible Microstrip Antenna for Wireless Systems," by G. A. Casula et al., the authors present a multiband printed microstrip antenna for wireless communications. The antenna, which consists of proximity-coupled annular rings printed on a flexible substrate, can cover both the WLAN frequencies (both S-band at 2.45 GHz and C-band at 5.2 GHz) and WiMAX frequency at 3.5 GHz. The considered antenna can be also employed for vehicle-to-vehicle (V2V) and Vehicle-to-Roadside (V2R) communications, relying on Wireless Access in Vehicular Environments (WAVE)/Dedicated Short-Range Communication (DSRC) based on Intelligent Transportation System (ITS).

# 7. Contributions to Channel Modeling and System Design

In "Impact on Antijamming Performance of Channel Mismatch in GNSS Antenna Arrays Receivers" by Z. Lu et al., the authors analyze the impact on antijamming performance of channel mismatch in GNSS antenna arrays receivers. The characteristics of channel mismatch and impact of mismatch level are studied through theoretical analysis and simulation experiments. To determine the antijamming performance of an antenna array the concept of channel mismatch impact factor is introduced.

In "Design and Performance Analysis of MISO-ORM-DCSK System over Rayleigh Fading Channels," by G. Zhang et al., the authors present a novel chaotic communication

system, named Orthogonality-Based Reference Modulated-Differential Chaos Shift Keying (ORMDCSK), to enhance the performance of RM-DCSK. It is demonstrated that by using an orthogonal chaotic generator the intrasignal interference components existing in RM-DCSK are eliminated. Moreover, it is shown that the proposed system shows excellent agreement between theoretical expressions and Monte Carlo simulations, while exhibiting a significant BER improvement.

### Acknowledgments

The editors would like to express their gratitude to the authors and the anonymous reviewers for their efforts and contributions to this special issue. As a final word to our readers, after compiling this set of papers, we believe that it gives a good and current overview of the selected topics. We hope you will enjoy reading this year's special issue as much as we have enjoyed putting it together.

Renato Cicchetti Antonio Faraone Diego Caratelli Massimiliano Simeoni Hindawi Publishing Corporation International Journal of Antennas and Propagation Volume 2017, Article ID 2390808, 45 pages http://dx.doi.org/10.1155/2017/2390808

### Review Article

### Wideband and UWB Antennas for Wireless Applications: A Comprehensive Review

### Renato Cicchetti, Emanuela Miozzi, and Orlandino Testa

Department of Information Engineering, Electronics and Telecommunications, University of Rome "La Sapienza", Via Eudossiana 18, 00184 Rome, Italy

Correspondence should be addressed to Renato Cicchetti; cicchetti@die.uniroma1.it

Received 22 July 2016; Revised 23 November 2016; Accepted 19 December 2016; Published 20 February 2017

Academic Editor: Ahmed Toaha Mobashsher

Copyright © 2017 Renato Cicchetti et al. This is an open access article distributed under the Creative Commons Attribution License, which permits unrestricted use, distribution, and reproduction in any medium, provided the original work is properly cited.

A comprehensive review concerning the geometry, the manufacturing technologies, the materials, and the numerical techniques, adopted for the analysis and design of wideband and ultrawideband (UWB) antennas for wireless applications, is presented. Planar, printed, dielectric, and wearable antennas, achievable on laminate (rigid and flexible), and textile dielectric substrates are taken into account. The performances of small, low-profile, and dielectric resonator antennas are illustrated paying particular attention to the application areas concerning portable devices (mobile phones, tablets, glasses, laptops, wearable computers, etc.) and radio base stations. This information provides a guidance to the selection of the different antenna geometries in terms of bandwidth, gain, field polarization, time-domain response, dimensions, and materials useful for their realization and integration in modern communication systems.

#### 1. Introduction

The antenna design for high-speed multimedia connectivity represents a challenging activity for designers of fixed and mobile wireless communication systems. In fact, the rapid growth of mobile systems toward the fifth-generation (5G systems) requires multiband, wideband, and UWB antennas suitable to cover mobile and wireless services and to reduce the system complexity, the overall device dimensions, and costs. Many efforts are underway to identify new antenna geometries suitable to satisfy the challenging requirements of the modern wireless communication systems [1–4]. This is particularly relevant in UWB applications operating in the extended frequency bands listed in Table 1, where the communication standards adopted by the major countries in the world are reported [5].

Planar, printed (2D profile), and 3D antennas have been developed with the aim of meeting the integration requirements and transportability of handheld devices (mobile phones, laptops, tablets, etc.) as well as those of radio base stations and vehicles (cars, airplanes, ships, etc.). In addition, antenna conformability may be a useful requirement to

reduce the size and improve the look of mobile devices, while it results in an essential requirement for on-body type communication systems. This is particularly meaningful in wireless body area networks (WBANs) where high performances, as well as antenna flexibility under bending conditions, are important issues.

In general, 2D and 3D antenna technologies developed for wideband, multiband, and UWB applications can be divided into the following groups: microstrip antennas, monopole antennas over metal plates, printed monopole/dipole antennas, wide-slot antennas, metamaterial antennas, and dielectric resonator antennas (DRAs). These antennas may in some cases meet the demanding requirements of the existing communication systems, while they can be the starting point from which to develop new radiating systems suitable for the future communication requirements. To this end, in this paper a comprehensive review of the scientific literature of the last decade concerning these aspects is taken into account with the aim to provide researchers and designers with a valuable support tool to the antenna design. Particular emphasis is given to geometries, radiation mechanisms, broadbanding methods, materials, and prediction numerical tools adopted

TABLE 1: UWB standards.

| Country         | Frequency bands   | Regulated by  |  |
|-----------------|---|---|--|
| America, Canada | 3.1–10.6 GHz<br>unlicensed band<br>without restrictions   | Federal<br>Communication<br>Commission (FCC)                          |  |
| Europe          | 3.1–4.8 GHz with<br>Detect And Avoid<br>(DAA) restrictions;<br>6–8.5 GHz band with<br>no restrictions | Electronic<br>Communications<br>Committee (ECC)                       |  |
| Japan           | 3.4–4.8 GHz with<br>DAA restrictions;<br>7.25–10.25 GHz<br>unlicensed band                            | Ministry of Internal<br>Affairs &<br>Communications<br>(MICs)         |  |
| Korea           | 3.1–4.8 GHz with<br>DAA restrictions;<br>7.2–10.2 GHz band<br>with no restrictions                    | Electronics and<br>Telecommunications<br>Research Institute<br>(ETRI) |  |
| Singapore       | 6–9 GHz band with<br>no restrictions;<br>3.4–4.2 GHz band<br>with DAA restrictions                    | Infocomm<br>Development<br>Authority (IDA)                            |  |

to the analysis and design of these important classes of antennas.

The paper is organized in 12 sections. In Section 2 the features of some wideband microstrip antennas are presented. In Section 3, the characteristics of monopole antennas over metal plates are discussed. In Sections 4, 5, and 6, the performances of planar printed monopole, wide-slot, and dipole antennas for wideband and UWB applications are illustrated. In Section 7, directional UWB antennas are presented, in Section 8 metamaterial antennas are discussed, and in Section 9 antennas and materials useful to realize wearable antennas are considered, while in Section 10 the most recent advances of DRA antennas are illustrated. The main techniques adopted to realize UWB antennas with notched bands are highlighted in Section 11. Finally, in Section 12 some remarks concerning the state of the art, the future trends, and the main limitations of the different antenna manufacturing technologies being considered are outlined.

#### 2. Wideband Planar Microstrip Antennas

Microstrip patch antennas (MPAs) were first introduced in the 1950s [6] but they found success only in the 1970s, driven by the fast growth of integration technology with active devices which allows realizing very compact structures. However, although these antennas exhibit low-profile, small size, limited manufacturing costs, and easy circuital integration, they typically present low fractional bandwidths (FBW = 7%) not compatible with the modern wireless communication systems. To overcome this drawback, a significant research activity has been performed in the last twenty years to identify new geometries suitable to satisfy those requirements. This required the identification of the physical mechanisms governing the radiative processes taking place in said antennas.

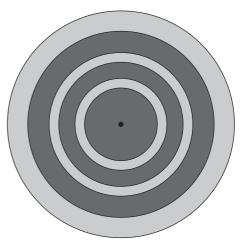


FIGURE 1: A monopolar patch antenna with a circular patch, circular ground plane, and two coupled metal rings [7]. The dot point indicates the coaxial probe pin. Dark gray monopole and light gray dielectric substrate.

In this section, some examples of the most recent antennas belonging to this important class are reported.

As a first structure, a wideband patch antenna having a radiation pattern similar to that of a monopole and consisting of two metal rings coupled to a circular patch radiator, presented in [7] is illustrated. The antenna is printed on a circular grounded dielectric substrate (DiClad 527), with relative permittivity  $\varepsilon_r = 2.5$ , thickness of 1.5 mm, and diameter 120 mm, while a coaxial probe, located at the center of the circular patch, is used to excite the antenna (see Figure 1). The antenna has been analyzed using the full-wave FEM-based HFSS [8]. The antenna return loss is principally affected by the distances between the rings, between the first ring and the central radiating element, and by the radius of circular metal strip. The monopole-like radiation characteristics of the pattern are due to the central position of the excitation probe as well as to the symmetric field configurations excited in each slot through which the emission of electromagnetic energy occurs. The measured impedance bandwidth covers the 5.45-7.16 GHz frequency band (FBW = 27.1%) making the antenna useful to be employed for wireless communication standards (WLAN, WiMAX). The realized measured peak gain ranges between 1.9 dBi and 6.3 dBi, while the crosspolarization levels are of about 15 dB and 20 dB in the *H*-plane and *E*-plane, respectively.

A different design solution for a broadside coverage, consisting of a compact perturbed E-shaped patch antenna printed on a grounded dielectric substrate RT/duroid 5880 of dimensions  $42 \,\mathrm{mm} \times 42 \,\mathrm{mm} \times 3.15 \,\mathrm{mm}$  (about  $0.82\lambda_0 \times 0.82\lambda_0 \times 0.0612\lambda_0$ , where  $\lambda_0$  is the free-space wavelength at the antenna central frequency  $f=5.38\,\mathrm{GHz}$ ) and dielectric permittivity  $\varepsilon_r=2.2$ , has been presented in [9]. Two zigzag slots and two rectangular notches have been inserted in the patch for achieving a wider impedance bandwidth with higher return loss levels. To excite the antenna, a  $50\,\Omega$  probe is inserted between the first teeth of the zig-zag slots (see Figure 2). The zig-zag slots extend the current paths on the

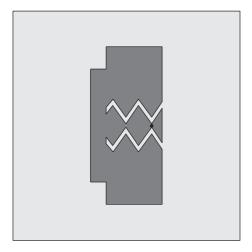


Figure 2: A compact perturbed E-shaped patch antenna [9]. Corner notches and zig-zag slots realized on the metallic patch are adopted to obtain a wideband behavior, while a 50  $\Omega$  probe is inserted between the first teeth of the zig-zag slots to excite the antenna. Dark gray monopole and light gray dielectric substrate.

metal patch making the antenna less longer along the teeth direction reducing in this way the antenna dimensions. In addition, they excite two low Q resonant modes, resulting in an impedance antenna bandwidth ranging between 4.96 GHz and 6.69 GHz (FBW = 30%), thus ensuring the coverage of the Hiperlan/2, IEEE 802.11a, and HiSWaNa frequency bands. A homemade numerical prediction tool based on a locally conformal finite-difference time-domain (FDTD) scheme, together with the surface equivalence theorem employing the free-space dyadic Green's functions, has been adopted to compute the field distributions near and outside the FDTD computational domain [10]. At lower frequency the radiation patterns are similar to that of a simple rectangular patch antenna, while at higher frequencies they show a tilt of about 16.2° from the boresight direction in the *E*-plane. This behavior can be explained with the presence of a surface current density traveling along the zig-zag region. Front-toback ratios are higher than 21 dB due to the adopted full ground solution, while the realized gains are between 4 and 7 dBi. An equivalent circuit useful to simplify the design of the RF front end and an analysis of the radiation mechanisms responsible for the antenna behavior are reported in [11].

To improve the impedance bandwidth a U-shaped antenna with a defect ground plane, adopted to reduce the reactive energy stored within the antenna cavity and in the neighboring region of the metal patch, has been proposed in [12]. Said antenna, useful for wideband wireless communications, is printed on a glass polytetrafluoroethylene (PTFE) dielectric substrate of permittivity  $\varepsilon_r=2.4$ , loss tangent 0.00022, and thickness of about 1.6 mm. A coaxial probe, placed in the antenna symmetry plane, is adopted to excite the antenna (see Figure 3). The effects of circular and square ground planes have been investigated. It is observed that antennas equipped with circular ground planes exhibit wider impedance bandwidth with respect to those equipped with a square ground plane having comparable

dimensions. In particular, the antenna having a diameter of 36 mm offers the best radiative performance and covers the frequency range from 4.5 GHz to 11.4 GHz (FBW = 86.79%). Parametric optimizations have been performed using the full-wave commercial software Ansoft based on the Method of Moments. The measured gain ranges between 2.2 dBi and 4.1 dBi over the entire frequency band.

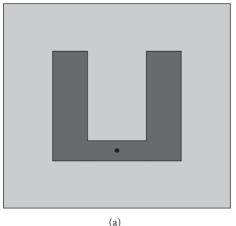
Other examples of wideband planar microstrip antennas can be found in [13–16].

### 3. Monopole Antennas over Metal Plates (3D Profile)

In 1976, Dubost and Zisler [17] introduced for the first time wideband monopole antennas arranged orthogonally on a metal ground plane. Even though their vertical size can prevent their integration into handset devices, different kinds of planar monopole antennas have been developed in the last twenty years, due to their several practical advantages. In particular, the metal plate can be usefully employed to increase the antenna gain and the front-to-back ratio, thus allowing obtaining a high electrical insulation with the RF circuitry of the communication system and preserving the antenna characteristics regardless of the installation site features [18]. Of particular practical interest are the monopoles or the folded antennas as they can be employed in base stations, avionics or automotive systems, and so forth. Said applications, which generally do not need compact communication systems, require instead low vertical-profile radiators when they are intended to be installed on highspeed mobile vehicles. A wide class of said antennas having the above-mentioned features have been proposed in the literature in order to obtain high radiative performance (see Figure 4). For the sake of brevity in this section an overview of the most significant results published in literature is provided.

Empirical formulas, to identify the frequency band covered by monopole antennas vertically placed on ground planes, useful during the preliminary design stage, are proposed in [19–22]. These formulas are derived assuming that the electromagnetic field, first to be radiated by the monopole, substantially propagates in the spatial region located between the lower edge of the monopole and the ground plane; that is, it experiences a propagation similar to that which occurs in a simple or tapered transmission line.

Adopting the lower profile of the monopole similar to that of a tapered transmission line, a planar inverted cone antenna (PICA) for broadband wireless applications has been proposed in [23]. Two different design solutions, intended for UWB applications related to imaging and communication, are considered (see Figure 5). In particular, the first design solution operates in the frequency range between 1 and 9 GHz, while the second one, provided with holes, covers between 1 and more than 10 GHz with a FBW = 163%. Both antennas are characterized by an adequate level of crosspolarization and frequency stability of the radiation diagrams (best performances are exhibited by the solution provided with holes) up to about 7 GHz. The antenna gain varies between 4 and 8 dBi in the frequency range between 1 and 10 GHz. The monopole, of length of about 76.2 mm ( $\lambda_0/4$ ,



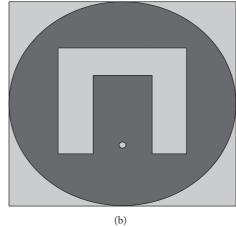


FIGURE 3: U-shaped patch antenna with a U-slot embedded in a circular/square ground plane [12]. Top view (a) and bottom view (b). The black dot point indicates the pin of the coaxial probe. Dark gray monopole and light gray dielectric substrate.

where  $\lambda_0$  is wavelength at the lower working frequency), is printed on a substrate of relative dielectric permittivity 2.33 and thickness 0.79 mm, while the metal plate has dimensions of 610 mm  $\times$  610 mm  $(2\lambda_0 \times 2\lambda_0)$ . The structure, fed by a coaxial probe, is spaced from the ground plane of 0.64 mm to increase the operating band. The antenna was analyzed and designed using a homemade software based on the full-wave FDTD numerical technique.

A similar design solution, but having a wider bandwidth, has been proposed in [24]. This solution adopts a leaf-shaped monopole having three circular holes, mounted vertically on a grounded dielectric slab of dimensions  $80 \text{ mm} \times 80 \text{ mm}$ , with dielectric constant  $\varepsilon_r = 3.5$  and thickness of 1.5 mm (see Figure 6). The holed monopole, of height 76.2 mm and thickness 1 mm, together with an air gap of 0.64 mm, is employed to improve the antenna bandwidth that extends from 1.3 GHz up to 29.7 GHz (FBW = 183%). The antenna gain ranges between 3.6 and 4.7 dBi in the frequency band between 3 and 9 GHz. The applications for which the antenna is proposed are of commercial and military nature. The antenna was analyzed by means of the full-wave FIT-based CST Microwave Studio [25]. The measurement results are in good agreement with the numerical simulations.

Simple monopoles, with bevels and with vertical foldings of the radiating surfaces, for broadband and UWB applications, have been analyzed in [20]. Both structures, vertically mounted on a ground plane of dimensions 260 mm×260 mm, have a height of 45 mm and an air gap of 1 mm, while the bevel angle is of 16° for the monopole and 20° for the accordion version. In particular, it is shown how both the monopole tapering and the bending are able to expand significantly the antenna operating band (see Figure 7). In fact, the adoption of the two mentioned techniques not only widens the antenna bandwidth but makes the radiation patterns more stable in frequency. The performances of the antennas were analyzed by means of the full-wave FIT-based CST Microwave Studio [25]. The results of the measurements performed on the antenna prototypes are found to be in good agreement with the numerical computations.

A modified bevel technique is adopted in [26], where two monopole antennas suitable to cover the AMPS (824-894 MHz), the GSM900 (890–960 MHz), and the DCS (1710– 1880 MHz) frequency bands were presented. The antennas are proposed for multiband mobile communication systems such as receivers for vehicle applications. A homemade fullwave method of moment (MoM), based on the Rao-Wilton-Glisson (CRWG) basis functions, has been employed to solve the electric field integral equation (EFIE) from which the antenna surface current distributions have been derived. The radiating element, of dimensions of 50 mm × 87 mm and thickness of 0.5 mm, with bevel cuts on its two lower corners, is connected to a 50  $\Omega$  SMA connector pin. The first radiant structure, composed of a rectangular monopole having a bevel angle of 22.3°, a suitable width of the feeding strip, and a gap distance of 3 mm from the ground plane, is depicted in Figure 8(a). The top edge of the radiating element is rounded to improve the high-frequency performance of the monopole. The geometrical parameters affecting the antenna bandwidth are the height of the monopole, which controls the lower frequency, and the bevel angle which controls the antenna upper frequency. In this way, an antenna whose gain varies from 4 to 7 dBi is obtained.

The second monopole antenna, having a staircase profile of its contour (see Figure 8(b)), presents a larger tapering region close to the feeding strip. The monopole of dimensions 68 mm  $\times$  69.5 mm, presenting an air gap of 1.8 mm, is placed vertically on a ground plane of size 500 mm  $\times$  500 mm. The radiation diagrams show a frequency behavior similar to those of the first monopole antenna even if the presence of a staircase profile introduces some ripples in the radiation diagrams, while the gain increases monotonically from about 2.5 up to 6.3 dBi in the frequency range of 800–1880 MHz. Note that the total height of the second antenna is only of 0.19 $\lambda_L$ , which is much lower than the height of the first antenna 0.24 $\lambda_L$  ( $\lambda_L$  is the wavelength at the lower edge of the AMPS frequency band).

A combined technique to realize a wideband antenna, consisting of a rectangular monopole with a bevel and

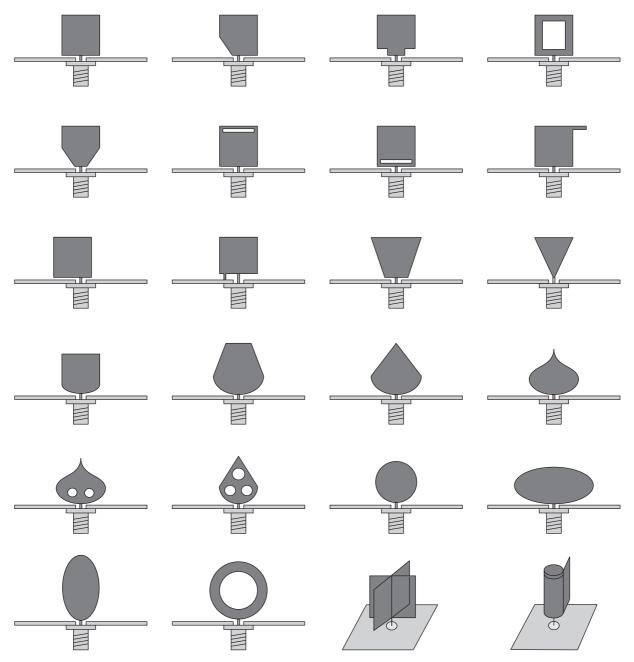


FIGURE 4: Examples of broadband and UWB monopole antennas over a metal plate. Dark gray monopole, medium gray ground plane, and light gray dielectric substrate.

a shorting post, has been proposed in [27]. The antenna exhibits a frequency band with a VSWR  $\leq$  3 ranging from 800 MHz to more than 10.5 GHz. Said antenna (see Figure 9) can meet the requirements of the GSM, PCS, IMT-2000, and DECT of the 2.4 GHz and 5.8 GHz ISM bands, U-NII, as well as those of the most recent UWB communication systems. The frequency behavior of the parameter VSWR was simulated by means of a homemade software based on the MoM technique, using a finite-gap voltage-feed source and a wire-grid mesh with piecewise sinusoidal basis functions. The experimental results performed on an antenna prototype show that the simultaneous adoption of the short circuit strip

and of the bevel (whose angle should not exceed  $40^\circ$ ) realized in the lower edge profile of the monopole is able to increase significantly the antenna bandwidth. The monopole has a size of  $60~\text{mm} \times 60~\text{mm} \times 0.2~\text{mm}$ , with a feed gap of 1.2~mm and a shorting post of 2~mm, while the ground plane has a size of approximately  $200~\text{mm} \times 200~\text{mm}$ .

An excitation system with three branches named trident-shaped feeding line, proposed to obtain an enhancement of the antenna bandwidth and a better polarization purity of the radiated field, has been presented in [28]. The antenna consists of a squared monopole (size  $40 \, \mathrm{mm} \times 40 \, \mathrm{mm} \times 0.2 \, \mathrm{mm}$ ) placed vertically with respect to a ground plane

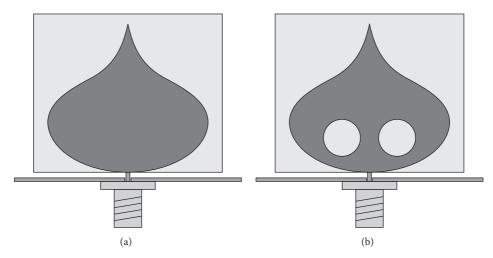


FIGURE 5: The PICA broadband antenna [23]. The design solutions (a) without holes and (b) with holes in the monopole are shown in the figure. Dark gray monopole and medium gray ground plane.

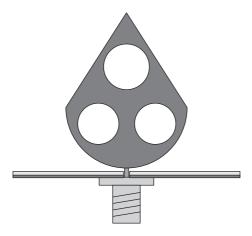


FIGURE 6: The leaf-shaped antenna [24]. The holes in the monopole are used to modify the surface currents distribution giving rise to a more favorable reactive energy configuration near the monopole. Dark gray monopole and medium gray ground plane.

of dimensions  $150 \text{ mm} \times 150 \text{ mm}$ . The improvement of the antenna characteristics is obtained thanks to a better spatial distribution of the vertical component of the surface current together with a drastic reduction of the transverse component excited on the monopole (see Figure 10). The experimental measurements confirm that the monopole exhibits a narrowband behavior when it is excited by a single feed point, while its behavior becomes broadband, with a frequency band ranging between 1.4 and about 11.5 GHz, when the monopole is fed in three equal-spaced points. The antenna is proposed for the applications concerning the new broadband wireless metropolitan area network system using the IEEE 802.16a (2-11 GHz) standard [29]. The antenna gain varies from about 4 to 7 dBi, in the frequency range between about 1.3 and 6 GHz, while maintaining fairly constant in the frequency range between 6 GHz and 10 GHz. The simulated results are obtained using the full-wave FEM-based HFSS [8].

A technique useful to improve the impedance bandwidth of a rectangular monopole antenna, consisting in the use of an additional rectangular metallization, placed orthogonal with respect to the monopole axis, so as to obtain a resulting crossshaped geometry, having the aim of obtaining an antenna suitable to cover the UWB band (3.1-10.6 GHz), has been proposed in [30]. The monopole of dimensions  $24\,\mathrm{mm}$  × 18 mm is placed vertically on a circular metal plate (see Figure 11) whose diameter is of about 150 mm (corresponding to about 3.2 $\lambda_0$ , where  $\lambda_0$  is the free-space wavelength relative to the central working frequency). The antenna gain ranges between about 3.1 and 5.8 dBi. The cross-polarization levels are similar to those of a rectangular monopole. The radiation phenomena occur near the lower edge of the monopole. The full-wave FIT-based CST Microwave Studio [25] and MoMbased WIPL-D [31] are used for the numerical simulations.

Finally, an example of a wideband antennas array is reported. The array is formed by four horizontal pinwheelshaped folded monopole planar antennas (PMAs) assembled with additional four vertical PMAs to improve the directivity and the performance of the circular polarization [32]. Since the overall antenna height is of 19 mm it can be easily integrated into low-profile devices. Moreover, supporting the circular polarization it may be useful to realize radio base stations for indoor applications. The antenna has an impedance bandwidth ranging between 1.05 and 2.55 GHz (FBW = 87%) in which the axial ratio AR < 3 dB. The antenna is realized on an RF-35 substrate with a dielectric constant of 3.5 and thickness of 0.5 mm, having a ground plane of 150 mm × 150 mm. The PMAs are excited by means of strip fed with bevels, used to increase the antenna bandwidth, connected to a planar balun formed by a broadband Wilkinson power divider and by a commercial hybrid coupler. The length of the folded part of the monopole, as well as its distance from the ground plane, determines the in-band entrance, while the width of each radiating element controls the array bandwidth. An excitation with increasing phase step of 90° between adjacent monopoles ensures the excitation of the circular

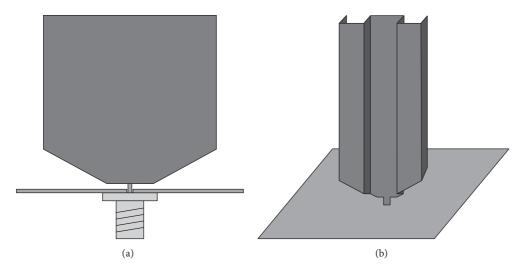


FIGURE 7: Hexagonal monopole antenna (a) and folded monopole antenna (b) for broadband and UWB applications [20]. The accordion version is adopted to reduce the transverse size of the monopole. Dark gray monopole and medium gray ground plane.

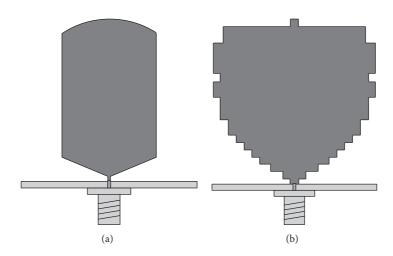


FIGURE 8: Monopole antenna (a) with bevels and (b) with staircase contours [26]. The bevels or the staircase contours are used to facilitate the energy emission in the monopole region near the ground plane. Dark gray monopole and medium gray ground plane.

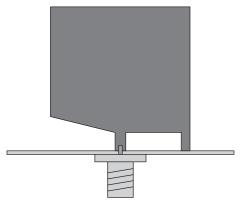


FIGURE 9: A rectangular monopole with a shorting post. Dark gray monopole and medium gray ground plane [27].

polarization along the boresight direction. The resulting antenna gain is of about 8.24 dBi. Two frequency notches are

introduced to avoid the energy emission at the frequencies of 2.03 and 2.39 GHz. This result is achieved through the adoption of a U-shaped resonant strip ( $f = 2.03 \,\text{GHz}$ ) and an inverted W-shaped resonant slot ( $f = 2.39 \,\text{GHz}$ ). The electromagnetic analysis was performed using the full-wave FIT-based CST Microwave Studio [25].

### 4. Printed Monopole Antennas (2D Profile)

Modern portable devices, working with high data rates, employ broadband antennas characterized by small sizes and low profiles. In fact, whereas monopoles antennas, having a tridimensional shape, are more suitable to be used in radio base stations and mobile radio systems (cars, trains, airplanes, ships, etc.), the printed monopole antennas not only reduce the vertical bulk of the portable device, but also enable an easy integration with the RF circuitry. Notice that typical smart phones, tablets, and laptops exhibit size of about  $130~\text{mm} \times 50~\text{mm} \times 6~\text{mm}$ ,  $240~\text{mm} \times 140~\text{mm} \times 140~\text{mm}$ 

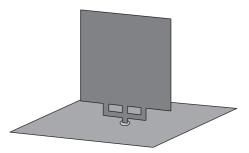


FIGURE 10: A planar metal plate monopole antenna employing a trident-shaped feeding network [28]. The multipoint excitation is used to increase the amplitude of vertical component of the surface current excited in the monopole. Dark gray monopole and medium gray ground plane.

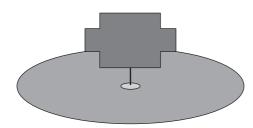


FIGURE 11: A cross-shaped monopole antenna [30]. The additional metal plate, placed orthogonal with respect to the main rectangular metallization, is employed to reduce the field discontinuity caused by the transition between the coaxial probe and the radiant monopole, resulting in a wideband antenna behavior. Dark gray monopole, medium gray ground plane, and light gray dielectric substrate.

8 mm, and  $260 \, \text{mm} \times 200 \, \text{mm} \times 21 \, \text{mm}$ , respectively. The need to satisfy these important requirements has given rise to a strong research activity that led to the development of a large class of antennas. In this context, of particular interest are the wideband [33–38], the multiband [39–48], and the UWB printed monopole antennas, simple [49–57] and with notched bands to avoid interference with other radio communication systems [58–68] or those suitable for supporting the circular polarization [33, 69–71].

A large class of geometries (rectangular, circular, elliptical, triangular, hexagonal, annular, etc.) has been proposed in order to improve the impedance matching of said antennas with the feeding line, generally consisting of a microstrip line, simple or tapered [40-42, 51-57, 62, 69, 72, 73], or based on a coplanar waveguide (CPW) having a single or multiple transition [34, 35, 39, 60, 71, 74]. Of particular interest are also the techniques based on the use of notches placed near the transition region between the ground plane and the radiating monopole [33, 36, 72], on the use of trapezoidal [35, 72, 74] or tapered ground planes [49, 58, 59, 63, 68, 75], having zig-zag shaping [76, 77], or with defects in the ground plane (DGS) [34, 37, 39, 62, 78, 79]. Additional techniques are those based on the use of bevels [37, 80] or of a particular shape of the upper region of the monopole [81]. For the sake of brevity in the following an overview of the most significant papers concerning the aforementioned design aspects is provided.

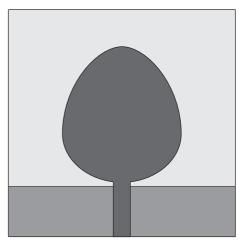


FIGURE 12: The printed Newton's egg curved monopole antenna [51]. The regular contour expressed by Newton's egg curve promotes the energy emission in the region close to the ground plane avoiding energy reflections toward the feeding line. Dark gray upper metal face, medium gray bottom metal face, and light gray dielectric substrate.

4.1. UWB Antennas. The UWB antennas are characterized by extremely high operating bands. In these bands the antennas have to ensure a low signal distortion as well as an adequate stability of the group delay, of the antenna gain, and of the angular behavior of the radiation patterns [82]. To this end, in this section, UWB antennas and suitable design solutions useful to improve the antenna bandwidth are presented.

A suitable low-profile geometry useful to radiate UWB signals is Newton's egg curved monopole antenna [51]. A prototype of said antenna (see Figure 12), of dimensions 40 mm× 40 mm, is printed on double-sided FR-4 substrate with relative permittivity  $\varepsilon_r = 4.4$ , loss tangent 0.018, and thickness h =1.6 mm. A parametric formula, based on Newton's egg curve, is proposed for the design of the monopole profile, while an empirical formula is introduced to determine the lower cut-off frequency of the impedance bandwidth. The antenna analysis and design have been performed using the full-wave FEM-based HFSS [8]. The experimental measurements show that the antenna has a FBW of 116.55% (2.9-11.0 GHz) and exhibits a stable gain of about 2.2-2.9 dBi. The proposed antenna exhibits almost omnidirectional radiation patterns with low cross-polarization in all directions and adequate group delay over the entire UWB bandwidth (3.1–10.6 GHz).

Three different UWB antenna geometries (see Figures 13 and 14) useful to transmit short pulse signals, and characterized by reduced overall dimensions, have been proposed in [52]. These antennas, having impedance bandwidth ranging from 3 up to 11 GHz, are realized using a Rogers 4350B substrate having a dielectric permittivity of 3.48 and thickness 0.8 mm. A thin substrate is used to limit the excitation of surface waves. In particular, the first antenna, of dimensions  $30 \text{ mm} \times 30 \text{ mm}$ , consists of an elliptic monopole excited by a tapered microstrip line and equipped with a trapezoidal ground plane. The second radiating structure, of dimensions  $15 \text{ mm} \times 30 \text{ mm}$ , is obtained by removing the left half part

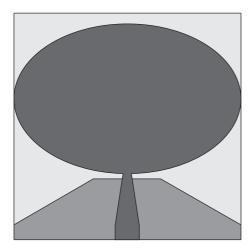


FIGURE 13: Configuration of the full-size UWB antenna [52]. Dark gray upper metal face, medium gray bottom metal face, and light gray dielectric substrate.

of the monopole, while the last geometry, of dimensions  $12 \,\mathrm{mm} \times 17 \,\mathrm{mm}$ , is derived by removing from said antenna, part of the upper and right side of the monopole and the lower part of the ground plane. Despite the considerable reduction of the antenna size observable in Figure 14(b), the antenna response to pulse signals having the waveform of the fifth-derivative of the Gaussian pulse is excellent. Further information useful to reduce the size and increase the performance of symmetric UWB antennas can be found in [3].

4.2. Monopole Antennas for Circular Polarization. The printed monopole antennas typically work in linear polarization. This kind of field polarization although useful in many applications cannot be very effective when the communication systems have to operate in indoor environments where multipath and scattering processes can reduce the quality of the radio link [83]. To this end, several kinds of printed monopole antennas suitable to support a circular polarization have been recently proposed in the literature [33, 36, 38, 69–71, 84, 85]. In particular, in the papers discussed below the main features of some of them are reported.

A very simple monopole antenna, obtained by extending the feeding microstrip line beyond the ground plane in the upper left part region of which two notches were made thus leading to an asymmetry in the metal screen (see Figure 15), has been proposed in [33]. The electromagnetic characteristics of the antenna have been derived using the full-wave FEM-based HFSS [8]. The measured impedance bandwidth is of about 5.96 GHz from 4.06 to 10.02 GHz, while the measured AR bandwidth is of about 2.64 GHz from 5.91 to 8.55 GHz. The antenna, of dimensions of 16 mm × 22 mm × 1 mm, is realized on a FR4 substrate with a dielectric permittivity of 4.6 and loss tangent of 0.02. The circular polarization is induced by the asymmetrical ground plane, which is responsible for the excitation of both the horizontal and vertical component of the surface current

with a phase shift of about 90°, while a notch placed under the monopole is used to increase the antenna impedance bandwidth. The radiation patterns are mainly left handed circularly polarized (LHCP) in the lower half-space and right handed circularly polarized (RHCP) in the upper half-space, while the cross-polarization can keep more than 15 dB lower than the copolarization in each plane. The antenna gain is between 1 and 2.8 dBi.

Similar radiation mechanisms are employed in the antenna proposed in [36] where a rectangular monopole, fed asymmetrically by means of a microstrip line and equipped with a ground plane integrating a metal stub and a slit, is adopted to obtain a circularly polarized electromagnetic field (see Figure 16). According to the measurement results, the antenna covers the frequency range between 2.32 and 8.88 GHz with an impedance bandwidth of 6.56 GHz. AR values of less than 3 dB are observed in the frequency range between 3.2 and 4.4 GHz (AR bandwidth of 1.2 GHz). The antenna, of dimensions of 45 mm  $\times$  40 mm  $\times$  1.6 mm, is printed on a FR4 substrate with a relative permittivity  $\varepsilon_r = 4.4$ , loss tangent 0.024, and thickness 1.6 mm. The full-wave FEM-based HFSS [8] was adopted to analyze the antenna.

The slit is adopted to increase the frequency band where the radiated field is circularly polarized, while the stub is used to restore the antenna impedance bandwidth perturbed by the presence of the slit. The antenna gain ranges between 1 and 2 dBi, while the efficiency is of about 78%.

A more complex design solution, consisting of a C-shaped monopole, coupled to an open metallic loop printed on the opposite face of a FR4 dielectric substrate with a relative permittivity of 4.4, a loss tangent of 0.02, and dimensions of  $25 \,\mathrm{mm} \times 25 \,\mathrm{mm} \times 1 \,\mathrm{mm}$ , has been proposed in [38]. A rectangular stub, integrated into the upper edge of the ground plane, and coupled to the open metallic loop, is used to improve the impedance and the axial ratio (AR) bandwidth (see Figure 17). The gap in the loop significantly influences the bandwidth of the AR but not that of the impedance. The antenna, analyzed using the full-wave FEM-based HFSS [8], has an impedance bandwidth ranging between 4.26 and 10.92 GHz (FBW = 87.7%) and an AR bandwidth ranging between 4.28 and 8.42 GHz (AR FBW = 65.2%). A solution equipped with a metal reflector, placed at a distance of about 16 mm from the antenna ground plane, is suggested to make unidirectional the radiation pattern and to increase the antenna gain of about 3 dB without affecting significantly the operating band of the antenna.

A different radiation mechanism is excited in the dual-band circularly polarized antenna in [85] consisting of a rectangular metal frame, acting as a ground, and an S-shaped monopole working as a radiator. The antenna having dimensions 37 mm × 37 mm × 1 mm has been fabricated on a FR4 substrate with dielectric permittivity of 4.4 and loss tangent 0.02 (see Figure 18). The proposed antenna is capable of operating in the 2.39–2.81 GHz and 5.42–5.92 GHz bands, thus suitable for the WLAN and WiMAX applications. The full-wave FEM-based HFSS [8] has been adopted to determine the antenna characteristics. The circular polarization is obtained by means of a suitable design of the S-shaped monopole and of the external metallic frame. This frame

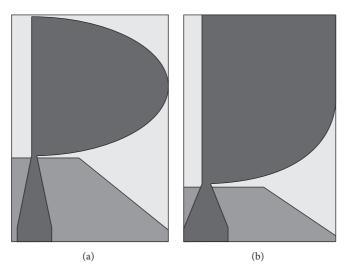


FIGURE 14: Configuration of the half-size (a) and of the compact UWB antenna (b) [52]. Dark gray upper metal face, medium gray bottom metal face, and light gray dielectric substrate.

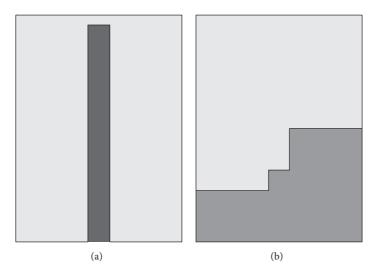


FIGURE 15: A planar monopole antenna with wideband circular polarization [33]. Dark gray upper metal face, medium gray bottom metal face, and light gray dielectric substrate. Top view (a) and bottom view (b).

determines the excitation of edge currents whose radiated field, along with that sustained by the monopole, is suitable to support a circular polarization in the band of interest. The radiation efficiency is approximately 80%, while the gain ranges between 3.2 and 4 dBi.

Further papers concerning printed monopole antennas suitable to support the circular polarization can be found in [69–71].

4.3. Design Solutions to Improve the Antenna Bandwidth. This section provides an overview of the most commonly used techniques to increase the operating band of the printed monopole antennas. In particular, trapeziform and rounded ground planes, with notches near the feeding lines or with a zig-zag shaping of the upper edge, have proven to be particularly effective in increasing the operating band of said antennas.

A compact CPW-fed monopole antenna composed of an elliptical monopole and a coplanar trapeziform ground plane has been proposed in [35]. The antenna depicted in Figure 19(e) achieves a ratio impedance bandwidth of 21.6:1 and exhibits a nearly omnidirectional radiation pattern with a gain ranging between about 0.4 and 4 dBi. The radiating structure is a suitably modified version of the planar discone antenna. In particular, it is composed of an elliptical monopole fed by a tapered coplanar waveguide (CPW) and of a ground plane having the shape of a trapezoid to improve the energy emission. The antenna is realized on a dielectric substrate of thickness 1.524 mm having a relative dielectric permittivity 3.48. The antenna size is approximately  $0.19\lambda_0 \times$  $0.16\lambda_0$  at the lower working frequency. The antenna characteristics have been evaluated by using the full-wave FITbased CST Microwave Studio [25]. The antenna presents a simulated impedance band ranging from 0.40 up to 9.51 GHz

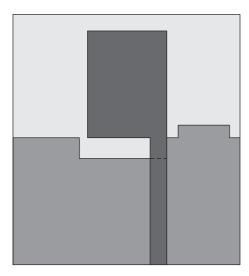


FIGURE 16: A microstrip-fed broadband circularly polarized monopole antenna with a stub integrated in the ground plane [36]. Dark gray upper metal face, medium gray bottom metal face, and light gray dielectric substrate.

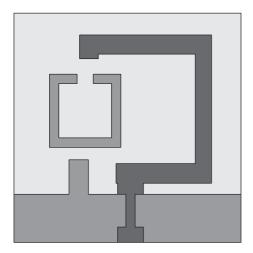


FIGURE 17: A C-shaped circularly polarized monopole antenna [38]. Dark gray upper metal face, medium gray bottom metal face, and light gray dielectric substrate.

and a measured operating band ranging from about 0.41 up to 8.86 GHz.

Best performances are obtained using an excitation technique making use of a trident-shaped tapered CPW to excite an elliptic monopole having a trapeziform ground plane [74] (see Figure 19(f)). The measured impedance bandwidth ranges from 1.0 to 24.1 GHz useful for satellite navigation applications, wireless LANs, and ultrawideband systems.

The antenna can support many existing wireless services, including GPS (1.57–1.58 GHz), GSM1800 (1.71–1.88 GHz), PCS1900 (1.93–1.99 GHz), WLAN (2.5 or 5-6 GHz), and multiband GNNS and UWB (3.1–10.6 GHz). As for the metal plate monopole antenna (3D profile), the adoption of a fork feeding line improves the excitation of the vertical component of the current density with respect to the horizontal one

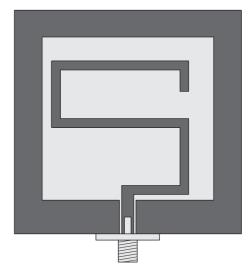


FIGURE 18: A dual-band circularly polarized rectangular slot antenna with an S-shaped monopole [85]. The excitation of edge currents together with those excited on the monopole is suitable to support a circular polarization. Dark gray upper metal face and light gray dielectric substrate.

on the monopole, making the antenna suitable to operate in a more extended frequency band. The antenna, printed on a dielectric substrate of thickness  $1.524\,\mathrm{mm}$  and relative dielectric permittivity of 3.48, has been characterized using the full-wave FIT-based CST Microwave Studio [25]. The radiation patterns show that in the H-plane the antenna has nearly omnidirectional radiation pattern at lower frequencies (from  $1\,\mathrm{GHz}$  to  $5\,\mathrm{GHz}$ ), while the E-plane radiation pattern shows a typical figure-of-eight at the frequency of  $1\,\mathrm{GHz}$ , which is similar to a conventional dipole or to that of a biconical antenna. Further geometries of printed antennas based on trapeziform ground are shown in Figure 19.

An example of an antenna consisting of a dome-topped, bowl-shaped patch with a tapered truncated ground plane is shown in [72]. A notch is introduced below the feeding line near the patch for widening the antenna impedance bandwidth (see Figure 20). In this way the antenna is capable of operating in the frequency band 2.65-13 GHz for UWB applications (FBW = 132%). The antenna, printed on a FR4 substrate having  $\varepsilon_r = 4.4$ , has dimensions of about 18 mm  $\times$  $20 \,\mathrm{mm} \times 1.6 \,\mathrm{mm} \, \left(0.47 \lambda_0 \times 0.53 \lambda_0 \times 0.04 \lambda_0\right)$ , where  $\lambda_0$  is the free-space wavelength at the central working frequency). From an analysis of the return loss, performed using the full-wave FEM-based HFSS [8], it appears that the antenna bandwidth typically depends on the width and depth of the notch realized in the ground plane and on the radius of the bottom part of the monopole. In particular, the upper frequency is greatly affected by the notch depth, while an optimum value of the gap between the radiator and ground plane promotes an increase in the electromagnetic coupling and therefore a widening of the operating band. Furthermore, the analysis of the current distribution excited on the metal surfaces reveals that the top of the radiator is little affected by the surface currents and therefore it has limited impact on the bandwidth. On the contrary, a higher current level

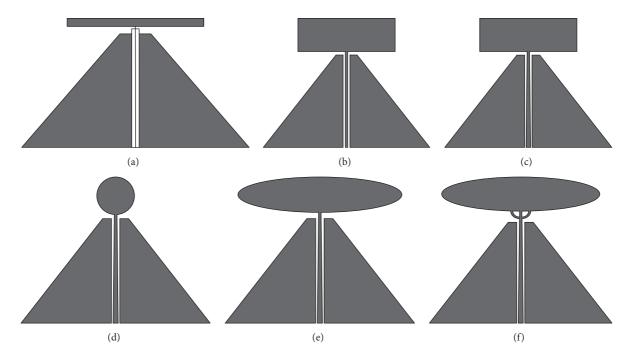


FIGURE 19: Printed antennas with trapeziform ground planes [74]. Different geometries of the monopole and of the excitation systems are shown in the figure.

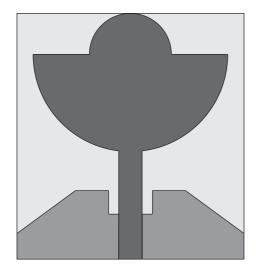


FIGURE 20: Miniaturized UWB printed monopole antenna with a dome-topped, bowl-shaped patch and truncated ground plane provided with a notch [72]. Dark gray upper metal face, medium gray bottom metal face, and light gray dielectric substrate.

is observed around the notch in the ground plane near the feeding line when the operating frequencies are lower, while in the lower patch region when the antenna working frequency increases.

Since antennas equipped with rounded ground plane have characteristics similar to those making use of trapeziform ground planes, for the sake of brevity they will not be taken into consideration. The reader interested in this subject can find information about this class of antennas in [49, 58, 59].

An example of a rectangular monopole antenna, for wireless personal area network (WPAN), wireless body area network (WBAN), indoor localization, biomedical imaging, and UWB applications, making use of a zig-zag shaping of the upper edge of the ground plane (see Figure 21), is reported in [76]. The patch of the proposed antenna, having dimensions of  $14.5 \,\mathrm{mm} \times 14.75 \,\mathrm{mm}$ , is printed on the top side of a FR4 substrate of size of  $30 \text{ mm} \times 22 \text{ mm}$ , thickness 1.6 mm, and relative dielectric permittivity of 4.6. The antenna band ranges from 3.8 up to 15.90 GHz (FBW = 135%), while the maximum gain reaches 5.9 dBi. The increase of the operative band, introduced by the zig-zag profile of the upper edge of the ground plane, is due to the distributed modulation of the distance between the ground plane and the lower part of the monopole. Such modulation allows performing a more effective capacitive coupling between the ground plane and the monopole in a more extended frequency band, thus increasing the bandwidth of the original design by about 45% with respect to the solution without zig-zag contour. In addition, the sawtooth shaping allows reducing the overall size of the antenna and the levels of cross-polarization due to those currents excited in the ground plane by the presence of the asymmetric monopole [86].

Islam and Azim have shown [86] that the effect of the sawtooth shaping becomes more effective at high frequencies. The full-wave MoM-based IE3D [87] has been employed to analyze and design the antenna. With an average gain of 4.04 dBi, the antenna achieves a maximum gain of 5.9 dBi at 9.4 GHz, while the gain variation is less than 2 dBi.

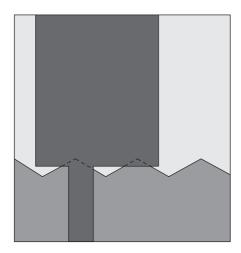


FIGURE 21: A monopole antenna making use of a zig-zag shaping of the upper edge of the ground plane [76]. The adopted zig-zag profile allows performing a more effective electromagnetic coupling between the feeding line and the monopole in a more extended frequency band. Dark gray upper metal face, medium gray bottom metal face, and light gray dielectric substrate.

A further radiating structure making use of a sawtooth ground plane, but with resonant elements placed under the rectangular monopole at the upper edge of the ground plane (where the magnetic field exhibits its maximum level) (see Figure 22) used to achieve three notched bands in the frequency ranges 3.26-3.71 GHz, 5.15-5.37 GHz, and 5.78-5.95 GHz, is presented in [77]. The antenna, which covers the frequency band ranging from 2 up to 11 GHz, has been proposed for UWB applications. A FR4 substrate, having  $\varepsilon_r =$ 4.6,  $\tan \delta = 0.02$ , and thickness 1.6 mm, has been employed to realize the antenna. The overall dimensions of the monopole antenna are of about 30 mm × 22 mm corresponding to about  $0.65\lambda_0 \times 0.48\lambda_0$ , where  $\lambda_0$  is the free-space wavelength at the center frequency of the UWB band. In particular, an analysis of the current distributions excited on the metal filters [88] highlights an inductive behavior of the metal strips, whose entity depends on the length and width of the strips, while the distances between the filter arms or their gap regions determine a capacitive effect. The resonance frequency of the filter can be tuned by varying these two geometrical parameters. The full-wave MoM-based IE3D [87] has been employed to analyze and design the antenna. In conclusion, by measurements and simulations [77] it appears that the strips parameters and their positions with respect to the sawtooth edge influence the width and the center frequency of the notched bands.

4.4. Printed Monopoles with DGS. The removal of metal parts in the radiator and/or in the ground plane, in the neighborhood of which the reactive energy is mainly stored, can be used to increase the antenna impedance bandwidth. This procedure, known in the literature as defected ground structure (DGS), has led to the development of different geometries of slots and notches. The concept of DGS is basically inspired by photonic/electromagnetic bandgap structures (EBG/PBG)

and metamaterials. In fact, EBG and PBG have the ability to inhibit the wave propagation in specific frequency ranges. On the other hand, metamaterials, whose dimensions of the intrusions should be lesser than a quarter wavelength, may not easily be engineered [78]. Given the lower structural complexity and the greater constructive simplicity, the DGS structures have found a greater spread in the design and realization of broadband antennas.

DGS technology is usually inserted beneath the microstrip feeding line since it usually acts as a capacitor and/or an inductance that compensates the original input impedance, thus widening the bandwidth. In fact, the presence of a defect in the ground plane modifies the surface current distributions with a remarkable impact on the antenna radiative performances [37]. Different efforts for improving the bandwidth [37], enhancing the gain [34], and reducing the size of printed monopole antennas [39] using DGSs are discussed in literature. In particular, they have been often employed in multiband and band-notched UWB systems to reduce the impact of electromagnetic interferences with other wireless systems [62, 79] as well as to suppress the higher order harmonics taking place in the active RF circuitry [89].

A large class of DGS structures (see Figure 23) together with some design formulas useful to identifying the working frequencies of said filtering structures is illustrated in [78]. These structures can also be employed in the feeding systems of printed antennas.

A trapezoidal monopole antenna, fed by a microstrip line printed on a dielectric substrate, and with two U-shaped slits, integrated in the ground plane (see Figure 24) to increase the antenna impedance bandwidth, has been presented in [37]. Using the mentioned DGS structure an antenna having a frequency band ranging between the 790 and 2060 MHz (FBW = 90.4%), which is higher of about 112.4% with respect to that without the DGS structure, is obtained. The antenna was analyzed and designed using the fullwave MoM-based IE3D [87]. The antenna, of dimensions of 60.4 mm×103.8 mm, was realized on a RO4003 substrate with a dielectric constant of 3.38 and thickness of 1.524 mm. A stub is placed near the transition between the microstrip line and the monopole to improve the impedance matching. Using two U-shaped DGS structures having different lengths, but identical width, two distinct bandgaps at 2.5 and 5 GHz are obtained. Finally, the measurements results of the radiation patterns show a behavior similar to that of a conventional monopole antenna.

A further example of a broadband monopole antenna, fed by CPW and with cross-shaped DGS structures, to cover the bands 2.44–2.58 GHz and 3.5–8.85 GHz useful for WLAN applications (2.4/5.2/5.8 GHz), WiMAX (2.5/3.5/5.5 GHz), and point-to-point high-speed wireless applications (5.925–8.5 GHz), was proposed in [34]. The antenna is printed on a FR4 substrate, of dimensions 30 mm  $\times$  28.8 mm, with dielectric permittivity  $\varepsilon_r=4.4$ , loss tangent of 0.02, and thickness 1.58 mm (see Figure 25). The antenna was analyzed using the full-wave FEM-based HFSS [8]. The measured gain varies between 4 and 10.8 dBi.

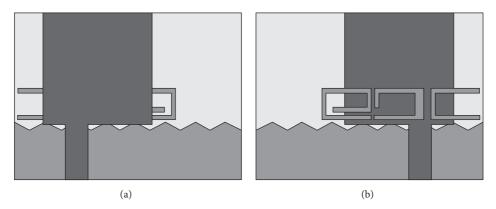


FIGURE 22: Monopole antenna printed on a sawtooth ground plane [77]. Resonant filters used to limit the electromagnetic emission in the frequency bands 3.26–3.71 GHz, 5.15–5.37 GHz, and 5.78–5.95 GHz are shown in figure. Top view (a) and bottom view (b). Dark gray upper metal face, medium gray bottom metal face, and light gray dielectric substrate.

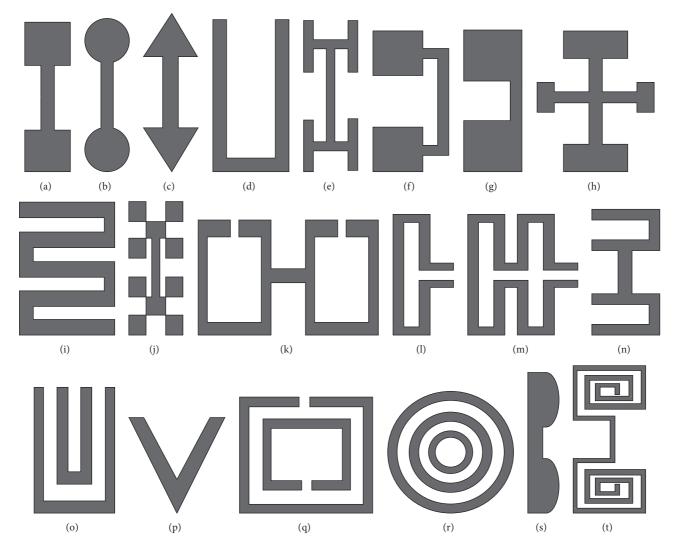


FIGURE 23: Some of the most common DGS structures employed in the applications [78]. (a) Dumbbell-shaped, (b) circular head dumbbell, (c) arrow head dumbbell, (d) U-shaped, (e) H-shaped, (f) squared heads connected with U-slots, (g) squared slots connected with narrow slot at edge, (h) cross-shaped, (i) interdigital, (j) fractal, (k) open loop dumbbell, (l) L-shaped, (m) meander lines, (n) U-head dumbbell, (o) double equilateral U, (p) V-shaped, (q) split-ring resonators, (r) concentric ring shaped, (s) half-circle, and (t) spiral-shaped.

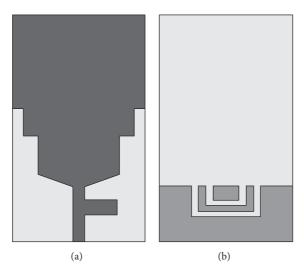


FIGURE 24: A microstrip monopole antenna with a defected ground structure [37]. The presence of the U-shaped DGS structure and of the stub is evident in the figure. Dark gray upper metal face, medium gray bottom metal face, and light gray dielectric substrate. Top view (a) and bottom view (b).

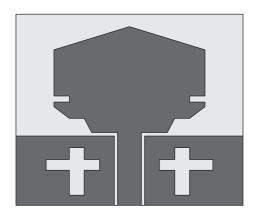


FIGURE 25: A CPW-fed monopole patch antenna with cross-shaped DGS [34]. The presence of the DGS structures is evident in the figure. Dark gray upper metal face and light gray dielectric substrate.

#### 5. Printed Slot Antennas

Recently, printed slot antennas have been introduced because they are very attractive for wideband and UWB applications, especially the so-called printed wide-slot monopole antennas (see Figure 26(a)), which usually consist of a monopole (see Figure 26(b)) and a slot realized in a metal frame acting as ground plane (see Figure 26(c)). In fact, printed slot antennas typically exhibit wide impedance bandwidths and low near-field coupling which make them very suitable for the reduction of the EMC/EMI problems with the nearby devices and objects [90]. However, wideband performances and compact low-profile antennas are generally conflicting requirements that lead to a trade-off between the bandwidth and the antenna size. For this reason, many efforts have been done in literature for reducing the dimensions of slot antennas keeping the same wideband performances [90-92]. To this purpose, several slots geometries, such as square, rectangular, triangular, circular, and elliptical together with suitable excitation techniques making use of cross, fork, triangle, square, and arc monopoles, have been employed and investigated. In particular, a microstrip-fed antenna with a rectangular tuning stub and a tapered slot has been proposed in [91] (see Figure 26(a)).

The structure has a dimensions of about 22 mm×24 mm× 1.6 mm  $(0.52\lambda_0 \times 0.57\lambda_0 \times 0.04\lambda_0)$ , where  $\lambda_0$  is the free-space wavelength at the central frequency) and it is realized on a FR4 Roger substrate having dielectric constant of about 4.6 and loss tangent 0.02. The obtained operational bandwidth, which ranges between 3 and 11.2 GHz (FBW = 115.5%) covering the UWB applications, has been optimized by choosing adequate monopole and slot geometries. In particular, the rectangular monopole shows a better coupling with respect to rounded monopoles, while the tapered slot exhibits a larger impedance bandwidth than circular, elliptical, and square slots, as the current paths around the tapered slot edges are longer. Moreover, the gap between the monopole and the metal frame, illustrated in Figure 26(a), has been opportunely set in order to increase the coupling between the microstrip feeding line and the radiating slot. These characteristics have been carried out using the full-wave MoM-based IE3D [87]. Realized gain ranges between 5.4 and 9.8 dBi, while the radiation patterns at lower frequencies show low crosspolarization (-20 dB) levels. However, when the frequencies increase the polarization purity reduces. Finally, the antenna group delay variations are below 1.3 ns, which can be retained acceptable in UWB communications systems.

Å more compact printed wide-slot antenna has been proposed in [90]. In fact, the structure having dimensions of  $16 \text{ mm} \times 16 \text{ mm}$  ( $0.41\lambda_0 \times 0.41\lambda_0$ , where  $\lambda_0$  is the free-space wavelength at the central frequency) is suitable to cover the 4.5–10.9 GHz frequency band (FBW = 83%) for breast cancer detection and medical imaging. The antenna, formed by a p-shaped slot excited by a rectangular monopole, is printed on a

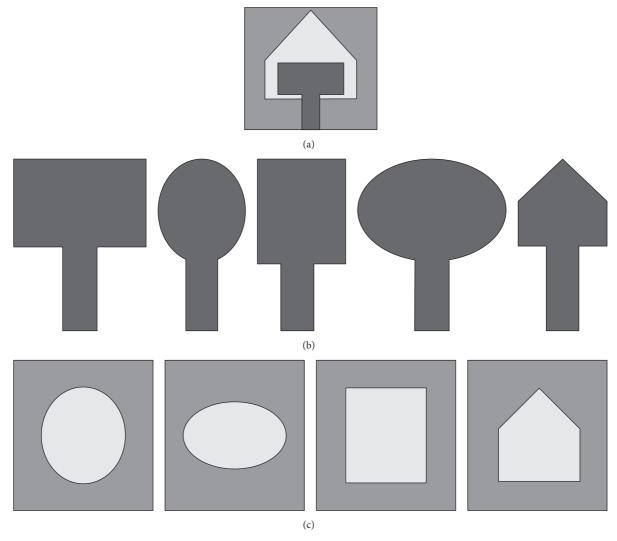


FIGURE 26: Example of a printed wide-slot monopole antenna (a) [91]. Monopole shapes (b) and frame geometries (c) adopted to realize printed wide-slot monopole antennas. Dark gray upper metal face, medium gray bottom metal face, and light gray dielectric substrate.

Rogers substrate of thickness 1.27 mm  $(0.03\lambda_0)$  and dielectric permittivity of 10.2. A 50  $\Omega$  microstrip feeding line connected to a SMA connector is used for the excitation of the antenna (see Figure 27).

The structure has been analyzed and designed with the full-wave FIT-based CST Microwave Studio [25]. Radiation patterns are typically donut-shaped and omnidirectional, resembling those of a dipole antenna. The antenna responses to UWB signals reveal a low distortion of the radiated field with values of the fidelity factor ranging within acceptable limits (>0.5).

As the bandwidth of printed wide-slot antennas is mainly affected by slots and monopoles geometries, a deep investigation of binomial structures has been provided in [93]. In particular, six kinds of antennas have been simulated and measured for different orders of the binomial function (N = 1, 2, 3, 6, 12, and infinite). In particular, when N = 1 the slot and the monopole have a triangular shape, while they



FIGURE 27: A compact UWB p-shaped wide-slot antenna for cancer detection [90]. Dark gray upper metal face, medium gray bottom metal face, and light gray dielectric substrate.

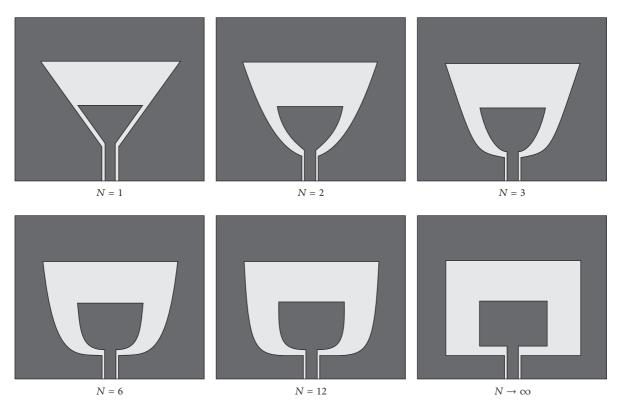


FIGURE 28: The CPW-fed printed binomial wide-slot antennas [93]. Dark gray upper metal face and light gray dielectric substrate.

assume a rectangular shape when N tends to infinite. Some examples of CPW-fed printed wide-slot antenna geometries for different values of the binomial order N are depicted in Figure 28.

The proposed antennas are fabricated on a 35 mm  $\times$  40 mm dielectric Arlon TC600 substrate of thickness 0.787 mm and relative permittivity  $\varepsilon_r=6.15$ . The antenna features have been determined by means of the full-wave FEM-based HFSS [8]. Simulated fractional bandwidths range between 10.8% (triangular case) and 108.4% (rectangular case) as the antenna binomial order increases, while the measured values range between 9.3% and 99.7%. In general, radiation patterns in the *E*-plane show cross-polarization levels that are lower than  $-30~{\rm dB}$  due to the symmetry of the structures. On the other hand, in *H*-plane antennas are asymmetric and thus cross-polarized components are higher. However, when *N* increases the structures exhibit a reduced cross-polarized field level in the *H*-plane. Realized antenna gains vary between 3.3 and 5.5 dBi.

### 6. Printed Dipole Antennas

Although monopoles antennas present several advantages they do not radiate along their axes, making an array of monopoles not suitable to radiate in that direction. This can be disadvantageous if a radiating system, having a high-gain and compact dimensions, has to be integrated into a low-profile host platform. To overcome these drawbacks printed

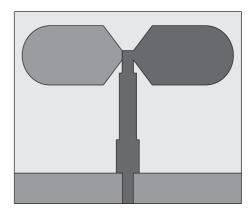
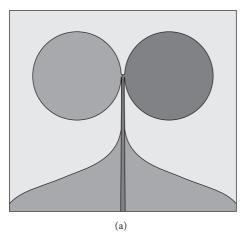


FIGURE 29: A printed double-sided rounded bow-tie antenna (DSRBA) [94]. Dark gray upper metal face, medium gray bottom metal face, and light gray dielectric substrate.

dipole antennas, having a proper geometry and equipped with a suitable metal screen, can be advantageously used. To this end, in this section a brief description of the main design solutions proposed in the literature is provided.

Two printed double-sided rounded bow-tie antennas (DSRBAs) for UWB applications (see Figure 29) have been proposed in [94]. The first antenna is printed on a dielectric substrate ROGER RO3600 of dimensions  $36 \, \mathrm{mm} \times 36 \, \mathrm{mm} \times 1.27 \, \mathrm{mm}$ , dielectric permittivity  $\varepsilon_r = 6$ , and loss tangent 0.002. The second one is printed on a liquid crystal polymer



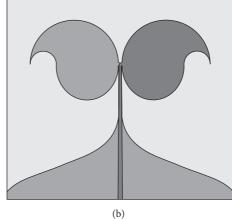


FIGURE 30: Geometry of the circular (a) and drop-shaped (b) antipodal dipole antenna employing an unbalanced feeding line [95]. Dark gray upper metal face, medium gray bottom metal face, and light gray dielectric substrate.

(LCP) of dimensions 32.4 mm  $\times$  32.4 mm  $\times$  1.14 mm,  $\varepsilon_r =$ 3.1, and  $\tan \delta = 0.002$ , whose properties are suitable for conformal applications. Even though for both antennas the radiation characteristics are similar, it is shown that the geometry presenting rounded arms exhibits better performances in terms of bandwidth and cross-polarization levels with respect to the design solution based on flat-ended arms (rounded arms limit the level of the electric charges generally excited on sharp metallic edges, thereby reducing the reactive energy storage). In fact, a 59% of additional bandwidth and a -10 dB lower cross-polarization level are achieved. The antenna gain ranges between 0.7 and 5.5 dBi, while the relative group delay is stable and acceptable within the UWB frequency spectrum. The main characteristics of the antennas have been derived using a homemade software based on a finite-element boundary integral formulation that employs tangential vector finite elements (TVFEs) and tetrahedral meshing and the full-wave FEM-based HFSS [8] typically used for high frequencies applications.

Two printed dipole antennas with antipodal circular and drop-shaped radiators have been proposed in [95] (see Figure 30). These antennas, which exhibit a lower level of surface waves and an excellent response to short pulse signals, are particularly useful for wideband, WLAN, WiMAX, and UWB applications. These antennas can be employed in portable devices (mobile PC, printers, scanners, DVD players, and digital projectors), in radio base stations, and in the nextgeneration textile fabrics for wearable applications, as they are printed on a CuClad217 thin flexible substrate that is more conformal and less prone to surface degradation. Such dielectric substrate has dimensions of about 51 mm×45 mm× 0.38 mm, dielectric permittivity  $\varepsilon_r = 2.17$ , and  $\tan \delta =$ 0.0009. The antenna is excited by a suitable tapered transmission line to achieve an adequate  $50 \Omega$  impedance matching within the UWB band. The two structures, which have been analyzed by means of a homemade locally conformal finitedifference time-domain (FDTD) numerical technique [96], are characterized by half-wavelength dipole-like radiation patterns up to 5.25 GHz. Furthermore, the particular contour

of the drop-shaped antenna is suitable to guide the electromagnetic energy along the backside contour of the antenna arms toward the boresight direction resulting in a higher radiation level, as well as in a reduced energy emission in the backward direction, where electronic circuitry is typically located. This feature is also enhanced by the rear shaped planar reflector. The relative group delay ranges between -0.1 and 0.25 ns resulting in being excellent for UWB radar and wireless applications [82, 97]. Finally, the antipodal characteristic of drop-shaped antenna allows obtaining compact antenna arrays for frequency or time-domain applications. These important features related to the particular radiative properties of said antenna make it particularly useful to be integrated not only in mobile devices, but also in high-gain RF base stations.

A different planar dipole antenna geometry has been introduced in [98]. The antenna, of overall dimensions  $40~\rm mm \times 65.3~\rm mm \times 0.8~\rm mm$ , exhibits an operative bandwidth ranging between 2.8 and 10.9 GHz (FBW = 118%) suitable for UWB applications. The dipole consists of two semi-elliptical-ended arms connected by a shorting bridge, which reduces the arms' length, increases the gain, enhances the response's quality, and improves the impedance bandwidth. The antenna is excited with a wideband balun composed of a Chebyshev three-section transformer connected to a 50  $\Omega$  microstrip line. The feeding line and the impedance transformer are printed on a grounded dielectric slab having dielectric permittivity  $\varepsilon_r=3.38$ , while the dipole is printed in a region of the dielectric slab without ground plane to increase the antenna operating band (see Figure 31).

Numerical simulations have been performed by means of the full-wave MoM-based IE3D [87]. Although the antenna is relatively small, its peak gains are comparable with those of a bulkier dipole antenna and their values range between 2.6 and 5 dBi with the balun and between 2.5 and 6.5 dBi without the balun. It is observed that the three impedance steps realized in the balun are the major cause for spurious radiation and high cross-polarization levels. On the other hand, the shorting bridge avoids the current to be concentrated around

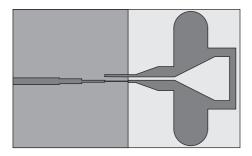


FIGURE 31: A UWB dipole antenna with semi-elliptical-ended arms and shorting bridge [98]. Dark gray upper metal face, medium gray bottom metal face, and light gray dielectric substrate.

the tapered V-shaped edges of the arms thus increasing the maximum gain of the antenna whose radiating process in this way mainly occurs along the shorting bridge. Finally, the transient antenna response to a sine modulated Gaussian monopulse shows that the antenna, provided with a shorting bridge, experiences a more stable linear phase response and a less spread of the received waveform with respect to the case without shorting bridge. Anyway, the UWB responses of both antennas are affected by small ringings.

A design solution useful to improve the radiation characteristics of an angle-dipole antenna for 5G mobile wireless communications, within the frequency band 26.7 GHz and 30.6 GHz (FBW = 13.6%), has been proposed in [99]. The printed dipole is realized on a dielectric substrate RT/Duroid 5880 having thickness of approximately 0.254 mm, dielectric relative permittivity  $\varepsilon_r = 2.2$ , and  $\tan \delta = 0.0009$ . On each side of the substrate two 45° angled-radiators, fed by a parallel-plate transmission line (see Figure 32), are printed. Anyway said dipole does not present high levels of frontto-back ratio, the gain is less than 3 dB, and the radiation pattern is asymmetric in the H-plane. For this reason, the antenna is equipped with a resonant cavity of dimensions  $5.2 \,\mathrm{mm} \times 5.2 \,\mathrm{mm} \times 3.5 \,\mathrm{mm} \,(0.5\lambda_0 \times 0.5\lambda_0 \times 0.34\lambda_0)$ , where  $\lambda_0$ is the free-space wavelength at  $f = 28 \,\text{GHz}$ ) within which the radiator is located. In this way, the bandwidth is increased by 5.4%, the gain is increased by about 4.5 dB reaching measured values ranging between 6.6 and 8 dBi, and the levels of frontto-back ratio are equal to approximately 18.5 dB, while the beamwidth is approximately equal to 72° for the E-plane and 69° for the H-plane in such a way that the desired symmetry of the radiation pattern is restored. The resulting structure has been used to realize a linear array of eight elements excited via a T-junction power divider in order to provide a tapered excitation. In this way, a maximum scan beam of about 40°, with side lobe levels (SLLs) of approximately −15 dB, is obtained. The full-wave FIT-based CST Microwave Studio [25] has been employed to analyze the antenna.

#### 7. Directional UWB Antennas

Omnidirectional antennas useful for mobile applications are not suitable to support high-gain point-to-point wireless communications, as well as to realize spatial diversity schemes useful to reduce multipath fading effects, or high resolution UWB radar for objects detection and imaging applications. To this end, directional UWB antennas making use of suitable reflective structures have been recently proposed in literature [53–57, 73]. In this section some examples of this important class of antennas are illustrated.

A low-profile directional self-grounded bow-tie antenna for UWB applications has been presented in [73]. The antenna, which covers a frequency range of 2-15 GHz with about −10 dB reflection coefficient, stable radiation patterns, and good time-domain impulse response, can be usefully employed for sensor networks, UWB short-range communication systems, UWB radar for high resolution imaging systems, and super sensitive UWB radio astronomy. The antenna of dimensions  $54 \,\mathrm{mm} \times 58 \,\mathrm{mm} \times 24 \,\mathrm{mm}$ , whose geometry is shown in Figure 33, assumes the so-called seagull-oversea configuration. The metallic arms are connected together, forming the metal reflector of the antenna, while a suitable balun, connected at the feeding point and housed behind the reflector, is employed to match a 50  $\Omega$  microstrip feeding line to a 150  $\Omega$  twin-line transmission line attached at the bow-tie arms. A careful full-wave analysis, performed using the FIT technique [25], has highlighted a directional antenna behavior with a directivity of about 5-8 dBi and a maximum group delay of about 1 ns, when the opening angle of the antenna arms is 60°. These radiation characteristics, induced by the full ground design solution, are strongly demanded in many applications, such as, UWB radar and tracking systems, UWB indoor geolocation systems, and UWB sensing and microwave tomography.

A UWB antenna with unidirectional radiation pattern, useful for broadband radar applications or for point-to-point wireless communications, consisting in a horizontal bowtie electric dipole, a center-fed loop antenna acting as a magnetic dipole, and a rectangular cavity, was proposed in [53]. The bow-tie electric dipole, printed on the top side of a dielectric substrate having relative permittivity 2.2 and thickness 0.508 mm, is connected through six vias to two rectangular patches printed on the dielectric backside (see Figure 34). These patches are joined to the feeding line by means of a vertical balun consisting in a microstrip-tostripline transition having the purpose to match the 50  $\Omega$ microstrip line to that of a 90  $\Omega$  balanced stripline. This transition, mounted vertically on the center of the ground plane, is printed on a dielectric substrate with  $\varepsilon_r = 2.2$ and thickness 0.787 mm. A series of high-impedance stub is introduced at the bottom of the balun to improve the impedance matching. Finally, two metal cylinders placed near the feed region connect the horizontal radiating structure to the ground plane, thereby allowing the realization of a center-fed loop antenna, which works as a magnetic dipole. The overall size of the structure including the reflector is  $60 \, \text{mm} \times 50 \, \text{mm} \times 12.4 \, \text{mm}$ . The full-wave FEM-based HFSS [7] was adopted to analyze and design the antenna. The impedance bandwidth ranges between 3.08 and 10.6 GHz (FBW of about 110%), while the realized antenna gain varies between 6.8 and 10.6 dBi. The radiation patterns show a good directional behavior characterized by a front-to-back ratio above 20 dB below 7 GHz, which drops to about 13 dB at

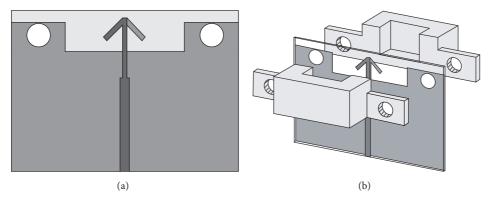


FIGURE 32: A cavity-backed angled-dipole antenna [99]. Front view (a) and tridimensional view (b). The flanged cavity is observable in the figure. Dark gray upper metal face, medium gray bottom metal face, and light gray dielectric substrate.

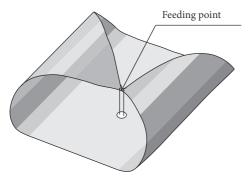


FIGURE 33: A low-profile directional self-grounded bow-tie antenna [73].

higher frequencies. The cross-polarization levels are below –20 dB in the whole frequency band. The antenna response to UWB signals (coincident with 5th-derivative of the Gaussian pulse) shows a limited signal distortion and a ringing tail caused by the resonant processes taking place in the radiator and in cavity acting as reflector.

A UWB low-profile antenna for low UWB frequencies applications (1–3 GHz) presenting directional characteristics and high front-to-back ratio is presented in [54]. These characteristics can be useful in ground-penetrating radar, microwave detection and imaging, and radio base stations. The antenna is realized using a slab of GIL GML 1032 substrate with relative dielectric permittivity 3.2 and thickness 1.52 mm on the opposite faces of which the arms of a bowtie-shaped flare are printed.

Two circular segments having a suitable radius are incorporated in each bow-tie arm to increase the effective edge length of the flare. In particular, in the upper face of the slab a 50  $\Omega$  microstrip line, whose ground is composed of the bow-tie-shaped arm printed on the opposite face (see Figure 35), is adopted to excite the antenna. Both arms have two slits separated by a small gap. The terminations of the two arms are welded to two vertical metal plates welded in turn on a grounded dielectric slab having the same characteristics as the one used to realize the upper part of the antenna. The overall size of the proposed antenna is of about

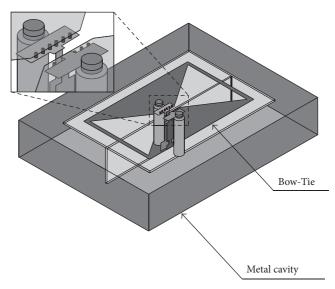


FIGURE 34: Geometry of the magnetoelectric dipole for unidirectional UWB communications [53]. The vias used to connect the antenna to the balun are indicated in the figure.

 $70~\mathrm{mm} \times 60~\mathrm{mm} \times 15~\mathrm{mm}$  corresponding to about  $\lambda_\mathrm{eff}/3 \times \lambda_\mathrm{eff}/4 \times 0.07 \lambda_\mathrm{eff}$ , where  $\lambda_\mathrm{eff}$  is the effective wavelength at the lower operative frequency. The antenna exhibits directional patterns with a fractional bandwidth of about 77% (from about 1.27 up to 2.57 GHz), average gain of about 5 dBi, up to 15 dB front-to-back ratio and  $-20~\mathrm{dB}$  of cross-polarization levels in both the E- and H-plane. Moreover, thanks to the shorting walls placed perpendicular to the edges of the top and bottom layers, most of the side radiation is blocked. The antenna analysis and design have been performed using the full-wave FEM-based HFSS [8]. A good agreement between numerical results and measurements is observed.

A suitable choice of the antennas should be made when they are integrated in communication systems working in environments where the multipath fading can result in a significant reduction of the communication system performance. In such environments, antenna diversity techniques should be employed, since they can improve transmission

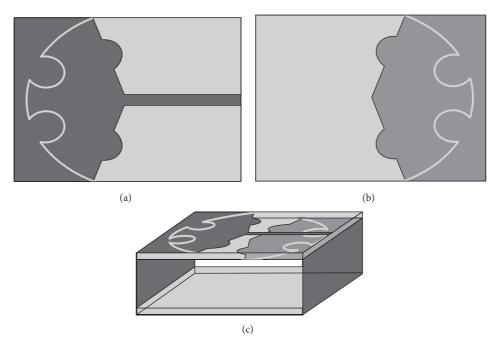


FIGURE 35: Geometry of a compact directional three-dimensional folded antenna for UWB applications [54]. Top view (a), bottom view (b), and tridimensional view (c).

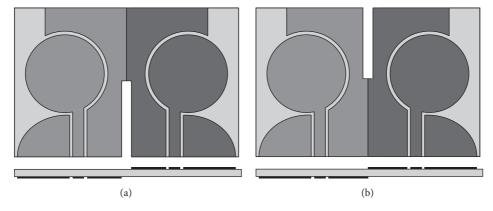


FIGURE 36: Geometry of the cross-configured directional UWB antenna [55]. The two structures (a) and (b) used to achieve a cross-configuration antenna are shown in figure. The radiation process takes place in the region between the monopole and rounded ground plane.

quality by mitigating the multipath fading effects [18]. To this end, a UWB antenna which can be used as a directional antenna for mobile systems, or to realize multidirectional antenna systems, having high interelement isolation, for radio base stations, has been presented in [55]. The antenna is printed on a FR4 substrate of size  $28 \, \mathrm{mm} \times 44 \, \mathrm{mm}$  (size  $28 \, \mathrm{mm} \times 88 \, \mathrm{mm}$  for the four-element cross-configuration) having thickness  $1.4 \, \mathrm{mm}$ ,  $\varepsilon_r = 4.4$ , and  $\tan \delta = 0.025$ . The antenna characteristics have been carried out using the full-wave FIT-based CST Microwave Studio [25].

The radiator consists of a circular monopole, excited by a CPW line shifted with respect to the symmetry plane of the monopole, surrounded by a suitably shaped ground plane acting as reflector (see Figure 36). The reflector profile and its asymmetry with respect to the feeding line give rise in an antenna radiation beam oriented in the orthogonal direction (right/left) of the feeding line. In fact, the profiles of the monopole and the ground plane realize a sort of pseudo-Vivaldi antenna in the region where the ground plane is rounded. These features can be used to achieve a cross-configuration composed of four monopoles. This configuration (see Figure 36) allows covering the four spatial quadrants maintaining a high interelement isolation (>20 dB) between the inputs of the four antennas allowing in this way achieving the required multidirectional pattern diversity characteristics. The experimental measurements performed on an antenna prototype have shown that the antenna gain varies between 4.3 and 7.5 dBi in the frequency range 1.3–10 GHz. Therefore, in addition to UWB applications it can also be adopted for Bluetooth/Wi-Fi and WiMAX applications.

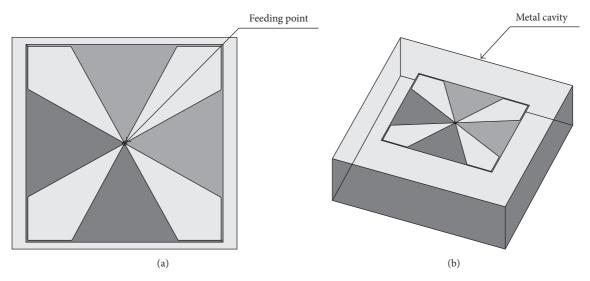


FIGURE 37: Geometry of a dual polarized wideband directional coupled sectorial loop antenna [56]. Top view (a) and tridimensional view (b).

Dual polarized wideband directional coupled sectorial loop antennas for radar and mobile base-station applications are presented in [56]. Two slightly different design solutions based on a dual polarized radiating element are proposed. For radar applications, the radiating element is used to excite the two degenerate modes (TE<sub>10</sub>, TE<sub>01</sub>) of a cavity with square cross-section. The cavity of dimensions 160 mm  $\times$  $160 \,\mathrm{mm} \times 60 \,\mathrm{mm}$  is employed to improve the directivity useful for radar applications, such as those employed in through-wall imaging systems, since at least two antennas are typically used (one as transmitter and one as receiver). As for such applications higher VSWR can be tolerated, the antenna was designed so as to achieve the maximum bandwidth (approximately one octave) with a VSWR of 2.5. The proposed antenna structure, printed on a RO4003C substrate with relative permittivity 3.55, loss tangent 0.0021, and thickness 1.524 mm, is shown in Figure 37. It consists of a dual polarized exciting element backed by a square cross-section cavity. The polarizing element consists of two orthogonal coupled sectorial loops antennas (OCSLAs). Each sectorial loop is composed of two opposite triangular patches and a rectangular ring around the outside. Two tapered microstrip lines arranged orthogonally and connected to two vertical coaxial cables placed inside the cavity are used to excite the antenna so as to support horizontally/vertically or circularly polarized radiated fields. Gains of about 10 dB, with similar beamwidth in the *H*- and *E*-plane, and high front-toback ratios are achieved.

A different design solution, useful for the mobile base-station applications (1710–2170 MHz), making use of the same radiating element placed over a ground plane, is instead adopted to obtain an antenna (size  $71 \, \text{mm} \times 71 \, \text{mm} \times 35 \, \text{mm}$ ) with a wider beam, a higher operating bandwidth, and a better SWR (less than 1.5). This design solution employs a printed balun to excite the antenna. Without cavity a maximum gain of about 8 dBi along the boresight is obtained. The

analysis and design of both antennas have been performed using the full-wave FEM-based HFSS [8].

#### 8. Metamaterial Antennas

Metamaterials are artificial structures composed of periodic or nonperiodic subwavelength macrocells, whose their effective medium properties can be controlled by designing the macrounits so as to realize special materials that do not exist in nature. Several structures, such as, the split-ring resonators (SRRs), the complementary SRRs (CSRRs), the transmission line- (TL-) based structures, and the artificial magnetic conductors (AMCs), have been introduced in literature with the aim of improving the performance of microwave circuits and antennas. In this section, some examples of this important class of antennas are provided with the aim to enable the reader to have a broader view of the technologies that can be used to realize wireless communication systems of new generation.

Two multiband antennas making use of metamaterials have been developed with the aim of covering the WiMAX 2.5/3.5/5.5 GHz and the WLAN 5.2/5.8 GHz bands [100]. Both the antennas are printed on a dielectric substrate with relative permittivity of 2.65 and thickness of 1mm. The overall dimensions of the radiating structures are of  $35 \,\mathrm{mm} \times 35 \,\mathrm{mm} \times 1 \,\mathrm{mm}$ . The full-wave FEM-based HFSS [8] was adopted to analyze and design the antennas. The first antenna consists of a rectangular monopole loaded by means of an electric-LC (ELC) structure placed under the monopole. This structure transforms the monopole from a dual-band in a three-band antenna providing coverage in the bands 2.5/3.5/5.5 GHz, thereby meeting the requirements for the WLAN and WiMAX applications. Two slits arranged near the feeding line are used to improve the impedance matching. In addition to the ELC structure placed under the monopole, the second antenna integrates an electronic

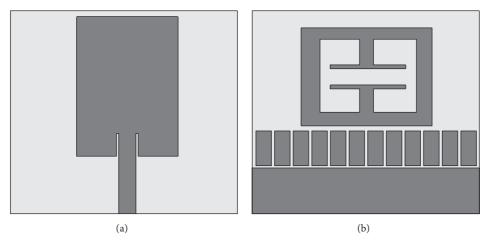


FIGURE 38: Geometry of a small metamaterial antenna with ELC structure [100]. Front view (a) and back view (b). Dark gray upper metal face and light gray dielectric substrate.

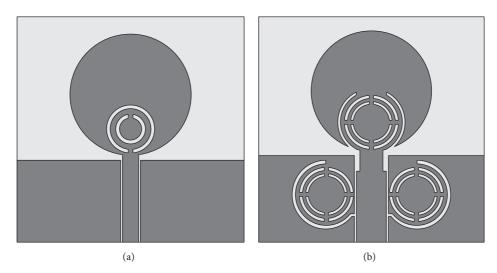


FIGURE 39: A UWB antenna employing metamaterials to realize a notched band useful to reduce interference with WLAN communication systems [101]. (a) CSRR integrated in the monopole; (b) CSRRs near the CPW. The CSRRs are located near the regions where the magnetic field exhibits its higher values. Dark gray upper metal face and light gray dielectric substrate.

band gap (EBG) structure in the upper part of the ground plane (see Figure 38) to get a good impedance matching in frequency range 2.49–2.53 GHz and a UWB behavior in the frequency range 2.95–6.07 GHz. It is observed that both antennas have stable omnidirectional radiation pattern in *H*-plane and an 8-shaped radiation pattern in the *E*-plane.

A transparent antenna useful for short-range UWB applications making use of metamaterials was presented in [101]. This antenna, which can be easily attached on glass panels and windows of homes and buildings, is realized using a transparent conductive material known as silver-coated thin films (AgHT-4). This film, consisting of a thin layer of AgHT-8 (height 0.053 mm) placed on a PET polymer substrate of relative permittivity 3.23, height 0.12 mm, and surface resistivity  $4\,\Omega/\text{m}^2$ , has been employed to realize a UWB antenna of about 30 mm  $\times$  30 mm (see Figure 39). To avoid

interference with WLAN communication systems working in the same environment a bandstop filter tuned at 5.8 GHz, and making use of complementary split-ring resonators (CSRRs), has been integrated in the antenna. Split-ring resonators have been adopted as they are one of the artificial metamaterial structures that exhibit negative permittivity/permeability properties. In any case, three CSRRs structures, two in the ground plane near the CWP and one in the circular monopole, where the magnetic field exhibits its higher values (see Figure 39), are necessary to obtain a notched band of only -4 dB at 5.8 GHz. Such poor performance occurs due to the high losses presented by the AgHT-4, which are responsible for a significant reduction of the resonant process taking place in the CSRRs. As expected the losses reduce the antenna gain that, within the UWB band, varies between -11 dBi and -5 dBi. These results are similar with those observed

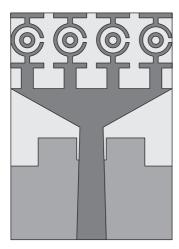


FIGURE 40: A metamaterial UWB antenna [102]. The four cells composed of two capacitance-loaded strips (CLSs), a split-ring, and a gapless ring, forming the metamaterial loading of the upper edge of the triangular patch, are evident in the figure. Dark gray upper metal face, medium gray bottom metal face, and light gray dielectric substrate.

in the transparent antennas. The analysis and design of the antenna have been performed using the full-wave FIT-based CST Microwave Studio [25].

A compact antenna based on metamaterial structures for UWB applications having a different geometry was presented in [102]. The antenna, whose overall dimensions are  $27.16\,\mathrm{mm} \times 18.97\,\mathrm{mm}$ , has been printed on both sides of a FR4 dielectric substrate of permittivity 4.6, loss tangent of 0.02, and thickness 1.6 mm. The antenna consists of four unit cells, which exhibit negative equivalent permeability and permittivity, attached to the upper edge of a triangular patch. Three rectangular slots are realized in the ground plane near the tapered microstrip feeding line (see Figure 40) to improve the impedance matching.

The metamaterial unit cell is composed of two capacitanceloaded strips (CLSs), a split-ring and a gapless ring. The four unit cells form a sort of periodic structure useful to provide an impedance bandwidth ranging from 3.07 up to 19.91 GHz with excellent radiation characteristics, high-gain, efficiency, and adequate capability of pulse handling. The measured gain exhibits its maximum level of 8.57 dBi at 13.5 GHz, a minimum level of 2.71 dBi at 18.6 GHz, and an average level of 5.62 dBi over the working frequency bands (3.07-19.91 GHz). A quite stable omnidirectional radiation pattern in *H*-plane and an 8-shaped radiation pattern in the *E*-plane are observed. The gain variations and the ringing observed in the antenna response to pulse signals reveal the presence of resonant phenomena taking place in the structure forming the metamaterial as well as in the antenna geometry. The analysis and design of the antenna have been performed using the full-wave FIT-based CST Microwave Studio [25].

Additional information concerning the same subject can be found in [103–108].

#### 9. Wearable Antennas

A growing interest in less bulky low-cost communication systems, which can be easily hidden into garments, helmets, glasses, or shoes, textile, and flexible wearable antennas is spreading among the scientific community. Indeed, wearable devices, exhibiting smaller profiles and lesser stiffness than the printed technological counterpart, can easily allow the civil defense, the police forces, the firefighters as well as the sportsmen, and so forth to focus directly on their specific activities. Moreover, the wearability of the communication system may be important also to support the remote control of biological parameters of not hospitalized patients or of athletes during sports activities. To this purpose, WBANs (Wireless Body Area Networks) for on-body, off-body, and in-body communications sceneries were regulated by the IEEE 801.15 standard [109].

Because of their relevance, in this section after an overview of the main dielectric and conductive textile materials useful to the realization of wearable antennas, some of the most recent progresses concerning this important class of antennas will be discussed.

9.1. Dielectric and Conductive Textile Materials for Wearable Antennas. In general, wearable antennas consist of metallic components (radiating patch and ground plane) printed on a dielectric substrate, whose geometries fall into the antenna classes analyzed in the previous sections. Therefore, for the sake of brevity the characteristics of the commonly employed materials for the realization of textile and flexible antennas are reported and analyzed in this subsection. In particular, some of their fundamental parameters such as conductivity, permittivity, and loss tangent are indicated for providing useful information during the design and realization phases of said antennas.

9.1.1. Dielectrics for Wearable Antennas. The dielectric materials used to realize wearable antennas are mostly affected by different factors such as frequency, temperature, surface roughness, and moisture content [110]. In particular, the level of the moisture absorbed by the fabrics is described by the Moisture Regain (MR), which is defined as follows:

$$MR = \frac{m_{\text{cond}} - m_{\text{dry}}}{m_{\text{dry}}},$$
 (1)

where  $m_{\rm cond}$  is the weight of the material at equilibrium after conditioning in a climate chamber and  $m_{\rm dry}$  is the mass of the material in dry state [110]. Some of the most common dielectric materials and their characteristics are reported in Table 2, while additional information of the mostly employed commercial fabrics is shortly described below.

Fleece is a common textile composed of synthetic woven polyester felted on both sides. As all the nonwoven synthetic materials that are classified as hydrophobic, fleece is a water-repellent material [110]. However, it is not waterproof. Its low-loss tangent makes it very suitable for high-gain and high-efficiency applications [125]. Fleece fabric is normally used for sportswear and leisurewear.

TABLE 2: Nonconductive fabrics characteristics.

| Nonconductive fabric           | $\mathcal{E}_r$ | $	an \delta$ | Ref.       |
|--------------------------------|-----------------|--------------|------------|
| Cordura®                       | 1.90            | 0.0098       | [111, 112] |
| Cotton                         | 1.60            | 0.0400       | [110-113]  |
| 100% polyester                 | 1.90            | 0.0045       | [111, 112] |
| Quartzel® Fabric               | 1.95            | 0.0004       | [111, 112] |
| Cordura/Lycra®                 | 1.50            | 0.0093       | [111, 112] |
| Jeans cotton                   | 1.67            | _            | [114]      |
| Polycot                        | 1.56            | _            | [114]      |
| Polyester                      | 1.44            | _            | [114]      |
| Foam (polyurethane)            | 1.24            | 0.0213       | [110]      |
| Rubber protective foam         | 1.495           | 0.016        | [110, 115] |
| Polyethylenteraphthalate (PET) | 1.173           | 0.0027       | [110]      |
| Pile                           | 1.12            | 0.009        | [116]      |
| Denim                          | 1.6-1.65        | 0.05         | [117]      |
| Polydimethylsiloxane (PDMS)    | From 3 to 20    | < 0.02       | [118, 119] |
| Velcro®                        | 1.34            | 0.006        | [120]      |
| Leather                        | 2.72            | 0.02         | [121]      |
| Silk                           | 1.75            | 0.012        | [122]      |
| Felt                           | 1.215-1.225     | 0.016        | [117]      |
| Fleece                         | 1.17            | 0.0035       | [122, 123] |
| Flannel (0.3–20 GHz)           | 1.7             | 0.0250       | [124]      |

Denim fabric is a typical textile substrate with firm surface, which is robust against compression operations. Besides, denim features durability, inelasticity (useful for keeping constant the dielectric permittivity under bending conditions [122]), cost-effectiveness, and low thickness (about 0.7 mm) [126]. However, when under wet conditions or after fully immersion in water, a degradation of UWB signals can be observed [127].

Felt is often used for textile antennas as it is flexible, soft, and comfortable. Antennas employing felt substrates exhibit lower return loss values with respect to those using fleece, foam, and conventional FR-4 substrates. In addition, monopole antennas realized with the fleece substrate show the wider fractional impedance bandwidth [128].

*Cotton* is an easy-care textile, strong, durable, and more cost-effective than other substrates such as denim, felt, and jeans [129]. However, cotton is more suitable than other rigid substrates when bending and crumpling conditions occur.

9.1.2. Conductive Textiles. To integrate metallic parts in a textile flexible patch antenna, some conductive fabrics, whose characteristics are reported in Table 3, have been analyzed for different kind of applications and under several environmental conditions. Among them, four kinds of conductive materials can be identified:

- (i) Flectron®
- (ii) Shieldex Nora®
- (iii) Shieldit Super®
- (iv) Shieldit Zelt®

TABLE 3: Conductive textiles characteristics.

| Conductive material                 | Surface resistance (Ω/square) | Equivalent conductivity (S/m) | Thickness (mm) |
|-------------------------------------|-------------------------------|-------------------------------|----------------|
| Flectron [130]                      | 0.07                          | $0.79 \times 10^5$            | 0.18           |
| Shieldit Super [131]                | 0.05                          | $1.18 \times 10^{5}$          | 0.17           |
| Shieldex Nora [132]                 | 0.03                          | $3.33 \times 10^{5}$          | 0.1            |
| Zelt [133]                          | 0.01                          | $16.7\times10^5$              | 0.06           |
| Copper foil [131]                   | 0.0005                        | $571\times10^5$               | 0.035          |
| Pure copper taffeta<br>fabric [131] | 0.05                          | $2.50\times10^5$              | 0.08           |

Flectron Nickel/Copper Polyester Nonwoven is a unique fabric, manufactured using a patented, proprietary technology. The base layer is copper, while the outer layer, made of nickel, is robust against corrosion. This technology combines the properties of these metals with the lightweight, permeability breathability, and flexibility of a nonwoven textile. Nickel/Copper Polyester Nonwoven textile offers excellent surface conductivity (<0.07  $\Omega$ /square), shielding effectiveness, soldering robustness, and corrosion resistance for a variety of applications (architectural shielding, gaskets, shielding materials, and ribbon) [134]. Some other kinds of Flectron textiles with different characteristics can be found in [135].

Nylon fabric, Shieldex Nora from Shieldex Trading, Inc., is a woven high conductivity metal (surface resistivity of  $0.03\,\Omega$ /square) which is suitable for RF circuits and antennas operating in the ISM (Industrial Scientific Medical) band. It is a nylon fabric, plated with three metallized layers (Ni/Cu/Ag),

which ensure protection against corrosion and abrasion, as well as extreme flexibility [132].

Shieldit Super is a kind of material produced by Less EMF Inc., useful for pouches, wall covering, gaskets, grounding, and liners. It is a high quality flame retardant fabric for radiofrequency and microwave shielding. It is plated with nickel and copper (for achieving excellent shielding and robustness against corrosion), and it is coated on one side with a nonconductive hot melt adhesive (which is activated at  $130^{\circ}$ C) so that it can be ironed on cotton, wood, glass, and paper or rolled into a tube and heat seal. It exhibits typical thickness of about 0.17 mm with surface resistivity below  $0.05~\Omega/s$ quare. It can be resistant to maximum temperatures of  $200^{\circ}$ C and it can be easily washed [124, 136].

Shieldit Zelt is a high conductivity nylon fabric (the surface resistivity is lower than  $1\Omega$ /square) coated with copper and tin. It is an excellent material for shielding and it can be easily cut and sewn offering excellent corrosion resistance. It can be used for curtains, bedding, garments, wire sheathing, enclosures, and so forth [133, 137]. Some vendors that sell conductive fabrics are Less EMF Inc., Swift Textile Metallizing, LLC, Marktek Inc., Shieldex, and Metal Textiles Corporation [138].

9.1.3. Embroidered Textiles. The so-called e-textiles are usually made of conductive yarns embroidered in warp and weft directions, typically plated on a polymer-based substrate. In some cases, conventional and conductive threads are used together to reduce the cost of the textile antenna, which usually is very expansive. Nevertheless, the e-textile antenna typically achieves lower gain values with respect to a conventional antenna made of an all-metallic radiator as it has been highlighted in [139]. In fact, the weft in the ground plane can induce a local anisotropic behavior or abrupt changes in the current paths. Therefore, soldering and conductive epoxy have been used to enable orthogonal current paths so as to achieve acceptable gain performances [139].

9.1.4. Conductive Inks. Textile and wearable antennas sometimes need to be washed and cleaned. To this purpose, in [140] the authors investigated the differences between conductive inks and electrotextiles behaviors during several wet-drywet cycles. In particular, the proposed printed antennas realized by means of conductive inks have been covered with a thermoplastic polyurethane coating with the aim to protect the structures from water and corrosion. After performing several washing cycles, it was observed that the combination of an external coating and a conductive ink for the antenna realization provides a more stable antenna behavior maintaining a high radiation efficiency, less fluctuations of the reflection coefficient, and a more restrained resonant frequency shift. In [140], the conductive ink was printed on the antenna substrate by means of a screenprinting technique, using a semiautomatic Johannes Zimmer Klagenfurt-type Mini MDF 482 machine. In [141], conductive inks employed in flexible, lightweight, thin textile antennas were investigated for life-vest and maritime emergency applications. The conductive materials have been characterized

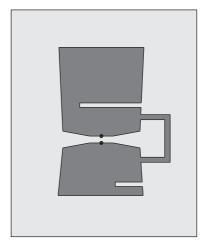


FIGURE 41: A triple band e-textile antenna [143]. The black dots indicate the feeding points. Dark gray upper conductive polymer fibers (e-fibers) and light gray dielectric textile substrate.

under several environmental conditions such as salt fog, salt water, humidity, and corrosion. A special attention has been given to silver-based inks. From the investigations carried out by the authors [141] it was observed that antennas keep stable behaviors and high efficiencies only if coated with at least two-sided laminates and two printed layers, especially in presence of salt fog. Dielectric substrate on which the antenna has been printed is a lightweight and low-loss foam featuring low moisture-absorption rate.

In Table 4 some conductive inks for we arable antennas are reported.

9.2. All-Textile Wearable Antennas. In [143], an e-fiber was used as a conductive patch of dimensions 60 mm × 100 mm opportunely sewed to a polymer-based substrate (PDMS:  $\varepsilon_r \simeq 3$ ,  $\tan \delta < 0.001$ ) to realize a triple band e-textile antenna (see Figure 41) covering the GSM, PCS, and WLAN (2.4 GHz). The loaded loop and the narrow slots realized on the two patches are critical for achieving a good impedance matching at all three frequency bands. As the 332-strand efibers textile has a high conductivity and resistivity of only  $0.8 \Omega/m$ , the e-textile antenna shows performances similar to its all-metallic counterpart, exhibiting 2 dBi of realized gain. In particular, higher radiative performances are observed when the antenna is located on the front or on the back of the human body. Finally, it should be noticed that the antenna maintains its performance even after repeated flexing and washing/drying cycles.

An all-textile antenna with full ground plane (ATA-FGP) useful for UWB and WBAN communications has been presented in [144]. The antenna, whose geometry is depicted in Figure 42, employs a full ground plane to achieve high radiative performances and excellent electromagnetic isolation with the users. The analysis and design of the antenna have been performed using the full-wave FIT-based CST Microwave Studio [25]. The antenna is realized using Shieldit Super as conductor and felt as dielectric substrate. The Shieldit Super from Less EMF Inc. (Latham,

| Conductive ink                     | Resistivity ( $\mu\Omega$ -cm) | Sintering temperature (°C) | Viscosity (mPa·s) | Fabrication technique |
|------------------------------------|--------------------------------|----------------------------|-------------------|-----------------------|
| NPS-J (silver)                     | 3                              | 210-220                    | 11                | Inkjet printing       |
| [141]                              | 3                              | 210-220                    | 11                |                       |
| Cabot CCI-300                      | 4-80                           | 100-350                    | 11–15             | Inkjet printing       |
| (silver nanoparticles) [141]       | 4-00                           | 100-330                    | 11-13             |                       |
| NovaCentrix ICI-003                |                                |                            |                   |                       |
| (copper inkjet)                    | 4.3                            | PulseForge™                | 1-6.5             | piezo-inkjet printing |
| [141]                              |                                |                            |                   |                       |
| NovaCentrix JS-015                 | 2.4                            | Thermal/PulseForge™        | 1–5               | piezo-inkjet printing |
| (silver nanoparticles) [141]       | 2.4                            | merman ruiserorge          |                   |                       |
| InkTec IJ-010                      |                                |                            |                   |                       |
| (soluble silver cluster & complex) | 4.2                            | 130-150                    | 9–15              | Inkjet printing       |
| [141]                              |                                |                            |                   |                       |
| NanoMas NTS05                      |                                |                            |                   |                       |
| (nanosilver ink)                   | 2.4                            | 70-150                     | 1–10              | _                     |
| [141]                              |                                |                            |                   |                       |
| Polymer thick film (PTF) ink       | 80                             | 120                        | 20000-30000       | Screen printing       |
| [142]                              | 00                             | 120                        |                   |                       |

TABLE 4: Conductive inks characteristics.

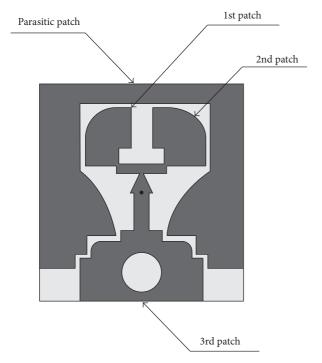


FIGURE 42: Geometry of the UWB all-textile antenna with full ground plane for off-body WBAN communications [144]. The three patches and the parasitic one forming the wearable antenna are indicated in the figure. The black dot point indicates the pin of the coaxial probe. Dark gray upper conductive textile and light gray dielectric textile substrate.

NY, USA) is a 0.17 mm thick flexible conductive textile having a conductivity of about  $1.18 \times 10^5$  S/m, while the felt is a thermally isolating material with thickness 3 mm, a relative permittivity of 1.45, and a loss tangent of 0.044.

The antenna is formed by three main radiators connected in parallel by means of a short transmission line. An additional parasitic radiator, excited through a capacitive coupling, surrounds the main radiators. The operating frequencies of the main radiators are designed to be closely spaced, enabling a combined wideband resonance for the ATA-FGP. The capacitive coupling between the active patches and the surrounding parasitic radiator contributes to increase the antenna bandwidth. Using said assembly an operating band between 3 and 10 GHz is obtained. The ATA-FGP exhibits a wide beam in the boresight direction, while the presence of the full ground drastically reduces the energy emission toward the user body. Antenna gain ranges between 5.1 and 6.3 dBi when the antenna is on the chest and between 3.2 and 6.9 dBi when it is on the back of a human body.

A different all-textile antenna, composed of Shieldit for the conductive part and of felt for the dielectric part, was proposed in [145] for WBAN and wearable computing. The structure consists of two patches and a ground plane implemented on two layers of 2 mm thick substrate. A full ground plane on the lower layer shields the user against on-body radiation and improves the quality of the radiated/received UWB signal. However, because full ground planes typically limit the impedance bandwidth of printed monopole antennas, a parasitic circular metal patch between the radiating octagonal patch and the full ground plane was employed to enhance the antenna bandwidth. In particular, the circular patch, connected by a thin strip to the ground, is inserted between two layers of dielectric material to prevent direct contact with the octagonal patch and the ground plane, realizing in this way a stacked configuration (see Figure 43). A step is introduced in the ground plane near the 50  $\Omega$  CPW feeding line to enhance the antenna impedance bandwidth.

The conductive parts of the antenna formed by Shieldit, a conductive textile from Less EMF Inc., have thickness of

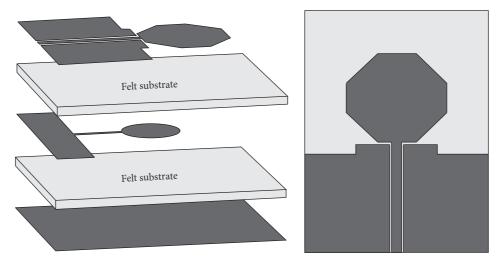


FIGURE 43: Geometry of an all-textile UWB antenna with low back radiation for WBAN applications [145]. Dark gray conductive textile and light gray dielectric textile substrate.

0.17 mm and an estimated conductivity of  $1.18 \times 10^5$  S/m, while the felt substrate layers have a relative permittivity of 1.45 and a loss tangent of 0.044. The overall dimensions of the antenna are  $80 \text{ mm} \times 61 \text{ mm} \times 4.51 \text{ mm}$ , corresponding to about  $0.85\lambda_0 \times 0.65\lambda_0 \times 0.05\lambda_0$  at the lowest operating frequency of 3.18 GHz. The antenna covers the UWB bandwidth ranging between 3.18 GHz and 11 GHz, achieving a maximum gain of about 7.2 dBi at 9 GHz with unidirectional radiation patterns. Measurements performed with the antenna placed on the arms and chest of a human being have highlighted excellent radiative performances with simulated SAR values lower than 2 W/kg averaged over 10 g of tissue when excited by signal of 0.5 W (rms). Fidelity factors and pulse distortions have been found comparable with those of other textile antennas proposed in literature. The analysis and design of the antenna have been performed using the full-wave FITbased CST Microwave Studio [25].

A dual-band wearable textile antenna based on a substrate integrated waveguide technology (SIW) featuring an integrated flexible solar harvesting system, consisting of a flexible solar cell, a power management system, and energy storage, has been presented in [146]. The antenna, working in the 2.4-2.4835 GHz industrial, scientific, and medical band and the 2.5-2.69 GHz 4G LTE band 7, can be used to monitor rescue workers during interventions and patients in hospitals and home-care. The proposed antenna consists of two layers of conductive material consisting of copper polyester Taffeta, with a surface resistivity  $0.18 \Omega/m^2$ , separated by a layer of expanded rubber protective foam with  $\varepsilon_r = 1.49$ , loss tangent 0.016, and thickness 3.94 mm. The backed cavity is realized by using a row of equally spaced flat flange copper tube eyelets along each side of the rectangular cavity. The cavity is split into two halves (see Figure 44) by a nonresonant rectangular slot. The dimensions of the slot and both parts of the cavity were carefully chosen so as to excite simultaneously two hybrid modes responsible for the antenna bandwidth. Finally, a thin and flexible solar cell is placed on the upper

part of the first cavity (see Figure 44), while on the rear side of the antenna is housed the power management system (PMS) so as to prevent antenna radiation into the electronic circuitry. The experimental measurements performed on an antenna prototype have shown that the antenna exhibits a gain ranging between 4.7 and 5.1 dB, a wide bandwidth, and a high front-to-back ratio. Moreover, its high robustness against bending, the low influence of the human body, and the flexible structure make the proposed antenna particularly suitable for wearable applications. The analysis and design of the antenna have been performed using the full-wave FIT-based CST Microwave Studio [25].

Other examples of wearable antennas, not reported for the sake of brevity, can be found in [113, 115, 147–149], while examples involving SIW antennas can be found in [150–154].

#### 10. Dielectric Resonator Antennas

High permittivity dielectric resonators (DRs) have been employed in the past to develop low losses microwave circuits [155], filters [156], and oscillators [157]. Although DRs were mainly conceived for said applications, in the early 1980s-1990s Long and others [158] proposed for the first time the use of dielectric resonators as high-efficiency radiating structures. In particular, they employed a magnetic walls model to analyze cylindrical resonators, having a dielectric constant lower than that typically used to excite high Q resonant processes [158]. Later, they analyzed the electromagnetic behavior of rectangular and hemispherical dielectric resonators [159, 160]. In particular, whereas for the rectangular resonator the same model used to analyze the cylindrical resonator was employed, for the hemispherical resonator a rigorous full-wave solution was adopted to identify the resonance frequencies of its resonant modes [160]. The geometries of the above-mentioned DRAs are depicted in Figure 45.

Later, in the 1990s Leung et al. [161] have deepened the research activities on the DRAs proposing some excitation

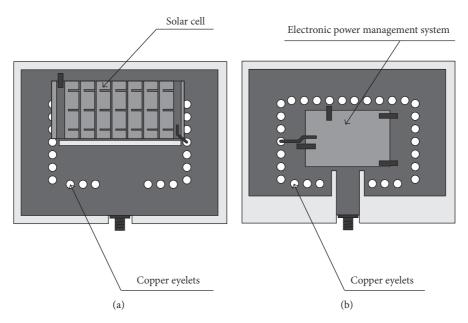


FIGURE 44: Geometry of the SIW cavity-backed slot wearable textile antenna with the integrated energy harvesting hardware [146]. Dark gray conductive textile and light gray dielectric textile substrate. The conductors employed to connect the solar cell and PMS are indicated in the figure. Top view (a) and bottom view (b).

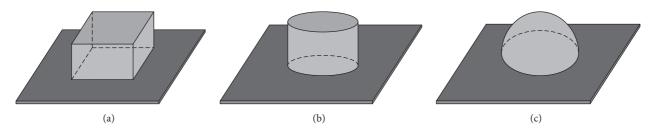


FIGURE 45: Rectangular (a), cylindrical (b), and hemispherical (c) DRA on a metallic ground plane.

techniques aimed at the integration of the antennas with the RF circuitry. In addition, they addressed the problem of the full-wave modeling using the MoM [162] and the FDTD [163] techniques aimed at assessing the quality factor, the input impedance, and antenna radiation patterns.

MoM techniques were also employed by Junker et al. to analyze structures having rotational symmetry (BOR) in order to reduce the computational burden necessary to the computation of the reflection coefficients [164] and of the radiation diagrams [165]. These authors also used a dyadic Green's function approach to assess the frequency behavior of the input impedance and of the quality factor of hemispherical resonators, and they extended the MoM analysis to the assessment of the electromagnetic coupling of bodies of revolution (BOR) with non-BOR feeding structures [166]. In addition, they expanded the MoM technique to determine the power delivered to cylindrical resonant structures excited by a narrow slot in a rectangular waveguide [167].

Finally, Mongia et al. have deepened the study of the characteristics of some geometries (dielectric ring resonator antenna [168], triangular resonator [169]), providing approximate formulas for the calculation of the resonance frequency

and the quality factor, as well as a standardization of the nomenclature of the modes excited in dielectric resonators and antennas [170].

The results obtained until the 2000s have allowed identifying several geometries, excitation techniques, and some heuristic formulas [170] useful to the assessment of the working frequencies of the resonators most commonly employed in practical applications [1, 158–160].

However, these structures were characterized by limited fractional bandwidths not compatible with the evolution of the modern wireless communication systems. For this reason, the research activities carried out in the last decades of the 2000s have been focused on the ways for widening the band, for increasing the gain, and for improving the quality of the linear or circular polarization, as well as for the miniaturization and integration of the radiating structures into portable devices. For the sake of brevity, in the following an overview of the most significant papers concerning the aforementioned design aspects is provided, while in Tables 5 and 6 the excitation techniques and typical high performance dielectric materials together with their suppliers are listed, respectively.

| Feeding technique  | Characteristics   | Reference |
|--|---|-----------|
| Waveguide  | High coupling with high permittivities DRAs achieved through a slot in the waveguide wall.  | [171–173] |
| Aperture coupled   | Used to excite a DRA using a microstrip line (a reduced surface waves level is excited).  | [174–178] |
| Microstrip<br>line   | Used to excite high permittivity DRAs. For low permittivity DRAs, tall microstrip lines (TMLs) with a dielectric support are used to enhance the coupling [115, 179]. | [179–181] |
| Electric probe   | Used to excite a DRA using a coaxial cable.   | [182–187] |
| Used to excite a DRA when broadband antenna behavior needs to be achieved. |   | [188–190] |

10.1. Broadband DRA. Since broadband communication systems allow offering a variety of wireless services in a single mobile device [21, 182], as well as higher data rate [191], several studies useful to provide guidelines to design wideband dielectric resonator antennas have been proposed in the scientific literature [192, 193]. In fact, the antenna geometry, the suitable choice of the dielectric materials, as well as that of the appropriate feeding techniques, can lead to the excitation of specific resonant modes characterized by low values of the antenna Q-factor. In particular, a new class of super shaped DRAs (see Figure 46), making use of low dielectric permittivity plastic materials [polyvinyl chloride (PVC) with  $\varepsilon_r = 2.8$ ] was proposed in [183] with the aim to obtain a high operating bandwidth (exceeding 70%), an antenna gain ranging from 5 up to 10 dBi, and an excellent linear/circular polarization purity. The antennas belonging to the mentioned class may be advantageously used to operate in indoor environments, as well as on access points of satellite terminal receivers. The geometrical dimensions of the considered DRAs are of  $100 \,\mathrm{mm} \times 27 \,\mathrm{mm}$  (about a wavelength within the material forming the DRA at the frequency of 7.5 GHz). The antenna analysis and design were carried out by means of the full-wave FIT-based CST Microwave Studio [25].

A different design solution has been proposed in [194]. This solution makes use of three cylindrical resonators having different dimensions and dielectric permittivities, stacked along the symmetry axis (boresight direction). The resulting antenna (see Figure 47), characterized by a broadband behavior (FBW = 26%) which extends from 5.4 to 7.5 GHz, for the

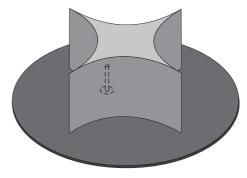


FIGURE 46: Geometry of the plastic-based super shaped dielectric resonator antenna [183].

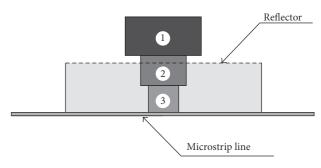


FIGURE 47: Geometry of the wideband high-gain stacked cylindrical dielectric resonator antenna [194]. The microstrip line adopted to excite the antenna is also indicated in the figure.

simulated, and from 5.4 to 7 GHz, for the measured, exhibits a high-gain ranging from about 9 up to 11 dBi.

The band widening is obtained by merging the fundamental resonant frequencies of the three DRs whose dielectric materials are the Rogers RT/Duroid 6010 with  $\varepsilon_{r1} = 10.2$ , the Rogers RT/Duroid 6006 with  $\varepsilon_{r2} = 6.15$ , and Rogers RT/Duroid 5880 with  $\varepsilon_{r3} = 2.2$ . To increase the antenna gain the stacked DRs are surrounded by a cylindrical metal reflector. The antenna, whose ground plane dimensions are  $120 \text{ mm} \times 120 \text{ mm}$  (about  $2.3\lambda_0 \times 2.3\lambda_0$ ) and whose height is equal to about  $0.65\lambda_0$  (where  $\lambda_0$  is the free-space wavelength at the central frequency of 6.5 GHz), is excited by a microstrip line coupled to the DRs assembly by means of a slot in the ground plane. The analysis and design have been performed using the full-wave FEM-based HFSS [8] and FIT-based CST Microwave Studio [25]. The radiation diagrams show a good angular behavior with a very limited level of crosspolarization along the boresight direction (-40 dB). The proposed solution presents a front-to-back ratio of about 22 dB at 6 GHz.

As discussed above, the adoption of low permittivity dielectric materials can be useful to extend the antenna bandwidth. To this end, in [1] some dielectric products having low dielectric permittivity are reported. In addition, in the same paper some geometrical shapes and some feeding systems useful for the excitation of circular polarization [195] (see Figure 48), as well as for the excitation of the higher order modes useful to increase the antenna gain or to confer

Table 6: Dielectric materials for DRAs realization.

| Company           | Material   | Permittivity   | A   | pplications   |  |
|-------------------|--|--|---|---|--|
| Emerson & Cuming  | ECCOSTOCK HiK500F<br>(low-loss)                      | $3-30 \pm 3\%$<br>( $\pm 10\%$ for dielectric<br>constant >16) | Outdoor applications, cavity tuning probes, partennas, dielectric lens antennas, and  |   |  |
|                   | ECCOSTOCK HiK  | $3-15 \pm 3\%$   | dielectric support pieces   |   |  |
|                   | D-100 Titania  | 100.0 ± 5% at 6.0 GHz  |   |   |  |
|                   | D-15 Mg-Ti (ceramic)                                 | $15.0 \pm 0.5$ at $9.4$ GHz                                    |   |   |  |
|                   | D-16 Mg-Ti (ceramic)                                 | $16.0 \pm 0.5$ at $9.4$ GHz                                    |   |   |  |
|                   | D-38 Ba-Ti (ceramic)                                 | $37.0 \pm 5\%$ at $6.0  \text{GHz}$                            |   |   |  |
| Trans-Tech™       | D-4 cordierite (hard ceramic)                        | $4.5 \pm 0.2\%$ at $9.4\mathrm{GHz}$                           | High-frequency DRs, patch antenna, matching structures for circulators and isolators, and miscellaneous support structures  Cellular base-station filters and combiners, broadcast satellite receivers, and WiMAX filters |   |  |
|                   | D-50 Ba-Ti   | $50.0 \pm 5\% \ 6.0  \text{GHz}$                               |   |   |  |
|                   | DS-6 forsterite (ceramic)                            | $6.3 \pm 0.3\%$ at $9.4\mathrm{GHz}$                           |   |   |  |
|                   | Magnesium aluminum titanate                          | $9-9.5 \pm 0.3\%$ at $9.4  GHz$                                |   |   |  |
|                   | (easy to machine ceramic)                            | $10-14 \pm 0.5\%$ at $9.4~\text{GHz}$                          |   |   |  |
|                   | Magnesium calcium titanate (easy to machine ceramic) | 18–140<br>(between ±3% and ±10%)                               |   |   |  |
|                   | Temperature stable ceramic dielectrics               | 21.5–73 (between $\pm 0.5\%$ and $\pm 1\%$ )                   |   |   |  |
| Magnetics Group   | From K-4 to K-250<br>(ceramic)                       | 4.3-250 ± 5%   | Patch antennas for automotive and GPS, dielectric roc<br>antennas, ceramic supports, sleeves for ferrites,<br>waveguide filters, phase shifters and tuning elements,<br>and sputtering targets                            |   |  |
|                   | From DR-30 to DR-80                                  | $29.5-46.5 \pm 1\%$<br>$80 \pm 2\%$                            | Base stations, filters and combiners, broadcast satellit receivers, wireless, and cable TV  |   |  |
|                   | U series   | $36-40 \pm 0.5\%$  | 1.5-12.5 GHz  |   |  |
|                   | M series   | $37-40 \pm 1\%$  | 1.5-12.5 GHz  |   |  |
|                   | V series   | $33-36 \pm 0.5\%$  | 2.9-13.2 GHz  | (i) Satellite antenna<br>(ii) Burglar alarms  |  |
| Murata            | R series   | $29-31 \pm 0.8\%$  | 4.6-24.2 GHz  |   |  |
| Manufacturing Co. | B series   | $27-29 \pm 0.5\%$  | 4.8-25.9 GHz  | (iii) Multichannel microwave  |  |
|                   | E series   | $24-25 \pm 0.4\%$  | 8.4 GHz-25 GHz<br>(also above 25 GHz<br>applications)   | communications systems<br>(iv) Radar systems<br>(v) Speed guns                                      |  |
|                   | F series   | $23-24 \pm 0.5\%$  | 10 GHz-25 GHz (also<br>above 25 GHz<br>applications)  | (vi) Mobile phone<br>(vii) CATV converters  |  |
|                   | Z series   | $6.4\pm0.6\%$  | Support of dielectric resonators  |   |  |
| Token Company     | TE21   | 19-22  | C/X/Ku/K/Ka band  | (i) LNB   |  |
|                   | TE30   | 29-30  | S/C/X/Ku band   | (ii) Radar detectors (iii) DRAs (iv) Cable TV (v) Anticollision sensors (vi) Filters, duplexer, and |  |
|                   | TE36   | 35–37  | L/S/C/X band  |   |  |
|                   | TE45   | 44-46  | UHF/L/S/C/X band  | combiners   |  |
|                   | TE80   | 79-81  | UHF/L/S/C band  | (vii) Cellular base filters,  |  |
|                   | TE90   | 89–91  | UHF/L/S band  | duplexer, and combiners   |  |
| Kyocera           | Microwave dielectric ceramics                        | 9.7–141<br>(between ±0.5% and ±3%)                             | Dielectric resonator, satellite broadcast, and base station   |   |  |

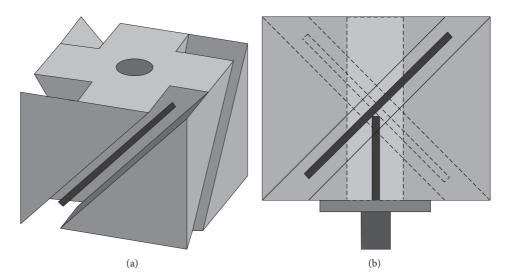


FIGURE 48: DRA working in circular polarization. The slits on the DR excite the circular polarization, while the metal strips (drawn in black) are used to increase the operating bandwidth of the axial ratio triggering a circular polarization that goes to overlap to that radiated by the DR [195]. Tridimensional view (a) and front view (b).

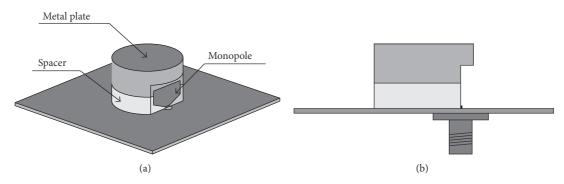


FIGURE 49: A dielectric resonator antenna excited by an electric probe having a trapezoidal shape [197]. Tridimensional view (a) and lateral view (b). The DR region with the notch is that where the strip-fed system used to excite the DRA is placed.

to the DR a dual or a multiband behavior, are discussed. This information can be beneficial whenever it is necessary to compact the communication system conferring to the DR a filtering [196] and radiant behavior [1].

In addition to geometry and to dielectric materials, the antenna excitation system may have a significant impact on the bandwidth of the radiating structure. In particular, an antenna composed of a dielectric spacer, made of foam having a dielectric constant close to one, on which a DR is placed, having a dielectric constant  $\varepsilon_r = 9.8$  (adopted dielectric material TMM10i), and with a metal plate placed on the top surface of the DR, has been proposed in [197]. The DR is excited by means of a trapezoidal monopole patch, attached to the side surface of the resonator on which a suitable notch is realized, connected to an SMA connector. The air-region, forming the spacer, behaves as a magnetic wall on which is mounted the dielectric resonator loaded with a top metal surface. The electromagnetic analysis was performed using the full-wave FEM-based HFSS [8]. The prototype antenna has a frequency band ranging between 2.9 and 6.7 GHz

(FBW = 75%) with a gain varying between 4.8 and 6.5 dBi. This result was achieved realizing a bevel on the exciting monopole, which allows an effective impedance matching with the coaxial line (see Figure 49). The dimensions of the ground plane are about 50 mm  $\times$  50 mm while the total height of the DRA is of about 15 mm. The structure has dimensions of about  $0.48\lambda_0\times0.48\lambda_0\times0.14\lambda_0$ , where  $\lambda_0$  is the wavelength at the lower frequency.

10.2. High-Gain DRAs. Typical dielectric resonator antennas exhibit gains of about 4-5 dBi (suitable for indoor coverage) which may be not suitable for some applications such as those concerning wireless base stations and satellite communications. In particular, radio base stations operating in outdoor environments may require gains that vary in the range of about 3 to 30 dBi depending on the type of radio links and coverage requirements [198], while for satellite applications such gains may oscillate between 12 dBi (or lower for small satellite applications) and 50 dBi (for high-gain satellite applications) [199]. Also the working frequency can

be important because in the frequency range of 60 GHz the atmospheric absorption of electromagnetic waves is particularly significant and consequently said frequency is adopted only for short-range wireless communications making use of high-gain antennas [174].

One of the main expedients used for increasing the antenna gains in a limited frequency band consists in the excitation of higher order modes [174, 184, 200-202]. In fact, when these modes are excited, the antenna appears electrically bigger and thus the realized gains are higher. Furthermore, because the realization of an array is not required, the complexity and size of the antenna are more limited. In addition, the mutual coupling between the array elements is finally avoided [200]. In particular, a high-gain rectangular dielectric resonator antenna, backed by a ground plane with a suitable slit excited by a microstrip line, has been proposed in [202]. The gain increase is achieved by exciting the resonator on the higher order modes. In this way a higher gain of about 5 dB compared to that obtained by a conventional excitation of the fundamental resonant mode is obtained. Three different DRAs, of relative dielectric permittivity 10 and  $\tan \delta = 0.02$ , having increasing heights, are used to excite modal configurations of higher order, highlighting how the increase of the modal order as well as that of the resonator's height results in an increase of the antenna gain. The ground plane of the DRA is approximately  $100 \,\mathrm{mm} \times 150 \,\mathrm{mm} \, (3.3\lambda_0 \times 5\lambda_0)$ , where  $\lambda_0$  is the freespace wavelength). A homemade full-wave FDTD numerical technique was adopted to analyze the antennas. Gains of about 10 dBi and FBW = 7.5% are obtained in the resonator having a height of about 30 mm ( $\lambda_0$ ).

In addition to the use of techniques aimed at the excitation of suitable higher order modes, the use of metal reflectors and of appropriate design solutions allows a considerable increase of the antenna gain [185, 187, 194]. In particular, the simultaneous use of stacked DRAs and of a cylindrical metal reflector placed in proximity of the DRAs (see Figure 47) allows achieving a gain of about 11 dBi with a FWB = 26% and a front-to-back ratio of about 17–30 dB [194].

Higher radiative performances, on a higher operating bandwidth (exceeding 65% fractional bandwidth), are reached using a suitably shaped metal reflector and equipping the DRA with a top-mount spherical cap-lens (see Figure 50) useful to focus the RF energy in the boresight direction [185]. The materials chosen to realize the DR ( $\varepsilon_r = 3$ ) and the dielectric lens ( $\varepsilon_r = 4$ ) belong to the ECCOS-TOCK® HiK 500F family, featuring a loss tangent less than 0.002 in the frequency range 1-10 GHz. The antenna has a diameter of about 114 mm (equal to about  $2.6\lambda_0$  at the central working frequency) and a height of about 48 mm ( $\lambda_0$ ). This design solution allows achieving a high-gain (exceeding 15 dBi), excellent linear/circular polarization purity, and a high front-to-back ratio (better than 20 dB). Said characteristics make the antenna suitable to be successfully employed in indoor/outdoor wireless communication systems as well as for satellite terminal receivers, for instance, to effect a transponder function between WiFi and satellites in the socalled 8/7 GHz X band. In addition, it can also be advantageously used in UWB wireless applications working with

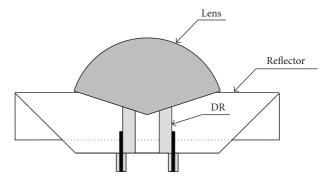


FIGURE 50: Geometry of the high-gain mushroom-shaped dielectric resonator antenna in the vertical symmetry plane of the antenna [185]. The DR, the lens, the reflector, and two of the four coaxial probes useful to excite the circular polarization are reported in the figure.

pulse signals. The antenna, making use of low permittivity dielectrics, can be realized with lightweight commercial-grade materials and thus may be suitable for space/airborne applications at a reasonable manufacturing cost and complexity. The full-wave FIT-based CST Microwave Studio [25] has been employed to design and characterize the antenna, while the singularity expansion method has been adopted to express the antenna response to arbitrary excitation waveforms.

10.3. Compact DRA. Tridimensional radiating structures may not be suitable to be integrated in portable devices where antennas of small size and low-profile are preferable. For this reason new geometries and excitation techniques for achieving more compact dielectric resonator antennas were proposed in [196, 203]. In particular, a DRA formed by a rectangular DR, having a dielectric permittivity 9.2 (commercial product TMM10), spaced from the ground plane by means of a dielectric insert of permittivity  $\varepsilon_r = 2.2$ (commercial product Rogers RT/Duroid 5880), and excited by a probe placed inside the DRA on the side wall of which a metal surface is placed (see Figure 51), was presented in [203]. The antenna, of size  $40 \,\mathrm{mm} \times 40 \,\mathrm{mm} \times 15.2 \,\mathrm{mm} \, (0.41 \lambda_0 \times 10^{-3})$  $0.41\lambda_0 \times 0.16\lambda_0$ , where  $\lambda_0$  is the free-space wavelength at f =3.1 GHz), analyzed by means of the full-wave commercial software tools FIT-based CST Microwave Studio [25] and FEM-based HFSS [8], is suitable to cover the UWB band (3.1– 10.6 GHz) with an antenna gain ranging between 4 and the 6.8 dBi.

A more compact and thin DRA (see Figure 52), of size  $12\,\mathrm{mm}\times30\,\mathrm{mm}\times6\,\mathrm{mm}$  (0.124 $\lambda_0\times0.31\lambda_0\times0.062\lambda_0$ , where  $\lambda_0$  is the free-space wavelength at 3.1 GHz), suitable for handheld devices, has been recently proposed in [196]. The antenna, having UWB characteristics, ensures low emissions in the WiMAX and WLAN frequency bands, so reducing the electromagnetic interferences (EMIs) with such systems.

The radiating structure, composed of two identical rectangular DRA of permittivity  $\varepsilon_r=10$  and  $\tan\delta=0.002$ , is excited by a microstrip feeding line, realized on a RO3003 having  $\varepsilon_r=3$  and thickness 0.75 mm, equipped with three teeth. The filters employed for the rejection of the

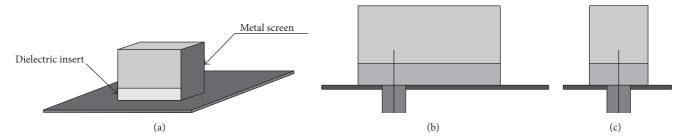


FIGURE 51: A compact rectangular dielectric resonator antenna with a low permittivity insert placed between the ground plane and the DR [203]. Tridimensional view (a), front view (b), and lateral view (c).

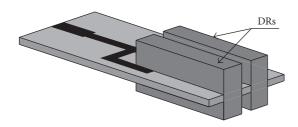


FIGURE 52: Tridimensional view of a compact UWB DRA with dual-band-rejection characteristics for WiMAX/WLAN bands [196].

WiMAX and WLAN bands are composed of a T-shaped microstrip resonator and by a rectangular slit integrated in the ground plane. The low dielectric permittivity adopted for the realization of the DRA allows obtaining a wide operating band (equal to approximately 122%) with limited geometric dimensions. The antenna characteristics were carried out by means of the full-wave FIT-based CST Microwave Studio [25] and with the FEM-based HFSS [8].

#### 11. UWB Antennas with Band-Notched Characteristics

Techniques useful to limit the interference between UWB and other communication systems operating in the same environment (WLAN, WiMAX, etc.) are presented in this section. These techniques employ suitable filter systems directly integrated in the radiator, in the ground plane, or near the feeding line, to reduce the complexity of the electronic circuitry and the cost of the whole UWB communication system. Specifically they consist of suitable resonators that are strongly coupled (at the resonance frequencies) with the electromagnetic field excited in their neighborhood, thereby causing a destructive field emission. Given their interest in practical applications, the main filtering techniques adopted in the antenna design are discussed in this section.

Spade-shaped antenna for UWB applications with triple notched bands at 3.3–3.9, 5.2–5.35, and 5.8–6.0 GHz, realized to avoid interference with communication systems sharing the same operative environment, has been proposed in [62]. The triple notched frequency bands are achieved by employing a hook-shaped defected ground structure (DGS) in each side of the ground plane, embedding an  $\Omega$ -shaped

slot on the radiating patch and adding a semi-octagon-shaped resonant ring on the backside of the antenna (see Figure 53). The analysis and design have been performed using the full-wave FEM-based HFSS [8]. The antenna is realized on a substrate of dimensions  $36~\text{mm} \times 34~\text{mm} \times 1~\text{mm}$  having a dielectric relative permittivity of 2.65. The average value of the gain is about 6 dBi, while the group delay is quite constant with the exception of the bands in which the antenna does not radiate.

A UWB planar slot antenna with dual-band-notched characteristics, useful to reduce interference with WiMAX and WLAN systems working in the same environment, has been presented in [64]. The basic antenna, realized on a FR4 dielectric substrate (dimensions 22 mm  $\times$  24 mm) with relative permittivity of 4.6, thickness 1.6 mm, and loss tangent 0.02, consists of a house-shaped slot excited by means of a rectangular monopole connected to a 50  $\Omega$  microstrip transmission line (see Figure 54).

To filter out the WiMAX band, an angle-shaped parasitic slit is asymmetrically etched out along with the rectangular monopole, while two symmetrical parasitic slits are placed inside the tapered slot to create another notched band for the WLAN frequency band. In particular, the parasitic slits introduce additional paths to the surface currents whose directions at the slits' resonant frequencies are opposite to those excited in the metal frame forming the slot antenna, thus reducing the energy emission. The antenna radiation pattern is omnidirectional in the H-plane, while in the Eplane two nulls similar to those of typical monopole antennas are present. The antenna exhibits a gain ranging between 2 and 5 dBi and a fairly stable group delay in the whole UWB band except at the notched frequency bands. The full-wave MoM-based IE3D [87] has been employed to analyze and design the antenna.

A flexible UWB antenna for wearable applications, with a notched band useful to prevent interference with WLAN communication systems, was presented in [65]. The antenna, excited by means of a CPW, is realized on an ultra-thin liquid crystal polymer (LCP) substrate with relative permittivity of 2.9 and thickness of 0.05 mm on which a copper layer of only 0.018 mm is placed to realize the radiating element. Thanks to the resistance of the LCP substrate to bending (up to about  $60^{\circ}$ ), to high temperatures, and to humidity, it can be employed by firefighters, sailors, and lifeguards. The antenna (size  $26 \text{ mm} \times 16 \text{ mm} \times 0.068 \text{ mm}$ ), whose geometry is shown

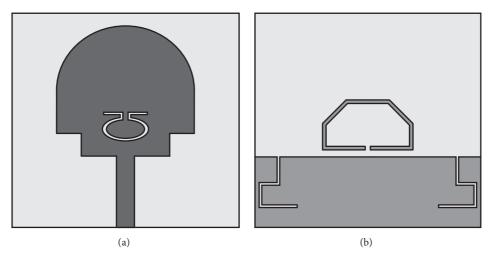


FIGURE 53: Geometry of a planar UWB monopole antenna with triple band-notched characteristics [62]. Top view (a) and bottom view (b). The resonant filters are shown in the figure. Dark gray upper metal face, medium gray bottom metal face, and light gray dielectric substrate.

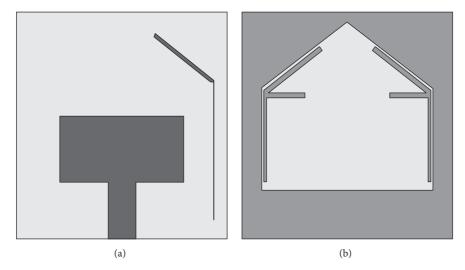


FIGURE 54: Geometry of the dual-band-notched UWB slot antenna [64]. (a) Front view. (b) Back view. The slits adopted to realize band-notched characteristics are indicated. Dark gray upper metal face, medium gray bottom metal face, and light gray dielectric substrate.

in Figure 55, has two tapered slots defined by arc of ellipses to get a better impedance bandwidth.

The frequency notch is obtained by using an H-shaped slot with equal arms and a small gap between them (see Figure 55). The H-shaped slot is placed near the feeding point so as to reflect the RF energy toward the feeding line when the slot resonates (at about  $5.35\,\mathrm{GHz}$ ). The structure has been analyzed and designed using the full-wave FIT-based CST Microwave Studio [25]. The radiation patterns are nearly omnidirectional over the entire frequency range in the H-plane, while in the E-plane they are similar to that of a dipole up to about  $3\,\mathrm{GHz}$ , while some fluctuations appear at higher frequencies where the antenna becomes more directive. The antenna has a gain of about 2-3 dBi and exhibits good time-domain characteristics, with measured fidelity factors ranging from 0.86 to 0.91.

A compact low-profile antenna (see Figure 56), suitable to cover the UWB band (from 2.98 up to 10.76 GHz), consisting

of a rectangular monopole, below which a triarms resonator, suitable to realize two notched bands around the frequencies of 3.5 (WiMAX) and 5.5 GHz (WLAN), is placed, has been presented in [66]. The rectangular monopole, of size of 14.5 mm  $\times$  14.75 mm, is printed on a FR4 substrate having a permittivity of 4.4 and loss tangent 0.02. The overall antenna size is of 29 mm  $\times$  20.5 mm. The two notched bands are realized by means of a triarm filter that, around the frequencies of 3.5 and 5.5 GHz, is excited by strong currents having opposite directions with respect to those excited on the ground plane. At the same time the strong electromagnetic coupling with the rectangular monopole produces a substantial reduction of the current amplitude excited on the metal patch with a consequent reduction of the antenna emission process.

The antenna, which exhibits omnidirectional radiation characteristics in the horizontal plane and monopole-type characteristics in vertical plane, presents a gain ranging from about 1.5 up to 5.9 dBi and a group delay less than 2 ns

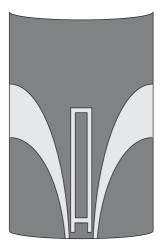


FIGURE 55: Geometry of the flexible band-notched UWB antenna [65]. The H-shaped slot adopted to realize the band-notched characteristics is indicated. Dark gray metal face and light gray dielectric substrate.

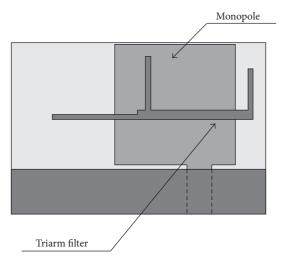


FIGURE 56: Geometry of a compact low-profile UWB antenna equipped with a triarms resonator [66]. Dark gray upper metal face, medium gray bottom metal face, and light gray dielectric substrate.

throughout the operating band, except in the notched bands, making the antenna suitable to support UWB pulse signals.

An example of a UWB rectangular dielectric resonator antenna (DRA) with bandstop performance has been presented in [67]. The antenna, whose geometry is shown in Figure 57, consists of a rectangular resonator of height 19 mm, made of Rogers 6010 with a dielectric permittivity of 10.2 and a loss tangent of 0.003, placed on a metallic ground of size of 90 mm × 90 mm. An air gap is placed under the DR to extend the antenna impedance bandwidth, while a metallic patch is used to excite the DR. To realize the 5.1–6 GHz notched band, two short-circuited metal strips are symmetrically attached on the opposite face of the DR, while a slit is realized on the metallic patch used to excite the DR. When both structures resonate, a marked impedance mismatch occurs between the feeding line and the antenna causing a frequency notch. The

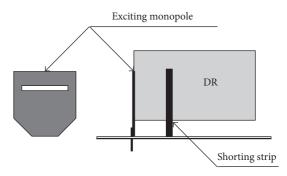


FIGURE 57: Geometry of a UWB rectangular DRA with a bandstop [67]. Dark gray metal and medium gray DR.

radiation patterns are symmetrical in the H-plane, while they are less symmetrical in the E-plane due to the excitation of the higher order modes. Finally, the antenna gain ranges between 6 and 9 dBi in the UWB frequency band. The structure has been analyzed and designed using the full-wave FIT-based CST Microwave Studio [25].

Two different design solutions were introduced in [63] with the aim of enhancing the broadside gain of a printed monopole antenna equipped with an elliptical metallic radiator and with a notch inserted on the top edge of a cornerrounded ground plane. Specifically, in the first prototype, an arc-shaped slot was inserted in the patch, near the microstrip line, for broadside gain enhancement in the E-plane at the higher frequencies of the UWB band. The second antenna (see Figure 58) has the same geometry of the first antenna but with an additional single-wing filter for a further gain enhancement. Both antennas have impedance bandwidth ranging from 3 up to 11 GHz. The antenna, realized on a Rogers 4350B dielectric substrate of thickness 1.524 mm, dielectric permittivity  $\varepsilon_r = 3.48$ , and  $\tan \delta = 0.0038$ , has dimensions of 25 mm  $\times$  37 mm. The full-wave FEM-based HFSS [8] has been adopted to perform the analysis and design of the mentioned antennas. The measured antenna gain ranges between 0 and 3 dBi, for the first antenna, and between 1 and 4 dBi, for the second antenna. Higher cross-polarization levels are observed in the second radiating structure due to horizontal currents excited on the multimode resonant filter (see Figure 58). Given the particular characteristics exhibited by these antennas, they can be used for highaccuracy positioning systems, portable devices, and cognitive radios.

A compact reconfigurable (bandstop/bandpass) and frequency-tunable radiating structure based on S-shaped split-ring resonators (S-SRRs) whose geometry is shown in Figure 59 has been proposed in [68]. This design solution can be usefully employed so as to avoid interference when other communication systems are installed in the same environment. The antenna, consisting in a standard UWB elliptical monopole excited by a 50  $\Omega$  CPW, was realized on a Rogers Duroid 5880 dielectric material with relative permittivity 2.2, thickness 0.257 mm, and loss tangent 0.0009. A suitable filter, consisting of a Skyworks [204] SMV1405 varactor (capacitance range extending from 0.63 to 2.67 pF)

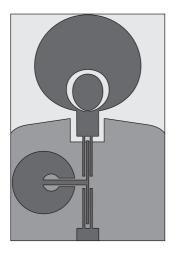


FIGURE 58: Printed monopole UWB antenna with an arc-shaped slot inserted in the patch and with a single-wing filter element employed to enhance the broadside antenna gain [63]. The multimode resonant filter is responsible for higher levels of cross-polarized field. Dark gray upper metal face, medium gray bottom metal face, and light gray dielectric substrate.

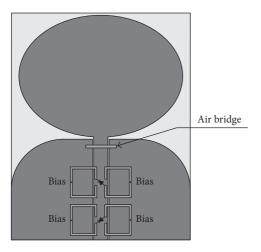


FIGURE 59: Geometry of the reconfigurable and tunable S-shaped split-ring resonators (S-SRRs) antenna for UWB applications [68]. An air bridge is adopted to suppress the slot line mode, which can be excited by the asymmetric structures forming the filter. Dark gray upper metal face, medium gray bottom split-ring resonator and air bridge, and light gray dielectric substrate.

placed at the center of an S-SRR, is integrated on the CPW line (where the magnetic field exhibits its maximum value) so as to realize a tunable bandstop frequency. Furthermore, the addition of two MACOM's [205] MADP-042305-130600 pin diodes arranged between the line and the ground plane acting as a pair of shunt inductors allows switching the behavior of the filter from bandstop to a bandpass characteristic. This makes it possible to realize a UWB antenna suitable to limit the electromagnetic interference with the WiMAX or WLAN systems. Experimental measurements performed on an antenna prototype confirm the numerical results carried out using the commercial full-wave FEM-based HFSS [8]. In

addition, they also highlight the low impact that the filter integrated on the CPW has on the antenna radiation patterns with respect to those design solutions making use of filters directly integrated in the radiating element.

Additional information concerning antennas having characteristics similar to those presented in this section can be found in [4, 58–61, 80, 81, 206–212].

#### 12. Conclusions

A comprehensive review concerning broadband, multiband, and UWB antennas for mobile and wireless communication systems has been carried out. Geometries, materials, design solutions, and numerical tools adopted for the analysis and design have been investigated. Several classes of antennas useful for the above-mentioned applications have been identified. The electromagnetic performances, the dimensions, and the materials, as well as the design solutions useful to improve the antenna bandwidth of monopole (2D and 3D profile), printed dipole, metamaterial, wearable, and dielectric resonator antennas, have been taken into account.

Starting from the investigation carried out in this review paper, the following general considerations concerning the presented antennas can be highlighted.

- (1) Monopole antennas placed over a ground plane emit energy in the spatial region located between the bottom edge of the monopole and the ground plane; therefore special attention should be paid to the shape of the monopole in this region. The emission process produces substantially radiation patterns with antenna beams oriented in the horizontal plane. Multipoint excitations (see, e.g., the trident-shaped feeding networks) tend to improve the operating band, the polarization purity, and the signal integrity of the radiated field useful in UWB applications. The ground plane makes it possible to limit interference with the sensitive electronic circuitry typically housed in the antenna back region. They are of simple realization and avoiding the use of dielectric materials does not exhibit the adverse effects caused by surface waves. The inherent 3D geometry limits their use to applications concerning base stations, automotive or avionics systems for high-speed vehicles.
- (2) Printed monopoles exhibit a low-profile that allows their use in both fixed (base stations, automotive systems, etc.) and mobile terminals (smartphones, tablets, glasses, laptops, wearable computers, etc.), as well as a simple integration with the RF circuits. The use of dielectric materials implies the presence of surface waves; therefore the use of thin dielectric materials having low dielectric permittivities is strongly recommended. For these applications it might be useful to limit the interference with WLAN and WiMAX systems that may be present in the same environment. To this end, several filtering systems (simple or tunable) integrated on the monopole, on the ground plane or on the feeding line, can be adopted. In both cases it should be noticed that said

filters are responsible for an alteration of the group delay, which can result in a significant distortion of the radiated signal with the appearance of a pronounced ringing. This process can be even more evident when use is made of metamaterials, which employ resonant structures to achieve special electromagnetic performances. In that case, a careful time-domain analysis of the radiated signal has to be performed if the antenna has to work also with pulse signals. To overcome these drawbacks additional research activities should be performed to find new metamaterial geometries suitable to guarantee stable group delay and limited ringing effects.

- (3) Wearable antennas present additional design requirements because the user's body should be shielded as much as possible from the electromagnetic field generated by the antenna. In fact, the interaction gives rise to an energy deposition in the user's body resulting in decreased efficiency and alteration of the antenna radiation patterns. A design solution to this problem is the use of radiant structures making use of full ground. Anyway, for these antennas, the design must take into account of the user, using human body models during the numerical simulations (see, e.g., that based on the "visible human") as well as during the experimental measurements (anthropomorphic dummies). Moreover, for said antennas, the development of dedicated transitions, connectors, and flexible feeding lines to be easily integrated with the e-textiles would be desirable.
- (4) Dielectric resonator antennas exhibiting 3D profile can be used in radio base stations or terrestrial and satellite radio links when a high energy efficiency is required, as they are not affected by metal losses or surface waves. The use of low permittivity dielectric materials and special geometries can ensure broadband behavior, while the choice of suitable excitation systems can guarantee excellent performance as concerns the linear/circular polarization. Moreover, metal reflectors and/or dielectric lenses can ensure higher gains over wide frequency ranges.

The analysis of the scientific literature has shown a remarkable technological readiness level reached by the 2D and 3D printed antenna geometries, while there are still ongoing research activities aimed to find new geometries and materials for advanced applications of dielectric resonator and wearable antennas. The full-wave commercial tools required for analysis and design of the considered antennas are reliable and user friendly. Even though further efforts should be made to develop appropriate numerical tools suitable to model more accurately the characteristics of the materials (roughness of simple and twisted fabrics) used to realize wearable antennas. As regards the substrates necessary for the realization of printed antennas, there is a large class of materials having high performances and low costs, while the dielectric materials useful for the realization of wearable and DRA antennas are still quite expensive. For these antennas the high material costs are the main causes that limit their broad

spread in the market. New generations of high performance antennas will be developed in the near future thanks to the advent of 3D printers having high spatial resolution.

#### **Competing Interests**

The authors declare that there is no conflict of interests regarding the publication of this paper.

#### References

- [1] K. W. Leung, E. H. Lim, and X. S. Fang, "Dielectric resonator antennas: from the basic to the aesthetic," *Proceedings of the IEEE*, vol. 100, no. 7, pp. 2181–2193, 2012.
- [2] Y. Liu, L. Si, M. Wei et al., "Some recent developments of microstrip antenna," *International Journal of Antennas and Propagation*, vol. 2012, Article ID 428284, 10 pages, 2012.
- [3] A. T. Mobashsher and A. Abbosh, "Utilizing symmetry of planar ultra-wideband antennas for size reduction and enhanced performance," *IEEE Antennas and Propagation Magazine*, vol. 57, no. 2, pp. 153–166, 2015.
- [4] R. Cicchetti, A. Faraone, D. Caratelli, and M. Simeoni, "Wideband, multiband, tunable, and smart antenna systems for mobile and UWB wireless applications 2014," *International Journal of Antennas and Propagation*, vol. 2015, Article ID 536031, 3 pages, 2015.
- [5] https://transition.fcc.gov/Bureaus/Engineering\_Technology/ Orders/2002/fcc02048.pdf.
- [6] G. A. Deschamps, "Microstrip microwave antennas," in *Proceedings of the 3rd USAF Symposium on Antennas*, October 1953.
- [7] Y. Zhang, J. Liu, Z. Liang, and Y. Long, "A wide-bandwidth monopolar patch antenna with dual-ring couplers," *Interna*tional Journal of Antennas and Propagation, vol. 2014, Article ID 980120, 6 pages, 2014.
- [8] ANSYS HFSS, http://www.ansys.com/Products/Electronics/ANSYS-HFSS.
- [9] D. Caratelli, R. Cicchetti, G. Bit-Babik, and A. Faraone, "A perturbed E-shaped patch antenna for wideband WLAN applications," *IEEE Transactions on Antennas and Propagation*, vol. 54, no. 6, pp. 1871–1874, 2006.
- [10] D. Caratelli and R. Cicchetti, "A full-wave analysis of interdigital capacitors for planar integrated circuits," *IEEE Transactions on Magnetics*, vol. 39, no. 3, pp. 1598–1601, 2003.
- [11] D. Caratelli, R. Cicchetti, G. Bit-Babik, and A. Faraone, "Circuit model and near-field behavior of a novel patch antenna for WWLAN applications," *Microwave and Optical Technology Letters*, vol. 49, no. 1, pp. 97–100, 2007.
- [12] K. Mandal and P. P. Sarkar, "High gain wide-band u-shaped patch antennas with modified ground planes," *IEEE Transac*tions on Antennas and Propagation, vol. 61, no. 4, pp. 2279–2282, 2013.
- [13] A. Agrawal, P. K. Singhal, and A. Jain, "Design and optimization of a microstrip patch antenna for increased bandwidth," *International Journal of Microwave and Wireless Technologies*, vol. 5, no. 4, pp. 529–535, 2013.
- [14] S. K. Pavuluri, C. Wang, and A. J. Sangster, "High efficiency wideband aperture-coupled stacked patch antennas assembled using millimeter thick micromachined polymer structures," *IEEE Transactions on Antennas and Propagation*, vol. 58, no. 11, pp. 3616–3621, 2010.

- [15] J. M. Kovitz and Y. Rahmat-Samii, "Using thick substrates and capacitive probe compensation to enhance the bandwidth of traditional CP patch antennas," *IEEE Transactions on Antennas and Propagation*, vol. 62, no. 10, pp. 4970–4979, 2014.
- [16] K. Noguchi, H. Rajagopalan, and Y. Rahmat-Samii, "Design of wideband/dual-band E-shaped patch antennas with the transmission line mode theory," *IEEE Transactions on Antennas and Propagation*, vol. 64, no. 4, pp. 1183–1192, 2016.
- [17] G. Dubost and S. Zisler, *Antennas a Large Band*, Masson, New York, NY, USA, 1976.
- [18] R. Cicchetti, O. Testa, and D. Caratelli, "A numerical procedure for the analysis of EMC/EMI problems in radio communication systems operating in complex environments," *IEEE Transactions on Electromagnetic Compatibility*, vol. 54, no. 6, pp. 1269– 1280, 2012.
- [19] D. Valderas, B. Sedano, A. Garcia-Alonso, and J. I. Sancho, "Synthesis of TLM-based UWB planar monopole impedance bandwidth," *IEEE Transactions on Antennas and Propagation*, vol. 55, no. 10, pp. 2874–2879, 2007.
- [20] D. Valderas, J. Legarda, I. Gutiérrez, and J. I. Sancho, "Design of UWB folded-plate monopole antennas based on TLM," *IEEE Transactions on Antennas and Propagation*, vol. 54, no. 6, pp. 1676–1687, 2006.
- [21] M. J. Ammann and Z. N. Chen, "Wideband monopole antennas for multi-band wireless systems," *IEEE Antennas and Propagation Magazine*, vol. 45, no. 2, pp. 146–150, 2003.
- [22] M. J. Ammann, "Control of the impedance bandwidth of wideband planar monopole antennas using a beveling technique," *Microwave and Optical Technology Letters*, vol. 30, no. 4, pp. 229–232, 2001.
- [23] S.-Y. Suh, W. L. Stutzman, and W. A. Davis, "A new ultrawideband printed monopole antenna: the planar Inverted Cone Antenna (PICA)," *IEEE Transactions on Antennas and Propagation*, vol. 52, no. 5, pp. 1361–1365, 2004.
- [24] X.-F. Bai, S.-S. Zhong, and X.-L. Liang, "Leaf-shaped monopole antenna with extremely wide bandwidth," *Microwave and Optical Technology Letters*, vol. 48, no. 7, pp. 1247–1250, 2006.
- [25] CST Microwave Studio, https://www.cst.com/.
- [26] Y. Chen, S. Yang, S. He, and Z. Nie, "Design and analysis of wideband planar monopole antennas using the multilevel fast multipole algorithm," *Progress In Electromagnetics Research B*, no. 15, pp. 95–112, 2009.
- [27] M. J. Ammann and Z. N. Chen, "A wide-band shorted planar monopole with bevel," *IEEE Transactions on Antennas and Propagation*, vol. 51, no. 4, pp. 901–903, 2003.
- [28] K.-L. Wong, C.-H. Wu, and S.-W. Su, "Ultrawide-band square planar metal-plate monopole antenna with a trident-shaped feeding strip," *IEEE Transactions on Antennas and Propagation*, vol. 53, no. 4, pp. 1262–1269, 2005.
- [29] The IEEE 802.16 Working Group on Broadband Wireless Access Standards, http://grouper.ieee.org/groups/802/16/index.html.
- [30] S. Ghosh, "Design of planar crossed monopole antenna for ultrawideband communication," *IEEE Antennas and Wireless Propagation Letters*, vol. 10, pp. 548–551, 2011.
- [31] WIPL-D Pro. Information, http://www.wipl-d.com/.
- [32] W.-S. Lee, K.-S. Oh, and J.-W. Yu, "A wideband planar monopole antenna array with circular polarized and band-notched characteristics," *Progress in Electromagnetics Research*, vol. 128, pp. 381–398, 2012.
- [33] B. Chen, Y.-C. Jiao, F.-C. Ren, and L. Zhang, "Broadband monopole antenna with wideband circular polarization,"

- *Progress in Electromagnetics Research Letters*, vol. 32, pp. 19–28, 2012.
- [34] A. Singh and S. Singh, "A novel CPW-fed wideband printed monopole antenna with DGS," AEU—International Journal of Electronics and Communications, vol. 69, no. 1, pp. 299–306, 2015.
- [35] S.-S. Zhong, X.-L. Liang, and W. Wang, "Compact elliptical monopole antenna with impedance bandwidth in excess of 21:1," *IEEE Transactions on Antennas and Propagation*, vol. 55, no. 11, pp. 3082–3085, 2007.
- [36] J. Wu, J. Ke, C. Jou, and C. Wang, "Microstrip-fed broad-band circularly polarised monopole antenna," *IET Microwaves*, Antennas and Propagation, vol. 4, no. 4, pp. 518–525, 2010.
- [37] K. H. Chiang and K. W. Tam, "Microstrip monopole antenna with enhanced bandwidth using defected ground structure," *IEEE Antennas and Wireless Propagation Letters*, vol. 7, pp. 532–535, 2008.
- [38] K. Ding, C. Gao, T. Yu, and D. Qu, "Broadband C-shaped circularly polarized monopole antenna," *IEEE Transactions on Antennas and Propagation*, vol. 63, no. 2, pp. 785–790, 2015.
- [39] M. A. Antoniades and G. V. Eleftheriades, "A compact multiband monopole antenna with a defected ground plane," *IEEE Antennas and Wireless Propagation Letters*, vol. 7, pp. 652–655, 2008.
- [40] Y. Li and W. Yu, "A miniaturized triple band monopole antenna for WLAN and WiMAX applications," *International Journal of Antennas and Propagation*, vol. 2015, Article ID 146780, 5 pages, 2015.
- [41] S. Verma and P. Kumar, "Compact arc-shaped antenna with binomial curved conductor-backed plane for multiband wireless applications," *IET Microwaves, Antennas and Propagation*, vol. 9, no. 4, pp. 351–359, 2015.
- [42] W. J. Krzysztofik, "Modified Sierpinski fractal monopole for ISM-bands handset applications," *IEEE Transactions on Antennas and Propagation*, vol. 57, no. 3, pp. 606–615, 2009.
- [43] M. A. Antoniades and G. V. Eleftheriades, "A multiband monopole antenna with an embedded reactance-cancelling transmission-line matching network," *IEEE Antennas and Wireless Propagation Letters*, vol. 9, pp. 1107–1110, 2010.
- [44] M. G. N. Alsath and M. Kanagasabai, "A shared-aperture multiservice antenna for automotive communications," *IEEE Antennas and Wireless Propagation Letters*, vol. 13, pp. 1417–1420, 2014.
- [45] N. A. Abbasi and R. J. Langley, "Multiband-integrated antenna/ artificial magnetic conductor," *IET Microwaves, Antennas and Propagation*, vol. 5, no. 6, pp. 711–717, 2011.
- [46] H. F. Abutarboush and A. Shamim, "Wide frequency independently controlled dual-band inkjet-printed antenna," *IET Microwaves, Antennas and Propagation*, vol. 8, no. 1, pp. 52–56, 2014.
- [47] Y. Yao, X. Wang, and J. Yu, "Multiband planar monopole antenna for LTE MIMO systems," *International Journal of Antennas and Propagation*, vol. 2012, Article ID 890705, 6 pages, 2012.
- [48] F. Paredes, G. Zamora, S. Zufanelli, F. J. Herraiz-Martínez, J. Bonache, and F. Martín, "Recent advances in multiband printed antennas based on metamaterial loading," *Advances in OptoElectronics*, vol. 2012, Article ID 968780, 12 pages, 2012.
- [49] D. R. Melo, M. N. Kawakatsu, D. C. Nascimento, and V. Dmitriev, "A planar monopole UWB antennas with rounded patch and ground plane possessing improved impedance matching," *Microwave and Optical Technology Letters*, vol. 54, no. 2, pp. 335–338, 2012.

- [50] S. H. Choi, J. K. Park, S. K. Kim, and J. Y. Park, "A new ultra-wideband antenna for UWB applications," *Microwave and Optical Technology Letters*, vol. 40, no. 5, pp. 399–401, 2004.
- [51] S. Verma and P. Kumar, "Printed Newton's egg curved monopole antenna for ultrawideband applications," *IET Microwaves, Antennas and Propagation*, vol. 8, no. 4, pp. 278–286, 2014.
- [52] J. Liu, K. P. Esselle, S. G. Hay, and S. Zhong, "Effects of printed UWB antenna miniaturization on pulse fidelity and pattern stability," *IEEE Transactions on Antennas and Propagation*, vol. 62, no. 8, pp. 3903–3910, 2014.
- [53] L. Ge and K. M. Luk, "A magneto-electric dipole for unidirectional UWB communications," *IEEE Transactions on Antennas and Propagation*, vol. 61, no. 11, pp. 5762–5765, 2013.
- [54] A. T. Mobashsher and A. Abbosh, "Three-dimensional folded antenna with ultra-wideband performance, directional radiation and compact size," *IET Microwaves, Antennas and Propa*gation, vol. 8, no. 3, pp. 171–179, 2014.
- [55] G. S. Reddy, A. Kamma, S. Kharche, J. Mukherjee, and S. K. Mishra, "Cross-configured directional UWB antennas for multidirectional pattern diversity characteristics," *IEEE Transactions on Antennas and Propagation*, vol. 63, no. 2, pp. 853–858, 2015.
- [56] A. Elsherbini, J. Wu, and K. Sarabandi, "Dual polarized wideband directional coupled sectorial loop antennas for radar and mobile base-station applications," *IEEE Transactions on Antennas and Propagation*, vol. 63, no. 4, pp. 1505–1513, 2015.
- [57] A. T. Mobashsher and A. M. Abbosh, "Performance of directional and omnidirectional antennas in wideband head imaging," *IEEE Antennas and Wireless Propagation Letters*, vol. 15, pp. 1618–1621, 2016.
- [58] Y. Zhu, F. S. Zhang, C. Lin, Q. Zhang, and J. X. Huang, "A novel dual band-notched monopole antenna for ultrawideband application," *Progress In Electromagnetics Research Letters*, vol. 16, pp. 109–117, 2010.
- [59] R. Eshtiaghi, R. Zaker, J. Nouronia, and C. Ghobadi, "UWB semi-elliptical printed monopole antenna with subband rejection filter," AEU—International Journal of Electronics and Communications, vol. 64, no. 2, pp. 133–141, 2010.
- [60] D. Dong, S. Chen, Z. Liao, and G. Liu, "A CPW-fed dual-band-notched antenna with sharp skirt selectivity for UWB applications," *International Journal of Antennas and Propagation*, vol. 2014, Article ID 629387, 7 pages, 2014.
- [61] D. Draskovic, J. R. O. Fernandez, and C. Briso Rodríguez, "Planar ultrawideband antenna with photonically controlled notched bands," *International Journal of Antennas and Propa*gation, vol. 2013, Article ID 924768, 6 pages, 2013.
- [62] W. T. Li, X. W. Shi, and Y. Q. Hei, "Novel planar UWB monopole antenna with triple band-notched characteristics," *IEEE Antennas and Wireless Propagation Letters*, vol. 8, pp. 1094–1098, 2009.
- [63] M.-C. Tang, T. Shi, and R. W. Ziolkowski, "Planar ultrawideband antennas with improved realized gain performance," *IEEE Transactions on Antennas and Propagation*, vol. 64, no. 1, pp. 61–69, 2016.
- [64] R. Azim, M. T. Islam, and A. T. Mobashsher, "Design of a dual band-notch UWB slot antenna by means of simple parasitic slits," *IEEE Antennas and Wireless Propagation Letters*, vol. 12, pp. 1412–1415, 2013.
- [65] Q. H. Abbasi, M. U. Rehman, X. Yang, A. Alomainy, K. Qaraqe, and E. Serpedin, "Ultrawideband band-notched flexible antenna for wearable applications," *IEEE Antennas and Wireless Propagation Letters*, vol. 12, no. 417, pp. 1606–1609, 2013.

- [66] R. Azim, M. T. Islam, and A. T. Mobashsher, "Dual band-notch UWB antenna with single tri-arm resonator," *IEEE Antennas* and Wireless Propagation Letters, vol. 13, pp. 670–673, 2014.
- [67] Y. F. Wang, T. A. Denidni, Q. S. Zeng, and G. Wei, "Band-notched UWB rectangular dielectric resonator antenna," *Electronics Letters*, vol. 50, no. 7, pp. 483–484, 2014.
- [68] A. K. Horestani, Z. Shaterian, J. Naqui, F. Martín, and C. Fumeaux, "Reconfigurable and tunable S-shaped split-ring resonators and application in band-notched UWB antennas," *IEEE Transactions on Antennas and Propagation*, vol. 64, no. 9, pp. 3766–3776, 2016.
- [69] A. Ghobadi and M. Dehmollaian, "A printed circularly polarized Y-shaped monopole antenna," *IEEE Antennas and Wireless Propagation Letters*, vol. 11, pp. 22–25, 2012.
- [70] Y.-M. Cai, K. Li, Y.-Z. Yin, and W. Hu, "Broadband circularly polarized printed antenna with branched microstrip feed," *IEEE Antennas and Wireless Propagation Letters*, vol. 13, pp. 674–677, 2014.
- [71] J.-Y. Sze, Z.-H. Zhou, C.-I. G. Hsu, and C.-H. Lin, "Broadband circularly polarized printed monopole antenna with unidirectional radiation patterns," *Microwave and Optical Technology Letters*, vol. 56, no. 7, pp. 1535–1540, 2014.
- [72] M. Koohestani, M. N. Moghadasi, and B. S. Virdee, "Miniature microstrip-fed ultra-wideband printed monopole antenna with a partial ground plane structure," *IET Microwaves, Antennas and Propagation*, vol. 5, no. 14, pp. 1683–1689, 2011.
- [73] J. Yang and A. Kishk, "A novel low-profile compact directional ultra-wideband antenna: the self-grounded Bow-Tie antenna," *IEEE Transactions on Antennas and Propagation*, vol. 60, no. 3, pp. 1214–1220, 2012.
- [74] J. Liu, S. Zhong, and K. P. Esselle, "A printed elliptical monopole antenna with modified feeding structure for bandwidth enhancement," *IEEE Transactions on Antennas and Prop*agation, vol. 59, no. 2, pp. 667–670, 2011.
- [75] R. Kumar and S. Gaikwad, "On the design of nano-arm fractal antenna for UWB wireless applications," *Journal of Microwaves, Optoelectronics and Electromagnetic Applications*, vol. 12, no. 1, pp. 158–172, 2013.
- [76] R. Azim, M. T. Islam, and N. Misran, "Ground modified doublesided printed compact UWB antenna," *Electronics Letters*, vol. 47, no. 1, pp. 9–11, 2011.
- [77] M. T. Islam, R. Azim, and A. T. Mobashsher, "Triple bandnotched planar UWB antenna using parasitic strips," *Progress* in *Electromagnetics Research*, vol. 129, pp. 161–179, 2012.
- [78] A. Kumar and K. V. Machavaram, "Microstrip filter with defected ground structure: a close perspective," *International Journal of Microwave and Wireless Technologies*, vol. 5, no. 5, pp. 589–602, 2013.
- [79] J. Liu, K. P. Esselle, S. G. Hay, and S. S. Zhong, "Study of an extremely wideband monopole antenna with triple band-notched charactersistics," *Progress in Electromagnetics Research*, vol. 123, pp. 143–158, 2012.
- [80] Y. Xiao, Z.-Y. Wang, J. Li, Z.-L. Yuan, and A. K. Qin, "Two-step beveled UWB printed monopole antenna with band notch," *International Journal of Antennas and Propagation*, vol. 2014, Article ID 173704, 11 pages, 2014.
- [81] O. Ahmed and A.-R. Sebak, "A printed monopole antenna with two steps and a circular slot for UWB applications," *IEEE Antennas and Wireless Propagation Letters*, vol. 7, pp. 411–413, 2008.

- [82] V. Sipal, B. Allen, D. Edwards, and B. Honary, "Twenty years of ultrawideband: opportunities and challenges," *IET Communications*, vol. 6, no. 10, pp. 1147–1162, 2012.
- [83] P. Bernardi, R. Cicchetti, and O. Testa, "An accurate UTD model for the analysis of complex indoor radio environments in microwave WLAN systems," *IEEE Transactions on Antennas* and Propagation, vol. 52, no. 6, pp. 1509–1520, 2004.
- [84] W. S. Lee, S. Y. Cha, K. S. Oh, and J. W. Yu, "Wideband circularly polarised planar monopole antenna array," *Electronics Letters*, vol. 47, no. 25, pp. 1358–1360, 2011.
- [85] B. Li, Y. Ding, and Y.-Z. Yin, "A novel dual-band circularly polarized rectangular slot antenna," *International Journal of Antennas and Propagation*, vol. 2016, Article ID 9071610, 8 pages, 2016.
- [86] M. T. Islam and R. Azim, "Recent trends in printed ultrawideband (UWB) antennas," in Advancement in Microstrip Antennas with Recent Applications, A. Kishk, Ed., pp. 173–201, InTech, Rijeka, Croatia, 2013.
- [87] IE3D Software. Information, https://www.mentor.com/pcb/xpedition/simulation.
- [88] H.-W. Liu, C.-H. Ku, T.-S. Wang, and C.-F. Yang, "Compact monopole antenna with band-notched characteristic for UWB applications," *IEEE Antennas and Wireless Propagation Letters*, vol. 9, pp. 397–400, 2010.
- [89] D. Guha, S. Biswas, and C. Kumar, "Printed antenna designs using defected ground structures: a review of fundamentals and state-of-the-art developments," in *Proceedings of the Forum for Electromagnetic Research Methods and Application Technologies* (FERMAT '14), vol. 2, pp. 1–13, April 2014.
- [90] S. S. Tiang, M. S. Hathal, N. S. Nik Anwar, M. F. Ain, and M. Z. Abdullah, "Development of a compact wide-slot antenna for early stage breast cancer detection featuring circular array full-view geometry," *International Journal of Antennas and Propagation*, vol. 2014, Article ID 309321, 11 pages, 2014.
- [91] R. Azim and M. T. Islam, "Printed wide slot ultra-wideband antenna," in Advancement in Microstrip Antennas with Recent Applications, A. Kishk, Ed., chapter 7, InTech, 2013.
- [92] S. Zhong, X. Yan, and X. Liang, "UWB planar antenna technology," *Frontiers of Electrical and Electronic Engineering in China*, vol. 3, no. 2, pp. 136–144, 2008.
- [93] X.-L. Liang, T. A. Denidni, L.-N. Zhang, R.-H. Jin, J.-P. Geng, and Q. Yu, "Printed binomial-curved slot antennas for various wideband applications," *IEEE Transactions on Microwave The*ory and Techniques, vol. 59, no. 4, pp. 1058–1065, 2011.
- [94] T. Karacolak and E. Topsakal, "A double-sided rounded bow-tie antenna (DSRBA) for UWB communication," *IEEE Antennas* and Wireless Propagation Letters, vol. 5, no. 1, pp. 446–449, 2006.
- [95] G. Cappelletti, D. Caratelli, R. Cicchetti, and M. Simeoni, "A low-profile printed drop-shaped dipole antenna for wideband wireless applications," *IEEE Transactions on Antennas and Propagation*, vol. 59, no. 10, pp. 3526–3535, 2011.
- [96] G. Cappelletti, D. Caratelli, and R. Cicchetti, "A locally conformal FDTD analysis of a thin printed antenna for wideband wireless applications," *International Journal of Numerical Modelling: Electronic Networks, Devices and Fields*, vol. 24, no. 3, pp. 257–270, 2011.
- [97] P. Bernardi, R. Cicchetti, S. Pisa, E. Pittella, E. Piuzzi, and O. Testa, "Design, realization, and test of a UWB radar sensor for breath activity monitoring," *IEEE Sensors Journal*, vol. 14, no. 2, pp. 584–596, 2014.

- [98] X. N. Low, Z. N. Chen, and T. S. P. See, "A UWB dipole antenna with enhanced impedance and gain performance," *IEEE Transactions on Antennas and Propagation*, vol. 57, no. 10, pp. 2959–2966, 2009.
- [99] S. X. Ta and I. Park, "Cavity-backed angled-dipole antennas for millimeter-wave wireless applications," *International Journal of Antennas and Propagation*, vol. 2016, Article ID 5083807, 11 pages, 2016.
- [100] K. Li, C. Zhu, L. Li, Y.-M. Cai, and C.-H. Liang, "Design of electrically small metamaterial antenna with ELC and EBG loading," *IEEE Antennas and Wireless Propagation Letters*, vol. 12, pp. 678–681, 2013.
- [101] M. S. A. Rani, S. K. A. Rahim, M. R. Kamarudin, T. Peter, S. W. Cheung, and B. M. Saad, "Electromagnetic behaviors of thin film CPW-fed CSRR loaded on UWB transparent antenna," *IEEE Antennas and Wireless Propagation Letters*, vol. 13, pp. 1239–1242, 2014.
- [102] M. M. Islam, M. T. Islam, M. Samsuzzaman, and M. R. I. Faruque, "Compact metamaterial antenna for UWB applications," *Electronics Letters*, vol. 51, no. 16, pp. 1222–1224, 2015.
- [103] J. Zhong, Y. Huang, G. Wen, H. Sun, O. Gordon, and W. Zhu, "Dual-band negative permittivity metamaterial based on cross circular loop resonator with shorting stubs," *IEEE Antennas and Wireless Propagation Letters*, vol. 11, pp. 803–806, 2012.
- [104] M. A. W. Nordin, M. T. Islam, and N. Misran, "Design of a compact ultrawideband metamaterial antenna based on splitring resonator and capacitively loaded strips unit cell," *Progress In Electromagnetics Research*, vol. 136, pp. 157–173, 2013.
- [105] W. Liu, Z. N. Chen, and X. Qing, "60-GHz thin broadband high-gain LTCC metamaterial-mushroom antenna array," *IEEE Transactions on Antennas and Propagation*, vol. 62, no. 9, pp. 4592–4601, 2014.
- [106] M. Alibakhshi-Kenari and M. Naser-Moghadasi, "Novel UWB miniaturized integrated antenna based on CRLH metamaterial transmission lines," AEU - International Journal of Electronics and Communications, vol. 69, no. 8, pp. 1143–1149, 2015.
- [107] M. Alibakhshi-Kenari, M. Naser-Moghadasi, R. A. Sadeghzadeh, and B. S. Virdee, "Metamaterial-based antennas for integration in UWB transceivers and portable microwave handsets," *International Journal of RF and Microwave Computer-Aided Engineering*, vol. 26, no. 1, pp. 88–96, 2016.
- [108] R. K. Saraswat and M. Kumar, "Miniaturized slotted ground UWB antenna loaded with metamaterial for WLAN and WiMax applications," *Progress In Electromagnetics Research B*, vol. 65, pp. 65–80, 2016.
- [109] IEEE, "Wireless Medium Access Control (MAC) and Physical Layer (PHY) Specifications for Wireless Personal Area Networks (WPANs) used in or around a body," IEEE P802.15.6/D01, 2010
- [110] F. Declercq, I. Couckuyt, H. Rogier, and T. Dhaene, "Environmental high frequency characterization of fabrics based on a novel surrogate modelling antenna technique," *IEEE Transactions on Antennas and Propagation*, vol. 61, no. 10, pp. 5200–5213, 2013.
- [111] R. Salvado, C. Loss, R. Gonçalves, and P. Pinho, "Textile materials for the design of wearable antennas: a survey," *Sensors*, vol. 12, no. 11, pp. 15841–15857, 2012.
- [112] Y. Ouyang and W. J. Chappell, "High frequency properties of electro-textiles for wearable antenna applications," *IEEE Transactions on Antennas and Propagation*, vol. 56, no. 2, pp. 381–389, 2008.

- [113] N. Chahat, M. Zhadobov, S. A. Muhammad, L. Le Coq, and R. Sauleau, "60-GHz textile antenna array for body-centric communications," *IEEE Transactions on Antennas and Propagation*, vol. 61, no. 4, pp. 1816–1824, 2013.
- [114] S. Sankaralingam and B. Gupta, "Determination of dielectric constant of fabric materials and their use as substrates for design and development of antennas for wearable applications," *IEEE Transactions on Instrumentation and Measurement*, vol. 59, no. 12, pp. 3122–3130, 2010.
- [115] S. Lemey, F. Declercq, and H. Rogier, "Dual-band substrate integrated waveguide textile antenna with integrated solar harvester," *IEEE Antennas and Wireless Propagation Letters*, vol. 13, pp. 269–272, 2014.
- [116] G. Monti, L. Corchia, and L. Tarricone, "UHF wearable rectenna on textile materials," *IEEE Transactions on Antennas and Propagation*, vol. 61, no. 7, pp. 3869–3873, 2013.
- [117] M. Mantash, A.-C. Tarot, S. Collardey, and K. Mahdjoubi, "Investigation of flexible textile antennas and AMC reflectors," *International Journal of Antennas and Propagation*, vol. 2012, Article ID 236505, 10 pages, 2012.
- [118] S. E. Morris, Y. Bayram, L. Zhang, Z. Wang, M. Shtein, and J. L. Volakis, "High-strength, metalized fibers for conformal load bearing antenna applications," *IEEE Transactions on Antennas and Propagation*, vol. 59, no. 9, pp. 3458–3462, 2011.
- [119] A. Tsolis, W. G. Whittow, A. A. Alexandridis, and J. Y. C. Vardaxoglou, "Embroidery and related manufacturing techniques for wearable antennas: challenges and opportunities," *Electronics*, vol. 3, no. 2, pp. 314–338, 2014.
- [120] B. Sanz-Izquierdo, J. C. Batchelor, and M. I. Sobhy, "Button antenna on textiles for wireless local area network on body applications," *IET Microwaves, Antennas and Propagation*, vol. 4, no. 11, pp. 1980–1987, 2010.
- [121] B. Mandal and S. K. Parui, "Wearable tri-band SIW based antenna on leather substrate," *Electronics Letters*, vol. 51, no. 20, pp. 1563–1564, 2015.
- [122] S. Zhu and R. Langley, "Dual-band wearable textile antenna on an EBG substrate," *IEEE Transactions on Antennas and Propagation*, vol. 57, no. 4, pp. 926–935, 2009.
- [123] H. S. Zhang, S. L. Chai, K. Xiao, and L. F. Ye, "Numerical and experimental analysis of wideband E-shaped patch textile antenna," *Progress In Electromagnetics Research C*, vol. 45, pp. 163–178, 2013.
- [124] M. A. R. Osman, M. K. A. Rahim, N. A. Samsuri, M. K. Elbasheer, and M. E. Ali, "Textile UWB antenna bending and wet performances," *International Journal of Antennas and Propagation*, vol. 2012, Article ID 251682, 12 pages, 2012.
- [125] P. J. Soh, G. A. E. Vandenbosch, S. L. Ooi, and M. R. N. Husna, "Wearable dual-band Sierpinski fractal PIFA using conductive fabric," *Electronics Letters*, vol. 47, no. 6, pp. 365–367, 2011.
- [126] M. E. Jalil, M. Kamal, A. Rahim, M. Azfar Abdullah, and O. Ayop, "Compact CPW-fed ultra-wideband (UWB) antenna using denim textile material," in *Proceedings of the International Symposium on Antennas and Propagation (ISAP '12)*, pp. 30–33, Nagoya, Japan, October-November 2012.
- [127] N. Lacerda Silva, L. M. Gonçalves, and H. Carvalho, "Deposition of conductive materials on textile and polymeric flexible substrates," *Journal of Materials Science: Materials in Electronics*, vol. 24, no. 2, pp. 635–643, 2013.
- [128] H. A. Rahim, M. F. Abd Malek, I. Adam et al., "Effect of different substrate materials on a wearable textile monopole antenna," in Proceedings of the IEEE Symposium on Wireless Technology and

- Applications (ISWTA '12), pp. 245–247, Bandung, Indonesia, September 2012.
- [129] M. S. Shakhirul, M. Jusoh, A. Sahadah, C. M. Nor, and H. A. Rahim, "Embroidered wearable textile antenna on bending and wet performances for UWB reception," *Microwave and Optical Technology Letters*, vol. 56, no. 9, pp. 2158–2163, 2014.
- [130] http://www.lairdtech.com/products/3055-233.
- [131] D. H. Werner and Z. H. Jiang, Electromagnetics of Body-Area Networks: Antennas, Propagation, and RF Systems, John Wiley & Sons, Hoboken, NJ, USA, 2016.
- [132] http://www.statex.biz/images/pdf/woven/ShieldexNora\_02.05.13 .pdf.
- [133] Q. Bai, J. Rigelsford, and R. Langley, "Crumpling of microstrip antenna array," *IEEE Transactions on Antennas and Propagation*, vol. 61, no. 9, pp. 4567–4576, 2013.
- [134] http://www.stockwell.com/data-sheets/3027217-nickel-polyesternonwoven.pdf.
- [135] http://th-energy.hu/docs/Conductive%20Metallized%20Products\_2.pdf.
- [136] http://www.lessemf.com/fabric.html.
- [137] M. I. Jais, M. F. Malek, M. F. Jamlos, and M. Jusoh, "Conductive E-textile analysis of 1.575 GHz rectangular antenna with H-slot for GPS application," in *Proceedings of the Loughborough Antennas and Propagation Conference (LAPC '12)*, IEEE, Leicestershire, UK, November 2012.
- [138] D. Baiya, On the development of conductive textile antennas [M.S. thesis], University of Tennessee, Knoxville, Tenn, USA, 2014, http://trace.tennessee.edu/utk\_gradthes/3138.
- [139] B. Ivsic, D. Bonefacic, and J. Bartolic, "Considerations on embroidered textile antennas for wearable applications," *IEEE Antennas and Wireless Propagation Letters*, vol. 12, pp. 1708–1711, 2013.
- [140] M. L. Scarpello, I. Kazani, C. Hertleer, H. Rogier, and D. V. Ginste, "Stability and efficiency of screen-printed wearable and washable antennas," *IEEE Antennas and Wireless Propagation Letters*, vol. 11, pp. 838–841, 2012.
- [141] J. Lilja, V. Pynttäri, T. Kaija et al., "Body-worn antennas making a splash: lifejacket-integrated antennas for global search and rescue satellite system," *IEEE Antennas and Propagation Magazine*, vol. 55, no. 2, pp. 324–341, 2013.
- [142] T. Kellomäki, J. Virkki, S. Merilampi, and L. Ukkonen, "Towards washable wearable antennas: a comparison of coating materials for screen-printed textile-based UHF RFID tags," *International Journal of Antennas and Propagation*, vol. 2012, Article ID 476570, 11 pages, 2012.
- [143] L. Zhang, Z. Wang, and J. L. Volakis, "Textile antennas and sensors for body-worn applications," *IEEE Antennas and Wireless Propagation Letters*, vol. 11, pp. 1690–1693, 2012.
- [144] P. B. Samal, P. J. Soh, and G. A. E. Vandenbosch, "UWB all-textile antenna with full ground plane for off-body WBAN communications," *IEEE Transactions on Antennas and Propagation*, vol. 62, no. 1, pp. 102–108, 2014.
- [145] L. A. Yimdjo Poffelie, P. J. Soh, S. Yan, and G. A. Vandenbosch, "A high-fidelity all-textile UWB antenna with low back radiation for off-body WBAN applications," *IEEE Transactions on Antennas and Propagation*, vol. 64, no. 2, pp. 757–760, 2016.
- [146] S. Lemey, T. Castel, P. Van Torre et al., "Threefold rotationally symmetric SIW antenna array for ultra-short-range MIMO communication," *IEEE Transactions on Antennas and Propaga*tion, vol. 64, no. 5, pp. 1689–1699, 2016.

- [147] P. B. Samal, P. J. Soh, and G. A. E. Vandenbosch, "A systematic design procedure for micro-strip-based unidirectional UWB antennas," *Progress in Electromagnetics Research*, vol. 143, pp. 105–130, 2013.
- [148] S. Yan, P. J. Soh, and G. A. E. Vandenbosch, "Wearable dual-band composite right/ left-handed waveguide textile antenna for WLAN applications," *Electronics Letters*, vol. 50, no. 6, pp. 424–426, 2014.
- [149] H. R. Khaleel, "Design and fabrication of compact inkjet printed antennas for integration within flexible and wearable electronics," *IEEE Transactions on Components, Packaging and Manufacturing Technology*, vol. 4, no. 10, pp. 1722–1728, 2014.
- [150] G. Q. Luo, Z. F. Hu, W. J. Li, X. H. Zhang, L. L. Sun, and J. F. Zheng, "Bandwidth-enhanced low-profile cavity-backed slot antenna by using hybrid SIW cavity modes," *IEEE Transactions on Antennas and Propagation*, vol. 60, no. 4, pp. 1698–1704, 2012.
- [151] D.-F. Guan, Z.-P. Qian, Y.-S. Zhang, and J. Jin, "High-gain SIW cavity-backed array antenna with wideband and low sidelobe characteristics," *IEEE Antennas and Wireless Propagation Letters*, vol. 14, pp. 1774–1777, 2015.
- [152] P. Wu, S. Liao, and Q. Xue, "A substrate integrated slot antenna array using simplified feeding network based on higher order cavity modes," *IEEE Transactions on Antennas and Propagation*, vol. 64, no. 1, pp. 126–135, 2016.
- [153] Q. Wu, H. Wang, C. Yu, and W. Hong, "Low-profile circularly polarized cavity-backed antennas using SIW techniques," *IEEE Transactions on Antennas and Propagation*, vol. 64, no. 7, pp. 2832–2839, 2016.
- [154] O. Caytan, S. Lemey, S. Agneessens et al., "Half-mode substrate-integrated-waveguide cavity-backed slot antenna on cork substrate," *IEEE Antennas and Wireless Propagation Letters*, vol. 15, pp. 162–165, 2016.
- [155] O. Ishihara, T. Mori, H. Sawano, and M. Nakatani, "A highly stabilized GaAs FET oscillator using a dielectric resonator feedback circuit in 9–14 GHz," *IEEE Transactions on Microwave Theory and Techniques*, vol. 28, no. 8, pp. 817–824, 1980.
- [156] S. B. Cohn, "Microwave bandpass filters containing high-Q dielectric resonators," *IEEE Transactions on Microwave Theory* and Techniques, vol. 16, no. 4, pp. 218–227, 1968.
- [157] S. J. Ha, Y. D. Lee, Y. H. Kim, J. J. Choi, and U. S. Hong, "Dielectric resonator oscillator with balanced low noise amplifier," *Electronics Letters*, vol. 38, no. 24, pp. 1542–1544, 2002.
- [158] S. A. Long, M. W. McAllister, and L. C. Shen, "The resonant cylindrical dielectric cavity antenna," *IEEE Transactions on Antennas and Propagation*, vol. 31, no. 3, pp. 406–412, 1983.
- [159] M. W. McAllister, S. A. Long, and G. L. Conway, "Rectangular dielectric resonator antenna," *Electronics Letters*, vol. 19, no. 6, pp. 218–219, 1983.
- [160] M. W. Mcallister and S. A. Long, "Resonant hemispherical dielectric antenna," *Electronics Letters*, vol. 20, no. 16, pp. 657– 659, 1984.
- [161] K. W. Leung, K. M. Luk, E. K. N. Yung, and S. Lai, "Characteristics of a low-profile circular disk DR antenna with very high permittivity," *Electronics Letters*, vol. 31, no. 6, pp. 417–418, 1995.
- [162] H. T. Hui, E. K. N. Yung, and K. W. Leung, "Numerical and experimental studies of a helical antenna loaded by a dielectric resonator," *Radio Science*, vol. 32, no. 2, pp. 295–304, 1997.
- [163] S. M. Shum and K. M. Luk, "Analysis of aperture coupled rectangular dielectric resonator antenna," *Electronics Letters*, vol. 30, no. 21, pp. 1726–1727, 1994.

- [164] G. P. Junker, A. A. Kishk, and A. W. Glisson, "Input impedance of dielectric resonator antennas excited by a coaxial probe," *IEEE Transactions on Antennas and Propagation*, vol. 42, no. 7, pp. 960–966, 1994.
- [165] A. A. Kishk, M. Cuhaci, A. Ittipiboon, and Y. M. M. Antar, "Slot excitation of the dielectric disk radiator," *IEEE Transactions on Antennas and Propagation*, vol. 43, no. 2, pp. 198–201, 1995.
- [166] G. P. Junker, A. A. Kishk, and A. W. Glisson, "Numerical analysis of dielectric resonator antennas excited in quasi-TE modes," *Electronics Letters*, vol. 29, no. 21, pp. 1810–1811, 1993.
- [167] I. A. Eshrah, A. A. Kishk, A. B. Yakovley, and A. W. Glisson, "Theory and implementation of dielectric resonator antenna excited by a waveguide slot," *IEEE Transactions on Antennas and Propagation*, vol. 53, no. 1, pp. 483–494, 2005.
- [168] R. K. Mongia, A. Ittipiboon, P. Bhartia, and M. Cuhaci, "Electric-monopole antenna using a dielectric ring resonator," *Electronics Letters*, vol. 29, no. 17, pp. 1530–1531, 1993.
- [169] A. Ittipiboon, R. K. Mongia, Y. M. M. Antar, P. Bhartia, and M. Cuhaci, "Aperture fed rectangular and triangular dielectric resonators for use as magnetic dipole antennas," *Electronics Letters*, vol. 29, no. 23, pp. 2001–2002, 1993.
- [170] R. K. Mongia and P. Bhartia, "Dielectric resonator antennas—a review and general design relations for resonant frequency and bandwidth," *International Journal of Microwave and Millimeter-Wave Computer-Aided Engineering*, vol. 4, no. 3, pp. 230–247, 1994.
- [171] A. B. Kakade and B. Ghosh, "Analysis of the rectangular waveguide slot coupled multilayer hemispherical dielectric resonator antenna," *IET Microwaves, Antennas and Propagation*, vol. 6, no. 3, pp. 338–347, 2012.
- [172] P. M. Jasmine, P. Abdulla, and P. M. Raphika, "Rectangular waveguide fed DRA using tapered waveguide section," *Microwave and Optical Technology Letters*, vol. 57, no. 9, pp. 2025–2028, 2015.
- [173] X.-Q. Sheng, K. W. Leung, and E. K.-N. Yung, "Analysis of waveguide-fed dielectric resonator antenna using a hybrid finite element method/moment method," *IEE Proceedings: Microwaves, Antennas and Propagation*, vol. 151, no. 1, pp. 91– 95, 2004.
- [174] A. Perron, T. A. Denidni, and A. R. Sebak, "Circularly polarized microstrip/elliptical dielectric ring resonator antenna for millimeter-wave applications," *IEEE Antennas and Wireless Propagation Letters*, vol. 9, pp. 783–786, 2010.
- [175] O. G. Avădănei, M. G. Banciu, I. Nicolaescu, and L. Nedelcu, "Superior modes in high permittivity cylindrical dielectric resonator antenna excited by a central rectangular slot," *IEEE Transactions on Antennas and Propagation*, vol. 60, no. 11, pp. 5032–5038, 2012.
- [176] M. Zou, J. Pan, and Z. Nie, "A wideband circularly polarized rectangular dielectric resonator antenna excited by an archimedean spiral slot," *IEEE Antennas and Wireless Propaga*tion Letters, vol. 14, pp. 446–449, 2015.
- [177] D. Hou, Y.-Z. Xiong, W.-L. Goh, S. Hu, W. Hong, and M. Madihian, "130-GHz on-chip meander slot antennas with stacked dielectric resonators in standard CMOS technology," *IEEE Transactions on Antennas and Propagation*, vol. 60, no. 9, pp. 4102–4109, 2012.
- [178] D. Hou, W. Hong, W.-L. Goh et al., "D-band on-chip higher-order-mode dielectric-resonator antennas fed by half-mode cavity in CMOS technology," *IEEE Antennas and Propagation Magazine*, vol. 56, no. 3, pp. 80–89, 2014.

- [179] A. Rashidian, L. Shafai, and D. M. Klymyshyn, "Tall microstrip transmission lines for dielectric resonator antenna applications," *IET Microwaves, Antennas and Propagation*, vol. 8, no. 2, pp. 112–124, 2014.
- [180] A. Rashidian and D. M. Klymyshyn, "Compact wideband multimode dielectric resonator antennas fed with parallel standing strips," *IEEE Transactions on Antennas and Propagation*, vol. 60, no. 11, pp. 5021–5031, 2012.
- [181] M. A. Saed and R. Yadla, "Microstrip-fed low profile and compact dielectric resonator antennas," *Progress in Electromagnetics Research*, vol. 56, pp. 151–162, 2006.
- [182] L. Zou and C. Fumeaux, "A cross-shaped dielectric resonator antenna for multifunction and polarization diversity applications," *IEEE Antennas and Wireless Propagation Letters*, vol. 10, pp. 742–745, 2011.
- [183] M. Simeoni, R. Cicchetti, A. Yarovoy, and D. Caratelli, "Plastic-based supershaped dielectric resonator antennas for wide-band applications," *IEEE Transactions on Antennas and Propagation*, vol. 59, no. 12, pp. 4820–4825, 2011.
- [184] D. Guha, A. Banerjee, C. Kumar, and Y. M. M. Antar, "New technique to excite higher-order radiating mode in a cylindrical dielectric resonator antenna," *IEEE Antennas and Wireless Propagation Letters*, vol. 13, pp. 15–18, 2014.
- [185] R. Cicchetti, A. Faraone, E. Miozzi, R. Ravanelli, and O. Testa, "A high-gain mushroom-shaped dielectric resonator antenna for wideband wireless applications," *IEEE Transactions on Antennas* and Propagation, vol. 64, no. 7, pp. 2848–2861, 2016.
- [186] B. Mukherjee, P. Patel, and J. Mukherjee, "A novel cup-shaped inverted hemispherical dielectric resonator antenna for wideband applications," *IEEE Antennas and Wireless Propagation Letters*, vol. 12, pp. 1240–1243, 2013.
- [187] R. Cicchetti, E. Miozzi, and O. Testa, "A novel wideband multipermittivity composite dielectric resonator antenna for wireless applications," in *Proceedings of the IEEE-APS Topical Conference on Antennas and Propagation in Wireless Communications* (APWC '16), pp. 70–73, Cairns, Australia, September 2016.
- [188] Y. Gao, Z. Feng, and L. Zhang, "Compact asymmetrical T-shaped dielectric resonator antenna for broadband applications," *IEEE Transactions on Antennas and Propagation*, vol. 60, no. 3, pp. 1611–1615, 2012.
- [189] B. Li and K. W. Leung, "Strip-fed rectangular dielectric resonator antennas with/without a parasitic patch," *IEEE Transactions on Antennas and Propagation*, vol. 53, no. 7, pp. 2200–2207, 2005.
- [190] A. S. Al-Zoubi and A. A. Kishk, "Wide band strip-fed rectangular dielectric resonator antenna," in *Proceedings of the 3rd European Conference on Antennas and Propagation (EuCAP '09)*, pp. 2379–2382, Berlin, Germany, March 2009.
- [191] D. Soren, R. Ghatak, R. K. Mishra, and D. R. Poddar, "Dielectric resonator antennas: designs and advances," *Progress in Electromagnetics Research B*, vol. 60, no. 1, pp. 195–213, 2014.
- [192] M. Simeoni, R. Cicchetti, A. Yarovoy, and D. Caratelli, "Super-shaped dielectric resonator antennas," in Proceedings of the IEEE International Symposium on Antennas and Propagation and USNC/URSI National Radio Science Meeting (APSURSI '09), June 2009
- [193] M. Simeoni, R. Cicchetti, A. Yarovoy, and D. Caratelli, "Circularly polarized supershaped dielectric resonator antennas for indoor ultra wide band applications," in *Proceedings of the IEEE International Symposium on Antennas and Propagation and CNC-USNC/URSI Radio Science Meeting—Leading the Wave (AP-S/URSI '10)*, pp. 1–4, Ontario, Canada, July 2010.

- [194] Y. Wang, T. A. Denidni, Q. Zeng, and G. Wei, "A wideband high-gain stacked cylindrical dielectric resonator antenna," *Progress in Electromagnetics Research Letters*, vol. 43, pp. 155–163, 2013.
- [195] Y. M. Pan and K. W. Leung, "Wideband omnidirectional circularly polarized dielectric resonator antenna with parasitic strips," *IEEE Transactions on Antennas and Propagation*, vol. 60, no. 6, pp. 2992–2997, 2012.
- [196] M. Abedian, S. K. A. Rahim, S. Danesh, S. Hakimi, L. Y. Cheong, and M. H. Jamaluddin, "Novel design of compact UWB dielectric resonator antenna with dual-band-rejection characteristics for WiMAX/WLAN bands," *IEEE Antennas and Wireless Propagation Letters*, vol. 14, pp. 245–248, 2015.
- [197] X. Li, Y. Yang, F. Gao, H. Ma, and X. Shi, "A compact dielectric resonator antenna excited by a planar monopole patch for wideband applications," *International Journal of Antennas and Propagation*, vol. 2016, Article ID 9734781, 9 pages, 2016.
- [198] Z. N. Chen, X. Qing, T. S. P. See, and W. K. Toh, "Antennas for WiFi connectivity," *Proceedings of the IEEE*, vol. 100, no. 7, pp. 2322–2329, 2012.
- [199] S. Gao, K. Clark, M. Unwin et al., "Antennas for modern small satellites," *IEEE Antennas and Propagation Magazine*, vol. 51, no. 4, pp. 40–56, 2009.
- [200] A. Perron, T. A. Denidni, and A.-R. Sebak, "High-gain hybrid dielectric resonator antenna for millimeter-wave applications: design and implementation," *IEEE Transactions on Antennas* and Propagation, vol. 57, no. 10, pp. 2882–2892, 2009.
- [201] D. Guha, A. Banerjee, C. Kumar, and Y. M. M. Antar, "Higher order mode excitation for high-gain broadside radiation from cylindrical dielectric resonator antennas," *IEEE Transactions on Antennas and Propagation*, vol. 60, no. 1, pp. 71–77, 2012.
- [202] A. Petosa and S. Thirakoune, "Rectangular dielectric resonator antennas with enhanced gain," *IEEE Transactions on Antennas* and Propagation, vol. 59, no. 4, pp. 1385–1389, 2011.
- [203] Y. Ge, K. P. Esselle, and T. S. Bird, "Compact dielectric resonator antennas with ultrawide 60%–110% bandwidth," *IEEE Transactions on Antennas and Propagation*, vol. 59, no. 9, pp. 3445–3448, 2011.
- [204] Skyworks Solutions, Inc., 2015, http://www.skyworksinc.com/.
- [205] MACOM, 2015, http://www.macom.com/.
- [206] G.-P. Gao, X. Yang, and J.-S. Zhang, "A printed volcano smoke antenna for UWB and WLAN communications," *Progress in Electromagnetics Research Letters*, vol. 4, pp. 55–61, 2008.
- [207] R. Azim, M. T. Islam, J. S. Mandeep, and A. T. Mobashsher, "A planar circular ring ultra-wideband antenna with dual bandnotched characteristics," *Journal of Electromagnetic Waves and Applications*, vol. 26, no. 14-15, pp. 2022–2032, 2012.
- [208] F. Zhu, S. Gao, A. T. S. Ho et al., "Multiple band-notched UWB antenna with band-rejected elements integrated in the feed line," *IEEE Transactions on Antennas and Propagation*, vol. 61, no. 8, pp. 3952–3960, 2013.
- [209] P. Gao, S. He, X. Wei, Z. Xu, N. Wang, and Y. Zheng, "Compact printed UWB diversity slot antenna with 5.5-GHz band-notched characteristics," *IEEE Antennas and Wireless Propagation Letters*, vol. 13, pp. 376–379, 2014.
- [210] M. S. A. Rani, S. K. A. Rahim, M. R. Kamarudin, T. Peter, S. W. Cheung, and B. M. Saad, "Electromagnetic behaviors of thin film CPW-Fed CSRR loaded on UWB transparent antenna," *IEEE Antennas and Wireless Propagation Letters*, vol. 13, pp. 1239–1242, 2014.
- [211] N. Jaglan, B. K. Kanaujia, S. D. Gupta, and S. Srivastava, "Triple band notched UWB antenna design using electromagnetic

- band gap structures,"  $Progress\ In\ Electromagnetics\ Research\ C,$  vol. 66, pp. 139–147, 2016.
- [212] W. Wu, Y. Li, R. Wu, C. Shi, and T. Cui, "Band-notched UWB antenna with switchable and tunable performance," *International Journal of Antennas and Propagation*, vol. 2016, Article ID 9612987, 6 pages, 2016.

Hindawi Publishing Corporation International Journal of Antennas and Propagation Volume 2017, Article ID 5901625, 14 pages http://dx.doi.org/10.1155/2017/5901625

## Research Article

## **Smart Cylindrical Dome Antenna Based on Active Frequency Selective Surface**

## Tongyu Ding, 1 Shaoqing Zhang, 2 Liang Zhang, 1 and Yanhui Liu 3

<sup>1</sup>College of Information Engineering, Jimei University, Xiamen 361021, China

Correspondence should be addressed to Liang Zhang; liangzhang@jmu.edu.cn

Received 8 July 2016; Revised 8 December 2016; Accepted 27 December 2016; Published 7 February 2017

Academic Editor: Diego Caratelli

Copyright © 2017 Tongyu Ding et al. This is an open access article distributed under the Creative Commons Attribution License, which permits unrestricted use, distribution, and reproduction in any medium, provided the original work is properly cited.

In this paper, we proposed a beamforming antenna, which is realized using an omnidirectional antenna in the center surrounded by a cylindrical smart dome. The smart dome is made of 16 active frequency selective surface columns of which the amplitude and phase response can be continuously tuned by varying the bias voltages of the employed varactors. Thus, the performance of the proposed antenna could achieve higher gain, better nulling level, and more agility than many switch methods-based cylindrical reconfigurable antennas. Moreover, in order to overcome the unavailable analytical synthesis caused by complex mutual coupling between columns, we develop a genetic algorithm based optimization system and conducted a serial of experiments to evaluate the high-gain, nulling, continuously steering, and frequency-invariant ability. The results show that, during the frequency tunable range of the AFSS (2.0 GHz to 2.7 GHz), the antenna can offer an additional gain of up to 6.57 dB and nulling level of -56.41 dBi. For the high-gain modes, the -3 dB beam widths are  $26^{\circ}-34^{\circ}$ , which offers enhanced angular resolution compared with other reported beam-sweeping work. Furthermore, the radiation pattern is continuously steerable.

#### 1. Introduction

With the development of wireless industry, adaptive and smart antenna systems are developed to solve the interference problems [1, 2]. Analog phased array and multiple-channel digital signal process can be used to build smart antenna systems [3, 4]. However, both of these methods are complicated and expensive. Electronically steerable antennas based on active frequency selective surface (AFSS) are studied in recent years to provide economical beam steering solutions. Both planar and cylindrical conformal arrays are reported [5–9]. The cylindrical ones have similar configurations; they are mostly constructed by a central omnidirectional antenna and several surrounding AFSS columns (with the shape of a cylinder). These designs offer low cost and highly agile solutions with the purpose of radiation pattern manipulation. The majority of these AFSSes are based on PIN diodes. There are only two states for PIN diodes, on and off. Thus, the idea of operating this kind of antenna is turning some of the AFSS

columns reflective, while turning the others transparent. In this way, nearly half of the radiation energy is reflected and a better additional gain is achieved. The 3 dB beam widths are about 70° in the azimuth plane [6–8]. A more recent research showed that the beam-width of this kind of antennas can be narrowed to 47° with an optimized dimension [10]. These on/off methods-based antennas are all sector antennas which means that they are not continuously steerable. In the previous work [9], varactors based AFSSes were used to achieve continuously steerable ability. However, amplitude and phase responses of the AFSSes were not considered in that work.

As reported in [11], manipulation of the radiation pattern of a horn antenna by using the amplitude and phase response of an AFSS proved to be available. Inspired by this work, for the cylindrical cases, if the amplitude and phase response can be controlled continuously, they are quite similar to conformal weighted and phased arrays. In such cases, higher gain, deeper nulling level, and better agility can be expected as

<sup>&</sup>lt;sup>2</sup>Aviation Key Laboratory of Science and Technology on Electromagnetic Environmental Effects, Shenyang Aircraft Design and Research Institute, Shenyang 110035, China

<sup>&</sup>lt;sup>3</sup>Department of Electronic Science, Xiamen University, Fujian 361005, China

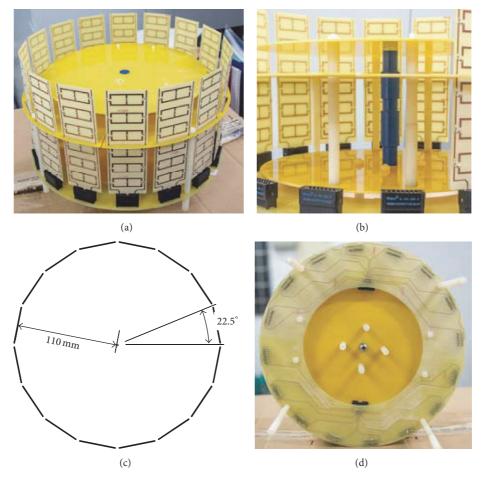


FIGURE 1: Antenna structure. (a) Photo of the antenna. (b) Central dipole antenna. (c) Cross section and dimensions. (d) Bottom plane.

a smart antenna [12]. For this purpose, a cylindrical AFSS based antenna was developed in this work. It takes advantage of the phase tuning ability of the AFSS to realize a higher additional gain and deeper nulling level. A self-contained optimization algorithm, which is capable of effectively enhancing the performance of the antenna, is also developed to realize the optimization. The radius of this prototype is enlarged to 1.76  $\lambda$  of the central frequency. Moreover, since this antenna has an essential different working mechanism compared with the reported ones [5-8, 10], which used PIN-diode for the AFSSes and can only switch between the on and off modes, we would prefer to reconsider it as a smart dome and an inner emitter. The emitter is a general omnidirectional antenna and it can be replaced by many different models with vertical polarization direction, while the radiation pattern manipulation ability is realized by the dome.

The rest of this paper is organized as follows. In Section 2, the structure of this antenna and the design of the AFSS are introduced. The amplitude and phase responses of the AFSS are discussed. The complexity of performing beamforming on this antenna is explained. In Section 3, an artificial intelligence (AI) based optimizing system is built to overcome the above-mentioned problems and evaluate the performance of the antenna. We use genetic algorithm (GA)

method to optimize the antenna for different purposes. The performances of the gain, nulling level, frequency-invariant beam, and agility are revealed. Finally, the paper is concluded in Section 4.

#### 2. Design of the Antenna

2.1. Structure of the Antenna. The antenna is constructed by a dipole antenna in the center and 16 AFSS columns surrounding it, as shown in Figure 1 (the number of AFSS columns is currently determined by the number of DA channels in the self-made voltage controller). The dipole acts as a radiator emitting omnidirectional vertically polarized signal. The bottom plane is an annular shaped, single-layer FR4 PCB with 16 golden-finger jackets and two multiple pin connectors. A pair of golden fingers is added to the bottom of each AFSS column so it can be plugged into the jacket, where the bias voltage is added. There are 6 unit cells within each column. The diameter of the antenna is 220 mm and the height is 133 mm. Dielectric FR4 board, nylon sticks, and screws are added to help holding the dipole antenna and AFSS columns in position.

The mechanism of this antenna is illustrated in Figure 2. The signal is emitted by the central omnidirectional dipole

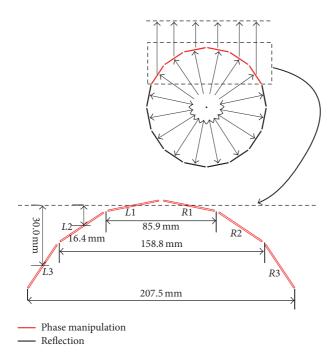


FIGURE 2: Illustration of the theory.

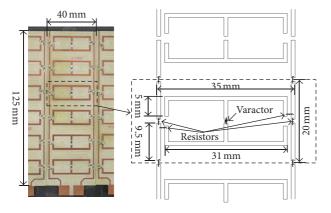


FIGURE 3: AFSS structure and dimensions.

and reflected on the AFSS columns, which are tuned into reflective status at the working frequency. The other AFSS columns (for this demonstration, there are six) work at different states between transparent and reflective modes to manipulate the phase. As shown in Figure 2, there are 16.4 mm and 30.0 mm distance differences. For different wavelength, they correspond to different phase differences.

2.2. Design, Measurement and Discussion of the AFSS. The structure and dimensions of the developed AFSS are shown in Figure 3. The AFSS patch is constructed by two mirrored *E* like patches. The original design of this patch can be traced back to [13], and it is also known as the electric-LC (ELC) resonator. It is later successfully modified into an AFSS with

broadband tunability [14]. In this work, the unit cells of the AFSS were fabricated on a single-layer FR4 board (thus no via holes or patches on the other side) and were rotated by 90° to manipulate the vertically polarized signal. We used 16 such AFSS columns, each applied with an independently controlled bias voltage, to form the designed smart dome. The bias voltages powered to each column were controlled by a self-contained artificial intelligence program, optimizing the combinations of bias voltages to an optimum status, thus making the AFSS behavior outperform those in [13, 14]. 10 Kohm resistors were added on the bias grid for the purpose of isolating the unit cells by choking the high frequency current between unit cells. The varactors used in this work are BB857, manufactured by Infineon. It is a surface-mounted model with SCD80 package. It is broadband tunable with a variable capacitance  $C_T$  from 0.54 pF to 6.6 pF, a low series resistance of  $r_S$  = 1.5 ohm, and the series inductance  $L_S$  = 0.6 nH. When the varactor is reversely biased, the maximum current is 200 nA ( $V_R = 30 \text{ V}$ ), implying that the minimum resistance is 150 M-ohm, it is much larger than the 10 K-ohm resistors. Thus, the DC bias voltage drop caused by the choke resistors is negligible. For the same purpose, two horizontally placed resistors were added to connect the bias grid and the mirrored *E* patches.

The amplitude and phase responses under different voltages were measured in a microwave anechoic chamber. As shown in Figure 4, an isolation screen was built using steel plate with an aperture in the center. RF anechoic material was glued on both sides of the screen. Two horn antennas were set up pointing to each other through the aperture.  $S_{21}$  between these two horn antennas were measured when FSS columns were installed covering the aperture with a distance of 45 mm to each other. The  $S_{21}$  difference between this setup and the open aperture setup is the transmission coefficient of the FSS. This method is already widely used such as in [15-18]. The measured FSS screen was constructed by 6 FSS columns and the bias voltage was added at the bottom. The dimensions in Figure 4 are as follows:  $L_1 = 1 \,\text{m}$ ,  $L_2 = 1.5 \,\text{m}$ ,  $H_1 = W_1 = 2 \,\text{m}$ ,  $W_2 = 30$  cm, and  $H_2 = 20$  cm. Since the aim of this preliminary experiment is mainly to validate the effectiveness of the designed prototype and its capability of frequency tuning, we choose these setup dimensions according to the experimental environment, which is a  $3 \text{ m} \times 3 \text{ m}$  anechoic chamber, due to the reason of economy, and so on (theoretically, the distance of the two antennas should be as large as possible to simulate the situation of far field plane wave).

Simulated and measured results are shown in Figure 5. The resonant frequency of this AFSS can be tuned from 2.0 GHz to 2.75 GHz with an insertion loss of more than 10 dB. As the performance of materials in the experiment may decrease from the standard value set in the simulation due to aging problems, and so on, the experimental results are slightly deviated from simulation ones. As discussed in the previous work [9], the total working frequency range  $BW_{working}$  is no more than the sum of the frequency tunable range  $BW_T$  and stop-band frequency range  $BW_R$  (1). Thus the developed AFSS can be used for building electronically steerable antennas from 2.0 GHz to 2.75 GHz, if an insertion loss of more than 10 dB is required. This frequency spectrum

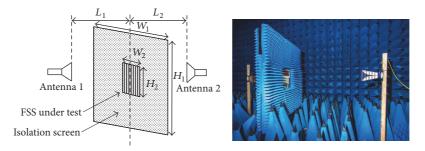


FIGURE 4: Measurement setup illustration and photo.

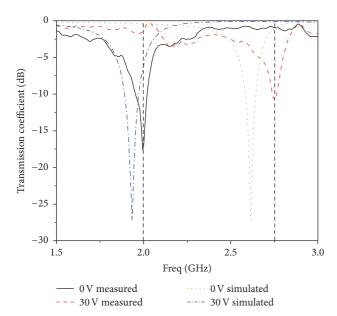


FIGURE 5: Simulated and measured transmission coefficients of the AFSS.

covers some part of WCDMA, some part of LTE, and 2.4 GHz ISM band:

$$BW_{\text{working}} \le BW_T + BW_R. \tag{1}$$

Besides the tunable range, the amplitude and phase response at a given frequency point is directly related to beamforming. To measure such data, we altered the bias voltage from 0 V to 30 V with a step of 0.1 V and read the transmission coefficient and phase response versus voltage data at each 100 MHz from the PNA 5227A using a Python program through LAN based VISA interface. Without loss of generality, the result at 2.4 GHz is shown in Figure 6. It is not difficult to find out that the relationship between the bias voltage and the amplitude or the phase response is nonlinear. At different frequencies, the transmission coefficients and phase respond to different voltages, and the phase tunable range is also different.

For the purpose of beamforming, phase response is an important parameter. The measured phase responses for different frequency samples from 2.0 GHz to 2.7 GHz stepping 0.1 GHz are shown in Figure 7 (simulations are not conducted

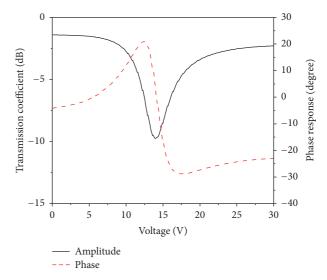


FIGURE 6: Measured results of transmission coefficient and phase response under different bias voltages at 2.4 GHz.

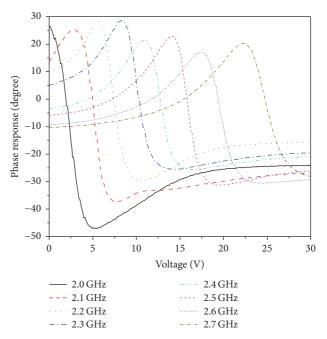


FIGURE 7: Measured phase response for different frequencies.

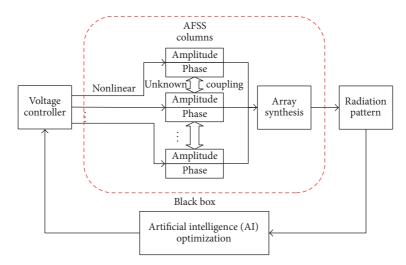


FIGURE 8: Measured phase response for different frequencies.

here for the reason of low efficiency and inaccuracy). The measured results show that the tunable phase response range is generally larger for the lower frequencies. At 2.1 GHz, the tunable range is 62.8°, while at 2.6 GHz it is 47.6°. This behavior means that this AFSS has a better phase shifting ability within lower frequency band than the higher. For the fixed structure, the phase tuning requirement is given by physical length as shown in Figure 2. In this work the phase needs to be tuned to compensate 16.4 mm and 30 mm. That is 43.5° and 79.4° for 2.1 GHz, while being 51.2° and 93.6° for 2.6 GHz. That means for the lower frequency band it is easier to satisfy the phase shifting requirement.

For the proposed antenna, the AFSS columns are very close to each other; thus the mutual coupling can be quite strong. Mutual coupling is usually considered when synthesizing a dense array. For a traditional array, multiple elements are fed though physically connected ports. It can be analyzed using a classical mutual impedance matrix method. This method is based on the voltage and current of the feed ports, as detailed in [19]. For the antenna in this work, these ports do not exist, and the interferences definitely happen before the signal reaches the AFSS columns. Thus, this method is not suitable for this case. An alternative approach is space-fed arrays [20–23]. However, to the best of the authors' knowledge, there is seldom discussion on the mutual coupling of these arrays.

Schneider and Munk proposed a method to calculate the scattering of super dense dipole array [24]. In this reference, the mutual coupling depends on the details of the unit cells, when the incident wave and the dipoles are not aligned. This method is based on the condition that all the elements are the same and uniformly distributed. This situation is very similar to our work. However, a big difference is that, in [24], all the elements are the same and static; in our work the AFSSes are supposed to be working under different voltages, which means that they have different states. This problem is much more complicated than the uniform cases. Also, Floquet mode is no longer suitable.

The flowchart of this problem and the idea to overcome it are shown in Figure 8. When 16-channel voltages are generated, the amplitudes and phases of the AFSS columns respond to the voltages. Radiation pattern can be synthesized if the amplitude and phase values are known. However, the relationship between the voltage and the states of the AFSS columns is nonlinear and the coupling between the columns is unknown. Furthermore, the amplitude and phase responses are not individual. Thus, the synthesis cannot be performed. To solve this problem, we considered the relationship between the voltages and the radiation pattern as a black box. An observer was added in the far field area to acquire the radiation level of the target direction. This radiation level is sent to an artificial intelligence (AI) based program and the relationship between the voltages and radiation pattern at the target direction is established. When a goal is assigned to the AI program, it can change the voltages to optimize the radiation pattern to reach the goal.

### 3. Genetic Algorithm Based Experimental Investigation

To realize the idea shown in Figure 8, we developed a genetic algorithm (GA) based program and a voltage controller. There are many other artificial intelligence methods. The reason we choose GA is because it is a global optimization method, and it is not complicated for programming.

3.1. The Genetic Algorithm Based Optimization System Setup. Artificial intelligence technologies have been well developed for decades. Studies on using GA to optimize arrays have been well reported [25–27], most of which used GA as a synthesis method to optimize the calculated radiation patterns. Different to these works, we developed the GA optimization system not only based on software but also on hardware. As can be seen from the block chart of Figure 9, the testing antenna and the developed antenna are both installed in a microwave anechoic chamber. Two coaxial

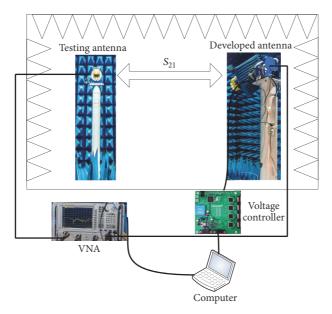


FIGURE 9: Illustration of the genetic algorithm based platform.

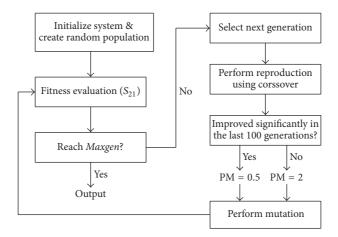


FIGURE 10: Program flowchart.

cables connect these two antennas and a N5227A vector network analyzer. When the measurement starts, the VNA is able to acquire the  $S_{21}$  parameter between the two antennas. A self-made multichannel voltage controller connects the AFSS smart dome to provide several channels of bias voltages, and the GA-based program running on a computer controls the values of these bias voltages.

The working flow is as follows. The GA program randomly generates a 16-value combination, the range of which is limited within 0 to 30. This combination is used as an *individual* in this GA program. Then the computer sends this combination command to the voltage controller to generate 16 voltage levels. The radiation pattern changes consequently. When the status is stable, the computer triggers the VNA to capture the  $S_{21}$  amplitude and takes it back. The score for this combination is calculated based on this  $S_{21}$  amplitude.

This 16-value combination is transformed to a binary code and used in the crossing-over and mutation procedure. For high-gain optimization, a higher score is given to a higher  $S_{21}$  amplitude; for the purpose of nulling, a higher score is given to a lower  $S_{21}$  amplitude. The flowchart of the GA part is shown in Figure 10. In this program, the population is 10; the Maxgen (max generation) is 500. During the optimization procedure, the program observes the improvement. If the improvement is not significant within the last 100 generations, the program will set PM (probability of mutation) to 0.5 to prevent the program being trapped in a local optimum. This program is written using Python language, and it is based on the Pyevolve package, created by Perone [28].

3.2. The GA Procedure. To guarantee that the GA program we used is functionally correct, it is run for 5 times to

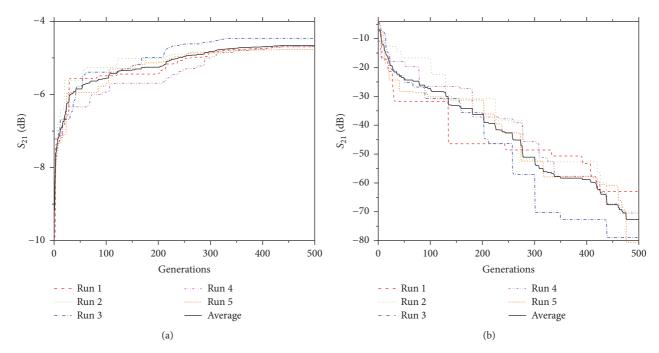


Figure 11:  $S_{21}$  variation of the GA procedure. (a) High-gain mode. (b) Nulling mode.

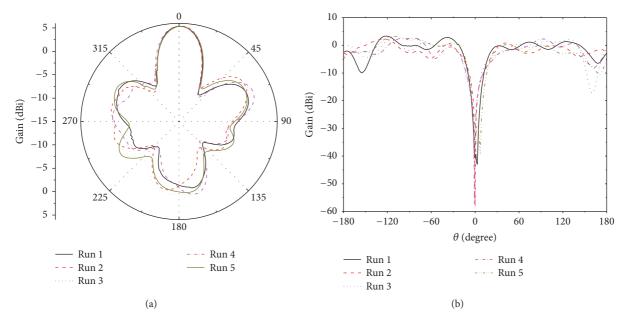


FIGURE 12: Radiation pattern for each 5 GA optimized results. (a) High-gain modes. (b) Nulling modes.

optimize the high-gain mode at 2.45 GHz. The best  $S_{21}$  of each generation are stored and presented in Figure 11. It shows that the procedure is not the same for each run, but the average curve shows a more stable trend. It reaches a good result every time.

We also measured the corresponding radiation pattern of these 10 time runs, and the results are shown in Figure 12. In both cases, different trials exhibit identical behavior at the  $0^{\circ}$  direction. For the 5 high-gain modes, the main lobes are

almost the same, but the side lobes and backward radiation are different. The 5 nulling modes are similar at 0° direction; all these 5 times can reach a deep nulling; besides this range, the radiation pattern is different for each time it runs. This is because at the other directions, there are no observation points. The GA program is not aware about the radiation of these directions. Of note, the measured nulling levels are different from the recoded ones shown in Figure 11. That is because all the environmental factors are actually considered

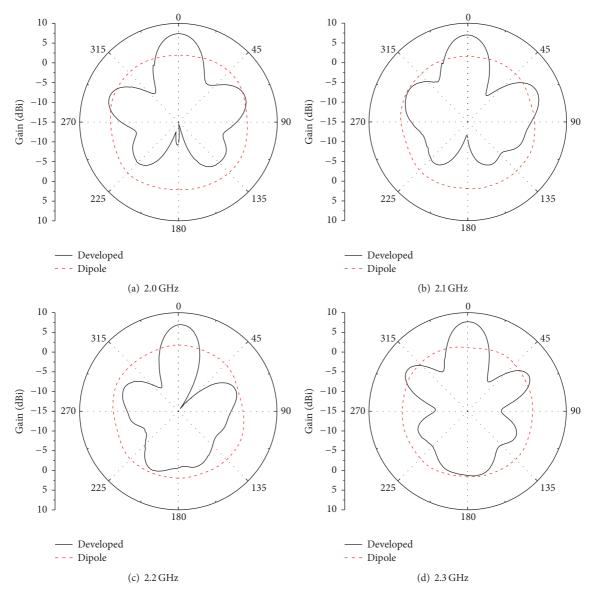


FIGURE 13: High-gain mode radiation patterns of the developed antenna from 2.0 GHz to 2.3 GHz.

during the optimization. We need to remove the control cable to prevent it from being stretched when performing the radiation pattern measurements.

3.3. High-Gain and Nulling Modes through the Tunable Range. We perform the high-gain modes optimization from 2.0 GHz to 2.7 GHz at each 100 MHz. We use two stander dipoles to cover this spectrum: a SD2050-174 for 2.0 GHz to 2.3 GHz and a SD2450-181 for the other frequencies. The data of these two dipole antennas can be found on SATIMO's website. The optimized radiation patterns are shown in Figures 13 and 14 compared with the radiation pattern of the dipoles. At 0° direction, which is the target direction, the gain is significantly higher than the dipoles. The data of gain, additional gain (AG) compared with the dipoles, 3 dB-beam width (3 dB-BW), side lobe level (SLL), and front-back ratio

(FBR) are shown in Table 1. The additional gain reaches 6.57 dB at 2.3 GHz, and it is higher than 5 dB from 2.0 GHz to 2.4 GHz. The 3 dB-beam width is from 26° to 34°. It is worthwhile to point out that, the 3 dB-beam-width in the azimuth plane obtained in this design is much smaller than those mentioned in [5–8, 10], the best of which achieves 47°. However, more efforts are being devoted to developing more smart GA-based optimization programs, for instance, a GA system that is capable of controlling all AFSS elements as independent ones (with higher degree of freedom) to achieve even higher level of gain or depression.

Another significant difference between this antenna and those mentioned in [5-8, 10] is that a very deep nulling level can be achieved. We alternated the goal of the GA program to achieve an increasingly lower  $S_{21}$  value. The measured radiation patterns of nulling mode are shown in Figures 15

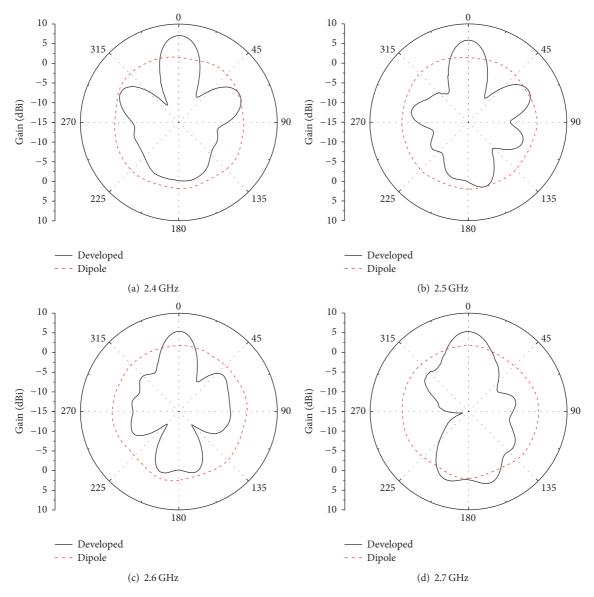


FIGURE 14: High-gain mode radiation patterns of the developed antenna from 2.4 GHz to 2.7 GHz.

Table 1: Survey of the high-gain modes.

| Freq<br>(GHz) | Gain<br>(dBi) | AG (dB) | 3 dB-BW<br>(degree) | SLL (dBi) | FBR (dB) |
|---------------|---------------|---------|---------------------|-----------|----------|
| 2.0           | 7.37          | 5.42    | 31                  | 3.54      | 16.84    |
| 2.1           | 6.99          | 5.40    | 30                  | 4.10      | 17.9     |
| 2.2           | 6.96          | 5.14    | 26                  | 0.50      | 7.56     |
| 2.3           | 7.69          | 6.57    | 27                  | 3.49      | 6.43     |
| 2.4           | 7.05          | 5.53    | 27                  | 1.98      | 7.26     |
| 2.5           | 5.86          | 4.44    | 27                  | 2.27      | 5.70     |
| 2.6           | 5.39          | 3.61    | 26                  | -0.45     | 5.55     |
| 2.7           | 5.30          | 3.53    | 34                  | Null      | 2.96     |

and 16. Here, we use Cartesian coordinate and the *x*-axis is transferred from  $0^{\circ}$ –360° to  $\pm$ 180° for a clearer look. At the

desired  $0^{\circ}$ , the nulling levels are below -30 dBi and even reach -56.41 dBi at 2.7 GHz. These results show that the proposed antenna can be used for noise cancelling and angle finding applications.

The antenna matching is influenced by the AFSS and the status. The measured  $S_{11}$  of 8 high-gain and 8 nulling modes are shown in Figure 17, compared with the dipoles' original  $S_{11}$ . For both of the dipoles,  $S_{11}$  are influenced by the AFSS and the working status. The results are still acceptable, since all the curves are around -10 dB. Moreover, it is obvious from Figure 17 that the  $S_{11}$  value of high-gain mode optimized for target frequency does not have a best value at each frequency; this is due to the reason that the optimization process is dominated by  $S_{21}$  performance and therefore makes sacrifice for the efficiency. However, this issue is still worthy of a further research to achieve a better matching performance, and more efforts are being devoted to

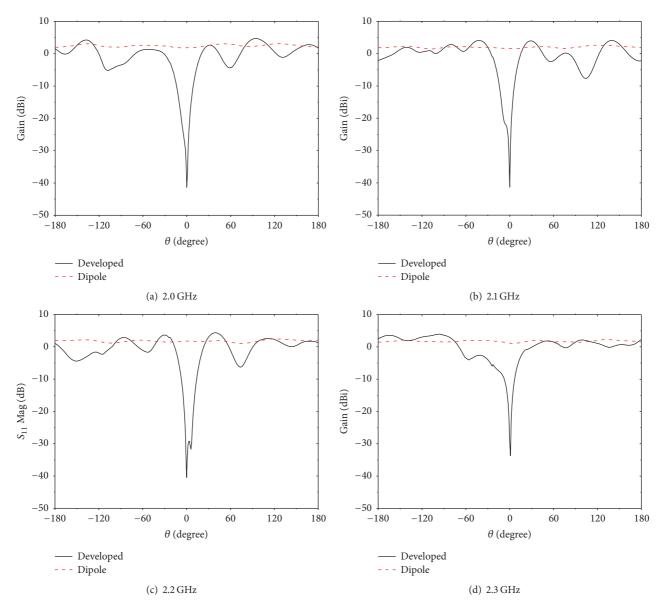


Figure 15: Nulling mode radiation patterns of the developed antenna from 2.0 GHz to 2.3 GHz.

developing independently controlled AFSS units and smart optimization algorithms, which would help improve such behavior significantly.

3.4. Continuously Steerable Ability. Another benefit of this antenna is that it is continuously tunable compared with the on/off method based electronically steerable antennas. The proposed antenna contains 16 AFSS columns and is perfectly central symmetric. Thus, there are 32 axes of symmetry. Therefore, we only need to prove that the antenna is continuously tunable within each 11.25° sector. To verify this ability, we shift the target direction from 0° to 11.25° by 3.75° to optimize the high-gain mode. Because for the purpose of communication, where high-gain mode is mostly employed, a 3.75° tunability is quite enough for a main lobe of

26° to 34° width. For the nulling mode, it is usually used for strong noise isolation and angle finding purpose, which often requires an accurate tunability; we shift the target direction for each 1° from 0° to 11°. The results are shown in Figure 18. For the 4 high-gain modes, the measured gains are 5.33 dBi, 5.17 dBi, 5.71 dBi, and 5.31 dBi, and they point to 0°, 7°, 9°, and 11°, respectively. The directions have some error, but the continuous tunability is basically approved. For the nulling modes, the nulling angles point to each 1° precisely.

3.5. Beam Bandwidth Investigation. Another important parameter for electronically steerable antenna is the beam bandwidth. For instance, to use this antenna for a 2.4 GHz WiFi system, there are two bandwidths we should be concerned about. One is 2.4–2.483 GHz, which is the total

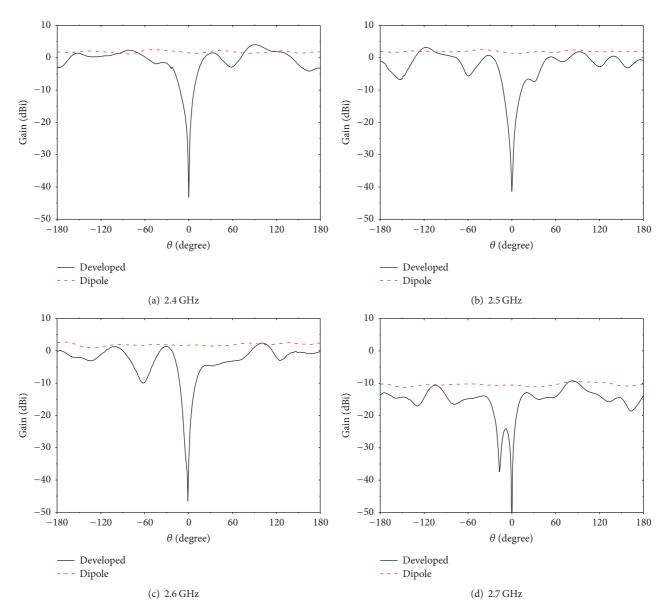


FIGURE 16: Nulling mode radiation patterns of the developed antenna from 2.4 GHz to 2.7 GHz.

2.4 GHz WiFi; the other bandwidth is the channel bandwidth, which is 22 MHz for IEEE 802.11b, 20-16 MHz for 802.11 g/n and some other standards. If the antenna control method is enclosed within the protocol, the bandwidth of the beam only needs to remain invariant in the channel bandwidth. Once the system changes the working channel, the antenna can change correspondingly. If the antenna control method is not included in the protocol, beam bandwidth has to cover the whole spectrum of this protocol. This is especially important for a frequency-hopping spread spectrum (FHSS) system such as the well-known Bluetooth system. In this work, the antenna is supposed to be narrow band. That is, because unlike attenuators and phase shifters based steerable antennas, the AFSS cannot maintain the same amplitude and phase value in a wide band. So, it is necessary to find out the beam bandwidth performance. We optimized the gain at 2.44 GHz and measured radiation pattern from 2.40 to 2.49 GHz by each 10 MHz. The results are shown in Figure 19(a). The gains are from 7.02 dBi to 5.53 dBi, which means that when using this antenna for a WiFi system without optimization to each channel or for a Bluetooth system, there will be 1.49 dB difference for different channels. It is no big problem, but we would like to see if this issue can be improved. To do so, we modified the program to observe the  $S_{21}$  of these 10 frequency points and scored the  $S_{21}$  with an additional condition to constrain the mean square error of the 10 amplitudes of  $S_{21}$  to be smaller than 0.2. The responding radiation patterns are shown in Figure 19(b). The difference of gain is smaller.

For a similar reason we performed a similar method to learn the beam bandwidth of the nulling mode. We set the average of these 10 amplitudes of  $S_{21}$  as the target instead of

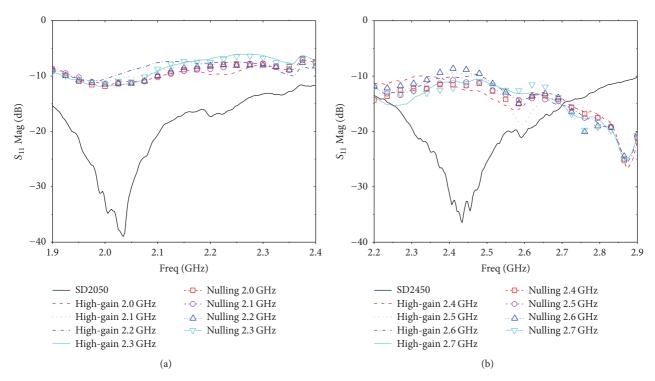


Figure 17: The influence on  $S_{11}$ . (a) SD2050 and 8 modes. (b) SD2450 and 8 modes.

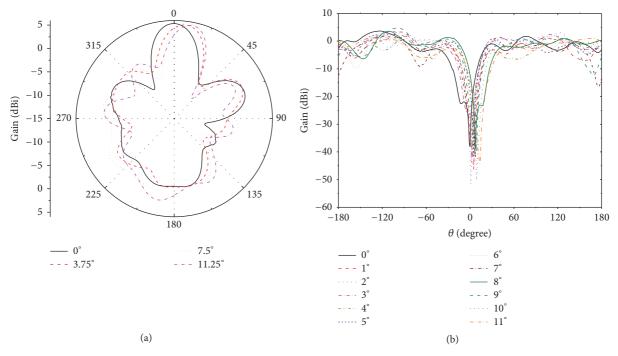


FIGURE 18: Radiation patterns for examining the continuous tunability. (a) High-gain modes. (b) Nulling modes.

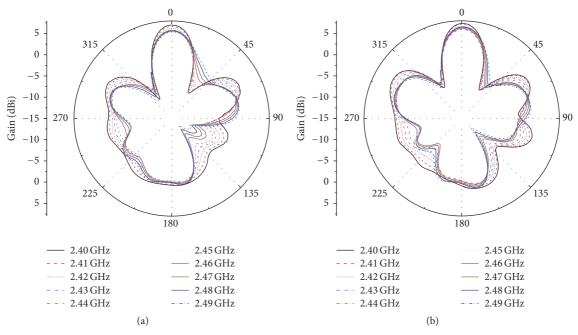


FIGURE 19: High-gain mode radiation patterns of WiFi band for the examination of beam bandwidth. (a) Without constraint. (b) Constrained by mean square error condition.

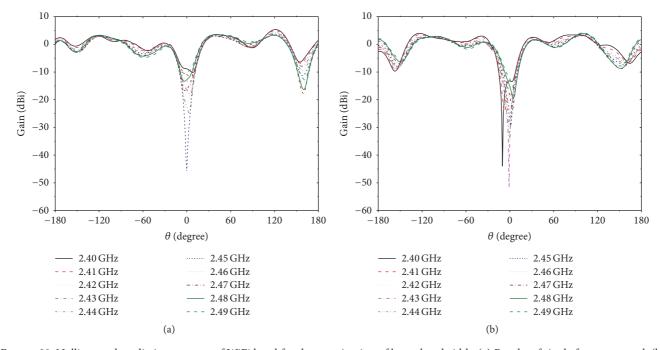


FIGURE 20: Nulling mode radiation patterns of WiFi band for the examination of beam bandwidth. (a) Results of single frequency goal. (b) Results of multiple frequency average goal.

the mean square error. The results are shown in Figure 20. The improvement is significant. For most frequencies, the nulling levels are below -20 dBi.

#### 4. Conclusion

In this paper, a highly agile electronically steerable active smart dome antenna is proposed. This antenna takes advantage

of the amplitude and phase response of the employed AFSS, as well as a self-made genetic algorithm based optimization system to experimentally realize high-gain modes and nulling modes within the frequency tunable range of 2.0 GHz to 2.7 GHz. The antenna is continuously steerable and outperforms many PIN-diode based FSS configurations in agility. The measured results achieved additional gain of up to 6.57 dB and a deep nulling level of –56 dBi. For the high-gain

modes, the -3 dB beam widths are  $26^{\circ}-34^{\circ}$ , while for the nulling mode, they can offer a steering resolution of 1°. Beam bandwidth measurement shows that it can offer stable highgain mode and nulling mode for 2.4 GHz WiFi band.

#### **Competing Interests**

The authors declare that they have no competing interests.

#### **Acknowledgments**

This work was supported by the National Natural Science Foundation of China (61601391) and Educational Commission of Fujian Province, China (JZ160449).

#### References

- [1] H. Krim and M. Viberg, "Two decades of array signal processing research: the parametric approach," *IEEE Signal Processing Magazine*, vol. 13, no. 4, pp. 67–94, 1996.
- [2] A. Alexiou and M. Haardt, "Smart antenna technologies for future wireless systems: trends and challenges," *IEEE Communications Magazine*, vol. 42, no. 9, pp. 90–97, 2004.
- [3] S. Farzaneh and A.-R. Sebak, "A novel amplitude-phase weighting for analog microwave beamforming," *IEEE Transactions on Antennas and Propagation*, vol. 54, no. 7, pp. 1997–2008, 2006.
- [4] J. Kennedy and M. C. Sullivan, "Direction finding and "smart antennas" using software radio architectures," *IEEE Communications Magazine*, vol. 33, no. 5, pp. 62–68, 1995.
- [5] M. Roig, M. Sazegar, Y. Zheng, and R. Jakoby, "Tunable frequency selective surface based on ferroelectric ceramics for beam steering antennas," in *Proceedings of the 7th German Microwave Conference (GeMiC '12)*, pp. 1–4, March 2012.
- [6] A. Edalati and T. A. Denidni, "High-gain reconfigurable sectoral antenna using an active cylindrical fss structure," *IEEE Transac*tions on Antennas and Propagation, vol. 59, no. 7, pp. 2464–2472, 2011.
- [7] M. N. Jazi and T. A. Denidni, "Agile radiation-pattern antenna based on active cylindrical frequency selective surfaces," *IEEE Antennas and Wireless Propagation Letters*, vol. 9, pp. 387–388, 2010.
- [8] M. Niroo-Jazi and T. A. Denidni, "Electronically sweeping-beam antenna using a new cylindrical frequency-selective surface," *IEEE Transactions on Antennas and Propagation*, vol. 61, no. 2, pp. 666–676, 2013.
- [9] L. Zhang, Q. Wu, and T. A. Denidni, "Electronically radiation pattern steerable antennas using active frequency selective surfaces," *IEEE Transactions on Antennas and Propagation*, vol. 61, no. 12, pp. 6000–6007, 2013.
- [10] B. Liang, B. Sanz-Izquierdo, E. A. Parker, and J. C. Batchelor, "Cylindrical slot FSS configuration for beam-switching applications," *IEEE Transactions on Antennas and Propagation*, vol. 63, no. 1, pp. 166–173, 2015.
- [11] W. Pan, C. Huang, P. Chen, M. Pu, X. Ma, and X. Luo, "A beam steering horn antenna using active frequency selective surface," *IEEE Transactions on Antennas and Propagation*, vol. 61, no. 12, pp. 6218–6223, 2013.
- [12] L. C. Godara, Smart Antennas, CRC Press, 2014.
- [13] D. Schurig, J. J. Mock, and D. R. Smith, "Electric-field-coupled resonators for negative permittivity metamaterials," *Applied Physics Letters*, vol. 88, no. 4, Article ID 041109, 2006.

- [14] W. Withayachumnankul, C. Fumeaux, and D. Abbott, "Planar array of electric-LC resonators with broadband tunability," *IEEE Antennas and Wireless Propagation Letters*, vol. 10, pp. 577–580, 2011
- [15] J. Y. Kim, D. S. Kim, D. W. Woo, D. S. Shin, W. S. Park, and W. Hwang, "Electromagnetic wave characteristics of secondorder composite frequency-selective surfaces fabricated by ebeam evaporator," *Electronics Letters*, vol. 50, no. 3, pp. 189–190, 2014.
- [16] J. M. Zendejas, J. P. Gianvittorio, Y. Rahmat-Samii, and J. W. Judy, "Magnetic MEMS reconfigurable frequency-selective surfaces," *Journal of Microelectromechanical Systems*, vol. 15, no. 3, pp. 613–623, 2006.
- [17] B. Schoenlinner, A. Abbaspour-Tamijani, L. C. Kempel, and G. M. Rebeiz, "Switchable low-loss RF MEMS Ka-band frequency-selective surface," *IEEE Transactions on Microwave Theory and Techniques*, vol. 52, no. 11, pp. 2474–2481, 2004.
- [18] J. P. Gianvittorio, J. Zendejas, Y. Rahmat-Samii, and J. Judy, "Reconfigurable MEMS-enabled frequency selective surfaces," *Electronics Letters*, vol. 38, no. 25, pp. 1627–1628, 2002.
- [19] I. J. Gupta and A. A. Ksienski, "Effect of mutual coupling on the performance of adaptive arrays," *IEEE Transactions on Antennas* and Propagation, vol. 31, no. 5, pp. 785–791, 1983.
- [20] K. S. Rao, "On the collimation phase error computation of a space-fed planar phased array," *IEEE Transactions on Antennas* and Propagation, vol. 31, no. 1, pp. 154–156, 1983.
- [21] C. H. Hightower, S. H. Wong, A. R. Perkons, and C. I. Igwe, "A space-fed phased array for surveillance from space," *IEEE Aerospace and Electronic Systems Magazine*, vol. 6, no. 5, pp. 13–17, 1991.
- [22] M. Stoneback, M. Stoneback, and Y. Kuga, "Feasibility study of a wirelessly controlled and powered space-fed phased array antenna," *IEEE Transactions on Antennas and Propagation*, vol. 61, no. 12, pp. 5984–5991, 2013.
- [23] E. Jacobs, "Phase error effects on gain and sidelobe level of a space-fed array," *IEEE Transactions on Antennas and Propaga*tion, vol. 28, no. 2, pp. 243–246, 1980.
- [24] S. W. Schneider and B. A. Munk, "The scattering properties of "super dense" arrays of dipoles," *IEEE Transactions on Antennas and Propagation*, vol. 42, no. 4, pp. 463–472, 1994.
- [25] R. L. Haupt, "Thinned arrays using genetic algorithms," *IEEE Transactions on Antennas and Propagation*, vol. 42, no. 7, pp. 993–999, 1994.
- [26] F. J. Ares-Pena, J. A. Rodriguez-Gonzalez, E. Villanueva-Lopez, and S. R. Rengarajan, "Genetic algorithms in the design and optimization of antenna array patterns," *IEEE Transactions on Antennas and Propagation*, vol. 47, no. 3, pp. 506–510, 1999.
- [27] K.-K. Yan and Y. Lu, "Sidelobe reduction in array-pattern synthesis using genetic algorithm," *IEEE Transactions on Antennas and Propagation*, vol. 45, no. 7, pp. 1117–1122, 1997.
- [28] C. S. Perone, Pyevolve project, http://pyevolve.sourceforge.net/.

Hindawi Publishing Corporation International Journal of Antennas and Propagation Volume 2016, Article ID 1909708, 9 pages http://dx.doi.org/10.1155/2016/1909708

## Research Article

# **Impact on Antijamming Performance of Channel Mismatch in GNSS Antenna Arrays Receivers**

#### Zukun Lu, Junwei Nie, Feigiang Chen, and Gang Ou

College of Electronic Science and Engineering, National University of Defense Technology, Changsha 410073, China

Correspondence should be addressed to Zukun Lu; luzukun@nudt.edu.cn

Received 28 June 2016; Accepted 20 November 2016

Academic Editor: Antonio Faraone

Copyright © 2016 Zukun Lu et al. This is an open access article distributed under the Creative Commons Attribution License, which permits unrestricted use, distribution, and reproduction in any medium, provided the original work is properly cited.

The performance of antijamming is limited by channel mismatch in global navigation satellite system (GNSS) antenna arrays receivers. Only when the amplitude and phase characteristics of each array channels are the same is the interference likely to be completely suppressed. This paper analyzes the impact on antijamming performance of channel mismatch. We built the model of channel mismatch and derived the impact on transfer function with space-time adaptive processor (STAP) of channel mismatch in theory. The impact factor of channel mismatch is proposed by the fuzzy transfer function, which could directly reflect the antijamming performance under channel mismatch. In addition, every characteristic in the channel mismatch model is analyzed. The analysis results show that the greatest impacts on antijamming performance are the range of amplitude wave and the group delay bias, while the influence of the number of amplitudes is next. As for the effect of group delay fluctuation is the smallest.

#### 1. Introduction

Since 1970s, global navigation satellite system (GNSS), whose representative is global position system (GPS), has a rapid development. GNSS has brought great convenience to people in traffic, and it is also widely used in military field [1]. The distance between earth surface and navigation satellite is about 27,000 km. The navigation signal is very weak when it reaches the ground. The navigation receivers get the signals with the signal/noise ratio (SNR) is about -30 dB, which makes receivers vulnerable to all kinds of intentional or unintentional interference. The performance of antijamming has become a key indicator in military and some civilian applications [2, 3]. According to the number of antennas, the antijamming technology of receivers can be divided into single antenna and antenna arrays, in which the single antenna could only suppress narrowband interference and the antenna arrays could suppress both narrowband and wideband interference [4]. Under the condition of navigation war, the receivers would face the strong wideband interference. The antenna arrays equipped with space-time adaptive processor (STAP) would be an optimal choice in the electromagnetic countermeasure [5]. The fundamental principle of STAP is array weight in digital baseband, which could suppress interference effectively when the amplitude and phase characteristics of each channel are unanimous [6]. However, each array channel is composed of the low noise amplifier (LNA), analog filter, inverter, and other analog devices. The manufacturing errors and environmental and other factors could lead to inconsistencies of amplitude and phase in each channel, which would cause channel mismatch [7, 8]

Channel mismatch has attracted the attention of scholars. The impact of channel mismatch on array gain is studied by space-only processor (SOP) in [9], which notes that the amplitude and phase mismatch would affect the performance of interference cancellation, which would lead to the degradation of antijamming performance. Literature [10] gives a preliminary analysis to the impact of channel mismatch on antenna arrays equipped with STAP. The estimated carrier phase would be biased due to the channel mismatch, and the greater mismatch would bring greater deviation. A correction method of channel mismatch based on the correction table is proposed in [11], which needs to measure the frequency response in all directions and estimate the bias of pseudocode and carrier phase which is introduced by antenna arrays, and it also needs to make the correction table bind to the

receivers, whereas the nonideal characteristic of the channel might be changed in some time, whose method lacks certain robustness.

This paper further analyzes the impact of channel mismatch on antijamming performance with antenna arrays. First of all, we establish a model of channel mismatch and deduce the impact of channel mismatch on transfer function with STAP in theory. Then, the impact on antijamming performance is analyzed. We propose a concept of channel mismatch impact factor and point out the largest impact characteristic of channel mismatch to antijamming performance. Finally, simulation experiments are implemented to validate the correctness of the analytical results.

#### 2. Channel Mismatch Model

Nonideal characteristics of the channel are mainly reflected in the nonflatness of the amplitude and nonlinearity of the phase. The impact of the interference suppression in antenna arrays is not the absolute value of each channel, but the different between each channel, which can be called channel mismatch [12].

Suppose the transfer function in the channel n is  $H_n(\omega)$ , and literature [13] gives a channel mismatch model which can be written as

$$H_{n}(\omega) = \begin{cases} A(\omega) e^{j\varphi(\omega)} & |\omega| \le \pi B \\ 0 & \text{else,} \end{cases}$$
 (1)

where B is the bandwidth of receivers.  $A(\omega)$  and  $\varphi(\omega)$  are the response of amplitude-frequency and phase-frequency, respectively. In the ideal case,  $A(\omega)$  and  $\varphi(\omega)$  satisfy the following relationship:

$$A(\omega) \equiv 1$$
 
$$\varphi(\omega) \equiv 0.$$
 (2)

A more accurate channel mismatch model has been demonstrated in [14] which can be expressed as

$$H_n(\omega)$$

$$= \begin{cases} \left(1 + R_a \cos \omega R_{an}\right) e^{j(R_p \cos \omega R_{pn} + \omega R_b)} & |\omega| \le \pi B \\ 0 & \text{else,} \end{cases}$$

where  $R_a$  and  $R_p$  are the range of amplitude and group delay wave, respectively.  $R_{an}$  and  $R_{pn}$  are the number of amplitude and group delay waves, separately.  $R_b$  is the group delay bias.

As for the antenna arrays with N elements, the channel mismatch model can be written as

$$\mathbf{H}(\omega) = \left[ H_1(\omega) \cdots H_N(\omega) \right]^{\mathrm{T}}. \tag{4}$$

#### 3. Impact on Transfer Function

STAP has obvious advantages compared to the simple time domain, frequency domain, and SOP. STAP could suppress a variety of interferences. Without increasing the antenna elements, the degree of freedom (DoF) of interference suppression can greatly increase, and its interference suppression capability has a quality improvement [15]. In addition, STAP could mitigate the impact of channel mismatch to interference suppression. The taps in STAP can compensate the channel mismatch.

The STAP equipped with N elements and M taps is shown in Figure 1 [16].

According to the STAP model shown in Figure 1, the received data in different sampling time could form a new data vector which could be expressed as

$$\mathbf{x} = \begin{bmatrix} \mathbf{X}^{\mathrm{T}}(t) & \mathbf{X}^{\mathrm{T}}(t-T) & \cdots & \mathbf{X}^{\mathrm{T}}(t-(M-1)T) \end{bmatrix}^{\mathrm{T}}, \quad (5)$$

where  $\mathbf{X}(t)$  is the received data vector at the time of t.

Array weightings could be written as

$$w = [w_{11}, \dots, w_{N1}, \dots, w_{1M}, \dots, w_{NM}]^{T}$$
 (6)

In order to conveniently perform analysis, assume the number of interferences is one and its power spectral density (PSD) is smooth. In addition, STAP is equipped with 2 elements and 2 taps.

The steering vector of time and space domain can be, respectively, denoted as

$$v^{t}(\omega) = \begin{bmatrix} 1 & \cdots & e^{-j\omega(M-1)T} \end{bmatrix}^{T}$$

$$v^{s}(\theta) = \begin{bmatrix} 1 & \cdots & e^{-j\omega_{R}(N-1)\tau(\theta)} \end{bmatrix}^{T},$$
(7)

where T is the sampling period,  $\omega_R$  is the radio frequency (RF), and  $\tau(\theta)$  is the delay of the two adjacent antenna elements and the signal or interference direction is  $\theta$  and it can be further expressed as [17]

$$\tau(\theta) = \frac{d\sin\theta}{c},\tag{8}$$

where d is the distance of the adjacent antenna elements with half wavelength and c is the propagation speed of signal or interference.

According to (7), the steering vector of space-time domain can be written as

$$\mathbf{a}\left(\omega,\theta\right) = v^{t}\left(\omega\right) \otimes v^{s}\left(\omega_{R},\theta\right). \tag{9}$$

Suppose channel 1 is desirable, and channel 2 represents the nonideal characteristics, and its transfer function is H that is related to the frequency with  $\omega$ . According to (4), the model of channel mismatch could be expressed as

$$\mathbf{H}\left(\omega\right) = \begin{bmatrix} H_0 & H \end{bmatrix}^{\mathrm{T}}.\tag{10}$$

As for all frequency,  $H_0$  in the above equation would satisfy the following relation:

$$H_0 \equiv 1. \tag{11}$$

Then, the steering vector of space-time domain could be improved as

$$\mathbf{a}\left(\omega,\theta\right) = v^{t}\left(\omega\right) \otimes \left[v^{s}\left(\omega_{R},\theta\right) \odot \mathbf{H}\left(\omega\right)\right],\tag{12}$$

where  $\otimes$  stands for Kronecker product and  $\odot$  indicates Hadamard product.

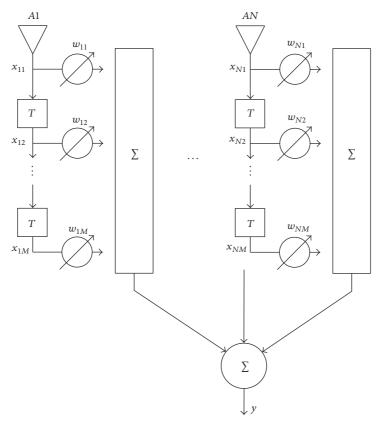


FIGURE 1: The STAP equipped with *N* elements and *M* taps.

The power of signal is about 30 dB lower than the noise, so the signal can be negligible in calculating the correlation matrix. Thus, the correlation matrix of the received data could be expressed as

$$\begin{split} \mathbf{R}_{xx} &= E\left[\mathbf{x}\left(t\right)\mathbf{x}^{H}\left(t\right)\right] \\ &= E\left[\mathbf{j}\left(t\right)\mathbf{j}^{H}\left(t\right)\right] + E\left[\mathbf{n}\left(t\right)\mathbf{n}^{H}\left(t\right)\right] \\ &= E\left[a_{j}\left(\omega_{I},\theta_{j}\right)j\left(t\right)\left(a_{j}\left(\omega_{I},\theta_{j}\right)j\left(t\right)\right)^{H}\right] \\ &+ E\left[\mathbf{n}\left(t\right)\mathbf{n}^{H}\left(t\right)\right] \end{split}$$

$$= E\left[a_{j}\left(\omega_{I}, \theta_{j}\right) j\left(t\right) j^{H}\left(t\right) a_{j}^{H}\left(\omega_{I}, \theta_{j}\right)\right]$$

$$+ E\left[\mathbf{n}\left(t\right) \mathbf{n}^{H}\left(t\right)\right]$$

$$= \sigma_{j}^{2} E\left[a_{j}\left(\omega_{I}, \theta_{j}\right) a_{j}^{H}\left(\omega_{I}, \theta_{j}\right)\right] + \sigma_{n}^{2} \mathbf{I},$$

$$(13)$$

where  $\mathbf{j}(t)$  and  $\mathbf{n}(t)$  stand for the interference and noise, separately.  $\sigma_n^2$  and  $\sigma_j^2$  are the power of noise and interference, respectively. I is a unit matrix,  $\theta_j$  is the incident direction of interference, and  $\omega_I$  is the intermediate frequency.

Then

$$E\left[a_{j}\left(\omega,\theta_{j}\right)a_{j}^{H}\left(\omega,\theta_{j}\right)\right]$$

$$= \zeta \begin{bmatrix} \|H_{0}\|_{2}^{2} & \langle H_{0},H \rangle e^{j\pi \sin\theta_{j}} & \|H_{0}\|_{2}^{2} e^{j\omega_{l}T} & \langle H_{0},H \rangle e^{j(\omega_{l}T+\pi \sin\theta_{j})} \\ \langle H,H_{0} \rangle e^{-j\pi \sin\theta_{j}} & \|H\|_{2}^{2} & \langle H,H_{0} \rangle e^{j(\omega_{l}T-j\pi \sin\theta_{j})} & \|H\|_{2}^{2} e^{j\omega_{l}T} \\ \|H_{0}\|_{2}^{2} e^{-j\omega_{l}T} & \langle H_{0},H \rangle e^{-j(\omega_{l}T-\pi \sin\theta_{j})} & \|H_{0}\|_{2}^{2} & \langle H_{0},H \rangle e^{j\pi \sin\theta_{j}} \\ \langle H,H_{0} \rangle e^{-j(\omega_{l}T+j\pi \sin\theta_{j})} & \|H\|_{2}^{2} e^{-j\omega_{l}T} & \langle H,H_{0} \rangle e^{-j\pi \sin\theta_{j}} & \|H\|_{2}^{2} \end{bmatrix},$$

$$(14)$$

where  $\zeta$  is related to the receiver bandwidth which is B, and it could be written as

$$\zeta = \frac{1}{2\pi B}.\tag{15}$$

 $\|H_n\|_2^2$  is the 2-norm of  $H_n$  and  $\langle H_m, H_n \rangle$  represents the inner product with  $H_m$  and  $H_n$ , which could be denoted as

$$\left\|H_{m}\right\|_{2} = \sqrt{\int_{-\pi R}^{\pi B} \left|H_{m}\left(\omega\right)\right|^{2} d\omega}$$

$$\langle H_m, H_n \rangle = \int_{-\pi B}^{\pi B} H_m(\omega) H_n^H(\omega) d\omega.$$
 (16)

Consequently, the correlation matrix could be expressed

 $\mathbf{R}_{xx}$ 

$$=\begin{bmatrix} \zeta\sigma_{j}^{2} \|H_{0}\|_{2}^{2} + \sigma_{n}^{2} & \zeta\sigma_{j}^{2} \langle H_{0}, H \rangle e^{j\pi \sin\theta_{J}} & \zeta\sigma_{j}^{2} \|H_{0}\|_{2}^{2} e^{j\omega_{I}T} & \zeta\sigma_{j}^{2} \langle H_{0}, H \rangle e^{j(\omega_{I}T + \pi \sin\theta_{J})} \\ \zeta\sigma_{j}^{2} \langle H, H_{0} \rangle e^{-j\pi \sin\theta_{J}} & \zeta\sigma_{j}^{2} \|H\|_{2}^{2} + \sigma_{n}^{2} & \zeta\sigma_{j}^{2} \langle H, H_{0} \rangle e^{j(\omega_{I}T - j\pi \sin\theta_{J})} & \zeta\sigma_{j}^{2} \|H\|_{2}^{2} e^{j\omega_{I}T} \\ \zeta\sigma_{j}^{2} \|H_{0}\|_{2}^{2} e^{-j\omega_{I}T} & \zeta\sigma_{j}^{2} \langle H_{0}, H \rangle e^{-j(\omega_{I}T - \pi \sin\theta_{J})} & \zeta\sigma_{j}^{2} \|H_{0}\|_{2}^{2} + \sigma_{n}^{2} & \zeta\sigma_{j}^{2} \langle H_{0}, H \rangle e^{j\pi \sin\theta_{J}} \\ \zeta\sigma_{j}^{2} \langle H, H_{0} \rangle e^{-j(\omega_{I}T + j\pi \sin\theta_{J})} & \zeta\sigma_{j}^{2} \|H\|_{2}^{2} e^{-j\omega_{I}T} & \zeta\sigma_{j}^{2} \langle H, H_{0} \rangle e^{-j\pi \sin\theta_{J}} & \zeta\sigma_{j}^{2} \|H\|_{2}^{2} + \sigma_{n}^{2} \end{bmatrix}.$$

$$(17)$$

The inverse of correlation matrix could be denoted as

$$\mathbf{R}_{xx}^{-1} = \frac{1}{|\mathbf{R}_{xx}|} \mathbf{R}_{xx}^*, \tag{18}$$

where  $|\mathbf{R}_{xx}|$  and  $\mathbf{R}_{xx}^*$  are the determinant and adjoint matrix of  $\mathbf{R}_{rr}$ , separately.

 $\mathbf{R}_{xx}$  is a Hermite matrix, so its determinant is a constant value. We suppose that  $v = |\mathbf{R}_{xx}|$ .

 $\mathbf{R}_{xx}^*$  can be simplified as

 $\mathbf{R}_{xx}^*$ 

$$=\sigma_{n}^{4}\begin{bmatrix} \left(2\sigma_{j}^{2}\zeta\left\|H\right\|_{2}^{2}+\sigma_{j}^{2}\zeta\left\|H_{0}\right\|_{2}^{2}+\sigma_{n}^{2}\right) & -\sigma_{j}^{2}\zeta\left\langle H_{0},H\right\rangle e^{j\pi\sin\theta_{j}}\\ -\sigma_{j}^{2}\zeta\left\langle H,H_{0}\right\rangle e^{-j\pi\sin\theta_{j}} & \left(\sigma_{j}^{2}\zeta\left\|H\right\|_{2}^{2}+2\sigma_{j}^{2}\zeta\left\|H_{0}\right\|_{2}^{2}+\sigma_{n}^{2}\\ -\sigma_{j}^{2}\zeta\left\|H_{0}\right\|_{2}^{2}e^{-j\omega_{l}T} & -\sigma_{j}^{2}\zeta\left\langle H_{0},H\right\rangle e^{j(\pi\sin\theta_{j}-\omega_{l}T)}\\ -\sigma_{j}^{2}\zeta\left\langle H,H_{0}\right\rangle e^{-j(\pi\sin\theta_{j}+\omega_{l}T)} & -\sigma_{j}^{2}\zeta\left\|H\right\|_{2}^{2}e^{-j\omega_{l}T} \end{bmatrix}$$

Power inversion (PI) is a typical blind criterion to suppress interference, which does not require any a priori information. It can form nulls in the direction of strong interference with superior adaptive performance, and its suitable application is in the condition of strong interference and weak signal, especially in GNSS receivers [18]. Its constraint can be written as

$$\min_{w} \quad \left\{ \mathbf{w}^{H} \mathbf{R}_{xx} \mathbf{w} \right\} 
\text{s.t.} \quad \mathbf{w}^{H} b = 1,$$
(20)

where  $b = \begin{bmatrix} 1 & 0 & \cdots & 0 \end{bmatrix}^T$  is the constraint vector. The weights can be further expressed as

$$\begin{split} \mathbf{w} &= \mu \mathbf{R}_{xx}^{-1} b = \mu \frac{1}{\left|\mathbf{R}_{xx}\right|} \mathbf{R}_{xx}^* b \\ &= \frac{\mu}{v} \left[ \left( 2\sigma_j^2 \zeta \left\| H \right\|_2^2 + \sigma_j^2 \zeta \left\| H_0 \right\|_2^2 + \sigma_n^2 \right) \sigma_n^4 \\ &- \sigma_n^4 \sigma_j^2 \zeta \left\langle H, H_0 \right\rangle e^{-j\pi \sin \theta_J} - \sigma_n^4 \sigma_j^2 \zeta \left\| H_0 \right\|_2^2 e^{-j\omega_I T} \\ &- \sigma_n^4 \sigma_j^2 \zeta \left\langle H, H_0 \right\rangle e^{-j(\pi \sin \theta_J + \omega_I T)} \right] = \varsigma \left[ 2\sigma_j^2 \zeta \left\| H \right\|_2^2 \right] \end{split}$$

$$=\sigma_{n}^{4}\begin{bmatrix} \left(2\sigma_{j}^{2}\zeta\,\|H\|_{2}^{2}+\sigma_{j}^{2}\zeta\,\|H_{0}\|_{2}^{2}+\sigma_{n}^{2}\right) & -\sigma_{j}^{2}\zeta\,\langle H_{0},H\rangle\,e^{j\pi\sin\theta_{j}} & -\sigma_{j}^{2}\zeta\,\|H_{0}\|_{2}^{2}\,e^{j\omega_{l}T} & -\sigma_{j}^{2}\zeta\,\langle H_{0},H\rangle\,e^{j(\pi\sin\theta_{j}+\omega_{l}T)} \\ -\sigma_{j}^{2}\zeta\,\langle H,H_{0}\rangle\,e^{-j\pi\sin\theta_{j}} & \left(\sigma_{j}^{2}\zeta\,\|H\|_{2}^{2}+2\sigma_{j}^{2}\zeta\,\|H_{0}\|_{2}^{2}+\sigma_{n}^{2}\right) & -\sigma_{j}^{2}\zeta\,\langle H,H_{0}\rangle\,e^{-j(\pi\sin\theta_{j}-\omega_{l}T)} & -\sigma_{j}^{2}\zeta\,\|H\|_{2}^{2}\,e^{j\omega_{l}T} \\ -\sigma_{j}^{2}\zeta\,\|H_{0}\|_{2}^{2}\,e^{-j\omega_{l}T} & -\sigma_{j}^{2}\zeta\,\langle H_{0},H\rangle\,e^{j(\pi\sin\theta_{j}-\omega_{l}T)} & \left(2\sigma_{j}^{2}\zeta\,\|H\|_{2}^{2}+\sigma_{j}^{2}\zeta\,\|H_{0}\|_{2}^{2}+\sigma_{n}^{2}\right) & -\sigma_{j}^{2}\zeta\,\langle H_{0},H\rangle\,e^{j\pi\sin\theta_{j}} \\ -\sigma_{j}^{2}\zeta\,\langle H,H_{0}\rangle\,e^{-j(\pi\sin\theta_{j}+\omega_{l}T)} & -\sigma_{j}^{2}\zeta\,\|H\|_{2}^{2}\,e^{-j\omega_{l}T} & -\sigma_{j}^{2}\zeta\,\langle H,H_{0}\rangle\,e^{-j\pi\sin\theta_{j}} & \left(\sigma_{j}^{2}\zeta\,\|H\|_{2}^{2}+2\sigma_{j}^{2}\zeta\,\|H_{0}\|_{2}^{2}+\sigma_{n}^{2}\right) \end{bmatrix}. \tag{19}$$

$$+ \sigma_{j}^{2} \zeta \|H_{0}\|_{2}^{2} + \sigma_{n}^{2} - \sigma_{j}^{2} \zeta \langle H, H_{0} \rangle e^{-j\pi \sin \theta_{j}}$$

$$- \sigma_{j}^{2} \zeta \|H_{0}\|_{2}^{2} e^{-j\omega_{I}T} - \sigma_{j}^{2} \zeta \langle H, H_{0} \rangle e^{-j(\pi \sin \theta_{j} + \omega_{I}T)}$$

$$\approx \zeta \sigma_{j}^{2} \zeta \left[ 2 \|H\|_{2}^{2} + \|H_{0}\|_{2}^{2} - \langle H, H_{0} \rangle e^{-j\pi \sin \theta_{j}}$$

$$- \|H_{0}\|_{2}^{2} e^{-j\omega_{I}T} - \langle H, H_{0} \rangle e^{-j(\pi \sin \theta_{j} + \omega_{I}T)} \right].$$
(21)

The above approximate condition is that the jammer power is much higher than the noise, which is suitable for the actual situation.

The weight vector could be normalized as

$$\mathbf{w} = \alpha \left[ 2 \|H\|_{2}^{2} + \|H_{0}\|_{2}^{2} - \langle H, H_{0} \rangle e^{-j\pi \sin \theta_{J}} - \|H_{0}\|_{2}^{2} e^{-j\omega_{I}T} - \langle H, H_{0} \rangle e^{-j(\pi \sin \theta_{J} + \omega_{I}T)} \right],$$
(22)

where  $\alpha$  is the factor of normalization and it could be denoted

$$\alpha = \frac{1}{\sqrt{\left(2\|H\|_{2}^{2} + \|H_{0}\|_{2}^{2}\right)^{2} + 2\left|\langle H, H_{0}\rangle\right|^{2} + \|H_{0}\|_{2}^{4}}}.$$
 (23)

According to Figure 1, (5), and (8), the array output signal in time domain can be represented as

$$y(t) = w^{H} \mathbf{x}$$

$$= \sum_{i=1}^{N} \sum_{m=1}^{M} x_{0} (t - (i-1)\tau(\theta) - (m-1)T) w_{im}^{*},$$
(24)

where  $x_0(t)$  is the sample value of reference array element in the time of t. The Fourier transform of (24) can be expressed as

$$Y(\omega) = \sum_{i=1}^{N} \sum_{m=1}^{M} X(\omega) e^{-j\pi(i-1)\sin\theta} e^{-j\omega(m-1)T} w_{im}^{*}$$

$$= X(\omega) \sum_{m=1}^{M} e^{-j\omega(m-1)T} \left[ \sum_{i=1}^{N} e^{-j\pi(i-1)\sin\theta} w_{im}^{*} \right].$$
(25)

Therefore, the transfer function of STAP can be obtained as

$$H(\omega, \theta) = \sum_{m=1}^{M} e^{-j\omega(m-1)T} \left[ \sum_{i=1}^{N} e^{-j\omega(i-1)\tau(\theta)} w_{im}^{*} \right].$$
 (26)

According to the space-time steering vector in (9), the transfer function of STAP in the direction of interference can be expressed as

$$H(\omega, \theta_{J}) = w^{H} \mathbf{a} (\omega, \theta_{J}) = \alpha \left( 2 \|H\|_{2}^{2} + \|H_{0}\|_{2}^{2} - \langle H_{0}, H \rangle - (\|H_{0}\|_{2}^{2} + \langle H_{0}, H \rangle) e^{-j(\omega - \omega_{I})T} \right)$$

$$= \alpha \left( 2 \int_{-\pi B}^{\pi B} |A(\omega)|^{2} d\omega + 2\pi B - \int_{-\pi B}^{\pi B} A(\omega) e^{-j\varphi(\omega)} d\omega - \left( 2\pi B + \int_{-\pi B}^{\pi B} A(\omega) e^{-j\varphi(\omega)} d\omega \right) e^{-j(\omega - \omega_{I})T} \right).$$

$$(27)$$

The mismatched steering vector is used in (17), because the received data are all from the mismatched channel. However, the ideal steering vector is used in (27), because the mismatched parameters are unknown when we estimate the transfer function. If the same steering vector is used in (17) and (27), the transfer function would be meaningless.

#### 4. Impact on Interference Suppression

If the channel is ideal, (27) could be expressed as

$$H\left(\omega,\theta_{J}\right) = \alpha\left(4\pi B - 4\pi B e^{-j(\omega-\omega_{I})T}\right) \approx 0. \tag{28}$$

Hence, the interference could be suppressed perfectly. However, the channels are always mismatched, and the performance of interference suppression is also limited.

Suppose the interference is the smooth Gaussian white noise, and its bandwidth has covered the entire bandwidth of signal. According to (27), the output power of interference can be expressed as

$$P_{J-\text{OUT}} = \frac{P_{J-\text{IN}}}{2\pi B} \int_{-\pi B}^{\pi B} \left| \left( 2 \int_{-\pi B}^{\pi B} |A(\omega)|^2 d\omega + 2\pi B \right) \right|^2 d\omega + 2\pi B$$

$$- \int_{-\pi B}^{\pi B} A(\omega) e^{-j\varphi(\omega)} d\omega$$

$$- \left( 2\pi B + \int_{-\pi B}^{\pi B} A(\omega) e^{-j\varphi(\omega)} d\omega \right)$$

$$\cdot e^{-j(\omega - \omega_I)T} \right)^2 d\omega = \frac{\sigma_J^2 \alpha^2}{2\pi B}$$

$$\cdot \int_{-\pi B}^{\pi B} \left| \left( 2 \int_{-\pi B}^{\pi B} |A(\omega)|^2 d\omega + 2\pi B \right) \right|^2 d\omega + 2\pi B$$

$$- \int_{-\pi B}^{\pi B} A(\omega) e^{-j\varphi(\omega)} d\omega$$

$$- \left( 2\pi B + \int_{-\pi B}^{\pi B} A(\omega) e^{-j\varphi(\omega)} d\omega \right)$$

$$\cdot e^{-j(\omega - \omega_I)T} \right)^2 d\omega.$$
(29)

For convenience, we only analyze the above equation in IF, which is supposed to be suitable, because the antijamming performance in other frequencies is close to the performance in IF. Constantly, the output power of interference could be simplified as

$$P_{J\text{-OUT}} = \frac{2\sigma_J^2 \alpha^2}{\pi B} \int_{-\pi B}^{\pi B} \left| \left( \int_{-\pi B}^{\pi B} |A(\omega)|^2 d\omega \right) \right|^2 d\omega$$
$$- \int_{-\pi B}^{\pi B} A(\omega) e^{-j\varphi(\omega)} d\omega \right|^2 d\omega. \tag{30}$$

Assume that

$$H_{J}(\omega) = \left| \int_{-\pi B}^{\pi B} |A(\omega)|^{2} d\omega - \int_{-\pi B}^{\pi B} A(\omega) e^{-j\varphi(\omega)} d\omega \right|^{2}$$

$$= \left| \int_{-\pi B}^{\pi B} \left( |A(\omega)|^{2} - A(\omega) e^{-j\varphi(\omega)} \right) d\omega \right|^{2}$$

$$\approx \int_{-\pi B}^{\pi B} \left| \left( |A(\omega)|^{2} - A(\omega) e^{-j\varphi(\omega)} \right) \right|^{2} d\omega.$$
(31)

Suppose the noise power is  $P_N$ . The interference cancellation ratio (ICR) can be expressed as

$$ICR = \frac{P_{J-IN} + P_N}{P_{J-OUT} + P_N}$$

$$= \frac{\sigma_J^2 + \sigma_n^2}{\left(2\sigma_J^2\alpha^2/\pi B\right) \int_{-\pi R}^{\pi B} H_J(\omega) d\omega + \sigma_n^2}.$$
(32)

According to (32), the ICR is limited by channel mismatch and its limits could be written as

$$ICR_{lim} = \lim_{\sigma_J^2 \to \infty} \frac{\pi B}{2\alpha^2 \int_{-\pi B}^{\pi B} H_J(\omega) d\omega}.$$
 (33)

The fundamental principle of interference suppression in antenna arrays is to achieve interference cancellation, and (31) can be further simplified as

$$H_{J}(\omega) = \int_{-\pi B}^{\pi B} \left( A^{2}(\omega) - 2A(\omega) \cos \varphi(\omega) + 1 \right) d\omega.$$
 (34)

The above equation is the main factor to affect the performance of interference suppression. According to (34), we define a channel mismatch impact factor that can be expressed as

$$F = H_I(\omega). \tag{35}$$

The smaller the value of the impact factor, the better the performance of interference suppression.

We define another parameter which can also reflect the performance of interference suppression and it can be expressed as

$$H_F(\omega) = A^2(\omega) - 2A(\omega)\cos\varphi(\omega) + 1. \tag{36}$$

According to (3), we can obtain that

$$\varphi(\omega) = R_p \cos \omega R_{pn} + \omega R_b \approx \omega R_b, \tag{37}$$

where  $R_p$  and  $R_b$  are in the same order of magnitude, but  $\cos \omega R_{pn}$  is less than 1 and also much less than  $\omega$ , so the above equation can be approximated.

According to (36) and (37), the main factors to affect the performance of interference suppression are the range of amplitude wave, the number of amplitude waves, and the group delay bias.

In the above analysis, channel 2 is nonideal and its mismatch parameters have not been taken into consideration, and we can recognize they are random. But, in the next plotting, the specific mismatch parameters are necessary, and the model in (3) is used and its parameters are listed in Table 1.

Figure 2 shows the impact factors to  $H_F(\omega)$  in (36). The curve of reference is with the mismatch in Table 1. The curves marked with  $R_a=1$  dB,  $R_{an}=3$  cycle, and  $R_b=10$  ns stand for resetting  $R_a$ ,  $R_{an}$ , and  $R_b$ , respectively, whose reset value is listed in the figure, and the other parameter is the same as Table 1 when the parameter has reset. Figure 2 further presents that the main factors to impact the performance of interference suppression are the range of amplitude wave and the group delay bias.

#### 5. Simulation Experiment

GNSS software receiver is used in this simulation. The analysis in this paper concerns the performance of interference suppression, and the PI criterion is adapted, so the navigation signals are unnecessary to be generated. The parameters utilized in simulation experiments are listed in Table 2.

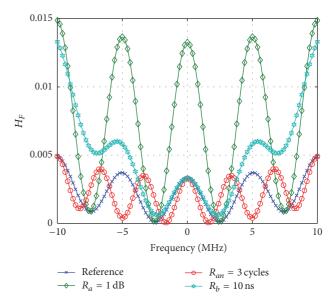


FIGURE 2: Impact factor to  $H_F(\omega)$ .

TABLE 1: Mismatch parameters.

| Parameters                | Value   |
|---------------------------|---------|
| Range of amplitude wave   | 0.5 dB  |
| Number of amplitude waves | 2 cycle |
| Range of group delay      | 3 ns    |
| Number of group delays    | 2 cycle |
| Group delay bias          | 4 ns    |

TABLE 2: Utilized parameters.

| Parameters type        | Parameters value       |  |
|------------------------|------------------------|--|
| Array type             | 2-element linear array |  |
| Interelement spacing   | 0.5 wavelength         |  |
| Time-domain taps       | 2                      |  |
| Interference type      | White Gaussian noise   |  |
| Interference bandwidth | 20 MHz                 |  |
| Interference DOA       | 15 degrees             |  |
| INR                    | 35 dB                  |  |
| Sampling frequency     | 124 MHz                |  |
| IF                     | 15 MHz                 |  |

We assume channel 1 is ideal and the characteristic of channel 2 is nonideal whose mismatch parameters are shown in Table 1.

Figure 3 shows the relationship between input INR and ICR. Whether the channel is ideal or mismatch, with the increase of ICR, ICR shows a rising trend. When the channel is ideal, the ICR is approximately equal to the INR and their relationship is linear, and the interference could be completely suppressed. But, in the case of channel mismatch, ICR has different limits in different degree of mismatch. The curve marked with reference shows the ICR in different INR under the channel mismatch whose parameters are set in Table 1. The curve of  $R_a = 1\,\mathrm{dB}$  expresses the impact of the

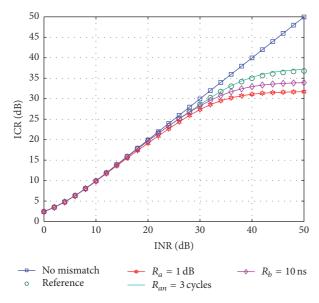


FIGURE 3: ICR in different INR.

range of amplitude wave reset to 1 dB and the other parameters are the same as reference, whose limit of ICR has decreased. The curve marked with  $R_b=10~\rm ns$  stands for the ICR in different INR under the group delay bias with 10 ns, whose limit of ICR has also been reduced. Nevertheless, when the range of amplitude is reset to 3 cycles, the ICR has little influence compared with the reference.

Figure 4 shows the impact of mismatch extent on ICR. According to the mismatch model in (3), the channel mismatch is related to the range of amplitude wave, the number of amplitude waves, the range of group delay wave, the number of group delay waves, and the group delay bias. In order to put the impact of these parameters on ICR to a diagram, the limits of the parameters are set which are shown in figure, and x-axis in figure represents the percentage of those limits. As can be seen from Figure 4, the main influence factors to ICR are the range of amplitude wave and the group delay bias, and the impact of the number of amplitude waves is weaker, and the group delay waves express a little effect on ICR, which is consistent with the conclusion of theoretical analysis.

In (21), (28), (31), (34), and (37), the approximate processing is used. The simulation has proved that the approximate processing is right.

The above simulation is executed only in 2 elements and 2 taps, but these STAP structure is scarce. In the following, we will do simulation with different STAP structure. In all STAP, the distance of the adjacent elements is half wavelength. Regardless of STAP structure, the reference element is ideal, and the other element is nonideal, which would meet the channel mismatch. The degree of channel mismatch is the same as Figure 4. The ICRs in 3 elements' linear array with 2 taps and 4 elements' square array with 2 taps are shown in Figures 5(a) and 5(b). Different elements have different ICRs, but the impact of channel mismatch on ICR is almost the same. The ICRs in 2 elements' linear array with 3 taps and 5 taps are shown in Figures 5(c) and 5(d). The taps are more

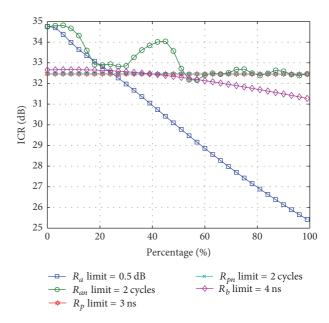


FIGURE 4: ICR in different mismatch degree.

complex on ICR compared to elements. With the increase of taps, the impact of channel mismatch on ICR would become weaker and weaker, because STAP can equalize part of channel mismatch, but its equalization effect is also limited. In addition, the amplitude mismatch is harder to be equalized compared to group delay mismatch.

#### 6. Conclusion

In this paper, we have analyzed the impact on antijamming performance of channel mismatch in GNSS antenna arrays receivers. The characteristics of channel mismatch and impact of mismatch level are studied, and the study has been developed through theoretical analysis and simulation experiment.

The outcome of the study is the following:

- (1) Under the condition of channel mismatch, the antijamming performance of antenna arrays is limited which is connected to the degree of channel mismatch.
- (2) A concept of channel mismatch impact factor is proposed, whose value could directly determine the antijamming performance of antenna arrays.
- (3) When the STAP is equipped with 2 elements and 2 taps, the range of amplitude wave and group delay bias are the main factors to impact the antijamming performance, and the number of amplitude waves is next, and the effect of group delay wave is the smallest.
- (4) STAP can equalize part of channel mismatch. More taps would bring better equalization effect, and the group delay mismatch is easier to be equalized compared to amplitude mismatch. With the increase of taps, the range and number of amplitude waves have become the main factors to impact the antijamming performance, and the impact of group wave and bias on antijamming performance would become weaker and weaker.

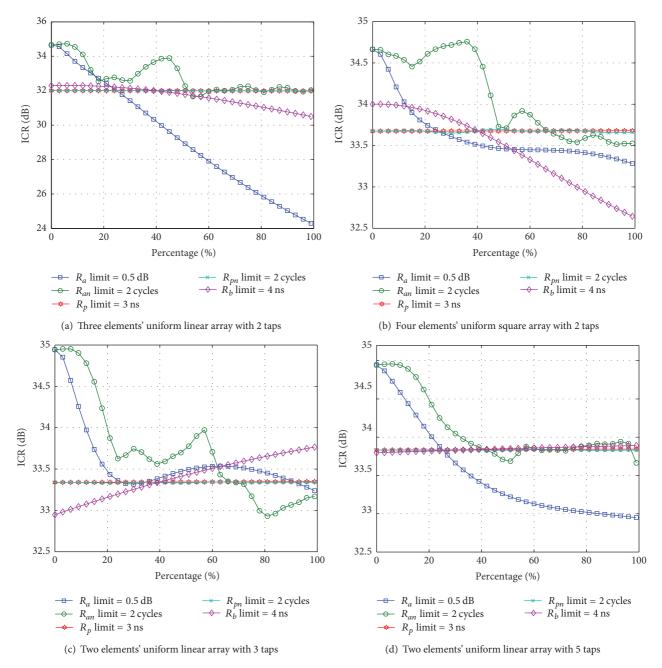


FIGURE 5: ICR in different STAP structure.

Although the effect of group delay wave is the smallest, the group delay wave might affect the measurement in pseudocode and carrier phase seriously, which is the future work for us.

#### **Competing Interests**

The authors declare that they have no competing interests.

#### References

[1] N. Kubo, M. Higuchi, T. Takasu, and H. Yamamoto, "Performance evaluation of GNSS-based railway applications," in

Proceedings of the International Association of Institutes of Navigation World Congress (IAIN '15), pp. 1–8, Prague, Czech Republic, October 2015.

- [2] W. Alshrafi, U. Engel, and T. Bertuch, "Compact controlled reception pattern antenna for interference mitigation tasks of global navigation satellite system receivers," *IET Microwaves*, *Antennas & Propagation*, vol. 9, no. 6, pp. 593–601, 2015.
- [3] G. S. Huang, Z. R. Yi, and Z. C. Zhu, "A novel narrow-band interference suppression scheme in GNSS receivers," in *Proceedings of the International Conference on Electronics, Communications and Control (ICECC '11)*, pp. 1252–1256, IEEE, Zhejiang, China, September 2011.

- [4] S. Huo, J. Nie, X. Tang, and F. Wang, "Minimum energy block technique against pulsed and narrowband mixed interferers for single antenna GNSS receivers," *IEEE Communications Letters*, vol. 19, no. 11, pp. 1933–1936, 2015.
- [5] M. G. Amin and W. Sun, "A novel interference suppression scheme for global navigation satellite systems using antenna array," *IEEE Journal on Selected Areas in Communications*, vol. 23, no. 5, pp. 999–1012, 2005.
- [6] S. Wu and Y. Li, "Adaptive channel equalization for space-time adaptive processing," in *Proceedings of the IEEE International Radar Conference*, pp. 624–628, Alexandria, Va, USA, May 1995.
- [7] A. Konovaltsev, M. Cuntz, L. A. Greda, M. V. T. Heckler, and M. Meurer, "Antenna and RF front end calibration in a GNSS array receiver," in *Proceedings of the 2010 IEEE International Microwave Workshop Series on 'RF Front-ends for Software Defined and Cognitive Radio Solutions' (IMWS '10)*, pp. 103–106, February 2010.
- [8] W. Ling, Y. Li, S. Xu, Z. Wei, and W. Kun, "Robustness analysis of adaptive anti-jamming algorithms with channel mismatch and mutual coupling for GNSS systems," in *Proceedings of the 2nd IEEE International Conference on Signal Processing, Communications and Computing, (ICSPCC '12)*, pp. 705–710, Hong Kong, China, August 2012.
- [9] M. Li, Study on key techniques of digital beamforming in satellite navigation [Ph.D. thesis], Chinese National University of Defense Technology, Changsha, China, 2011.
- [10] R. L. Fante and J. J. Vaccaro, "Wideband cancellation of interference in a GPS receive array," *IEEE Transactions on Aerospace* and Electronic Systems, vol. 36, no. 2, pp. 549–564, 2000.
- [11] D. S. De Lorenzo, J. Rife, P. Enge, and D. M. Akos, "Navigation accuracy and interference rejection for an adaptive GPS antenna array," in *Proceedings of 19th International Technical Meetings of the Satellite Division of the Institute of Navigation (ION GNSS '06)*, pp. 763–773, Fort Worth, Tex, USA, September 2006.
- [12] F. Gao, Y.-L. Wang, H. Chen, and X.-F. Xue, "Effect of channel mismatch on STAP performance," in *Proceedings of the 1st International Congress on Image and Signal Processing (CISP* '08), pp. 85–89, IEEE, Hainan, China, May 2008.
- [13] K. R. Dandekar, H. Ling, and G. Xu, "Smart antenna array calibration procedure including amplitude and phase mismatch and mutual coupling effects," in *Proceedings of the IEEE International Conference on Personal Wireless Communications*, pp. 293–297, Hyderabad, India, December 2000.
- [14] F. Gao, Y. Wang, H. Chen, and W. Xie, "Effect and equalization results of channel mismatch on STAP performance," *Signal Processing*, vol. 25, no. 4, pp. 563–565, 2009.
- [15] A. J. O'Brien and I. J. Gupta, "Comparison of output SINR and C/N0 for GNSS adaptive antennas," *IEEE Transactions on Aerospace and Electronic Systems*, vol. 45, no. 4, pp. 1630–1640, 2009
- [16] H. Zhao, Y. Shi, B. Zhang, and M. Shi, "Analysis and simulation of interference suppression for space-time adaptive processing," in *Proceedings of the IEEE International Conference on Signal Processing, Communications and Computing (ICSPCC '14)*, pp. 724–727, IEEE, Guilin, China, August 2014.
- [17] Q. Han, J. Nie, S. Huo, and F. Wang, "A high-precision and low-cost planar array signal simulator based on cable delays," *IEEE Antennas & Wireless Propagation Letters*, vol. 13, pp. 353–356, 2014.

[18] Z. Ahmad, S. Yaoliang, Q. Du, and I. Ali, "Convergence analysis of null steering antenna utilizing power inversion algorithm," in *Proceedings of the 2015 20th IEEE International Seminar/Workshop on Direct and Inverse Problems of Electromagnetic and Acoustic Wave Theory (DIPED '15)*, pp. 97–101, Lviv, Ukraine, September 2015.

Hindawi Publishing Corporation International Journal of Antennas and Propagation Volume 2016, Article ID 2829357, 14 pages http://dx.doi.org/10.1155/2016/2829357

## Research Article

# A Compact Novel Three-Port Integrated Wide and Narrow Band Antennas System for Cognitive Radio Applications

#### N. Anvesh Kumar and A. S. Gandhi

Department of ECE, VNIT, Nagpur, India

Correspondence should be addressed to N. Anvesh Kumar; nellaanvesh@gmail.com

Received 24 June 2016; Revised 15 August 2016; Accepted 20 September 2016

Academic Editor: Renato Cicchetti

Copyright © 2016 N. A. Kumar and A. S. Gandhi. This is an open access article distributed under the Creative Commons Attribution License, which permits unrestricted use, distribution, and reproduction in any medium, provided the original work is properly cited.

The design of a three-port radiating structure, integrating wide and narrow band antennas for cognitive radio applications, is presented. It consists of a UWB antenna for spectrum sensing and two narrow band antennas for wireless communication integrated on the same substrate. The UWB antenna covers the complete UWB spectrum (3.1 GHz to 10.6 GHz) approved by FCC. In the two narrow band antennas, each antenna presents dual bands. In particular, the first narrowband antenna resonates at 6.5 GHz, covering the frequency band between 8.78 GHz and 9.23 GHz, presenting minimum return loss values of 28.3 dB at 6.5 GHz and 20.5 dB at 9 GHz, respectively. Similarly, the second one resonates at 7.5 GHz, covering the frequency band between 9.23 GHz and 9.82 GHz, presenting minimum return loss values of 19.6 dB at 19.6 GHz, covering the frequency band between 19.6 GHz and 19.6 GHz, respectively. Isolation among the three antennas is less than 10.6 GHz over the UWB frequency spectrum. These antennas are realized on a FR4 substrate of dimensions 10.6 GHz, 10.6

#### 1. Introduction

In today's wireless communication, because of the increasing growth of applications, there is a great demand for bandwidth. But, as for the requirements, the spectrum bandwidth cannot be increased beyond limits due to frequency and economic constraints. In licensed spectrum, many channels are free due to their inefficient utilization. So, these empty channels can be utilized to overcome the problem of limited spectrum. In 2002, FCC has proposed several solutions to enhance the licensed spectrum utilization efficiency. These solutions are divided into three categories, the spectrum leasing, the spectrum reallocation, and the spectrum sharing [1–4]. The spectrum sharing is also divided into three types. The first one is the open spectrum sharing, the second one is the hierarchical spectrum sharing, and the third one is the dynamic spectrum allocation. In the hierarchical spectrum sharing approach, we employ cognitive radio technology to utilize unused or free licensed channels. In this model, the licensed spectrum is assumed to be owned by the primary

users, who do not fully utilize their channels. Hence, the secondary users utilize these free channels until the primary users demand them. In this case, the secondary users have to shift on to other free channels to maintain the continuous communication as shown in Figure 1(b). In cognitive radio applications, the radio environment is continuously monitored for spectrum holes. In this process, if any spectrum hole is identified, then that channel is used for other wireless communication applications. In general, UWB antennas are adopted for spectrum sensing while frequency reconfigurable narrow band (NB) antennas are employed for communication [5, 6]. In modern wireless and portable systems, conventional antennas are not compatible with these applications. Therefore, planar monopole antennas are highly preferred due to their advantages like small size, low cost, lightweight, easy integration with planar structures, and easy fabrication

In recent years, dual port integrated UWB and frequency reconfigurable NB antenna systems are becoming very popular for cognitive radio applications. In these systems, the

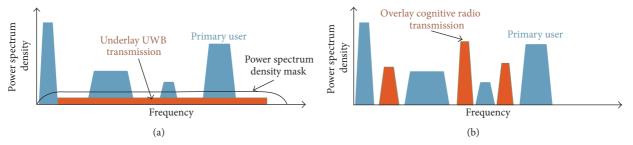


FIGURE 1: Hierarchal spectrum sharing approaches. (a) Spectrum underlay. (b) Spectrum overlay [1].

UWB antennas are used for spectrum sensing and the reconfigurable narrow band antennas are used for communication. In the NB antennas reconfiguration is introduced to support many communication frequencies by using a single antenna. We investigated numerous dual port integrated antenna structures presented in the literature [8-15]. An integrated UWB and rotatable NB antennas structure of dimensions  $70 \text{ mm} \times 50 \text{ mm} \times 1.6 \text{ mm}$  is reported in [8]. In this paper, the authors make use of a stepper motor controlled by a computer to switch between five different NB antennas printed on a circular substrate. These NB antennas are able to obtain single resonance in each case within 2 to 10 GHz frequency spectrum. In [9], the authors focused on an integrated wide-narrow band antenna structure of dimensions  $68 \,\mathrm{mm} \times 54 \,\mathrm{mm} \times 0.79 \,\mathrm{mm}$  for multistandard radio. In this structure, the reconfiguration is implemented by introducing three different resonant matching circuits. In each case, the NB antennas are able to yield one resonating band within 4 to 10 GHz frequency spectrum. An integrated dual port UWB and reconfigurable NB antennas structure of dimensions  $50 \text{ mm} \times 50 \text{ mm} \times 1.6 \text{ mm}$  is discussed in [11]. In this design, the reconfiguration is performed by employing three switches on the NB antenna to achieve eight resonating bands in four cases within 3 to 10 GHz frequency spectrum. In [12], the authors presented an integrated UWB and optically controlled reconfigurable NB antennas structure having dimensions  $50 \text{ mm} \times 45.5 \text{ mm} \times 1.6 \text{ mm}$ . In this structure, the NB antenna is reconfigured by pumping a laser light on to the two silicon switches to attain three resonating bands within 3 to 6 GHz frequency spectrum.

However, the discussed reconfigurable mechanisms have some drawbacks, like the negative effect of biasing lines used to control switches states, the power consumption, the nonlinearity effects of switches, and the slow tuning. Moreover, sometimes they require additional biasing circuitry or motors to achieve antenna reconfigurability [4, 16]. In cognitive radio applications, the main purposes of employing the reconfigurable antennas are to reduce cost and space and for fast tuning. But all these reconfigurable mechanisms make the printed antennas bulky and complex, which nullify all the advantages of planar antennas. Even these reconfigurable mechanisms are very difficult to implement in practice. So, to overcome these drawbacks and maintain all the advantages of planar antennas, we propose an integrated three-port planar antennas design. Among these three ports, a UWB

antenna that is accessible at the first port is used for spectrum sensing and the two NB antennas, which are accessible at the remaining two ports, are used for communication. Here also reconfiguration may be performed between the two NB antennas such that only one NB antenna is operated at a time. The selection of a particular narrow band antenna depends on the sensed hole in the frequency spectrum to which it is matched. The main challenges in these designs are isolation and space reduction.

In this paper, a three-port antenna system for cognitive radio applications is presented. The radiating system is composed of a UWB antenna for spectrum sensing and two narrow band antennas for wireless communications. The antennas are printed on a low cost FR4 substrate having dimensions  $30~\text{mm} \times 30~\text{mm} \times 1.6~\text{mm}$ . The analysis and design of the proposed antenna system were performed using the full-wave commercial software HFSS 14.0 based on the finite element method (FEM). The paper is organized into 4 sections. In Section 2, the design of a simple and small size planar monopole UWB antenna is illustrated. In Section 3, the analysis, design, and results of the proposed three-port antenna system is presented and finally in Section 4 some concluding remarks are provided. Details of the proposed antenna are given in the next sections.

#### 2. Proposed Single Port UWB Antenna Design

In this section, the preliminary design of a one-port UWB antenna is presented. This design takes into account the scientific results available in the literature [17–23]. These results show that round shapes, round edges, partial grounds, and partial grounds with specially designed slots play a major role in obtaining UWB performance [6, 18, 19]. So, on the basis of these observations, a circular monopole with a partial ground as shown in Figure 2 was chosen as a radiating element.

For this antenna design, the equation proposed in [23] is used to find out its geometrical parameters. By using this equation

$$f_L = \frac{7.2 \,\text{GHz}}{\{(L+r+p) \times k\}},$$
 (1)

where  $f_L$  is selected lower band edge of the UWB frequency spectrum ( $f_L = 3 \text{ GHz}$ ), p (feed gap) = 0.14 cm, L = 2 \* a and

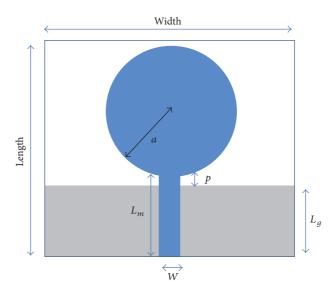


FIGURE 2: Geometry of a circular planar monopole UWB antenna. The main geometrical parameters are indicated in the figure.

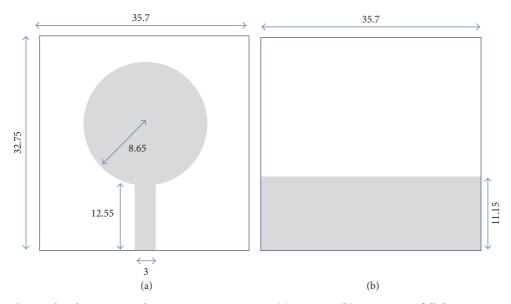


FIGURE 3: The circular planar monopole UWB antenna geometry. (a) Top view. (b) Bottom view [all dimensions are in mm].

r=a/4, and k=1.15 (constant), it is possible to evaluate radius (a) of monopole suitable to ensure the input in-band to the frequency  $f_L$ , with an accuracy of about 10%. Using (1) the radius (a) is found to be 8.65 mm. Then, the substrate size was optimized so as to obtain an impedance bandwidth with VSWR  $\leq 2$  in the UWB frequency band (from 3.1 GHz up to 10.6 GHz). After completing the optimization process a substrate having dimensions 32.75 mm  $\times$  35.7 mm has been found. The geometry of the UWB monopole antenna, including the optimized geometrical parameters, is reported in Figure 3.

For a proper impedance matching over the complete UWB spectrum, a microstrip line of 12.55 mm  $\times$  3 mm size

was selected. The return loss performance of the discussed antenna design can be inferred from Figure 4. The resulting monopole antenna covers a frequency band from 2.62 GHz up to 11.15 GHz with VSWR  $\leq$  2, thus including the complete UWB spectrum (from 3.1 GHz to 10.6 GHz) approved by FCC in 2002 [24]. However, the proposed antenna's return loss performance is poor, while the dielectric substrate and the partial ground dimensions are larger than the active patch (see Figure 3). Therefore, to reduce the antenna dimensions and to achieve better UWB performances, we modified the proposed antenna in a systematic way. Initially, the substrate dimensions are reduced to 30 mm  $\times$  19 mm. These dimensions cannot be reduced further because the active

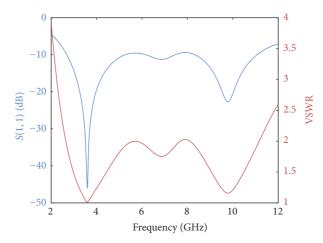


FIGURE 4: Frequency behavior of the UWB monopole antenna input reflection coefficient.

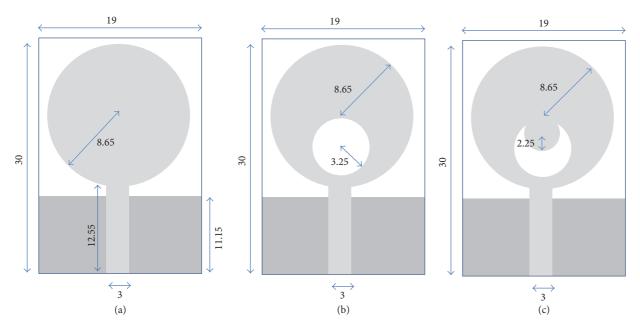


FIGURE 5: Design steps adopted to realize the UWB monopole antenna: (a) first step, (b) second step, and (c) third step.

patch almost exists on the entire substrate as shown in Figure 5(a). Then, a step-by-step optimization process, as shown in Figures 5(a), 5(b), 5(c), and 7, to obtain better UWB performances has been employed. To do this, one circular slot and one circular fill in the top layer and a circular slot on the bottom layer are introduced (see Figure 7(b)). The geometry, the dimensions, and positions of these shapes are carefully optimized using the adopted full-wave software.

Round shapes and round edges have been employed because, as pointed out earlier, they yield better UWB performances. These aspects can be appreciated by looking at the frequency behavior of the return loss of the three design solutions described above (see Figure 6). Return loss performances of the three-step design are shown in Figure 6. Even though the realization of suitable shaped slots in the metal patch is able to increase the antenna bandwidth, it

prevents covering the entire UWB band as it appears in Figure 6. Therefore, an optimized circular slot of 1.75 mm is realized on the upper edge of the ground plane in order to improve the performance of the return loss (see Figure 7(b)). This slot allows for obtaining the desired antenna impedance matching in the UWB band as shown in Figure 8. Return loss performance of the optimized UWB monopole antenna is shown in Figure 8.

As it appears from Figure 8, the etched shapes realized on the top and bottom layers have a significant impact on achieving a UWB spectrum ranging from 2.62 GHz to 12.63 GHz. From the simulated result it is obvious that the proposed UWB antenna is suitable to cover the complete UWB spectrum. Because of small size and better performance, the proposed UWB antenna can be used in many UWB wireless communication applications.

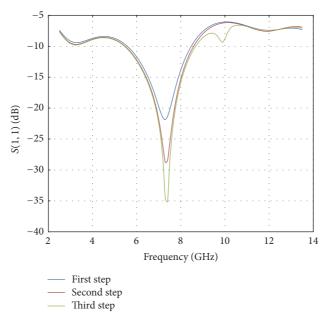


FIGURE 6: Antenna input reflection coefficient versus frequency. The curves refer to the first three steps' design.

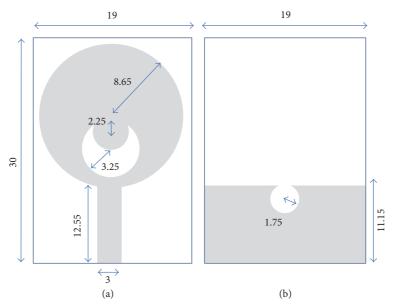


Figure 7: The final UWB antenna geometry. (a) Top view. (b) Bottom view.

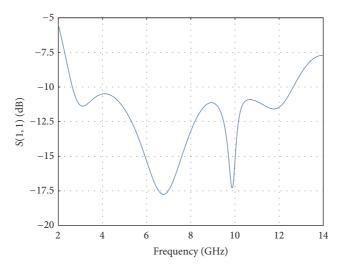


Figure 8: Antenna input reflection coefficient versus frequency of the final version of the UWB antenna.

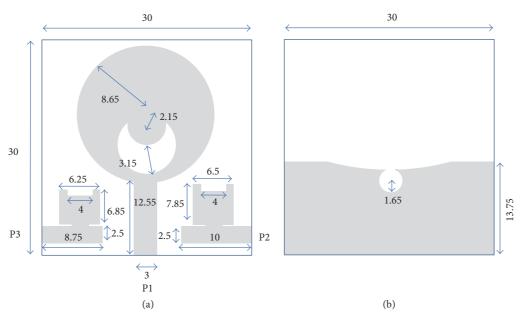


FIGURE 9: Proposed integrated UWB and NB antennas geometry. (a) Top view. (b) Bottom view.

# 3. Analysis and Design of the Three-Port Radiating Structure

In this section, we discuss the proposed three-port antenna system composed of a UWB and two NB antennas integrated on the same substrate. As discussed earlier, each antenna has an independent excitation port as shown in Figure 9(a). Therefore, to achieve good isolation characteristics between each antenna, the substrate dimensions, the active patch, and the ground plane structures are carefully modified. In particular, a UWB antenna linked with the first port is used for spectrum sensing, while the remaining two NB antennas linked with the other two ports of the antenna system are used for wireless communications. The UWB and the two NB antennas are printed on top surface of FR4 dielectric substrate in such a way that electromagnetic isolation among them is very high. In general, for UWB antennas partial grounds are highly preferred, while for narrow band antennas full grounds are widely used. Here also the bottom layer shown in Figure 9(b) is acting as a partial ground for the UWB antenna and as a full ground for the two narrow band antennas. In the proposed design, we incorporated various slots on the top and bottom layers to enhance return loss performance. Top and bottom views of the proposed three-port antenna system are shown in Figure 9.

In particular, the monopole of the UWB antenna has been further optimized (see Figure 10(b)) with respect to the initial design discussed in the previous section (see Figure 10(a)), while a chamfer has been introduced in the upper part of the ground plane, as shown in Figure 9(b), to enhance the UWB antenna performance.

After completing the design of the UWB antenna the analysis and design of two narrow band antennas forming the proposed antenna system are presented. In the proposed design, each of the two NB antennas has been designed so as

to achieve a dual-band behavior useful for various wireless applications. To obtain this behavior on each rectangular patch antenna a slot has been realized, while a stub has been introduced along its feeding microstrip line (see Figure 9(a)). In particular, the slot realized on the rectangular patch controls the upper resonant band, while the stub inserted along the microstrip line allows for controlling the lower resonant band. The rectangular slot realized in the patch allows for increasing the electrical length enabling a shift of the upper resonant band toward lower frequencies. Note that the usual mathematical relationships between the length and the width, useful to design of rectangular patch antennas, are no longer applicable because of the irregular shapes, the small size, and the mutual coupling effects between the three antennas forming the radiating system. Furthermore, the small size of the realized NB antennas allows for obtaining a high electrical insulation. Top and bottom views of the prototype of the proposed antenna system are shown in Figure 11.

In the cognitive radio applications, during the operation of the proposed antenna system, the UWB antenna and one of the two NB antennas are operated for sensing and communication, while the other NB antenna is on standby. The selection of the particular NB antenna depends on the sensed hole in the frequency spectrum to which it is matched. This makes two possible different operative conditions. In the first condition the UWB antenna and the first NB antenna are operative, whereas in the second case the UWB antenna and the second NB antenna are active. This means that in the first case the antennas connected to Port 1 and Port 2 are excited, while the antenna connected to Port 3 is closed on a 50  $\Omega$  matched load. Similarly, in the second case the antennas connected to Port 1 and Port 3 will be excited, while the antenna connected to Port 2 will be closed on a matched

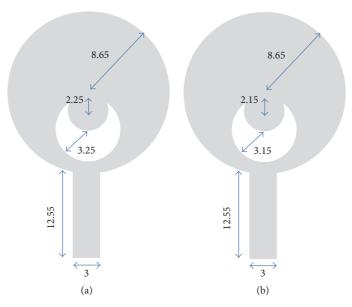


FIGURE 10: Geometry of the UWB antenna. (a) Preliminary design and (b) final design.

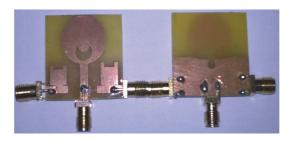


FIGURE 11: Top and bottom views of the fabricated prototype.

load. These two operative situations have been tested using a vector network analyzer (VNA).

3.1. Performance of the Radiating System in the First Operative Condition. The performances of the radiating system in the first operative condition, namely, with Ports 1 and 2 excited and with Port 3 closed on matched load, are derived by the analysis of the frequency behavior of the scattering parameters, of the gains, and of the radiation patterns of the three-port network forming the antenna system. In particular, by analyzing the frequency behavior of the parameter  $S_{11}$ , depicted in Figure 12, it results that the UWB antenna covers the frequency band ranging between 2.76 GHz and 13.96 GHz, with an increasing gain which varies between about 0.54 dBi and 5.58 dBi (see Figure 13) and with E- and E-radiation patterns described by the curves reported in Figure 14.

Different is the radiative behavior of the first NB antenna which resonates at 6.5 GHz and 9 GHz (see Figure 15) with return loss values of 28.3 dB at 6.5 GHz and 20.5 dB at 9 GHz, respectively. As it appears from Figure 15 the antenna exhibits a dual-band behavior covering the frequency bands between

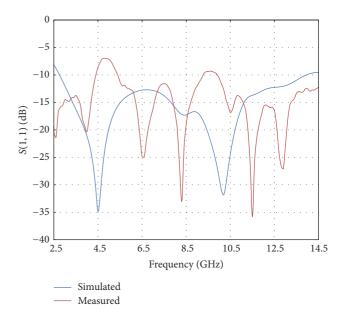


FIGURE 12: Comparison of simulated and measured reflection coefficients of the UWB antenna.

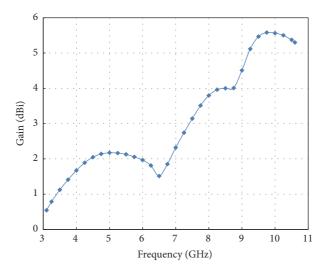


FIGURE 13: Peak gains versus frequencies plot of the UWB antenna.

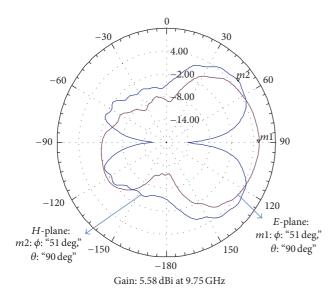


FIGURE 14: 2D radiation pattern of the UWB antenna at 9.75 GHz.

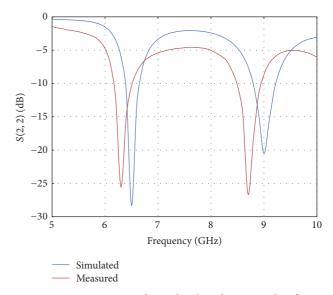


FIGURE 15: Comparison of simulated and measured reflection coefficients of the first NB antenna.

6.36 GHz and 6.63 GHz and between 8.78 GHz and 9.23 GHz, respectively. As discussed earlier, the slot in the rectangular patch is employed to generate the upper resonant band, while the stub added to the microstrip line is used to achieve the lower resonant band. To better understand the role of these shapes, the computed surface current distributions, excited on the first proposed NB antenna at the frequencies of 6.5 GHz and 9 GHz, are shown in Figure 16.

As it can be observed from Figure 16, the strong surface currents are distributed along the edges of microstrip line stub at 6.5 GHz and along the edges of slot on the rectangular patch at 9 GHz. Thus it is clearly evident that the radiation in the 6.5 GHz band is due to microstrip line added with stub and the radiation in 9 GHz band is due to slotted rectangular

patch. The radiation patterns in the *E*- and *H*-plane at the two mentioned resonant frequencies are shown in Figure 17.

From these diagrams it appears that the antenna exhibits gains of approximately 3.03 dBi and 2.53 dBi, respectively. The characteristics of the narrow band antenna discussed above were derived by means of an extensive parametric analysis obtained by varying the length of the slot and of the microstrip stub. In particular, as discussed before, the rectangular slot controls the higher frequency band, while the microstrip stub controls the lower one. In particular, Figure 18(a) shows the frequency behavior of the reflection coefficient of the first NB antenna when the slot length varies. As it can be seen the optimal size is obtained for a slot length

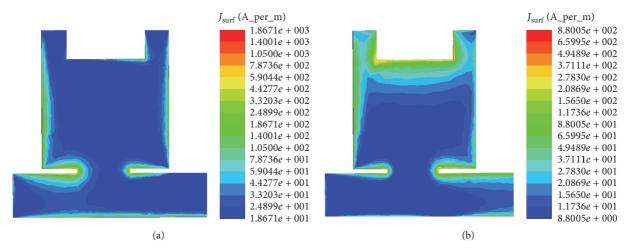


FIGURE 16: Simulated surface current distribution on the NB antenna at (a) 6.5 GHz and (b) 9 GHz.

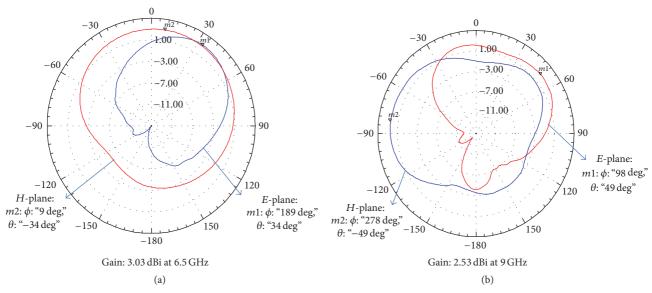


FIGURE 17: 2D radiation patterns of the NB antenna at (a) 6.5 GHz and (b) 9 GHz.

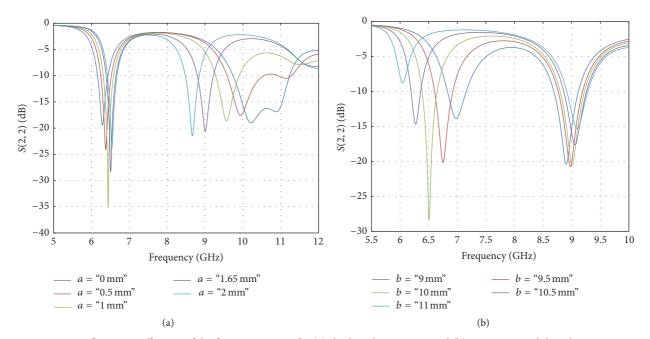


Figure 18: Reflection coefficients of the first NB antenna for (a) slot length variations and (b) microstrip stub length variations.

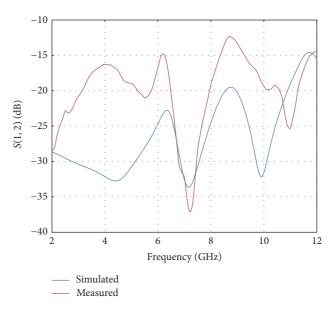


FIGURE 19: Comparison of simulated and measured transmission coefficients between the UWB and the first NB antenna ports.

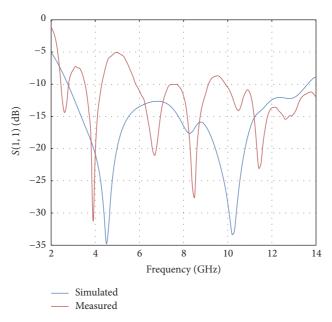


FIGURE 20: Comparison of simulated and measured reflection coefficients of the UWB antenna.

of 1.65 mm. Then the stub length, useful for tuning the lower frequency band, has been varied. From Figure 18(b) it appears that the optimized value of its length is 10 mm.

Finally, the frequency behavior of the scattering parameter  $S_{12}$ , depicted in Figure 19, shows that the electrical insulation with the UWB antenna is kept below -20 dB.

3.2. Performance of the Radiating System in the Second Operative Condition. After analyzing the behavior of the antenna system in the first operative condition, the behavior of the same, in the second operative condition, is considered. This

last situation refers to the UWB antenna excited at Port 1 with the second NB antenna excited at Port 3 and with the first NB antenna closed on a matched load. Also in this case the UWB antenna covers the UWB band. In fact, as shown in Figure 20 the return loss is above 10 dB in the frequencies band ranging from 2.74 GHz to 13.6 GHz.

The second NB antenna, connected to Port 3, resonates at the frequencies of 7.5 GHz and 9.5 GHz (see Figure 21) which correspond to return loss values equal to 19.6 dB and 28.8 dB, respectively. Even in this case the antenna exhibits a dual-band behavior covering the frequency bands between

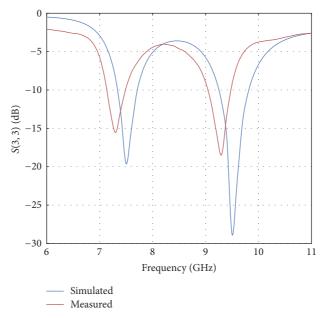


FIGURE 21: Comparison of simulated and measured reflection coefficients of the second NB antenna.

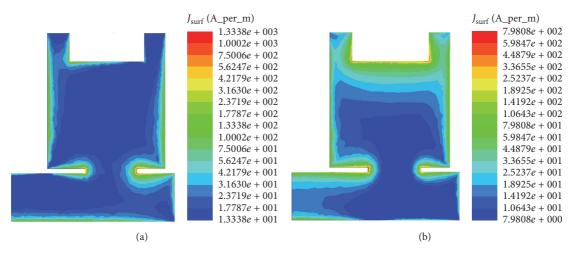


FIGURE 22: Simulated surface current distribution on the NB antenna at (a) 7.5 GHz and (b) 9.5 GHz.

7.33 GHz and 7.7 GHz and between 9.23 GHz and 9.82 GHz. Surface current distributions on the proposed NB antenna at 7.5 GHz and 9.5 GHz are shown in Figure 22. From Figure 22, it appears that the stub added to the microstrip line is responsible for the energy emission in the lower resonating band, while the slot realized in the rectangular patch excites the higher resonating band. From the radiation patterns in Figure 23, it appears that the antenna gains reach values of 3.64 dB and 3.2 dB, respectively. Also in this case the antenna sizing has required an accurate parametric study aimed at identifying the length of the slot and the stub used to realize a dual-band behavior. For the sake of completeness in Figure 24

the frequency behaviors of the scattering parameter  $S_{33}$  as the length of the slot and the stub increases are shown. From these curves it results that the optimized length of the slot is 1.45 mm, while that of the stub is 8.75 mm. Finally, Figure 25 shows the frequency behavior of the scattering parameter  $S_{13}$  from which the excellent electrical isolation between the UWB antenna and the second NB antenna can be noticed. All measured data clearly state that there is a good agreement between the simulated and measured results. However, there are slight shifts and changes that may be caused by fabrication faults, connector losses, improper soldering, and measurement process.

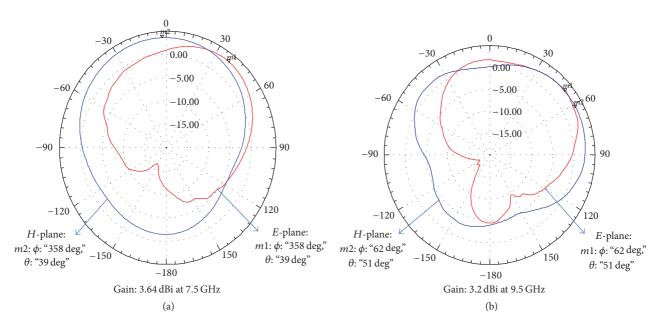


FIGURE 23: 2D radiation patterns of the NB antenna at (a) 7.5 GHz and (b) 9.5 GHz.

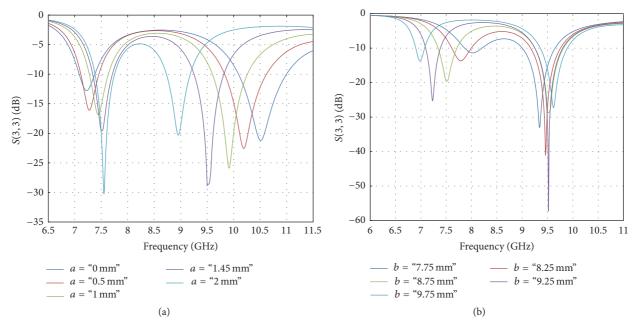


FIGURE 24: Reflection coefficients of the second NB antenna for (a) slot length variations and (b) microstrip stub length variations.

#### 4. Conclusion

In this paper, an antenna system composed of three antennas integrated in the same substrate, employed for the realization of cognitive radios, has been presented. It is employed with two narrow band antennas to overcome the drawbacks of the reconfigurable antennas during their practical implementation. So, after a brief discussion concerning the characteristics

of cognitive radios, purposes of the UWB antenna and of the two narrow band antennas forming the proposed antenna system have been described. Then, the analysis and design of each antenna have been illustrated in detail. A full-wave commercial software based on the FEM method has been used for an accurate prediction of the proposed antennas performances. The antenna measurements carried out on an antenna prototype have shown a good agreement with the

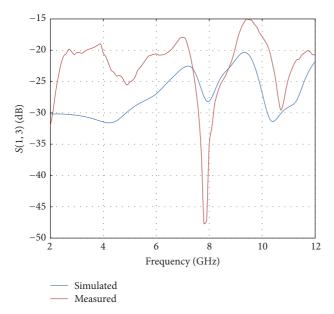


FIGURE 25: Comparison of simulated and measured transmission coefficients between the UWB and the second NB antenna ports.

experimental measurements. Because of compact structure and better performance, proposed system can be a good candidate for emerging cognitive radio technology.

### **Competing Interests**

The authors declare that they have no competing interests.

#### References

- [1] M. Al-Husseini, K. Kabalan, A. El-Hajj, and C. Christodoulou, "Cognitive radio: UWB integration and related antenna design," in *New Trends in Technologies: Control, Management, Computational Intelligence and Network Systems*, M. J. Er, Ed., INTECH, Rijeka, Croatia, 2010.
- [2] Y. Tawk, M. Bkassiny, G. El-Howayek, S. K. Jayaweera, K. Avery, and C. G. Christodoulou, "Reconfigurable front-end antennas for cognitive radio applications," *IET Microwaves, Antennas and Propagation*, vol. 5, no. 8, pp. 985–992, 2011.
- [3] S. K. Jayaweera and C. Mosquera, "A dynamic spectrum leasing (DSL) framework for spectrum sharing in cognitive radio networks," in *Proceedings of the 43rd Asilomar Conference on Signals, Systems and Computers*, pp. 1819–1823, Pacific Grove, Calif, USA, November 2009.
- [4] A. Rajaie Raslan, *Metamaterial antennas for cognitive radio applications [thesis]*, Electronics Engineering Department, American University in Cairo School of Sciences and Engineering, 2013.
- [5] N. Murtaza, R. K. Sharma, R. S. Thomä, and M. A. Hein, "Directional antennas for cognitive radio: analysis and design recommendations," *Progress in Electromagnetics Research*, vol. 140, pp. 1–30, 2013.
- [6] L. Safatly, M. Bkassiny, M. Al-Husseini, and A. El-Hajj, "Cognitive radio transceivers: RF, spectrum sensing, and learning algorithms review," *International Journal of Antennas and Propagation*, vol. 2014, Article ID 548473, 21 pages, 2014.

- [7] H. G. Schantz, "Three centuries of UWB antenna development," in *Proceedings of the IEEE International Conference on Ultra-Wideband (ICUWB '12)*, pp. 506–512, Syracuse, NY, USA, September 2012.
- [8] Y. Tawk, J. Costantine, and C. G. Christodoulou, "A rotatable reconfigurable antenna for cognitive radio applications," in *Proceedings of the IEEE Radio and Wireless Symposium (RWS '11)*, pp. 158–161, Phoenix, Ariz, USA, January 2011.
- [9] E. Ebrahimi, J. R. Kelly, and P. S. Hall, "Integrated widenarrowband antenna for multi-standard radio," *IEEE Transactions on Antennas and Propagation*, vol. 59, no. 7, pp. 2628–2635, 2011.
- [10] Y. Tawk and C. G. Christodoulou, "A new reconfigurable antenna design for cognitive radio," *IEEE Antennas and Wireless Propagation Letters*, vol. 8, pp. 1378–1381, 2009.
- [11] M. Al-Husseini, A. Ramadan, K. Y. Kabalan, A. El-Hajj, Y. Tawk, and C. G. Christodoulou, "A simple dual-port antenna system for cognitive radio applications," in *Proceedings of the International Conference on High Performance Computing and Simulation (HPCS '10)*, pp. 549–552, Caen, France, June 2010.
- [12] Y. Tawk, J. Costantine, S. Hemmady, G. Balakrishnan, K. Avery, and C. G. Christodoulou, "Demonstration of a cognitive radio front end using an optically pumped reconfigurable antenna system (OPRAS)," *IEEE Transactions on Antennas and Propagation*, vol. 60, no. 2, pp. 1075–1083, 2012.
- [13] S.-H. Zheng, X.-Y. Liu, and M. M. Tentzeris, "A novel optically controlled reconfigurable antenna for cognitive radio systems," in *Proceedings of the IEEE Antennas and Propagation Society International Symposium (APSURSI '14)*, pp. 1246–1247, Memphis, Tenn, USA, July 2014.
- [14] E. Erfani, J. Nourinia, C. Ghobadi, M. Niroo-Jazi, and T. A. Denidni, "Design and implementation of an integrated UWB/ reconfigurable-slot antenna for cognitive radio applications," *IEEE Antennas and Wireless Propagation Letters*, vol. 11, pp. 77–80, 2012.
- [15] Y. Li, W. Li, and R. Mittra, "Integrated dual-purpose narrow/ ultra-wide band antenna for cognitive radio applications," in Proceedings of the IEEE International Symposium on Antennas and Propagation and USNC-URSI National Radio Science Meeting (APSURSI '12), Chicago, Ill, USA, July 2012.
- [16] C. G. Christodoulou, Y. Tawk, S. A. Lane, and S. R. Erwin, "Reconfigurable antennas for wireless and space applications," *Proceedings of the IEEE*, vol. 100, no. 7, pp. 2250–2261, 2012.
- [17] M. Al-Husseini, A. El-Hajj, and K. Y. Kabalan, "A 1.9–13.5 GHz low-cost microstrip antenna," in *Proceedings of the IEEE International Wireless Communications and Mobile Computing Conference (IWCMC '08)*, pp. 1023–1025, Crete, Greece, August 2008.
- [18] M. Al-Husseini, Y. Tawk, A. El-Hajj, and K. Y. Kabalan, "A low-cost microstrip antenna for 3G/WLAN/WiMAX and UWB applications," in *Proceedings of the International Conference on Advances in Computational Tools for Engineering Applications* (ACTEA '09), pp. 68–70, Zouk Mosbeh, Lebanon, July 2009.
- [19] N. A. Kumar and A. S. Gandhi, "Small size planar monopole antenna for high speed UWB applications," in *Proceedings of the 22nd National Conference on Communication (NCC '16)*, pp. 1–5, Guwahati, India, March 2016.
- [20] M. Al-Husseini, A. Ramadan, Y. Tawk, A. El-Hajj, and K. Y. Kabalan, "Design and ground plane optimization of a CPW-fed ultra-wideband antenna," *Turkish Journal of Electrical Engineering and Computer Sciences*, vol. 19, no. 2, pp. 243–250, 2011.

- [21] S. R. Zahran, O. H. El Sayed Ahmed, A. T. El-Shalakany, S. S. Saleh, and M. A. Abdalla, "Ultra wide band antenna with enhancement efficiency for high speed communications," in *Proceedings of the 31st National Radio Science Conference (NRSC '14)*, pp. 65–72, Cairo, Egypt, April 2014.
- [22] G. M. Dandime and V. G. Kasabegoudar, "A slotted circular monopole antenna for wireless applications," *International Journal of Wireless Communications and Mobile Computing*, vol. 2, no. 2, pp. 30–34, 2014.
- [23] K. P. Ray, "Design aspects of printed monopole antennas for ultra-wide band applications," *International Journal of Antennas and Propagation*, vol. 2008, Article ID 713858, 8 pages, 2008.
- [24] FCC 1st Report and Order on Ultra-Wideband Technology, February 2002.

Hindawi Publishing Corporation International Journal of Antennas and Propagation Volume 2016, Article ID 8459109, 8 pages http://dx.doi.org/10.1155/2016/8459109

# Research Article

# Design and Performance Analysis of MISO-ORM-DCSK System over Rayleigh Fading Channels

## Gang Zhang, 1 Chuan gang Wang, 1 Guo quan Li, 2 and Jin zhao Lin<sup>2</sup>

<sup>1</sup>Chongqing Key Laboratory of Signal and Information Processing, Chongqing University of Posts and Telecommunications, Chongqing 400065, China

Correspondence should be addressed to Chuan gang Wang; 332694781@qq.com

Received 25 June 2016; Revised 4 September 2016; Accepted 4 October 2016

Academic Editor: Massimiliano Simeoni

Copyright © 2016 Gang Zhang et al. This is an open access article distributed under the Creative Commons Attribution License, which permits unrestricted use, distribution, and reproduction in any medium, provided the original work is properly cited.

A novel chaotic communication system, named Orthogonality-based Reference Modulated-Differential Chaos Shift Keying (ORM-DCSK), is proposed to enhance the performance of RM-DCSK. By designing an orthogonal chaotic generator (OCG), the intrasignal interference components in RM-DCSK are eliminated. Also, the signal frame format is expanded so the average bit energy is reduced. As a result, the proposed system has less interference in decision variables. Furthermore, to investigate the bit error rate (BER) performance over Rayleigh fading channels, the MISO-ORM-DCSK is studied. The BER expressions of the new system are derived and analyzed over AWGN channel and multipath Rayleigh fading channel. All simulation results not only show that the proposed system can obtain significant improvement but also verify the analysis in theory.

#### 1. Introduction

Chaos based digital communication systems have been proposed and studied in recent years [1–7]. The differential chaos shift keying (DCSK) and its constant power version called frequency-modulated DCSK (FM-DCSK) are widely studied. However, the drawbacks of DCSK or FM-DCSK are low data rate and poor security [1, 2]. In order to address those problems, NR-DCSK, OFDM-DCSK, and short reference DCSK are proposed in [8-10]. Based on the robustness of DCSK against linear and nonlinear channel distortions, Kaddoum et al. studied DCSK for PLC applications. On the other hand, smart antenna technology can eliminate the multipath wave propagation [11]. Therefore, MIMO-DCSK and STBC-DCSK are proposed to improve the performance of DCSK system [12–14]. Furthermore, the reference modulated DCSK (RM-DCSK) is proposed in [15]. In RM-DCSK system, the chaotic signal sent in each time slot not only carries one bit of information but also serves as the reference signal of the information bit transmitted in its following slot. For this reason, the attainable data rate of RM-DCSK is doubled in

comparison to DCSK. However, the intrasignal interference is produced in decision variables at the receiver. Therefore, compared to DCSK, BER performance of RM-DCSK is not improved.

In this paper, the ORM-DCSK system is proposed as an improved version for RM-DCSK. A novel orthogonal chaotic generator (OCG) is designed to generate orthogonal chaos signal. Also, the signal frame format is extended. Furthermore, two transmit antennas are used in the transmitter of the ORM-DCSK and BER formula is derived.

The remainder of this paper is organized as follows: in Section 2, the principle of MISO-ORM-DCSK is presented. In Section 3, the BER expressions are analyzed. In Section 4, simulation results are shown to evaluate the performance of the new system. Finally, summaries are given in Section 5.

#### 2. MISO-ORM-DCSK

In this section, the baseband implementation of MISO-ORM-DCSK is introduced and some details are explained.

<sup>&</sup>lt;sup>2</sup>Chongqing Key Laboratory of Photoelectronic Information Sensing and Transmitting Technology, Chongqing University of Posts and Telecommunications, Chongqing 400065, China

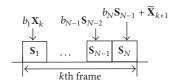


FIGURE 1: Signal frame format of ORM-DCSK.

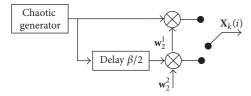


FIGURE 2: Block diagram of OCG.

2.1. Signal Format. Figure 1 shows the frame format of ORM-DCSK system. Different with RM-DCSK, there are N adjacent time slots in each frame, in which average bit energy (labeled as  $E_b$ ) decreases from  $1.5\beta E(x_i^2)$  to  $(1+1/N)\beta E(x_i^2)$ . The time slot is divided into  $\beta$  chips to carry the chaotic sequences and  $b_l$  is the lth information bit in kth frame. Concretely,  $\mathbf{X}_k$  is modulated by the information bit  $b_1 \in \{+1,-1\}$  in the first time slot of kth frame. In the second time slot,  $b_2b_1\mathbf{X}_k$  is sent. In the kth time slot, kth kth reference sequence of kth frame. In Figure 1, kth reference sequence of kth frame. In Figure 1, kth reference sequence of kth frame. In Figure 1, kth reference sequence of kth frame. In Figure 1, kth reference sequence of kth frame. In Figure 1, kth reference sequence of kth frame. In Figure 1, kth reference sequence of kth frame. In Figure 1, kth reference sequence of kth frame. In Figure 1, kth reference sequence of kth frame. In Figure 1, kth reference sequence of kth frame. In Figure 1, kth reference sequence of kth frame. In Figure 1, kth reference sequence of kth frame. In Figure 1, kth reference sequence of kth frame.

2.2. Transmitter Structure. Figure 2 shows the block diagram of orthogonal chaotic generator (OCG). It is necessary to make the chaotic carriers transmitted in neighboring two frames orthogonal to erase the intrasignal interference components included in decision variables clearly. We assume that the spreading factor is six ( $\beta = 6$ ). In the first-time slot period, as shown in Figure 2, the switch is connected to bottom. The chaotic sequence U = [a, b, c] is multiplied by  $\mathbf{w}_2^2 = [+1, -1]$ . In other words,  $\mathbf{X}_k = \mathbf{U} \cdot \mathbf{w}_2^2 =$ [a, -a, b, -b, c, -c]. During second- to (N-1)th-slots period, the switch is suspended. In the Nth-time slot period, the switch is connected to bottom. The chaotic sequence V =[x, y, z] is multiplied by  $\mathbf{w}_2^1 = [+1, +1]$ .  $\widetilde{\mathbf{X}}_{k+1} = \mathbf{V} \cdot \mathbf{w}_2^1 =$ [x, x, y, y, z, z]. In the first-time slot period of (k+1)th frame, the switch is connected to bottom again.  $X_{k+1} = V \cdot w_2^2 =$ [x, -x, y, -y, z, -z].

The chaotic sequences generated by the OCG satisfy

$$\mathbf{X}_{k} \perp \widetilde{\mathbf{X}}_{k+1},$$

$$\widetilde{\mathbf{X}}_{k+1} \perp \mathbf{X}_{k+1},$$

$$\mathbf{X}_{k+1} = (\widetilde{\mathbf{X}}_{k+1}\mathbf{W}),$$

$$\mathbf{X}_{k+1} \perp (\mathbf{X}_{k}\mathbf{W}).$$
(1)

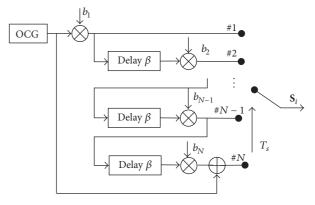


FIGURE 3: Block diagram of the proposed system transmitter.

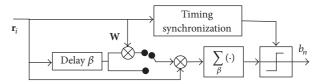


FIGURE 4: Block diagram of the proposed system receiver.

Here 
$$\mathbf{W} = \underbrace{[+1, -1 \cdots + 1, -1]}_{\beta}$$
 is a modification function.

Figure 3 shows the block diagram of ORM-DCSK transmitter. There are two transmitting antennas ( $M_T=2$ ) and one receiving antenna in MISO-ORM-DCSK system. The two transmitting antennas are independent. The signal can be sent by number 1 antenna and the replica of the signal can be sent by number 2 antenna. The transmit signal and replica can be sent at the same time in theory. However, it may be hardly implementable at present due to plenty of delay lines in transmitter. To replace the delay circuit, some excellent algorithms could be employed here, which are provided in [16]. As described in Figure 1, the transmitted signal in kth frame is denoted by

$$\mathbf{S}_{1} = b_{1} \mathbf{X}_{k},$$

$$\mathbf{S}_{l} = b_{l} \mathbf{S}_{l-1} \quad (l = 2, ..., N-1),$$

$$\mathbf{S}_{N} = b_{N} \mathbf{S}_{N-1} + \widetilde{\mathbf{X}}_{k+1}.$$
(2)

2.3. Receiver Structure. The receiver structure of ORM-DCSK is depicted in Figure 4, which has similar appearance to RM-DCSK detector. In our receiver, to demodulate  $b_1$ , we make the switch up. The modification function **W** is used to adjust the relationship between signal in first bit period of kth frame and signal in its former time slot. When decoding  $b_l$  ( $l=2,3,\ldots,N$ ) of kth frame, we make the switch down. Furthermore, the information extraction could work quite well if the receiver knows the starting time of each time slot. As a result, there is a timing synchronization circuit in our receiver, as done in RM-DCSK. To acquire perfect bit synchronization, many traditional timing techniques could be adopted, like data-aided timing synchronization algorithm designed for DCSK [17].

2.4. Channel Model. The channel between each transmit antenna and the receive antenna is two-ray Rayleigh quasistatic block faded channel.  $\xi$  denotes a noise sample following a Gaussian distribution with zero mean and variance  $N_0/2$ . Further,  $\alpha_{m,1}$  and  $\alpha_{m,2}$  denote the gains of the two paths between mth (m=1,2) transmit antenna and the receive antenna, which are independent, Rayleigh distributed random variables. It is assumed that the channel state remains constant during each bit period.

According to different channel gains, we consider the following two cases:

Case 1: 
$$E\{(\alpha_1)^2\} = E\{(\alpha_2)^2\} = \frac{1}{2}$$
,  
Case 2:  $E\{(\alpha_1)^2\} = \frac{2}{3}$ , (3)  
 $E\{(\alpha_2)^2\} = \frac{1}{3}$ 

At the receiver, we denote the received signal vector during the bit duration by  $\mathbf{r}_l$  ( $l=1,\ldots,N$ ). Then,  $\mathbf{r}_l$  can be given by

$$\mathbf{r}_{l} = \sum_{m=1}^{M_{T}} \alpha_{m,1} \mathbf{s}_{m,l}^{\tau_{m,1}} + \sum_{m=1}^{M_{T}} \alpha_{m,2} \mathbf{s}_{m,l}^{\tau_{m,2}} + \boldsymbol{\xi}_{l}.$$
 (4)

Here,  $\mathbf{s}_{m,l}^{\tau_{m,i}}$  (i=1,2) is delayed signal transmitted during lth bit duration and  $\boldsymbol{\xi}_l$  is the additive white Gaussian noise vector.

As described in Figure 1, the chaotic wavelet sent in each time slot not only carries one bit of data but also serves as the reference signal of the data bit transmitted in its next time slot. Then,  $\mathbf{r}_{l-1}$  can be denoted as the reference segment for  $\mathbf{r}_l$ . In this case, the outputs of the demodulators should be given by

$$c_1 = \mathbf{r}_1 \cdot \mathbf{r}_0 \cdot \mathbf{w},$$

$$c_l = \mathbf{r}_l \cdot \mathbf{r}_{l-1} \quad (l = 2, \dots, N).$$
(5)

In (5),  $\mathbf{r}_0$  is signal of last slot time of previews frame. Finally, based on the following rule, the estimated information bit is decided as "+1" or "-1":

$$\hat{b}_l = \begin{cases} +1, & c_i > 0, \\ -1, & c_i < 0. \end{cases}$$
 (6)

#### 3. Performance Analysis

In this section, BER expression is derived over Rayleigh fading channels. Based on Figure 1 and (5), it can be easily found that the statistical properties of  $c_l$  (l = 1, 2, ..., N) are different. Then, we must calculate the BER performance of each bit, which differs from RM-DCSK.

The logistic map  $x_{i+1} = 1 - 2x_i^2$ ,  $-1 < x_i < 1$ ,  $x_i \ne \{0, \pm 0.5\}$ , is used with  $E(x_i) = 0$  and  $E(x_i^2) = 0.5$ ,  $Var(x_i^2) = 0.125$ , where  $E(\cdot)$  and  $Var(\cdot)$  denote the expectation operator and variance operator, respectively. We can get the average bit energy  $E_b = (1 + 1/N)\beta E(x_i^2)$ .

To further simplify the analysis, we can assume that  $\tau_{m,1} = 0$ ,  $\tau_{m,2} = \tau$ , and multipath time delay is much smaller than the spreading factor; that is,  $0 < \tau \ll \beta$ . Thus, (4) can be rewritten as

$$\mathbf{r}_{l} = \sum_{m=1}^{M_{T}} \alpha_{m,1} \mathbf{s}_{m,l} + \sum_{m=1}^{M_{T}} \alpha_{m,2} \mathbf{s}_{m,l}^{\mathsf{T}} + \boldsymbol{\xi}_{l}$$
 (7)

Therefore, without loss of generality, we consider the error rate of the bit  $b_2$ . Substituting (7) into (5) for l=2, we can get

$$c_{2} = \mathbf{r}_{2} \cdot \mathbf{r}_{1}$$

$$= \left[ \frac{1}{\sqrt{M_{T}}} \left( b_{2}b_{1}\mathbf{X}_{k} \sum_{m=1}^{M_{T}} \alpha_{m,1} + b_{2}b_{1}\mathbf{X}_{k}^{T} \sum_{m=1}^{M_{T}} \alpha_{m,2} \right) + \boldsymbol{\xi}_{2} \right]$$

$$\cdot \left[ \frac{1}{\sqrt{M_{T}}} \left( b_{1}\mathbf{X}_{k} \sum_{m=1}^{M_{T}} \alpha_{m,1} + b_{1}\mathbf{X}_{k}^{T} \sum_{m=1}^{M_{T}} \alpha_{m,2} \right) + \boldsymbol{\xi}_{1} \right]$$

$$= \mathbf{A} + \mathbf{B} + \underline{\boldsymbol{\xi}_{1} \cdot \boldsymbol{\xi}_{2}}, \tag{8}$$

where

$$A = \frac{1}{M_{T}} \left( b_{2}b_{1}X_{k} \sum_{m=1}^{M_{T}} \alpha_{m,1} + b_{2}b_{1}X_{k}^{\tau} \sum_{m=1}^{M_{T}} \alpha_{m,2} \right) \cdot \left( b_{1}X_{k} \sum_{m=1}^{M_{T}} \alpha_{m,1} + b_{1}X_{k}^{\tau} \sum_{m=1}^{M_{T}} \alpha_{m,2} \right),$$

$$B = \frac{1}{\sqrt{M_{T}}} \left( b_{2}b_{1}X_{k} \sum_{m=1}^{M_{T}} \alpha_{m,1} + b_{2}b_{1}X_{k}^{\tau} \sum_{m=1}^{M_{T}} \alpha_{m,2} \right) \xi_{1}$$

$$+ \frac{1}{\sqrt{M_{T}}} \left( b_{1}X_{k} \sum_{m=1}^{M_{T}} \alpha_{m,1} + b_{1}X_{k}^{\tau} \sum_{m=1}^{M_{T}} \alpha_{m,2} \right) \xi_{2}.$$

$$(9)$$

Assuming  $b_2 = 1$ , the instantaneous mean of the decision variable is  $E(c_2) = E(A) + E(B) + E(C)$ . Here,

$$E(A) = \left[ \left( \sum_{m=1}^{M_T} \alpha_{m,1} \right)^2 + \left( \sum_{m=1}^{M_T} \alpha_{m,2} \right)^2 \right] \frac{NE_b}{(N+1)M_T}, \quad (10)$$

$$E(B) = E(C) = 0.$$

The variance of decision variable can be easily expressed as  $Var(c_2) = Var(A) + Var(B) + Var(C)$ . Here,

$$\operatorname{Var}\left(\mathbf{A}\right) = \frac{\beta \left[ \left( \sum_{m=1}^{M_{T}} \alpha_{m,1} \right)^{4} + \left( \sum_{m=1}^{M_{T}} \alpha_{m,2} \right)^{4} \right]}{8M_{T}^{2}} + \frac{2 \left( \sum_{m=1}^{M_{T}} \alpha_{m,1} \right)^{2} \left( \sum_{m=1}^{M_{T}} \alpha_{m,2} \right)^{2} N^{2} E_{b}^{2}}{\beta \left( N+1 \right)^{2} M_{T}^{2}}$$

$$\operatorname{Var}(B) = \frac{\left[ \left( \sum_{m=1}^{M_{T}} \alpha_{m,1} \right)^{2} + \left( \sum_{m=1}^{M_{T}} \alpha_{m,2} \right)^{2} \right] N E_{b} N_{0}}{(N+1) M_{T}}$$

$$\operatorname{Var}(C) = \beta \frac{N_{0}^{2}}{4}.$$
(11)

Based on the above results, the mean and variance of  $c_2$  are

$$E\left(c_{2} \mid b_{2} = +1\right)$$

$$= \left[\left(\sum_{m=1}^{M_{T}} \alpha_{m,1}\right)^{2} + \left(\sum_{m=1}^{M_{T}} \alpha_{m,2}\right)^{2}\right] \frac{NE_{b}}{(N+1) M_{T}}.$$

$$Var\left(c_{2} \mid b_{2} = +1\right)$$

$$= \frac{\beta \left[\left(\sum_{m=1}^{M_{T}} \alpha_{m,1}\right)^{4} + \left(\sum_{m=1}^{M_{T}} \alpha_{m,2}\right)^{4}\right]}{8M_{T}^{2}}$$

$$+ \frac{2\left(\sum_{m=1}^{M_{T}} \alpha_{m,1}\right)^{2}\left(\sum_{m=1}^{M_{T}} \alpha_{m,2}\right)^{2} N^{2}E_{b}^{2}}{\beta (N+1)^{2} M_{T}^{2}}$$

$$+ \frac{\left[\left(\sum_{m=1}^{M_{T}} \alpha_{m,1}\right)^{2} + \left(\sum_{m=1}^{M_{T}} \alpha_{m,2}\right)^{2}\right] NE_{b}N_{0}}{(N+1) M_{T}}$$

$$+ \beta \frac{N_{0}}{4}$$

Similarly, if  $b_2 = -1$  is sent, the mean and variance of  $c_2$  are equal to

$$E(c_2 \mid b_2 = -1) = -E(c_2 \mid b_2 = +1)$$

$$Var(c_2 \mid b_2 = -1) = Var(c_2 \mid b_2 = +1).$$
(13)

Based on the above results, the BER for decoding  $b_l$  is computed as

$$BER_{c_2}(\gamma_b) = \frac{1}{2} \operatorname{erfc} \left[ \frac{E(c_2 \mid b_2 = +1)}{\sqrt{2 \operatorname{Var}(c_2 \mid b_2 = +1)}} \right]$$

$$= \frac{1}{2} \operatorname{erfc} \left[ \left( \frac{\Lambda_1}{\beta} + \frac{2\Gamma}{\gamma_b} + \frac{\beta\Gamma^2}{2\gamma_b^2} \right)^{-1/2} \right].$$
(14)

Similarly, for  $l \in \{3, 4, ..., N - 1\}$  the BER is

$$BER_{c_{1}}(\gamma_{h}) = BER_{c_{2}}(\gamma_{h}). \tag{15}$$

For l = 1, we can get

$$c_{1} = \mathbf{r}_{1} \cdot \mathbf{r}_{0} \cdot \mathbf{w} = \left[ \frac{1}{\sqrt{M_{T}}} \left( b_{1} \mathbf{X}_{k} \sum_{m=1}^{M_{T}} \alpha_{m,1} + b_{1} \mathbf{X}_{k}^{\mathsf{T}} \sum_{m=1}^{M_{T}} \alpha_{m,2} \right) + \boldsymbol{\xi}_{1} \right]$$

$$\cdot \left[ \frac{1}{\sqrt{M_{T}}} \left( \left( b_{0} \mathbf{X}_{k-1} + \widetilde{\mathbf{X}}_{k} \right) \mathbf{w} \sum_{m=1}^{M_{T}} \alpha_{m,1} + \left( b_{0} \mathbf{X}_{k-1}^{\mathsf{T}} + \widetilde{\mathbf{X}}_{k}^{\mathsf{T}} \right) \mathbf{w}^{\mathsf{T}} \sum_{m=1}^{M_{T}} \alpha_{m,2} \right) + \boldsymbol{\xi}_{0} \mathbf{w} \right] = \mathbf{D} + \mathbf{E}$$

$$+ \underline{\boldsymbol{\xi}}_{1} \cdot \underline{\boldsymbol{\xi}}_{0} \mathbf{w},$$

$$\mathbf{E}$$
(16)

where

$$D = \frac{1}{M_{T}} \left( b_{1} \mathbf{X}_{k} \sum_{m=1}^{M_{T}} \alpha_{m,1} + b_{1} \mathbf{X}_{k}^{T} \sum_{m=1}^{M_{T}} \alpha_{m,2} \right)$$

$$\cdot \left[ (b_{0} \mathbf{X}_{k-1} \mathbf{w} + \mathbf{X}_{k}) \sum_{m=1}^{M_{T}} \alpha_{m,1} + (b_{0} \mathbf{X}_{k-1}^{T} \mathbf{w}^{T} + \mathbf{X}_{k}^{T}) \sum_{m=1}^{M_{T}} \alpha_{m,2} \right],$$

$$E = \frac{1}{\sqrt{M_{T}}} \left( b_{1} \mathbf{X}_{k} \sum_{m=1}^{M_{T}} \alpha_{m,1} + b_{1} \mathbf{X}_{k}^{T} \sum_{m=1}^{M_{T}} \alpha_{m,2} \right) \xi_{0} \mathbf{w}$$

$$+ \frac{1}{\sqrt{M_{T}}} \left[ (b_{0} \mathbf{X}_{k-1} \mathbf{w} + \mathbf{X}_{k}) \sum_{m=1}^{M_{T}} \alpha_{m,1} + (b_{0} \mathbf{X}_{k-1}^{T} \mathbf{w}^{T} + \mathbf{X}_{k}^{T}) \sum_{m=1}^{M_{T}} \alpha_{m,2} \right] \xi_{1}.$$
(17)

Similarly, we can get

$$E(D) = \left[ \left( \sum_{m=1}^{M_T} \alpha_{m,1} \right)^2 + \left( \sum_{m=1}^{M_T} \alpha_{m,2} \right)^2 \right] \frac{NE_b}{(N+1)M_T}, \quad (18)$$

$$E(E) = E(F) = 0, \quad (19)$$

Var(D)

$$= \frac{\beta \left[ \left( \sum_{m=1}^{M_T} \alpha_{m,1} \right)^4 + \left( \sum_{m=1}^{M_T} \alpha_{m,2} \right)^4 \right]}{8M_T^2}$$

$$+ \frac{4 \left( \sum_{m=1}^{M_T} \alpha_{m,1} \right)^2 \left( \sum_{m=1}^{M_T} \alpha_{m,2} \right)^2 N^2 E_b^2}{\beta (N+1)^2 M_T^2},$$
(20)

$$Var (E) = \frac{3\left[\left(\sum_{m=1}^{M_T} \alpha_{m,1}\right)^2 + \left(\sum_{m=1}^{M_T} \alpha_{m,2}\right)^2\right] N E_b N_0}{2(N+1) M_T}, \quad (21)$$

$$Var(F) = \beta \frac{N_0^2}{4}.$$
 (22)

So, the mean and variance of  $c_1$  are

$$E\left(c_{1} \mid b_{1} = +1\right)$$

$$= \left[\left(\sum_{m=1}^{M_{T}} \alpha_{m,1}\right)^{2} + \left(\sum_{m=1}^{M_{T}} \alpha_{m,2}\right)^{2}\right] \frac{NE_{b}}{(N+1)M_{T}}, \quad (23)$$

$$Var\left(c_{1} \mid b_{1} = +1\right)$$

$$= \frac{\beta\left[\left(\sum_{m=1}^{M_{T}} \alpha_{m,1}\right)^{4} + \left(\sum_{m=1}^{M_{T}} \alpha_{m,2}\right)^{4}\right]}{8M_{T}^{2}}$$

$$+ \frac{4\left(\sum_{m=1}^{M_{T}} \alpha_{m,1}\right)^{2}\left(\sum_{m=1}^{M_{T}} \alpha_{m,2}\right)^{2}N^{2}E_{b}^{2}}{\beta(N+1)^{2}M_{T}^{2}} \quad (24)$$

$$+ \frac{3NE_{b}N_{0}\left[\left(\sum_{m=1}^{M_{T}} \alpha_{m,1}\right)^{2} + \left(\sum_{m=1}^{M_{T}} \alpha_{m,2}\right)^{2}\right]}{2(N+1)M_{T}}$$

$$+ \beta\frac{N_{0}}{4}.$$

Based on (23)-(24), the BER for decoding  $b_1$  is computed as

$$BER_{c_1}(\gamma_b) = \frac{1}{2}erfc\left[\frac{E(c_1 \mid b_1 = +1)}{\sqrt{2Var(c_1 \mid b_1 = +1)}}\right]$$

$$= \frac{1}{2}erfc\left[\left(\frac{\Lambda_2}{\beta} + \frac{3\Gamma}{\gamma_b} + \frac{\beta\Gamma^2}{2\gamma_b^2}\right)^{-1/2}\right].$$
(25)

Here,

$$\Lambda_{1} = 1 + \frac{2\left(\sum_{m=1}^{M_{T}} \alpha_{m,1} \sum_{m=1}^{M_{T}} \alpha_{m,2}\right)^{2}}{\left(\left(\sum_{m=1}^{M_{T}} \alpha_{m,1}\right)^{2} + \left(\sum_{m=1}^{M_{T}} \alpha_{m,2}\right)^{2}\right)^{2}},$$

$$\Lambda_{2} = 1 + \frac{6\left(\sum_{m=1}^{M_{T}} \alpha_{m,1} \sum_{m=1}^{M_{T}} \alpha_{m,2}\right)^{2}}{\left(\left(\sum_{m=1}^{M_{T}} \alpha_{m,1}\right)^{2} + \left(\sum_{m=1}^{M_{T}} \alpha_{m,2}\right)^{2}\right)^{2}},$$

$$\Gamma = 1 + \frac{1}{N}$$

$$\gamma_{b} = \underbrace{\left(\sum_{m=1}^{M_{T}} \alpha_{m,1}\right)^{2} E_{b}}_{M_{T} N_{0}} + \underbrace{\left(\sum_{m=1}^{M_{T}} \alpha_{m,2}\right)^{2} E_{b}}_{M_{T} N_{0}}.$$
(26)

We denote  $\overline{\gamma_1} = E(\gamma_1)$  and  $\overline{\gamma_2} = E(\gamma_2)$  to represent the average SNR per path. Moreover, for a multipath Rayleigh fading channel, the PDF of  $\gamma_b$  is given by

$$f\left(\gamma_{b}\right) = \begin{cases} \frac{\gamma_{b}}{\overline{\gamma_{1}}^{2}} e^{-\gamma_{b}/\overline{\gamma_{1}}}, & E\left(\alpha_{1}^{2}\right) = E\left(\alpha_{2}^{2}\right), \\ \frac{e^{-\gamma_{b}/\overline{\gamma_{1}}} - e^{-\gamma_{b}/\overline{\gamma_{2}}}}{\overline{\gamma_{1}} - \overline{\gamma_{2}}}, & E\left(\alpha_{1}^{2}\right) \neq E\left(\alpha_{2}^{2}\right). \end{cases}$$
(27)

Based on (14)–(16), the BER is

BER 
$$(\gamma_b) = \frac{N-2}{2N} \operatorname{erfc} \left[ \left( \frac{\Lambda_1}{\beta} + \frac{2\Gamma}{\gamma_b} + \frac{\beta\Gamma^2}{2\gamma_b^2} \right)^{-1/2} \right] + \frac{1}{N} \operatorname{erfc} \left[ \left( \frac{\Lambda_2}{\beta} + \frac{3\Gamma}{\gamma_b} + \frac{\beta\Gamma^2}{2\gamma_b^2} \right)^{-1/2} \right].$$
 (28)

Finally, using (20) and (21), the BER of MISO-ORM-DCSK is derived as

$$BER = \int_0^\infty BER(\gamma_b) f(\gamma_b) d\gamma_b.$$
 (29)

Moreover, we can get the theoretical lower bound of the BER when N tends to infinity.

BER<sub>lowerBound</sub> 
$$(\gamma_b) = \lim_{N \to \infty} BER(\gamma_b)$$
  

$$= \frac{1}{2} \operatorname{erfc} \left\{ \left[ \frac{\Lambda_1}{\beta} + \frac{2}{\gamma_b} + \frac{\beta}{2\gamma_b^2} \right]^{-1/2} \right\}, \qquad (30)$$
BER<sub>lowerBound</sub>  $= \int_0^\infty BER_{lowerBound}(\gamma_b) f(\gamma_b) d\gamma_b.$ 

On the other hand, (28) can be extended to the AWGN channel case by choosing  $\alpha_{m,1}=1$  and  $\alpha_{m,2}=0$ . Hence, the BER would simplify to

$$BER = \frac{N-2}{2N} erfc \left[ \left( \frac{1}{\beta} + \frac{\Gamma N_0}{E_b} + \frac{\beta \Gamma^2 N_0^2}{8E_b^2} \right)^{-1/2} \right] + \frac{1}{N} erfc \left[ \left( \frac{1}{\beta} + \frac{3\Gamma N_0}{2E_b} + \frac{\beta \Gamma^2 N_0^2}{8E_b^2} \right)^{-1/2} \right].$$
(31)

#### 4. Simulation

In order to validate the BER performance of the MISO-ORM-DCSK and compare it with MISO-RM-DCSK, the BER is evaluated under AWGN and multipath fading channels. To facilitate the expression, the Monte Carlo simulations and theory results are labeled as "Sim" and "Theory" respectively.

4.1. AWGN Channel. Since the theoretical BERs for the 2nd to (N-1)th bits and the BER for Nth bit are different, Figure 5 shows BERs for (N-1)th bit and Nth bit in the AWGN channel of MISO-ORM-DCSK for  $\beta=256$  and N=4.

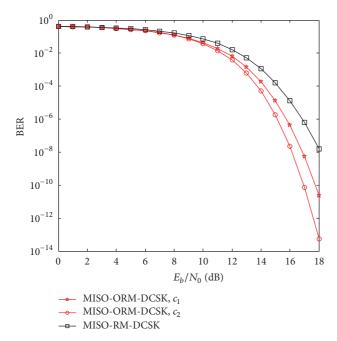


FIGURE 5: Each BER in the AWGN channel for MISO-ORM-DCSK.

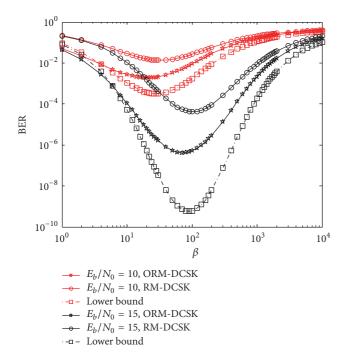


FIGURE 6: BER performance versus spreading factor  $\beta$ .

From Figure 5, it is shown that as  $E_b/N_0$  increases, the BERs become better. In addition, the error rate of  $c_2$  is superior to that of  $c_1$  in the proposed system. This can be explained as follows: the decision variable of  $c_1$  has an interference term, which does not exist in that of  $c_2$ . It is visible that, with less intrasignal interference and noise interference components, MISO-ORM-DCSK is always better than MISO-RM-DCSK.

Figure 6 shows the relationship between BER performance and spreading factor  $\beta$ . It can also be noticed that

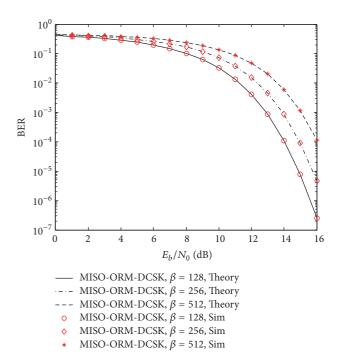


FIGURE 7: Relationships between analytical BER and Monte Carlo results for MISO-ORM-DCSK and MISO-RM-DCSK with N = 2.

ORM-DCSK is always better than RM-DCSK. In addition, it is obvious that the BER can maximize an optimal value by choosing the certain value of spreading factor; for example, the certain value is about 30 and 100 when  $E_b/N_0=10\,\mathrm{dB}$  and  $E_b/N_0=15\,\mathrm{dB}$ , respectively. BER starts to degrade if the spreading factor is beyond it, which is caused by fluctuations in  $E_b$  at small  $\beta$  and the noise-noise cross correlation at large  $\beta$ 

Figure 7 shows the relationships between analytical BER and Monte Carlo of MISO-ORM-DCSK in the AWGN channel. From Figure 7, it is easily found that clear matching between analytical expression and Monte Carlo simulations result can be obtained. This confirms that the Gaussian approximation works well when the spreading factor is relatively lager.

Figure 8 plots the relationships between BER performance and N with  $E_b/N_0=18\,\mathrm{dB}$  and  $\beta=256$ . The BER is smaller with larger N. We can get the theoretical lower bound of the BER when N tends to infinity. However, the complexity of system is increasing. We think  $N\leq 50$  is the best choice and it can bring a trade-off between the BER and complexity.

4.2. Rayleigh Fading Channel. Figure 9 plots the relationships between BER performance and  $E_b/N_0$  for MISO-ORM-DCSK and MISO-RM-DCSK system with N=4. Through the examination of Figure 9, the proposed system achieves a performance gain of about 2 dB over the MISO-RM-DCSK at BER =  $1 \times 10^{-4}$ . In other words, the new system shows an enhanced robustness in Rayleigh fading channel.

Figure 10 shows the relationships between analytical BER and Monte Carlo results in Rayleigh fading channel when spreading factors  $\beta = 128$  and 512 and N = 2. It is easily

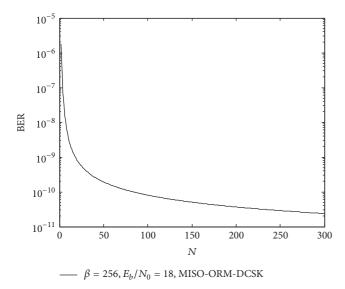


FIGURE 8: Relationships between BER and N for MISO-ORM-DCSK.

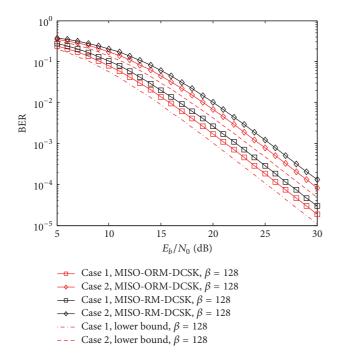


FIGURE 9: BER performance in Rayleigh fading channel with different gains.

found that analytical results correspond with simulation results perfectly. This can be explained by identical reason in Figure 7 and the Gaussian approximation works well when the spreading factor is relatively lager. In addition, the BERs for all cases become worse as  $\beta$  increases, which can be attributed to the increasing negative contribution from interference components generated from the chaotic sequence and Gaussian noise.

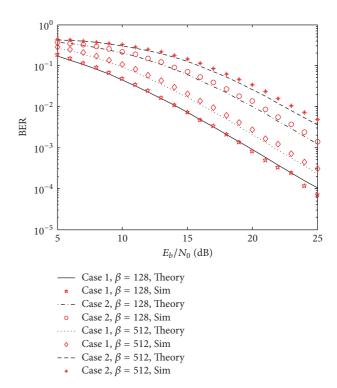


FIGURE 10: Relationships between analytical BER and Monte Carlo results in Rayleigh fading channel.

#### 5. Conclusion

In this paper, ORM-DCSK is proposed to improve the BER performance of RM-DCSK. The intrasignal interference components existing in RM-DCSK are eliminated clearly by designing an orthogonal chaotic generator. Without any cost in data rate, the proposed system not only shows excellent agreement between theoretical expressions and Monte Carlo simulations but also shows significance of BER improvement.

However, the proposed system is slightly more complex than RM-DCSK due to additional delay and switch. This complexity cost is worthy and it provides a huge BER improvement. We believe that the proposed system has significant potential in chaotic communication environment.

#### **Competing Interests**

The authors declare that they have no competing interests.

#### **Acknowledgments**

This work was supported in part by the National Natural Science Foundation of China under Grants no. 61371164, no. 61301124, and no. 61671091 and in part by the Chongqing Distinguished Youth Foundation no. CSTC2011jjjq40002, as well as the University Innovation Team Construction Plan of Smart Medical System and Core Technology.

#### References

- [1] G. Kolumban, B. Vizvari, W. Schwarz et al., "Differential chaos shift keying: a robust coding for chaos communications," in *Proceedings of the IEEE Workshop on Nonlinear Dynamics of Electronic Systems (NDES '96)*, pp. 87–92, Seville, Spain, 1996.
- [2] G. Kolumban, G. Kis, M. P. Kennedy et al., "FM-DCSK: a new and robust solution to chaos communications," in *Proceedings* of the International Symposium on Nonlinear Theory and Applications, pp. 117–120, 1997.
- [3] L. Wang, G. Cai, and G. R. Chen, "Design and performance analysis of a new multiresolution *M*-Ary differential chaos shift keying communication system," *IEEE Transactions on Wireless Communications*, vol. 14, no. 9, pp. 5197–5208, 2015.
- [4] A. Kumar and P. R. Sahu, "Performance analysis of DCSK-SR systems based on best relay selection in multiple MIMO relay environment," *International Journal of Electronics and Communications*, vol. 70, no. 1, pp. 18–24, 2016.
- [5] G. Kaddoum and F. Shokraneh, "Analog network coding for multi-user multi-carrier differential chaos shift keying communication system," *IEEE Transactions on Wireless Communica*tions, vol. 14, no. 3, pp. 1492–1505, 2015.
- [6] Y. Fang, L. Wang, P. Chen, J. Xu, G. Chen, and W. Xu, "Design and analysis of a DCSK-ARQ/CARQ system over multipath fading channels," *IEEE Transactions on Circuits and Systems. I. Regular Papers*, vol. 62, no. 6, pp. 1637–1647, 2015.
- [7] G. Kaddoum and F. Gagnon, "Design of a high-data-rate differential chaos shift keying system," *IEEE Transactions on Circuits and Systems II: Express Briefs*, vol. 59, no. 7, pp. 448–452, 2012.
- [8] G. Kaddoum and E. Soujeri, "NR-DCSK: a noise reduction differential chaos shift keying system," *IEEE Transactions on Circuits and Systems II: Express Briefs*, vol. 63, no. 7, pp. 648–652, 2016.
- [9] G. Kaddoum, "Design and performance analysis of a multiuser OFDM based differential chaos shift keying system," *IEEE Transactions on Communications*, vol. 64, no. 1, pp. 249–260, 2016.
- [10] G. Kaddoum, E. Soujeri, and Y. Nijsure, "Design of a short reference noncoherent chaos-based communication systems," *IEEE Transactions on Communications*, vol. 64, no. 2, pp. 680– 689, 2016.
- [11] Y. Xiao, MIMO: Multiple Antenna Communication System, Post & Telecom Press, Beijing, China, 1st edition, 2009.
- [12] Y. Fang, J. Xu, L. Wang, and G. Chen, "Performance of MIMO relay DCSK-CD systems over nakagami fading channels," *IEEE Transactions on Circuits and Systems I: Regular Papers*, vol. 60, no. 3, pp. 757–767, 2013.
- [13] L. Wang, X. Min, and G. Chen, "Performance of SIMO FM-DCSK UMB system based on chaotic pulse cluster signals," *IEEE Transactions on Circuits and Systems. I. Regular Papers*, vol. 58, no. 9, pp. 2259–2268, 2011.
- [14] P. Chen, L. Wang, and F. C. M. Lau, "One analog STBC-DCSK transmission scheme not requiring channel state information," *IEEE Transactions on Circuits and Systems I: Regular Papers*, vol. 60, no. 4, pp. 1027–1037, 2013.
- [15] H. Yang and G.-P. Jiang, "Reference-modulated DCSK: a novel chaotic communication scheme," *IEEE Transactions on Circuits* and Systems II: Express Briefs, vol. 60, no. 4, pp. 232–236, 2013.
- [16] G. Kaddoum, E. Soujeri, C. Arcila, and K. Eshteiwi, "I-DCSK: an improved noncoherent communication system architecture,"

- *IEEE Transactions on Circuits and Systems II: Express Briefs*, vol. 62, no. 9, pp. 901–905, 2015.
- [17] S. Y. Chen, L. Wang, and G. R. Chen, "Data-aided timing synchronization for FM-DCSK UWB communication systems," *IEEE Transactions on Industrial Electronics*, vol. 57, no. 5, pp. 1538–1545, 2010.

Hindawi Publishing Corporation International Journal of Antennas and Propagation Volume 2016, Article ID 7641382, 8 pages http://dx.doi.org/10.1155/2016/7641382

# Research Article

# Wideband, Low-Profile, Dual-Polarized Slot Antenna with an AMC Surface for Wireless Communications

# Wei Hu, 1,2 Rui-Na Lian, 1 Zhao-Yang Tang, 1 and Ying-Zeng Yin 1

 $^1$ National Laboratory of Science and Technology on Antennas and Microwaves, Xidian University, Xi'an, Shaanxi 710071, China  $^2$ Collaborative Innovation Center of Information Sensing and Understanding, Xidian University, Xi'an, Shaanxi 710071, China

Correspondence should be addressed to Wei Hu; mwhuwei@163.com

Received 22 July 2016; Revised 27 September 2016; Accepted 4 October 2016

Academic Editor: Renato Cicchetti

Copyright © 2016 Wei Hu et al. This is an open access article distributed under the Creative Commons Attribution License, which permits unrestricted use, distribution, and reproduction in any medium, provided the original work is properly cited.

A wideband dual-polarized slot antenna loaded with artificial magnetic conductor (AMC) is proposed for WLAN/WIMAX and LTE applications. The slot antenna mainly consists of two pairs of arrow-shaped slots along the diagonals of the square patch. Stepped microstrip feedlines are placed orthogonally to excite the horizontal and vertical polarizations of the antenna. To realize unidirectional radiation and low profile, an AMC surface composed of  $7 \times 7$  unit cells is designed underneath a distance of  $0.09\lambda_0$  ( $\lambda_0$  being the wavelength in free space at 2.25 GHz) from the slot antenna. Both the dual-polarized slot antenna and the AMC surface are fabricated and measured. Experimental results demonstrate that the proposed antenna achieves for both polarizations a wide impedance bandwidth (return loss 10 dB) of 36.7%, operating from 1.96 to 2.84 GHz. The isolation between the two input ports keeps higher than 29 dB whereas the cross-polarization levels basically maintain lower than -30 dB across the entire frequency band. High front-to-back ratios better than 22 dB and a stable gain higher than 8 dBi are obtained over the whole band.

#### 1. Introduction

Dual-polarized antennas have led to a wide range of applications in modern wireless communication systems since they can effectively mitigate multipath fading problem and enhance channel capacity. To cover several wireless communication services, the antenna should be designed to operate in a wide band. Furthermore, the space to accommodate antennas becomes more and more limited, resulting in high demand for low-profile antennas. Nevertheless, it is still difficult to design a low-profile antenna to simultaneously achieve wide band, high port isolation, and low crosspolarization. Microstrip antenna is a good candidate for base-station application due to its light weight, low cost, low profile, and easy conformability for dual-polarization implementation [1-3]. As known, both the bandwidth and port isolation of the microstrip antenna are not good enough. In recent years, various attractive feeding mechanisms, such as meandering probes [4], L-probes [5], T-type probes [6], Γ-shaped probes [7], hybrid feeding mechanisms [8, 9], aperture-coupled feeds [10], and differential feeds [11, 12], are proposed to enhance the performance of dual-polarized

patch antennas. However, all these techniques lead to high profiles and nonplanar feeding structures, which bring great difficulties in integration and fabrication. In [13], a wideband dual-polarized patch antenna employing a broadband balun has been proposed. Unfortunately, it is hard to design a balun suitable to cover all the requirements of wideband dual-polarized antennas.

By contrast, slot antenna has a planar structure but with high back radiation [14]. For unidirectional radiation, a metallic ground plane is needed to suppress back radiation. However, when the antenna is located close to the metallic plane its radiation efficiency reduces because of the electromagnetic energy reflection due to the metal reflector. To tackle the problem, the antenna is generally placed at a distance of  $0.25\lambda$  or higher from the metallic ground plane, and this results in a high profile which may be impractical for modern wireless communication systems. Recently, the artificial magnetic conductor (AMC) surface attracts much interest owing to its good properties including in-phase reflection for plane waves and suppression of surface waves. AMC can act as a reflector for enhanced radiations in the frequency range where it reflects the incoming

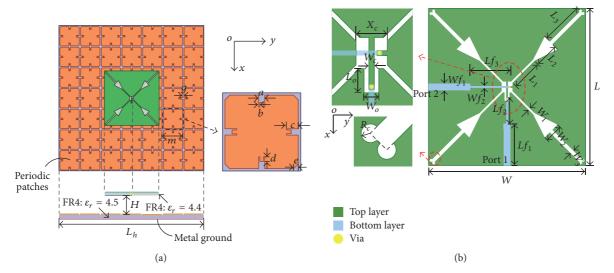


FIGURE 1: Geometry of the proposed dual-polarized antenna. (a) Top and side views and (b) dual-polarized slot antenna.

radiations with a phase coefficient ranging between  $-90^{\circ}$  and  $+90^{\circ}$  [15, 16]. Additionally, the antenna works well when it is positioned very closely to the AMC surface, which makes it possible to design an antenna having a low profile.

In our previous study [17], a stepped-impedance slot structure has been successfully employed in the dual-polarized antenna design as a kind of slot resonator to realize broadband operation. In this paper, two pairs of arrow-shaped slots are instead introduced along the diagonals of a squared patch and combined with an AMC surface, so as to realize a lower profile and a wider impendence bandwidth with respect to the antenna proposed in [17], as well as good dual-polarized operation performance. The paper extends the previous study and provides a new effective approach to the design of wideband low-profile dual-polarized antennas based on radiating slots and AMC surfaces. Furthermore, measured results performed on a prototype show that the antenna exhibits low cross-polarization levels and high port isolation.

#### 2. Antenna Configuration and Design

Figure 1 shows the geometry of the proposed antenna. It consists of a dual-polarized slot antenna and an AMC surface located underneath the antenna to act as a reflector. The slot antenna is constructed on a 1 mm thick FR4 substrate ( $\varepsilon_r = 4.4$ ,  $\tan \delta = 0.02$ ) while the AMC structure is printed on a 3 mm thick FR4 substrate ( $\varepsilon_r = 4.5$ ,  $\tan \delta = 0.02$ ). As shown in Figure 1(b), the slot antenna selects two identical pairs of arrow-shaped slots along the diagonals as the radiation aperture and two orthogonal stepped strips as feedlines. Each arrow-shaped slot, formed by three slotline resonators, is composed of a narrow rectangular slot, a triangular slot, and a slightly wide rectangular slot loaded with two circular slots at its end. It is noteworthy that two-circular-slot design is employed in each arrow-shaped slot to increase the operating bandwidth and improve the impedance matching.

The resonant condition of the antenna depends upon the length  $(L_1 + L_2 + L_3)$  of the arrow-shaped slot, which is approximately equal to half of the wavelength. Both the length and width of each section of the arrow-shaped slot can be adjusted for the slot antenna to achieve broadband property. In addition, the microstrip feeding lines are provided with stepped strips for a better impedance matching. The excitation network consists of two narrow rectangular strips extending to the end of the stepped feedlines where they electrically join with each other by two slender pins (see Figure 1).

The AMC surface consists of metallic ground, grounded dielectric substrate, and periodical patches, without any grounded via. Generally, the periodicity of the patches is much smaller than the wavelength. The unit cell of the proposed AMC surface, shown in Figure 1(a), has a size of  $16.5 \, \text{mm} \times 16.5 \, \text{mm}$  and exhibits a gap width of  $1.5 \, \text{mm}$ between adjacent cells. According to the working mechanism of the AMC surface, when the phase of the reflected wave on the AMC surface in the desired band varies from  $-90^{\circ}$  to  $90^{\circ}$ , it presents in-phase property. The performance of an infinite repetition of the unit cell is simulated by ANSYS HFSS. As shown in Figure 2(a), the HFSS model is based on simulating scattering parameters of a single port air-filled waveguide with two perfect electric conductors (PEC) and two perfect magnetic conductors (PMC) walls. The propagating plane wave is polarized parallel to the PMC walls and normal to the PEC walls. Figure 2(b) plots the simulated phase reflection response of the AMC structure for a normally incident plane wave. It can be obviously seen that the  $\pm 90^{\circ}$ reflection phase of the AMC structure covers from 1.85 GHz to 3.16 GHz. Based upon the unit cell, a  $7 \times 7$  periodic AMC array is developed and positioned underneath at a distance of 12 mm (0.09 $\lambda_0$ ,  $\lambda_0$  being the wavelength in free space at 2.25 GHz) from the antenna. This array acts as a reflector to achieve unidirectional radiation patterns with high front-toback ratios.

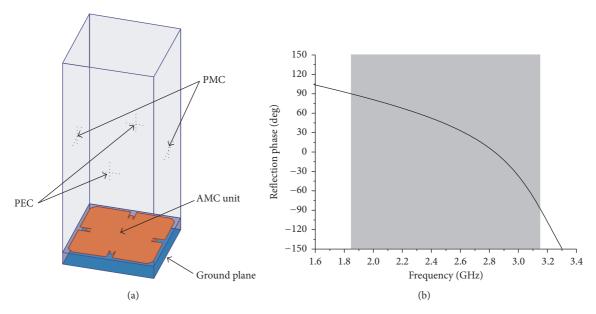


FIGURE 2: (a) Simulation model of AMC unit. (b) Simulated reflection phase of the proposed AMC unit.

#### 3. Results and Discussions

The antenna combined with the AMC structure is analyzed and optimized. The final values of the parameters defined in Figure 1 are listed in Table 1.

To have an insight into the mechanism governing the behavior of the proposed antenna, a detailed study on the antenna without reflector and that over a finite PEC (30 mm away with the same size as the AMC reflector) has been performed for comparison. Figure 3 plots the simulated reflection coefficients ( $|S_{11}|$ ) of three dual-polarized slot antennas. As it can be observed, the antenna over the AMC reflector achieves the widest operating bandwidth with good impedance matching. This behavior is confirmed by the input impedance curves exhibited by the different dualpolarized slot antennas depicted in Figure 4. In particular, the impedance curve related with the AMC reflector shows that one extra resonance, with resistance of about 50 Ohm and null reactance at 2.07 GHz, is generated by the introduction of the AMC surface, which results in antenna miniaturization and broadband property.

The effects of key design parameters such as  $W_1$ ,  $W_3$ , H, m and the number of AMC units on the antenna S-parameter are investigated. In particular, when the narrow rectangular slot width  $W_1$  increases, the second resonant frequency shifts to higher frequency whereas the first resonant frequency almost keeps unchanged as it appears in Figure 5. Simultaneously, the middle band is significantly deteriorated. This means that  $W_1$  plays an important role in controlling the second resonant frequency and in the improvement of the impedance matching. Figure 6 shows the frequency behavior of  $|S_{11}|$  of the proposed antenna for different values of parameter  $W_3$ . From this figure it appears that as  $W_3$  increases from 0.5 to 1.5 mm the first deep in the resonant frequency shifts up, while the second deep in the resonant frequency increases. Finally,  $W_3 = 1$  mm is

TABLE 1: Optimized parameters of the proposed antenna.

| Para.  | Values (mm) |  |
|--------|-------------|--|
| L      | 43.5        |  |
| W      | 43.5        |  |
| $L_1$  | 8.6         |  |
| $L_2$  | 6.8         |  |
| $L_3$  | 12.0        |  |
| $W_1$  | 0.7         |  |
| $W_2$  | 5.0         |  |
| $W_3$  | 1.0         |  |
| $Lf_1$ | 12.5        |  |
| $Lf_2$ | 6.25        |  |
| $Lf_3$ | 10.25       |  |
| $Wf_1$ | 1.5         |  |
| $Wf_2$ | 0.5         |  |
| $X_c$  | 3.0         |  |
| $W_c$  | 0.5         |  |
| $L_o$  | 2.3         |  |
| $W_o$  | 1.4         |  |
| g      | 1.5         |  |
| m      | 16.5        |  |
| Н      | 12.0        |  |
| $L_h$  | 115.5       |  |
| a      | 1.3         |  |
| b      | 0.25        |  |
| С      | 2.5         |  |
| d      | 1.0         |  |
| e      | 1.0         |  |

chosen as the optimized value. In the process of designing the antenna with the AMC reflector, the distance *H* between

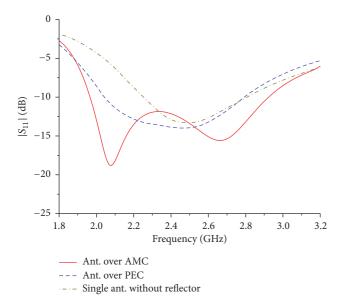


FIGURE 3: Simulated  $|S_{11}|$  of the different dual-polarized slot antennas.

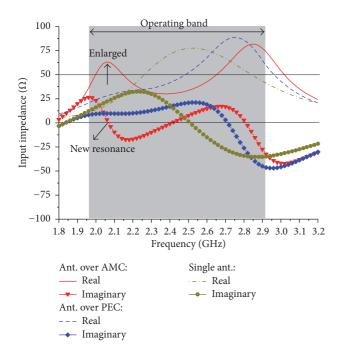


FIGURE 4: Simulated input impedance of the different dual-polarized slot antennas.

the slot antenna and the AMC structure has to be considered. Figure 7 illustrates the frequency behavior of  $|S_{11}|$  of the dual-polarized slot antenna, placed over the AMC plane, for different values of the distance H. From this figure it appears that the bandwidth is almost unaffected, while the impedance matching strongly depends on parameter H. In particular, an increase of the distance between the antenna and the AMC surface leads to a good impedance matching. For a low-profile dual-polarized antenna,  $H=12~\mathrm{mm}$  is finally selected. In addition, the frequency behavior of  $|S_{11}|$  of the proposed

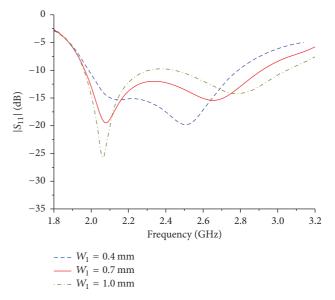


FIGURE 5: Simulated  $|S_{11}|$  of the proposed dual-polarized antenna with different  $W_1$ .

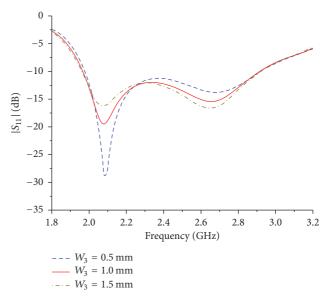


FIGURE 6: Simulated  $|S_{11}|$  of the proposed dual-polarized antenna with different  $W_3$ .

antenna for different sizes of the AMC unit is represented in Figure 8. It is clear that as parameter m increases from 13.5 to 19.5 mm, the operating band of the antenna shifts to lower frequency. When m increase to 19.5 mm, the impedance matching is improved in the lower band but the working bandwidth shrinks obviously at the higher frequency. Thus, the optimum parameter m is set at 16.5 mm. Figure 9 depicts the simulated  $|S_{11}|$  of the proposed antenna with different number of AMC units. From this figure it appears that the number of AMC units mainly affects both the working bandwidth at the higher frequency and impedance matching in the lower band. By balancing the overall dimension of the

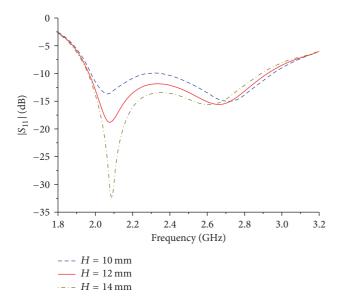


FIGURE 7: Simulated  $|S_{11}|$  of the proposed dual-polarized antenna with different H.

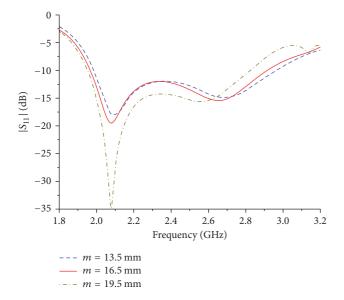


FIGURE 8: Simulated  $|S_{11}|$  of the proposed dual-polarized antenna with different m.

AMC surface and the impedance bandwidth of the antenna, a  $7 \times 7$  AMC array has been finally selected.

To further investigate the dual-polarized operation mechanism of the slot antenna, inspired by [18], the simulated electric-field distributions on the proposed antenna excited by Port 1 and Port 2 at 2.4 GHz are illustrated in Figure 10. From this figure it appears that the maximum electric-field intensity is concentrated in the two pairs of arrow-shaped slots, meaning that these give the main contributions to the total field radiated by the antenna. So, when Port 1 is excited the resulting electric field is linearly polarized along the *x*-axis (see in Figure 10(a)). Similarly, as shown in Figure 10(b),

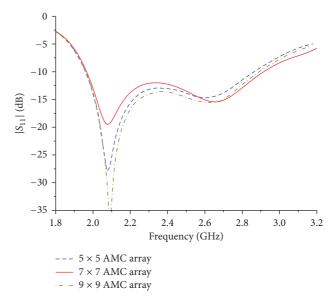


FIGURE 9: Simulated  $|S_{11}|$  of the proposed dual-polarized antenna with different number of AMC units.

the *y*-directed linearly polarized radiation is produced when Port 2 is excited.

To validate the design concept, the proposed dualpolarized slot antenna employing an AMC structure as reflector has been realized and measured. The photograph of the antenna prototype is depicted in Figure 11. In Figure 12 the frequency behavior of the computed and measured results concerning the antenna scattering parameters is reported. From an analysis of this figure it results that while the numerical results show a 38.9% bandwidth, covering from 1.97 GHz to 2.92 GHz, those measured show that the antenna covers a bandwidth of 36.7%, operating from 1.96 GHz to 2.84 GHz. In addition, the isolation between the antenna ports, that in the numerical results, is higher than 32 dB across the entire frequency band and keeps higher than 29 dB in the measurement results. The slight discrepancies observed between the computed and measured results are mainly due to the fabrication tolerance and the soldering of the SMA connectors employed to excite the antenna.

Since the antenna is symmetrical the radiation patterns related with Port 1 and Port 2 are similar. So, for the sake of brevity only the radiation patterns for Port 1 at 2, 2.4, and 2.8 GHz are illustrated in Figure 13. From these diagrams it can be observed that the main beams are always in the broadside direction without unwanted tilting or splitting. In addition, the measured cross-polarization levels in both *xz*-plane and *yz*-plane are of about 30 dB lower with respect to the copolarization levels across the entire operating frequency band, while the front-to-back ratios maintain in the range of 25±3 dB. Finally, the gain and the radiation efficiency presented in Figure 14 show that the antenna achieves a stable gain higher than 8 dBi with an average radiation efficiency of 84%.

The comparisons of the measured performances of the proposed antenna and of those having dual-polarization

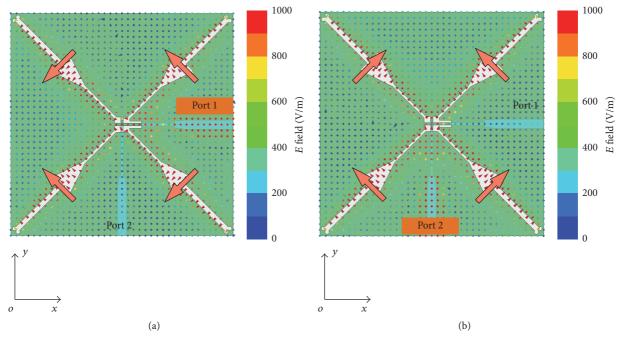


FIGURE 10: Electric-field distributions of the proposed antenna for (a) Port 1 and (b) Port 2.

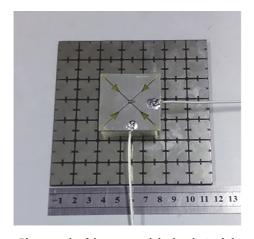


Figure 11: Photograph of the proposed dual-polarized slot antenna.

characteristics reported in literature [1–4, 8, 11, 13, 17] are listed in Table 2. As it can be observed, the proposed antenna exhibits a wider impedance bandwidth ( $|S_{11}| < -10 \, \mathrm{dB}$  or VSWR < 2) than other referenced designs listed in Table 2, except for the designs in [8, 11]. Notably, the antenna profile of our design is only  $0.13\lambda_c$ , which is lower than that of designs reported in [8, 11]. Besides, the proposed antenna exhibits stable gain (>8 dB) and desirable electric isolation (>29 dB), whose results are good enough for many wireless communication applications.

#### 4. Conclusion

A wideband dual-polarized slot antenna excited by two stepped microstrip feedlines has been presented. An AMC surface, acting as reflector, has been employed to drastically

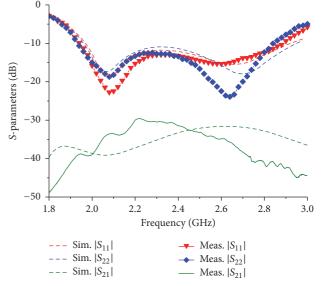
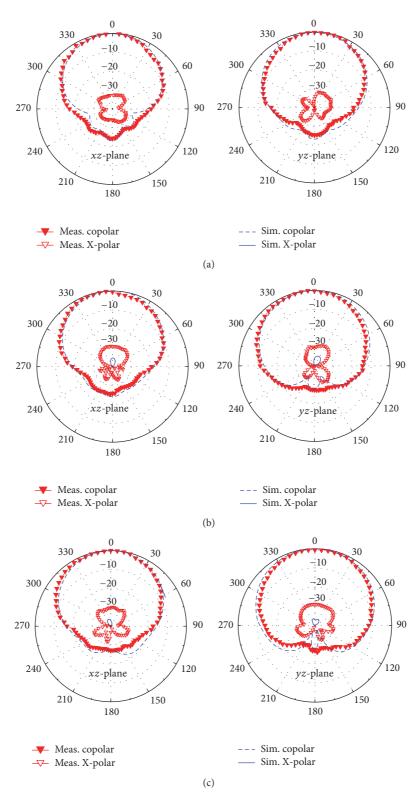


FIGURE 12: Measured and simulated *S*-parameters of the proposed antenna.

reduce the profile of the proposed antenna. The realized prototype exhibits good performances in terms of wide operating band, high electrical isolation, low back side lobes, and stable antenna gain, meaning that it appears a good candidate to be employed in radio base stations for WLAN/WIMAX and LTE applications.

### **Competing Interests**

The authors declare that there is no conflict of interests regarding the publication of this paper.



FIGURE~13:~Radiation~patterns~for~Port~1~of~the~proposed~antenna~(a)~2~GHz,~(b)~2.4~GHz,~and~(c)~2.8~GHz.

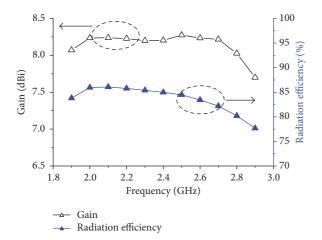


FIGURE 14: Measured gain and radiation efficiency of the proposed antenna.

Table 2: Comparisons of various dual-polarized antennas.

| Ref. | BW, % | Height, $\lambda_c$ | Isolation, dB | Gain, dBi |
|------|-------|---------------------|---------------|-----------|
| [1]  | 14.5  | 0.09                | >40           | Around 7  |
| [2]  | 21.3  | 0.11                | >34           | /         |
| [3]  | 34.9  | 0.19                | >40           | 8.7-9.1   |
| [4]  | 26.0  | 0.11                | >25           | Around 10 |
| [8]  | 47.0  | 0.18                | >37           | >8        |
| [11] | 67.6  | 0.23                | >36           | 6.6-9.6   |
| [13] | 28.9  | 0.15                | >30           | Around 7  |
| [17] | 31.2  | 0.15                | >30           | /         |
| Pro. | 36.7  | 0.13                | >29           | >8        |

 $<sup>\</sup>lambda_c$  is the wavelength at the center frequency of the working band.

#### Acknowledgments

This work was supported by the National Natural Science Foundation of China (no. 61501340).

#### References

- [1] T.-W. Chiou and K.-L. Wong, "Broad-band dual-polarized single microstrip patch antenna with high isolation and low cross polarization," *IEEE Transactions on Antennas and Propagation*, vol. 50, no. 3, pp. 399–401, 2002.
- [2] S. Gao and A. Sambell, "Dual-polarized broad-band microstrip antennas fed by proximity coupling," *IEEE Transactions on Antennas and Propagation*, vol. 53, no. 1, pp. 526–530, 2005.
- [3] J.-J. Xie, Y.-Z. Yin, J.-H. Wang, and X.-L. Liu, "Wideband dual-polarised electromagnetic patch antenna with high isolation and low cross-polarisation," *IET Electronics Letters*, vol. 49, no. 3, pp. 171–173, 2013.
- [4] H.-W. Lai and K.-M. Luk, "Dual polarized patch antenna fed by meandering probes," *IEEE Transactions on Antennas and Propagation*, vol. 55, no. 9, pp. 2625–2627, 2007.
- [5] Z.-Y. Zhang, S. Li, S.-L. Zuo, J.-Y. Zhao, X.-D. Yang, and G. Fu, "Dual-polarized crossed bowtie dipole array for wireless communication applications," *International Journal of Antennas and Propagation*, vol. 2014, Article ID 349516, 8 pages, 2014.

- [6] M. Ciydem, "Isolation enhancement in wideband dual-polarised suspended plate antenna with modified T-type probes," *Electronics Letters*, vol. 50, no. 5, pp. 338–339, 2014.
- [7] Y. Liu, H. Yi, F.-W. Wang, and S.-X. Gong, "A novel miniaturized broadband dual-polarized dipole antenna for base station," *IEEE Antennas and Wireless Propagation Letters*, vol. 12, pp. 1335–1338, 2013.
- [8] K. M. Mak, X. Gao, and H. W. Lai, "Low cost dual polarized base station element for long term evolution," *IEEE Transactions on Antennas and Propagation*, vol. 62, no. 11, pp. 5861–5865, 2014.
- [9] Y.-X. Guo, K.-M. Luk, and K.-F. Lee, "Broadband dual polarization patch element for cellular-phone base stations," *IEEE Transactions on Antennas and Propagation*, vol. 50, no. 2, pp. 251–253, 2002.
- [10] R. Caso, A. A. Serra, M. Rodriguez-Pino, P. Nepa, and G. Manara, "A wideband slot-coupled stacked-patch array for wireless communications," *IEEE Antennas and Wireless Propagation Letters*, vol. 9, pp. 986–989, 2010.
- [11] Q. Xue, S. W. Liao, and J. H. Xu, "A differentially-driven dual-polarized magneto-electric dipole antenna," *IEEE Transactions on Antennas and Propagation*, vol. 61, no. 1, pp. 425–430, 2013.
- [12] Y. Luo and Q.-X. Chu, "Oriental crown-shaped differentially fed dual-polarized multidipole antenna," *IEEE Transactions on Antennas and Propagation*, vol. 63, no. 11, pp. 4678–4685, 2015.
- [13] Y.-X. Guo, K.-W. Khoo, and L. C. Ong, "Wideband dual-polarized patch antenna with broadband baluns," *IEEE Transactions on Antennas and Propagation*, vol. 55, no. 1, pp. 78–83, 2007.
- [14] X. Jiang, Z. Zhang, Y. Li, and Z. Feng, "A wideband dual-polarized slot antenna," *IEEE Antennas and Wireless Propagation Letters*, vol. 12, pp. 1010–1013, 2013.
- [15] D. Sievenpiper, L. Zhang, R. F. J. Broas, N. G. Alexöpolous, and E. Yablonovitch, "High-impedance electromagnetic surfaces with a forbidden frequency band," *IEEE Transactions on Microwave Theory and Techniques*, vol. 47, no. 11, pp. 2059–2074, 1999.
- [16] A. Foroozesh and L. Shafai, "Application of combined electricand magnetic-conductor ground planes for antenna performance enhancement," *Canadian Journal of Electrical and Computer Engineering*, vol. 33, no. 2, Article ID 4621833, pp. 87–98, 2008.
- [17] R. N. Lian, Z. D. Wang, Y. Z. Yin, J. J. Wu, and X. Y. Song, "Design of a low-profile dual-polarized stepped slot antenna array for base station," *IEEE Antennas and Wireless Propagation Letters*, vol. 15, pp. 362–365, 2016.
- [18] D. Caratelli, R. Cicchetti, G. Bit-Babik, and A. Faraone, "Circuit model and near-field behavior of a novel patch antenna for WWLAN applications," *Microwave and Optical Technology Letters*, vol. 49, no. 1, pp. 97–100, 2007.

Hindawi Publishing Corporation International Journal of Antennas and Propagation Volume 2016, Article ID 6075680, 20 pages http://dx.doi.org/10.1155/2016/6075680

#### Review Article

## Dielectric Resonator Antennas: Basic Concepts, Design Guidelines, and Recent Developments at Millimeter-Wave Frequencies

#### S. Keyrouz<sup>1</sup> and D. Caratelli<sup>1,2</sup>

<sup>1</sup>The Antenna Company, High Tech Campus 41, Eindhoven, Netherlands

Correspondence should be addressed to S. Keyrouz; shady.keyrouz@antennacompany.com

Received 18 July 2016; Revised 18 September 2016; Accepted 22 September 2016

Academic Editor: Ahmed T. Mobashsher

Copyright © 2016 S. Keyrouz and D. Caratelli. This is an open access article distributed under the Creative Commons Attribution License, which permits unrestricted use, distribution, and reproduction in any medium, provided the original work is properly cited.

An up-to-date literature overview on relevant approaches for controlling circuital characteristics and radiation properties of dielectric resonator antennas (DRAs) is presented. The main advantages of DRAs are discussed in detail, while reviewing the most effective techniques for antenna feeding as well as for size reduction. Furthermore, advanced design solutions for enhancing the realized gain of individual DRAs are investigated. In this way, guidance is provided to radio frequency (RF) front-end designers in the selection of different antenna topologies useful to achieve the required antenna performance in terms of frequency response, gain, and polarization. Particular attention is put in the analysis of the progress which is being made in the application of DRA technology at millimeter-wave frequencies.

#### 1. Introduction

The release of the unlicensed 60 GHz band and the development of 5G technologies aimed at increasing data rate on wireless communication network by a factor of 100 [1] will impose stinging specifications (large bandwidth, high gain, small size, and temperature independent performance) on the design of the radio frequency (RF) electronics. Various front-end antenna solutions relying on monopoles, dipoles, and patch antennas have been proposed for millimeter-wave applications. These antennas are characterized by small size, low weight, and low cost and can be easily integrated on chip. However, unless advanced design solutions based on the integration of suitable dielectric superstrates or lensing structures are adopted, these antennas typically suffer from reduced radiation efficiency and narrow impedance bandwidth due to the effect of lossy silicon substrate materials. On the other hand, dielectric resonator antennas (DRAs) are promising candidates to replace traditional radiating elements at high frequencies, especially for applications at millimeter waves and beyond. This is mainly attributed to the fact that DRAs

do not suffer from conduction losses and are characterized by high radiation efficiency when excited properly.

DRAs rely on radiating resonators that can transform guided waves into unguided waves (RF signals). In the past, these antennas have been mainly realized by making use of ceramic materials characterized by high permittivity and high Q factor (between 20 and 2000). Currently, DRAs made from plastic material (PolyVinyl Chloride (PVC)) are being realized. The main advantages of DRAs are summarized as follows:

(i) The size of the DRA is proportional to  $\lambda_0/\sqrt{\varepsilon_r}$  with  $\lambda_0=c/f_0$  being the free-space wavelength at the resonant frequency  $f_0$  and where  $\varepsilon_r$  denotes the relative permittivity of the material forming the radiating structure. As compared to traditional metallic antennas whose size is proportional to  $\lambda_0$ , DRAs are characterized by a smaller form factor especially when a material with high dielectric constant  $(\varepsilon_r)$  is selected for the design.

<sup>&</sup>lt;sup>2</sup>Tomsk Polytechnic University, 84/3 Sovetskaya Street, Tomsk, Russia

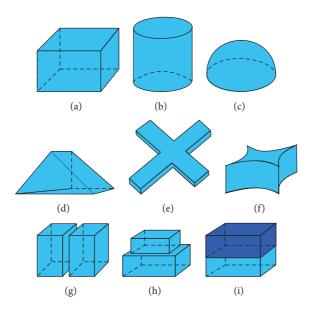


FIGURE 1: Different radiating structures used for dielectric resonator antennas (DRAs).

- (ii) Due to the absence of conducting material, the DRAs are characterized by high radiation efficiency when a low-loss dielectric material is chosen. This characteristic makes them very suitable for applications at very high frequencies, such as in the range from 30 GHz to 300 GHz. As a matter of fact, at these frequencies, traditional metallic antennas suffer from higher conductor losses.
- (iii) DRAs can be characterized by a large impedance bandwidth if the dimensions of the resonator and the material dielectric constant are chosen properly.
- (iv) DRAs can be excited using different techniques which is helpful in different applications and for array integration.
- (v) The gain, bandwidth, and polarization characteristics of a DRA can be easily controlled using different design techniques.

The main target of this paper is to present an up-to-date review study summarizing the most relevant techniques to control circuital characteristics and radiation properties of DRAs. In this way, guidance will be provided to RF frontend designers to achieve the required antenna performance in terms of gain, bandwidth, and polarization. Different geometries of radiating resonators will be discussed first, turning then our attention to advantages and disadvantages of different feeding techniques proposed so far in the literature. Various methodologies that have been used to enhance the impedance bandwidth and the antenna gain will be explored. Furthermore, different techniques to achieve circular polarization are summarized. Finally, the most recent implementation of DRAs on chip and off chip will be presented.

#### 2. Dielectric Resonators

By using a suitable excitation technique, any dielectric structure can become a radiator at defined frequencies. It is to be

noticed that, for a given resonant frequency, the size of the dielectric resonator is inversely proportional to the relative permittivity of the constitutive material. The lowest dielectric constant material adopted in DRA design is reported in [2–4], where commodity plastics with relative dielectric constant smaller than 3 have been utilized for the realization of supershaped DRAs.

The basic principle of operation of dielectric resonators is similar to that of the cavity resonators [5] and is thoroughly discussed in literature. The most two popular radiating dielectric resonators are the cylindrical and the rectangular ones. They will be reviewed in this section. Design equations to calculate the relevant resonant frequencies are given. More complex dielectric resonators, such as the spherical/hemispherical, cross-shaped, and supershaped (see Figure 1) ones, will be also discussed in this section.

2.1. Cylindrical DRA. Cylindrical DRAs have been studied extensively in literature. Figure 2 shows the three-dimensional view (a) and the cross-sectional view (b) of a probe-fed cylindrical DRA. The antenna consists of a cylindrical dielectric resonator (DR) with height h, radius a, and dielectric constant  $\epsilon_r$ . The DR is placed on top of a ground plane and fed by a coaxial connector. The main advantages of the cylindrical DRA consist in the ease of fabrication and the ability to excite different modes.

The resonant frequency of the modes supported by a cylindrical DRA can be calculated using the following equations [6]:

$$f_{\text{TE}_{npm}} = \frac{c}{2\pi\sqrt{\epsilon_r \mu_r}} \sqrt{\left(\frac{X_{np}}{a}\right)^2 + \left(\frac{(2m+1)\pi}{2h}\right)^2}, \quad (1)$$

$$f_{\text{TM}_{npm}} = \frac{c}{2\pi\sqrt{\epsilon_r \mu_r}} \sqrt{\left(\frac{X'_{np}}{a}\right)^2 + \left(\frac{(2m+1)\pi}{2h}\right)^2}, \quad (2)$$

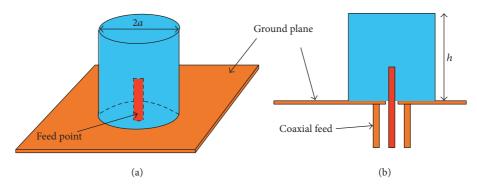


FIGURE 2: Three-dimensional (a) and cross-sectional view (b) of the probe-fed cylindrical DRA.

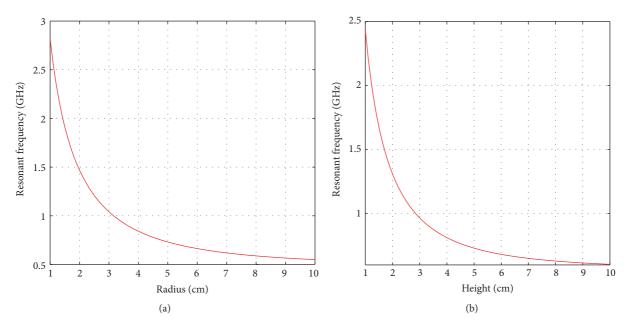


FIGURE 3: Resonant frequency as a function of the radius (a) and height (b) of a cylindrical DRA with relative permittivity  $\epsilon_r = 10$ .

Table 1: Roots of the Bessel functions of the first kind,  $X_{np}$ .

| P     |       |       | n      |        |        |
|-------|-------|-------|--------|--------|--------|
|       | n = 1 | n = 2 | n = 3  | n = 4  | n = 5  |
| p = 0 | 2.404 | 5.520 | 8.653  | 11.791 | 14.930 |
| p = 1 | 3.831 | 7.015 | 10.173 | 13.323 | 16.470 |
| p = 2 | 5.135 | 8.417 | 11.619 | 14.795 | 17.959 |
|       |       |       |        |        |        |

TABLE 2: Roots of the first-order derivative of the Bessel functions of the first kind,  $X'_{np}$ .

| ħ     |       |       | n      |        |        |
|-------|-------|-------|--------|--------|--------|
| Р     | n = 1 | n = 2 | n = 3  | n = 4  | n = 5  |
| p = 0 | 3.831 | 7.015 | 10.173 | 13.323 | 16.470 |
| p = 1 | 1.841 | 5.331 | 8.536  | 11.706 | 14.863 |
| p = 2 | 3.054 | 6.706 | 9.969  | 13.170 | 16.347 |

where  $X_{np}$  and  $X'_{np}$  denote the roots of the Bessel functions of the first kind and of the relevant first-order derivatives, respectively (see Tables 1 and 2).

The impact of the geometrical parameters of a cylindrical DRA (radius and height) as well as of the relative dielectric constant  $(\epsilon_r)$  on the resonant frequency is investigated. Equation (2) is used to calculate the resonant frequency of the fundamental model  $\text{TM}_{110}$  of the cylindrical DRA. Figure 3 shows the resonant frequency as a function of the DRA's radius (see Figure 3(a)) and as a function of the DRA's height (see Figure 3(b)). The dielectric constant used to calculate the

resonant frequencies is set to  $\epsilon_r = 10$ . It is indicated in the figures that the resonant frequency decreases by increasing either the radius or the height or both of them simultaneously.

Figure 4 shows the effect of the relative dielectric constant  $(\epsilon_r)$  on the resonant frequency. It can be noticed that the resonant frequency of the fundamental mode decreases by increasing the dielectric constant of the DRA. This behavior is the most important characteristic of the DRA since it allows decreasing the size of the DRA by increasing its dielectric constant. It is to be noted that the impedance bandwidth is inversely proportional to the relative permittivity of the DR.

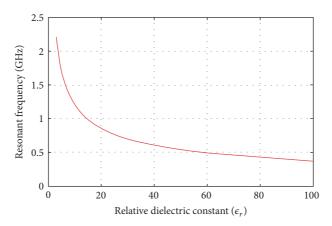


FIGURE 4: Resonant frequency of a cylindrical DRA with radius a = 2.5 cm and height h = 5 cm as a function of the relative dielectric constant.

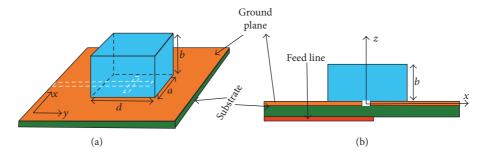


FIGURE 5: Three-dimensional view (a) and cross-sectional view (b) of an aperture-fed rectangular DRA.

Therefore, the use of materials with high dielectric constant can result in a narrowband antenna behavior.

2.2. Rectangular DRA. Figure 5 shows the three-dimensional and cross-sectional views of a rectangular DRA fed by a slot aperture. The rectangular DRA consists of a rectangular dielectric resonator with relative dielectric constant  $\epsilon_r$ . The dimensions of the rectangular DR are  $a \times d \times h$  (width  $\times$  length  $\times$  height).

The main advantage of the rectangular DRA is that it is characterized by three independent geometrical dimensions, a, b, and d (see Figure 5(a)); this offers more design flexibility as compared to the cylindrical DRA. Furthermore, the rectangular DRA is characterized by low cross-polarization level as compared to the cylindrical DRA [7].

The dielectric waveguide model [8] is used to analyze the rectangular DRA. When the DRA is mounted on a ground plane, TE modes are excited. The resonant frequency of the fundamental mode,  $TE_{111}$ , is calculated by means of the following equations [9]:

$$f_0 = \frac{c}{2\pi\sqrt{\epsilon_r}}\sqrt{k_x^2 + k_y^2 + k_z^2},$$
 
$$k_x = \frac{\pi}{a},$$
 
$$k_z = \frac{\pi}{2b},$$

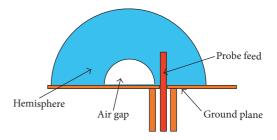


FIGURE 6: Probe-fed hemispherical DRA with an air gap for bandwidth enhancement as suggested in [10].

$$d = \frac{2}{k_y} \tanh\left(\frac{k_{y0}}{k_y}\right), \quad k_{y0} = \sqrt{k_x^2 + k_z^2},$$
(3)

where  $\epsilon_r$  is the relative dielectric constant of the material forming the resonator.

2.3. Hemisphere and Cross-Shaped and Supershaped DRAs. In this section attention is put also on the hemisphere and the cross-shaped and the supershaped DRAs.

A probe-fed hemispherical DRA with an air gap of hemispherical shape between the dielectric structure and the ground plane is presented in [10] and is shown in Figure 6. It has been found that, by incorporating this gap, the DRA achieves an impedance bandwidth which is nearly twice that

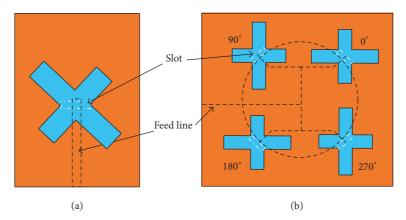


FIGURE 7: Cross-shaped DRA (a) and a sequentially fed cross-shaped DRA array (b) as suggested in [12].

without an air gap. A dedicated section summarizing the most relevant techniques to improve the impedance bandwidth will be presented later in the paper.

The authors in [11] demonstrated for the first time the possibility of using glass dielectric resonators as light covers. A dual-band hollow and solid hemispherical glass DRAs are presented in [11]. The hollow hemisphere is excited by a slot while the solid one is a probe-fed DRA. By taking advantage of the transparency of the glass an LED was inserted into the air gap through the ground plane resulting in a DRA that can be used as a light cover. It has been demonstrated in the paper that the insertion of an LED inside the DRA (for both solid and hollow DRA) has a negligible effect on the antenna performance.

The cross-shaped dielectric resonator is mainly suggested to design circularly polarized antenna. A cross-shaped DRA as suggested in [12] is shown in Figure 7(a). To achieve a wideband circular polarization bandwidth the cross DRA should be rotated 45° with respect to the slot and the length of the arms should be optimized [12]. The individual cross-shaped DRA supports a circular polarization bandwidth of 5% with an axial ratio less than 3 dB. In addition to the circular polarization (CP), the measured impedance bandwidth of the cross DRA reaches 16% at 10 dB return-loss level [12].

In order to achieve higher impedance bandwidth and larger circular polarization bandwidth, a sequentially fed array of cross DRA is proposed in the same paper as shown in Figure 7(b). In this way, the impedance bandwidth and the CP bandwidth are increased to 25% and 15%, respectively.

Recently, a very similar concept has been adopted in [13] to design an mm-wave DRA. The presented design consists of a four-by-four array of sequentially fed rectangular dielectric resonators excited by a cross-shaped slot in order to achieve circular polarization. The simulated impedance bandwidth extends from 26.9 GHz to 33.7 GHz, whereas the simulated axial ratio bandwidth at 3 dB level extends from 24.1 GHz to 31.1 GHz.

A plastic-based supershaped DRA has been presented in [2–4] and is shown in Figure 8. The reported impedance bandwidth is extended to 74% by using a supershaped dielectric resonator.

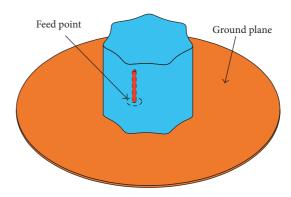


FIGURE 8: Probe-fed supershaped DRA [2].

The main advantage of the presented supershaped DRA is that it uses plastic (PolyVinyl Chloride (PVC)) as dielectric material which makes it very cost effective and easily manufacturable.

In addition to the basic dielectric resonators that have been discussed in this section, numerous attempts have been performed to combine different dielectric resonators together in order to optimize antenna performance. Figures 1(d), 1(e), and 1(f) show different configurations of combined DRAs. The advantages of combining different DRs will be presented later in the paper but first different feeding structures of DRAs will be discussed in the following section.

#### 3. Feeding Structures

One of the main advantages of DRA technology is that various feeding techniques can be used to excite the radiating modes of a dielectric resonator.

3.1. Probe-Fed DRA. The probe-fed DRA is among the first reported DRAs [10, 14] and is shown in Figure 9. In this configuration, the DR is directly disposed on the ground plane and is excited by a coaxial feed through the substrate. The coaxial probe can either penetrate the DR (see Figure 9(a)) or can be placed adjacent to the DR as shown in Figure 9(b).

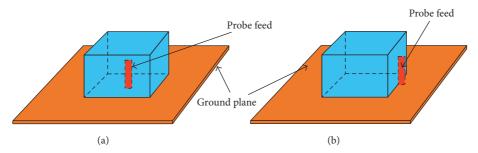


FIGURE 9: Probe-fed rectangular DRA.

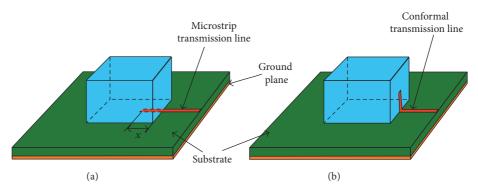


FIGURE 10: Three-dimensional view of conventional (a) and conformal (b) microstrip transmission line feeding networks.

By optimizing length and position of the feeding probe, the input impedance of the DRA can be tuned [15] and, consequently, the resonance frequency can be controlled. The main benefit associated with a probe penetrating the DRA (see Figure 9(a)) is that it provides high coupling to the DR which, in turn, results in high radiation efficiency. The main drawback of such configuration is that a hole needs to be drilled in the DRA. The dimensions of the drilled hole need to match the dimensions of the probe (length and radius) otherwise the effective dielectric constant of the resonator will be affected, this causing a shift in the resonance frequency of the antenna. It is to be noticed, furthermore, that drilling a hole in the DR complicates the manufacturing process and makes it more expensive.

A reduced manufacturing complexity is achieved by placing the excitation probe adjacent to the DR (see Figure 9(b)). This technique is cost-effective but results in a smaller coupling to the DR, which eventually affects the radiation characteristics of the structure.

For high-frequency applications where the antenna is manufactured on a Printed Circuit Board (PCB), or is directly integrated on chip, probe-fed DRAs are not practical.

3.2. Microstrip Transmission Line-Fed DRA. Another way to feed the DRA is by using printed transmission lines. Figure 10 shows the three-dimensional view of a rectangular DRA fed by a microstrip line (see Figure 10(a)) and by a conformal transmission line (see Figure 10(b)). In conventional microstrip line-fed DRAs, the dielectric resonator is directly placed on the transmission line that is printed on the PCB substrate. One of the first reported DRAs fed by

a microstrip line is reported in [16]. It has been shown in [16] that the overlap distance x (see Figure 10(a)) determines the coupling strength and the specific mode that is excited by the transmission line. The strongest coupling occurs when x is slightly shorter than one-quarter of a dielectric wavelength of the resonance frequency. The main drawback of the microstrip transmission line feed is that the feeding line is not isolated from the dielectric resonator which can affect the radiation performance of the DRA. In addition, when placing the dielectric resonator directly on the top of a transmission line, an undesired air gap is created between the resonator and the substrate of the PCB.

In a conformal transmission line-fed DRA, the resonator is placed directly on the PCB substrate and the feeding microstrip is bent over the resonator as shown in Figure 10(b). By using this configuration, the input transmission line is integrated with the DR without creating an air gap. The shape of the transmission line that is bent over the dielectric resonator can be optimized to improve the performance of the DRA. As an example, a conformal elliptical patch that feeds an U-shaped DRA is suggested in [17] where an impedance bandwidth of 72% is achieved.

3.3. Coplanar-Waveguide-Fed DRA. The coplanar waveguide excitation was first introduced in [18], where a coplanar waveguide (CPW) circular-loop network that feeds a cylindrical DRA is presented. A rectangular DRA fed by a similar structure is shown in Figure 11(a). The main advantage of the CPW excitation is that the coupling slot that is underneath the dielectric resonator can be modified to optimize the performance of the DRA. In [19] the circular-loop feeding

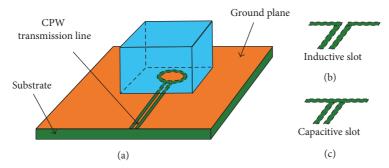


FIGURE 11: Rectangular DRA fed by a CPW circular-loop network (a). Inductive slot feed (b). Capacitive slot feed (c).

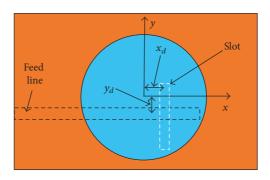


FIGURE 12: Top view of an aperture-coupled hemispherical DRA as presented in [20].

network is replaced by an inductive slot (see Figure 11(b)) and by a capacitive slot (see Figure 11(c)) in combination with a hemispherical DRA. It has been shown that the capacitive slot provides an additional resonance which results in a dual-band behavior, with two resonances associated with the DR and the feeding slot itself, respectively. CPW feeding structures are widely used for millimeter-wave applications especially when the DRA is integrated in a system on chip (SoC). As a matter of fact, by using CPW transmission lines, it is possible to achieve high antenna efficiency since the ground plane separates the dielectric resonator from the lossy silicon substrate.

3.4. Slot-Fed DRA. The most popular feeding technique for DRAs is via a slot in the ground plane. This excitation method is known as aperture coupling. The guided wave propagating along the transmission line is coupled, through the slot, to the resonant modes of the DR.

Figure 12 shows the top view of an aperture-coupled hemispherical DRA as presented in [20]. The effect of the slot displacements  $x_d$  and  $y_d$  (see Figure 12) from the center of the DRA is investigated in [20]. It has been found that best resonance (impedance matching) is achieved when the DR is perfectly centered on top of the slot ( $x_d = y_d = 0$ ). The main advantage of this method is that it avoids a direct electromagnetic interaction between the feed line and the DRA as indicated in Figure 13. By using this topology, the spurious radiation from the feeding network can be reduced, thus enhancing the polarization purity of the DRA. The drawback of such excitation method is that the slot length

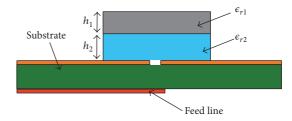


FIGURE 13: Cross-sectional view of a two-layer rectangular DRA for size reduction as suggested in [21].

should be around  $\lambda/2$  which is a challenge to realize at lower frequencies while keeping the size of the DRA compact.

#### 4. DRA Size Reduction Methods

The two most common techniques to minimize the size of a DRA are either to use material with high dielectric constant or to insert a metal plate in the symmetry plane of the DR. These techniques are reviewed in this section.

4.1. High Relative Dielectric Constant ( $\epsilon_r$ ). In general, the size of the DRA is inversely proportional to the dielectric constant ( $\epsilon_r$ ) of the resonator as seen in Figure 4. So in order to decrease the size of the DRA, a material with a high dielectric constant can be chosen; however, this should be carefully done since the impedance bandwidth can be affected negatively by the choice of the dielectric material. In [9] a low-profile rectangular DRA  $(0.026\lambda_0)$  with very high relative

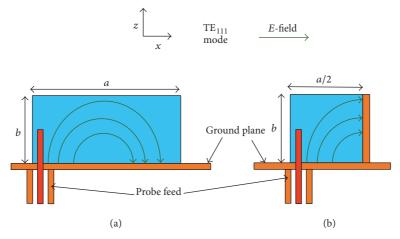


FIGURE 14: Cross-sectional view of a probe-fed rectangular DRA (a) and its miniaturized version (b) by placing a conducting plate at x = a/2.

permittivity ( $\epsilon_r = 100$ ) is presented. It is demonstrated that, even when using such a high dielectric constant material, a reasonable impedance bandwidth of 1.1% to 3.3% can be achieved.

To overcome the limitation related to reduced bandwidth a multilayer DRA topology can be adopted. By optimizing the dielectric constant and height of each layer, the DRA parameters (size, impedance bandwidth, and gain) can be controlled and optimized. Figure 13 shows the cross-sectional view of a two-layer rectangular DRA as suggested in [21]. This configuration offers additional degrees of freedom ( $\epsilon_{r2}$  and  $h_2$ ) in the design of a DRA as compared to the single-layer antenna configuration. Using this methodology, the authors in [21] were able to design a low-profile rectangular DRA (having height of  $0.1\lambda_0$ ) with an impedance bandwidth of 40% and an average gain of 9 dBi.

4.2. Metal Plate along Symmetry Plane. The second design technique to minimize the size of a DRA consists in the integration of metal plates along the relevant symmetry planes, as it easily follows from the application of image theory [22]. Figure 14(a) shows the cross-sectional view of a probe-fed rectangular DRA with length a and height b. Its corresponding miniaturized version is shown in Figure 14(b).

As indicated in the figure, the size of the DRA can be halved by placing a conducting plate along the central cross-section of the dielectric resonator at x=a/2. The effect of the miniaturization on the resonant frequency and the impedance bandwidth of a DRA was investigated in [23] and the results are summarized in Table 3. The dimensions, a and b, listed in the table are specified in accordance with Figure 14. One can clearly notice that the insertion of the metal plate allows halving the volume of the DRA but, at the same time, results in a reduction of the available impedance bandwidth by a factor of three. It should be mentioned that when a conducting plate is used, the position as well as the length of the feeding probe should be fine-tuned in order to match the input impedance of the antenna at the desired resonant frequency.

TABLE 3: Effect of the miniaturization of a rectangular DRA [23].

| a<br>(mm) | b<br>(mm) | Volume<br>(cm³) | $\epsilon_r$ | Conducting plate | $f_0$ (GHz) | Impedance<br>bandwidth |
|-----------|-----------|-----------------|--------------|------------------|-------------|------------------------|
| 88        | 40        | 70.4            | 12           | No               | 1.22        | 16%                    |
| 44        | 40        | 35.2            | 12           | Yes              | 0.918       | 5.4%                   |

TABLE 4: Measured gain of a DRA with and without SMSH [25].

| Frequency (GHz)         | 5.8 | 5.9 | 6.0 | 6.1 | 6.2 |
|-------------------------|-----|-----|-----|-----|-----|
| Gain without SMSH (dBi) | 1.4 | 2.8 | 3.8 | 4.2 | 2.7 |
| Gain with SMSH (dBi)    | 7.9 | 8.8 | 8.2 | 8.2 | 6.9 |

Similarly, the size of a cylindrical DRA can be reduced by 75% by placing a Perfect Electric Conductor (PEC) and a Perfect Magnetic Conductor (PMC) at the symmetry planes of cylinder, as shown in [24].

#### 5. DRA Gain Enhancement Methods

The most straightforward approach to increase the gain of a DRA is by arraying individual DRAs. The gain of a DRA array increases by increasing the number of DR elements in the array. However this approach is not the main goal of this section. Attention is put here on two alternative techniques to enhance the gain of a single DRA element.

5.1. Integration of Additional Structures. An efficient way to increase the gain of a DRA relies on the integration of additional structures useful to focus the antenna radiation in one direction and increase, in this way, its gain. A straightforward example of such design approach is the surface mounted short horn (SMSH) DRA presented in [25]. A cross-sectional view of the SMSH is shown in Figure 15.

The suggested DRA consists of a slot-fed rectangular dielectric resonator with four additional inclined metallic plates used to form a horn-like structure. The effect of the SMSH structure on the DRA gain is quantified in Table 4. The figures of merit listed in the table are taken from [25].

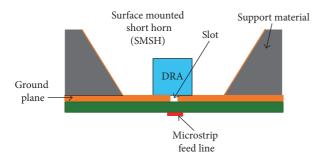


FIGURE 15: A surface mounted short horn (SMSH) configuration as suggested in [25].

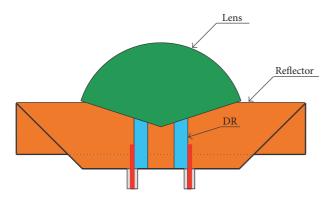


FIGURE 16: High-gain mushroom-shaped DRA structure as presented in [27].

It can be noticed that the addition of the SMSH results in a 4.4 dB increase of the antenna gain at 6 GHz. The same approach has been used in [26] where a cylindrical DRA integrated on a periodic substrate composed of circular metal strips is presented. By optimizing the distribution of the strips around the DRA a 3 dB enhancement of the antenna gain at the design frequency has been achieved.

Recently a high-gain mushroom-shaped DRA has been presented in [27]. The suggested design is shown in Figure 16 and consists of a probe-fed hollow cylindrical DRA. A spherical-cap lens is placed on top of the cylindrical DRA to increase the antenna gain. It has been shown that the addition of the lens on top of the cylinder will increase the gain by 3 dB to 5.8 dB. The front-to-back ratio is increased between 4.6 dB and 8.8 dB across the operational frequency band. In addition to the lens, the suggested cylindrical DRA is surrounded by a metal truncated-cone reflector. The measured antenna gain of the suggested DRA is larger than 10 dBi between 4.5 GHz and 9.5 GHz with a maximum of 16 dBi around 8.5 GHz.

5.2. Excitation of Higher-Order Modes. The second method to increase the gain of an individual DRA is by exciting the relevant higher-order modes, thus making the DRA electrically larger with respect to its fundamental resonant frequency. It has been shown in [28] that when the  $\text{TE}_{\delta15}$  mode of the rectangular DRA is excited, a 6 dB increase of the antenna directivity is achieved as compared with the

directivity obtained when exciting the fundamental resonant mode (TE $_{\delta11}$ ).

The design of a pattern-reconfigurable cylindrical DRA with high gain resulting from the excitation of higher-order  $\text{HEM}_{21(1+\delta)}$  modes has been reported in [29].

Recently, a cylindrical DRA with a measured peak gain of 11.6 dBi has been reported in [30]. In this design, the higher-order  ${\rm HEM}_{133}$  mode of a cylindrical dielectric resonator is excited in order to achieve the desired antenna performance.

#### 6. Circular Polarization

One of the advantages of DRAs is that their polarization can be easily controlled. In this section different techniques to design circularly polarized DRAs are reviewed.

6.1. Dual-Feed Excitation. Exciting a DRA by using two ports with a 90° phase shift is a simple but effective means for achieving circular polarization of the radiated electromagnetic field. Figure 17 shows a probe-fed cylindrical DRA relying on the mentioned approach [31]. The measured axial ratio along the broadside direction of this antenna has been reported to be 0.45 dB, thus indicating a very good circular polarization property.

The same design strategy has been applied in [32], where a cylindrical DRA is excited by two conformal microstrip transmission lines. The suggested design offers a 3 dB axial ratio bandwidth of 40%.

6.2. Single-Feed Excitation. Circularly polarized DRAs can be designed also by using a single feed placed at a location where two orthogonal modes can be excited. This technique has been applied in [33] in combination with a circular sector dielectric resonator. The probe feed is placed between the center of the sector (where the  $TM_{21\delta}$  is excited) and the edge of the sector (where the  $TM_{11\delta}$ ). A 3 dB axial ratio bandwidth of 10% has been measured for the DRA presented in [33].

In order to achieve circular polarization in slot-fed DRAs, the dielectric resonator and the feeding slot are to be properly rotated relative to each other, so that two orthogonal modes can be excited with the desired phase difference. Figure 18 shows the cross-sectional view (a) and the top view of a slot-fed rectangular DRA. As indicated in Figure 18(b), the DRA is rotated with an angle  $\phi$  with respect to the slot. When  $\phi=45^\circ$  two orthogonal modes with 90° phase differences can be excited which results in a circularly polarized pattern. This technique has been used in [34, 35] to design circularly polarized rectangular DRAs with a 3 dB axial ratio bandwidth of 1.8% and 3%, respectively. The same strategy has been used in [12] to excite the cross-shaped DRA shown in Figure 7.

A novel circularly polarized three-layer stacked DRA has been presented in [36]. Each layer is made out of a homogeneous dielectric material with relative permittivity  $\epsilon_r = 10.7$  and rotated by an angle of  $\phi = 30^\circ$  relative to the adjacent one. In this way, a 3 dB axial ratio bandwidth of 6% has been obtained, in combination with a wide impedance bandwidth of 21%.

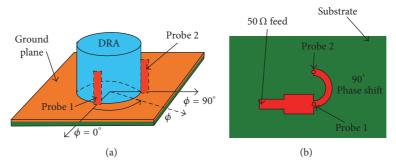


FIGURE 17: Circularly polarized dual-fed cylindrical DRA as suggested in [31].

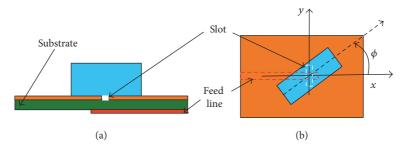


FIGURE 18: Cross-sectional view (a) and top view (b) of a rotated rectangular DRA as suggested in [34, 35].

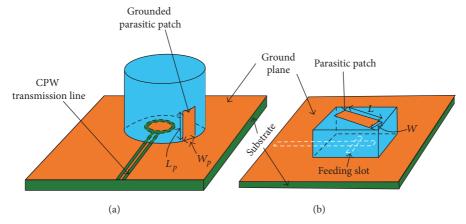


FIGURE 19: Three-dimensional view of a cylindrical DRA with a grounded parasitic patch (a) as introduced in [40] and three-dimensional view of a rectangular DRA with a parasitic patch placed on its top face (b) as presented in [39].

Instead of rotating the DR itself, location and geometry of the feeding slot can be optimized in order to achieve circular polarization. This technique has been used in [37, 38] where cross-shaped slots have been proposed for the mentioned design goal. In particular, the dual-band circularly polarized rectangular DRA presented in [37] features measured 3 dB axial ratio bandwidths of 9.7% and 20%, respectively, in the two operational frequency ranges. In [38], an offset cross-shaped slot has been used to excite a cylindrical DRA, thus achieving a measured 3 dB axial ratio bandwidth of 4.6%.

6.3. Single-Feed Excitation with Parasitic Metal Strip. Another method for exciting two orthogonal modes and enforcing a circular polarization of the radiated electromagnetic

field relies on the use of parasitic metal strips/patches attached to the surface of the dielectric resonator. The parasitic metallic element introduces an asymmetry in the DRA structure which eventually leads to the excitation of two orthogonal modes with the desired phase difference [39]. The parasitic patch can be as shown in Figure 19(a) or kept floating on the top of the DRA as shown in Figure 19(b). An example of circularly polarized rectangular DRA with floating parasitic metal strip placed on its top face is reported in [39]. By adjusting the width, W, and length, L, of the strip (see Figure 19(b)), the axial ratio of the antenna can be easily tuned. By virtue of this design approach, a 2 dB axial ratio bandwidth of 6% can be achieved.

A circularly polarized cylindrical DRA with grounded parasitic strip has been presented in [40] and shown in

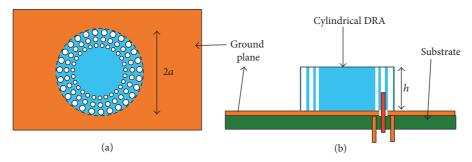


FIGURE 20: Top (a) and cross-sectional view (b) of a perforated DRA as suggested in [46].

Figure 19(a). It has been demonstrated that the location of the parasitic patch is not very critical for the purity of the circular polarization (see Figure 19(a)). On the other hand, the axial ratio of the antenna is strongly affected by the length of the patch,  $L_p$ , whereas the width of the parasitic patch,  $W_p$ , plays a none significant role. By tuning  $L_p$  and  $W_p$  the polarization properties of the DRA can be tuned. Similar conclusions have been reported in [41] where a rectangular DRA with grounded parasitic patch has been investigated.

## 7. Impedance Bandwidth Enhancement Methods of DRAs

In this section, different techniques useful to broaden the impedance bandwidth of a DRA are summarized.

7.1. Combining Different Dielectric Resonators. Dielectric resonators can be combined together to broaden the impedance bandwidth of the resulting DRA structure. Figures 1(g), 1(h), and 1(i) show different configurations of combined DRAs. By placing multiple dielectric resonators of different dimensions on top of each other (see Figure 1(h)), different modes can be excited. In this way, dual-band or broadband behavior can be achieved. By using such approach, a staircase-shaped DRA has been designed and presented in [42, 43]. A 10 dB return-loss impedance bandwidth of 36.6%, from 7.56 GHz to 10.95 GHz, has been obtained by using the three-step staircase-shaped DRA proposed in [42]. A very similar configuration consisting of a two-step staircase-shaped probe-fed DRA has been presented in [44]. The measured impedance bandwidth of the suggested design is 44% and covers a frequency range from 7.45 GHz to 11.6 GHz. Recently, a dual-band circular DRA with staircase geometry has been proposed in [45].

An alternative design approach, useful to achieve large impedance bandwidths, consists in the tapering of the permittivity distribution within the DR. This can be done either by combining multiple layers with different dielectric constants or by drilling holes of different diameters into the DR in order to taper the effective permittivity of the structure. The geometry of a perforated DRA is shown in Figure 20. This concept has been investigated in [46], where an impedance bandwidth of 26.7% ( $\epsilon_r = 10.2$ ) has been reported.

Dual-band or wide-band characteristics can be easily synthesized by exciting different resonant modes in multilayered

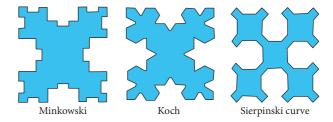


FIGURE 21: Different fractal boundary structures proposed and simulated in [50].

DRAs consisting of different dielectric laminates with properly selected permittivity. A cross-sectional view of a two-layer DRA is shown in Figure 13. It has been shown that when  $\epsilon_{r2}$  (dielectric constant of the bottom layer) is smaller than  $\epsilon_{r1}$  (dielectric constant of the top layer), an impedance bandwidth of 40% at 10 dB return-loss level can be obtained [21]. Based on these findings, the antenna impedance bandwidth can be further broadened by using an air gap ( $\epsilon_{r2}=1$ ) as bottom layer [47, 48]. Both DRAs presented in [47, 48] are fed by a tapered strip printed on one side of the dielectric resonator, the relevant impedance bandwidth being of 120% (2.6–11 GHz) and 96% (2.13–6.08 GHz), respectively.

An alternative antenna topology that can feature wide impedance bandwidth or dual-band operation is the one consisting of two dielectric resonators next to each other and separated by a gap, as shown in Figure 1(g). This design approach has been suggested in [49] where two rectangular DRs are placed on the top of edges of the feeding slot produced in the antenna ground plane. By optimizing the dimensions of the dielectric resonators, the desired dual-band or wide-band behavior can be synthesized.

7.2. Shaping the Dielectric Resonator. When shaping the dielectric resonator, different modes can be excited and, in this way, a wide impedance bandwidth achieved. A U-shaped DRA ( $\epsilon_r=9.8$ ), fed by means of a conformal elliptical patch, has been proposed in [17]. The suggested design offers a 72% impedance bandwidth in the frequency range between 3.82 GHz and 8.12 GHz.

A CPW-fed fractal DRA topology has been proposed in [50] in order to excite higher-order modes with quasi-degenerate resonant frequencies resulting in a wide impedance bandwidth. Different fractal DRAs, with Minkowski, Koch, and Sierpinski profiles, have been investigated in [50] (see Figure 21). The numerically predicted characteristics

| TABLE 5: Numerically   | Simulated | Characteristics | of | fractal-based |
|------------------------|-----------|-----------------|----|---------------|
| DRAs as Reported in [5 | 50].      |                 |    |               |

| DRA profile         | Resonant<br>frequency<br>(GHz) | Impedance<br>bandwidth<br>(MHz) | Gain<br>(dBi) |
|---------------------|--------------------------------|---------------------------------|---------------|
| Minkowski           | 6.59                           | 2870                            | 4.12          |
| Koch                | 6.8                            | 2540                            | 3.51          |
| Sierpinski<br>curve | 8.0                            | 1610                            | 1.05          |

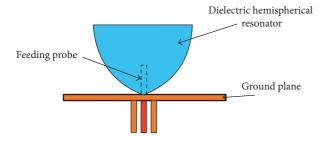


FIGURE 22: Cup-shaped inverted hemispherical DRA as suggested in [51] for impedance bandwidth enhancement.

of the mentioned fractal-based DRAs are summarized in Table 5. One can notice that the Minkowski DRA features the highest gain and largest impedance bandwidth as compared to the Koch and Sierpinski ones. The simulated results for the Minkowski DRA have been verified by experimental measurements, and in this way an impedance bandwidth of 64% (from 5.52 GHz to 10.72 GHz) has been demonstrated.

An alternative antenna topology that provides a large impedance bandwidth is the supershaped DRA shown in Figure 8. By optimizing the shape of the DRA an impedance bandwidth of 74% (from 6.7 GHz to 14 GHz) has been achieved. To this end, a plastic-based dielectric resonator having relative permittivity  $\epsilon_r = 2.73$  has been used [2].

Finally, the cup-shaped inverted hemispherical DRA design presented in [51] is to be mentioned in this survey. The configuration of the suggested DRA is shown in Figure 22. The impedance bandwidth of such DRA is 83% around the central resonant frequency of 2.3 GHz. The permittivity of the dielectric material adopted for the manufacturing of said antenna is  $\epsilon_r = 9.2$ .

7.3. Effect of the Feeding Slot. In order to increase the impedance bandwidth of an aperture-fed DRA, an annular slot can be used as proposed in [40, 52]. The configuration of the annular slot is shown in Figure 23. Using this solution, the impedance bandwidth can be increased to 18%, while using a dielectric material with relative permittivity  $\epsilon_r \simeq 10$ .

The annular slot-based approach has been extended in [53], becoming a circular aperture excited by a microstrip line with fork-like tuning stub. The configuration of the feeding network and the circular aperture are shown in Figure 24(a). In order to suppress the spurious backward radiation from the circular aperture, a hollow hemispherical backing cavity is placed beneath the tuning fork. In this way, an impedance

bandwidth of 38% has been achieved in combination with a cylindrical DRA having relative permittivity  $\epsilon_r \approx 10$ .

An alternative feeding aperture geometry which allows broadening the impedance bandwidth of a DRA is the U-shaped slot shown in Figure 24(b) [54]. This solution has the advantage of having two arms ( $L_A$  and  $L_C$ ) and, therefore, an additional degree of freedom in the design and optimization of the DRA feeding. By fine-tuning the length and the width of each arm of the slot, the impedance bandwidth and/or the polarization of the antenna can be controlled. It has been shown in [54] that the length ratio of the two arms should be close to the unity in order to achieve a beneficial enhancement of the impedance bandwidth. On the other hand, a large length ratio results in a circular polarization of the antenna.

7.4. Hybrid Approach. Hybrid design approaches rely on the combination of DRAs and radiating patch/slot antennas. By tuning the resonant frequency of the radiating patch/slot antenna in order to be close to that of the combined DRA, a wide impedance bandwidth can be achieved. A hybrid DRA resulting from the combination of a ring-shaped dielectric resonator and a circular microstrip patch, fed by a resonant slot, is presented in [55] and shown in Figure 26. The measured impedance bandwidth of this hybrid DRA is such to cover the 60 GHz unlicensed frequency band from 57 GHz to 65 GHz. Another hybrid DRA design solution relying on the combination of a monopole antenna with a ring dielectric resonator is proposed in [56] (see Figure 25(a)). Such antenna structure is characterized by three main resonances. Two of such resonances are associated with the monopole and the dielectric ring resonator, respectively, whereas a third, intermediate, resonance results from the combination of the other ones. The operational frequency band of the physical prototype presented in [56] extends from 5 GHz to 13 GHz with the magnitude of the input reflection coefficient smaller than -10 dB. Similar hybrid DRAs with the dielectric ring resonator replaced by one having conical or hemispherical (see Figure 25(b)) geometry have been presented in [57]. In particular, by using a hemispherical DR, the impedance bandwidth of the radiating structure has been increased to 126%, covering in this way the frequency range between 5 GHz and 21 GHz.

A hybrid DRA combining a rectangular DR and a CPW inductive slot (see Figure 11(b)) has been introduced in [58] in order to achieve a wide-band behavior. As a matter of fact, the resonant frequencies of the rectangular DR and of the inductive slot are designed to be 5.4 GHz and 5.8 GHz, respectively, resulting in a measured impedance bandwidth of 23%, between 4.86 GHz and 6.15 GHz.

A similar design approach is adopted in [59], where a hybrid DRA resulting from the combination of a radiating inductive slot and a cylindrical DR has been proposed. The two resonances associated with the feeding slot and the dielectric resonator, respectively, result in a dual-band behavior with measured impedance bandwidths of 9% (from 3300 MHz to 3612 MHz) and 4.8% (from 4681 MHz to 4912 MHz), respectively.

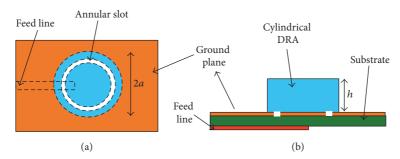


FIGURE 23: Top (a) and cross-sectional view (b) of a rectangular DRA excited by an annular slot.

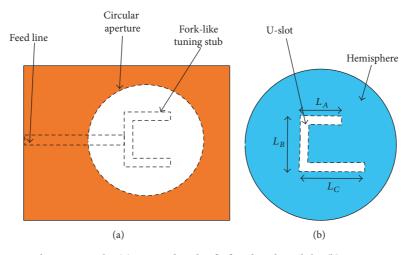


FIGURE 24: Circular aperture slot (a) as introduced in [53] and U-shaped slot (b) as investigated in [54].

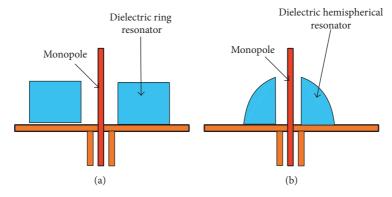


FIGURE 25: Cross-sectional view of a hybrid DRA consisting of a monopole and a ring DR (a) as suggested in [56]. Cross-sectional view of a hybrid DRA consisting of a monopole and a conical DR (b) as suggested in [57].

#### 8. Millimeter-Wave DRAs

One of the intrinsic characteristics of DRAs is the absence of conduction losses. This property makes DRAs very suitable for high-frequency applications. In this section, major and more recent advances of DRA technology at mm-wave frequencies are summarized.

8.1. Off-Chip DRA. At millimeter-wave frequencies and beyond, the size of dielectric resonators become very small, which makes the manufacturing of the DRA challenging without resorting to expensive fabrication techniques. In

order to overcome this limitation and, at the same time, improve antenna gain, electrically large DRAs exploiting higher-order modes are to be adopted.

A hybrid approach combining the excitation of higher-order modes with the radiation from the antenna feed has been presented in [55]. Figure 26 shows the top view (a) and the cross-sectional view (b) of the suggested design resulting from the combination of a ring-shaped dielectric resonator and a circular microstrip patch fed by a resonant slot. The HEM $_{15\delta}$  mode of the DRA is excited. A constant measured antenna gain of approximately 12 dBi is reported for the proposed hybrid DRA [55]. The antenna covers the 60 GHz

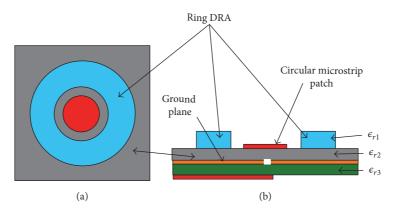


FIGURE 26: Top view (a) and cross-sectional view (b) of a hybrid ring/patch DRA as introduced in [55].

Table 6: Most Recent Advances in dielectric resonator antennas for millimeter-wave Applications.

| Reference/Year | DRA<br>topology            | Relative<br>permittivity | Feeding<br>mechanism | Technology         | Frequency<br>(GHz) | Impedance<br>bandwidth<br>(%) | Gain<br>(dBi) |
|----------------|----------------------------|--------------------------|----------------------|--------------------|--------------------|-------------------------------|---------------|
| [55]/2009      | Ring with microstrip Patch | 10                       | Coupling slot        | PCB                | 60                 | 15                            | 12            |
| [61]/2010      | Cylindrical                | 10                       | Coupling slot        | PCB                | 60                 | 24                            | 5.5           |
| [62]/2011      | Rectangular                | 10                       | Coupling slot        | PCB                | 24                 | 3.8                           | 6.3           |
| [63]/2011      | Rectangular                | 10.2                     | Capacitive slot/CPW  | PCB                | 60                 | 17.4                          | 10.2          |
| [64]/2012      | Cylindrical                | 10.2                     | Coupling slot        | PCB                | 60                 | 14.3                          | 15.7          |
| [65]/2013      | Cylindrical                | 10.2                     | Coupling slot        | PCB                | 60                 | 22.9*                         | 8.6           |
| [66]/2016      | Cylindrical                | 10.2                     | Coupling slot        | PCB                | 60                 | 10*                           | _             |
| [60]/2016      | Ring with microstrip Patch | 10.2                     | Coupling slot        | PCB                | 60                 | 12                            | 16.5          |
| [67]/2007      | Rectangular                | 48                       | CPW                  | Integrated on chip | 60                 | 2.8                           | 3.2           |
| [68]/2008      | Cylindrical                | 42                       | Folded<br>dipole/CPW | Integrated on chip | 27.7               | 9.8                           | 1             |
| [69]/2010      | Rectangular                | 38                       | H-slot/CPW           | Integrated on chip | 35                 | 12                            | 0.5           |
| [70]/2012      | Rectangular                | 10                       | Meander<br>slot/CPW  | Integrated on chip | 130                | 12                            | 2.7           |
| [70]/2012      | Two-layer<br>rectangular   | 10                       | Meander<br>slot/CPW  | Integrated on chip | 130                | 11                            | 4.7           |
| [71]/2013      | Rectangular                | 12.6                     | Coupling slot        | Integrated on chip | 60.5               | 6.1                           | 6             |
| [72]/2015      | Rectangular                | 9.8                      | E-<br>shaped/CPW     | Integrated on chip | 340                | 12                            | 10            |
| [73]/2015      | Circular                   | 12.6                     | Dipole/CPW           | Integrated on chip | 60                 | 3.78                          | 7             |

<sup>\*</sup> is estimated from graph.

unlicensed frequency band (from 57 GHz to 65 GHz) with a nearly flat gain of about 12 dBi. A similar concept has been recently proposed in [60] where the resonances of a circular patch and a ring-shaped DRA are combined together in order to achieve a broadband behavior while improving the antenna gain. An impedance matching bandwidth of 12% (from 57 GHz to 64 GHz) has been predicted numerically for such radiating structures. The simulated antenna gain is 16.5 dBi, this being reported as the largest gain level featured by a single-element DRA. The characteristics of the considered antenna are listed in Table 6.

A class of linearly and circularly polarized cylindrical DRAs fed by substrate integrated waveguides is presented in [61]. The proposed DRAs are designed in such a way as to resonate at 60 GHz. The measured impedance bandwidths are 24% and 4.5% for the linearly and circularly polarized DRAs, respectively. The performance characteristics of the linearly polarized DRA are summarized in Table 6.

The effect of the fabrication tolerances on the frequency shift of higher-order modes is investigated in [62] and listed in Table 7. It is clearly indicated in the table that higher-order modes are less affected by fabrication errors which is very

TABLE 7: Simulated frequency shift of higher order modes of a rectangular DRA due to fabrication tolerances [62].

| Fabrication error (mm) | $TE_{111}$ mode $\Delta f$ (%) | TE <sub>115</sub> mode<br>Δf (%) | TE <sub>119</sub> mode<br>Δf (%) |
|------------------------|--------------------------------|----------------------------------|----------------------------------|
| 0.01                   | 0.38                           | 0.21                             | 0.12                             |
| 0.05                   | 2.04                           | 1.00                             | 0.74                             |
| 0.1                    | 3.99                           | 1.83                             | 1.41                             |

Table 8: Comparison between the volume of DRAs excited at 24 GHz by  $TE_{111}$ ,  $TE_{115}$ , and  $TE_{119}$  modes.

| Resonant mode     | Dimensions $a \times d \times b$ (mm) | DR volume (mm³) |
|-------------------|---------------------------------------|-----------------|
| TE <sub>111</sub> | $2.5 \times 2.5 \times 2.1$           | 13.13           |
| TE <sub>115</sub> | $4.0\times4.0\times6.1$               | 97.6            |
| TE <sub>119</sub> | $4.2\times4.2\times10.7$              | 188.75          |

encouraging especially for mm-wave applications where the size of the DRA becomes very small.

The reduced sensitivity of higher-order modes to fabrication errors can be readily understood by observing that a DRA driven on a higher-order mode is physically much larger as compared to the same DRA when operating on the relevant fundamental mode. In order to highlight this point, the volume of rectangular DRAs excited at the higher-order modes  $\rm TE_{115}$  and  $\rm TE_{119}$  is compared, in Table 8, to that of a DRA operating on the  $\rm TE_{111}$  mode. Said DRAs are all designed in order to resonate at the frequency of 24 GHz. As it can be easily noticed in Table 8, the rectangular DRAs excited at  $\rm TE_{115}$  and  $\rm TE_{119}$  modes are, respectively, 7.4 and 14.4 times bulkier than the equivalent radiating structure excited at its fundamental mode. Additional characteristics of the mentioned DRA driven on the  $\rm TE_{119}$  mode are summarized in Table 6.

The gain of a single DRA element can be further increased by placing a superstrate on the top of the DR. This approach has been suggested in [63]. A cross-sectional view of the suggested antenna topology is shown in Figure 27, where a coplanar waveguide with capacitive slot (see Figure 11(c)) is used to excite the DRA. The radiating structure proposed in [63] is designed to resonate in the 60 GHz unlicensed ISM frequency band. It has been shown, in particular, that the antenna gain can be tuned by changing the distance, ds, between the superstrate and the ground plane (see Figure 27). A large impedance bandwidth of 17.4% is obtained thanks to the combined excitation of the resonances of the DRA (fundamental and higher-order modes), as well as of the feeding slot. The integration of the superstrate allows improving the antenna gain by 9 dB as compared to a conventional DRA without superstrate. In this way, a peak gain of 14.44 dBi at 60 GHz has been achieved.

An extensive study on the effect of dielectric superstrates in combination with millimeter-wave DRAs has been reported in [64]. The considered antenna topologies are shown in Figure 28. The first antenna consists of a cylindrical

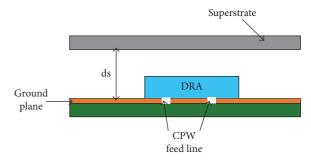


FIGURE 27: Rectangular DRA with superstrate for gain improvement as suggested in [63].

Table 9: Performance comparison between the DRAs shown in Figure 28.

|                                | Antenna 1 | Antenna 2 | Antenna 3 | Antenna 4 |
|--------------------------------|-----------|-----------|-----------|-----------|
| Impedance<br>bandwidth (%)     | 36.5      | 14.36     | 13.5      | 14.36     |
| Antenna gain<br>@ 60 GHz (dBi) | 6.9       | 7.8       | 14.36     | 15.7      |

DRA fed by a coupling slot (see Figure 28(a)). In the second antenna configuration (see Figure 28(b)) an intermediate substrate is integrated between the cylindrical DR and the coupling slot. By adding this dielectric layer, one gains an extra degree of freedom in the design that can be used to tune the frequency response of the DRA. The third antenna topology studied in [64] and illustrated in Figure 28(c) relies on the integration of a suitable superstrate above the DR. This concept was already presented by the same authors in [63]. The superstrate results in a focusing process of the electromagnetic field along the broadside direction of the DRA and, thanks to that, in an increase of the antenna gain [63]. The fourth antenna configuration investigated in [64] (see Figure 28(d)) is characterized by a square ring Frequency Selective Surface (FSS) printed on the superstrate. The FSS layer provides an effective means to further increase the realized gain of the antenna. The performances of the four antennas shown in Figure 28 are summarized in Table 9. It can be noticed that the integration of an intermediate dielectric substrate has a detrimental effect on the impedance bandwidth of the antenna. On the other hand, using a superstrate has a negligible impact on the bandwidth, while greatly improving the gain of the basic DRA structure. Finally, the FSS layer enables an additional gain enhancement of about 36%. The characteristics of the resulting antenna configuration 4 as shown in Figure 28(d) are summarized in Table 6.

A novel cylindrical DRA for 60 GHz applications has been presented in [65]. In such design, the dielectric resonator is surrounded by five periods of mushroom-like Electromagnetic Band Gap (EBG) elements in order to achieve a 3 dB antenna gain enhancement, while suppressing undesired surface waves.

The integration of a suitable FSS wall has been suggested in [66] in order to decrease the mutual coupling between

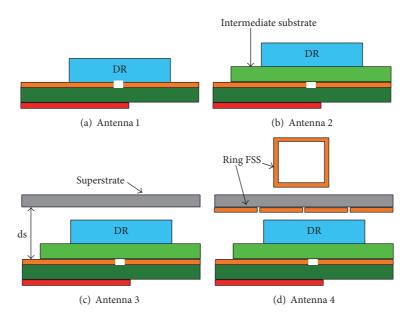


FIGURE 28: Millimeter-wave DRA topologies presented in [64].

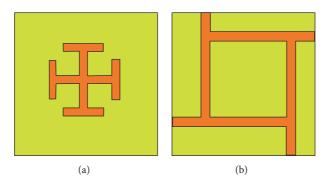


FIGURE 29: Front side (a) and back side (b) of the FSS unit cell useful to reduce the mutual coupling between DRAs [66].

DRAs. The proposed design is based on the combination of a Jerusalem-cross slot and a fan-like structure printed on the front and back side of the individual cell of the FSS, respectively, as shown in Figure 29. It has been proven that when such FSS wall is inserted between two cylindrical DRAs operating in the frequency band between 57 GHz and 63 GHz and placed 2.5 mm apart from each other, an 8 dB enhancement of the antenna isolation can be achieved in comparison to the identical structure without FSS wall.

8.2. On-Chip DRAs. In this section, different DRA topologies for SoC integration are reviewed. The direct integration of the antenna on chip eliminates the need of bond-wiring with a beneficial impact on manufacturing costs and miniaturization.

A 60 GHz rectangular DRA and a 27 GHz circular DRA integrated on silicon substrate are reported in [67, 68], respectively. By selecting the relative permittivity of the dielectric resonator in such a way as to be larger than the one of the silicon substrate ( $\epsilon_r = 11.9$ ), a reduction of the

fringing field effect and reduction of the losses in the substrate are achieved thanks to the focusing of the RF power toward the dielectric resonator. It has been shown that the gain and radiation efficiency of said antennas are maximum when the permittivity of DR is chosen to be  $40<\epsilon_r<70$ .

A cylindrical DRA printed on silicon substrate with 45% efficiency and 1 dBi gain is reported in [68], whereas a rectangular DRA printed on similar substrate is presented in [67]. The latter antenna shows an enhanced gain of 3.2 dBi at 60 GHz mainly thanks to the CPW feeding mechanism which isolates the DR from the lossy substrate and, at the same time, directs the radiation beam along the broadside direction. Detailed characteristics of the DRAs introduced in [67, 68] are listed in Table 6.

A rectangular DRA excited by a H-slot in CPW technology is presented in [69]. The DR is designed in such a way as to resonate at 35 GHz. The measured impedance bandwidth and radiation efficiency of such antenna are 12% and 48%, respectively.

Single- and two-layer DRAs realized in CMOS technology for applications at 130 GHz are presented in [70]. Said

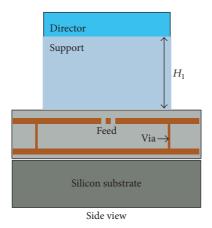


FIGURE 30: Side view of the suggested on-chip antenna as presented in [72].

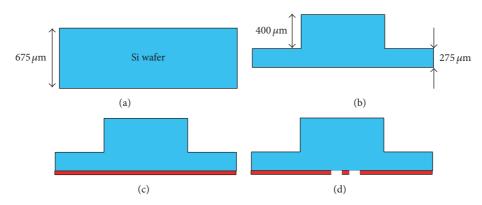


FIGURE 31: Manufacturing process of the DRA as suggested in [73]. (a) Single silicon wafer. (b)  $400 \,\mu\text{m}$  etching. (c) Back side coated with copper film. (d) Back side patterned for the feeding network.

DRAs are fed by a CPW meander slot. In this way, a gain level of 2.7 dBi and 4.7 dBi has been achieved with the single-layer DRA and the stacked one, respectively. In [71] a slot-coupled rectangular DRA for mm-wave applications is presented. The relevant characteristics are summarized in Table 6.

An on-chip DRA operating at 340 GHz is presented in [72]. A Yagi-like antenna geometry is used to achieve high gain and high radiation efficiency. In order to suppress surface waves and decouple the radiator from the lossy silicon substrate, the driver, which is a Substrate Integrated Waveguide (SIW) cavity-backed antenna, is placed underneath a coplanar waveguide E-shaped patch radiator. A dielectric resonator (DR) director is kept at a suitable distance from the feed point by means of a low-permittivity mechanical support. Figure 30 shows the cross-sectional view of the proposed antenna. The relevant relative bandwidth at 10 dB return-loss level has been simulated to be 12%, ranging from 319 GHz to 360 GHz. A peak gain of 10 dBi has been measured at the central operating frequency of 340 GHz. The characteristics of the considered antenna are summarized in Table 6.

In the aforementioned on-chip DRA designs, the two main challenges are associated with the alignment of the DR to the feed, as well as the manufacturing of the DR with

the prescribed shape. Recently, a cylindrical DRA realized starting from a single silicon wafer has been presented in [73]. The proposed DRA is a complete on-chip system since the DR is micromachined in a cost-effective way on the same silicon wafer. The relevant fabrication process is detailed in [73] (see Figure 31). The resulting antenna characteristics are summarized in Table 6.

#### 9. Conclusion

Recent developments in millimeter-wave DRA technology have been presented and discussed in detail in this survey. Furthermore, useful design guidelines have been provided to RF front-end designers in order to control circuital characteristics and radiation properties of this class of antennas.

Different feeding techniques for DRAs have been first introduced, while outlining the relevant advantages and disadvantages. Furthermore, design approaches useful to achieve size reduction of DRAs have been discussed in detail. By using high permittivity materials or by placing conducting plates along specific symmetry planes of the resonator body, one can make DRAs considerably smaller. On the other hand, the gain of a DRA can be increased either by exciting the

relevant higher-order modes (electrically large DRAs), or by integrating horn-like structures.

Particular attention has been put on hybrid design techniques which rely on the combination of DRAs and radiating patch/slot antennas. In this way, the antenna impedance bandwidth can be easily tuned in such a way as to synthesize a dual-band rather than wide-band frequency response. Circular polarization of the electromagnetic field radiated by DRAs can be achieved by using various design methodologies. In this respect, the cross-shaped feeding slot-based approach provides different benefits in terms of high coupling to the DR and additional degrees of freedom to control the polarization purity (axial ratio) of the DRA, in combination with ease of manufacturing and integration.

Finally, advances in the application of DRA technology at millimeter-wave frequencies have been presented, and the most recent implementation of on-chip DRAs and off-chip DRAs has been reviewed. It has been shown that DRAs realized on silicon substrates with standard CMOS process can be characterized by good efficiency and gain, thus proving the good potential of dielectric resonator antennas for said applications.

#### **Competing Interests**

The authors declare that they have no competing interests.

#### Acknowledgments

This study has been carried out in the framework of the research and development program running at *the Antenna Company Nederland B. V.* For further information, please visit the Web site http://www.antennacompany.com/.

#### References

- [1] TU/e to develop 5G technology with European grant, https://www.tue.nl/en/university/news-and-press/news/13-05-2016tue-to-develop-5g-technology-with-european-grant/.
- [2] M. Simeoni, R. Cicchetti, A. Yarovoy, and D. Caratelli, "Plastic-based supershaped dielectric resonator antennas for wide-band applications," *IEEE Transactions on Antennas and Propagation*, vol. 59, no. 12, pp. 4820–4825, 2011.
- [3] M. Simeoni, R. Cicchetti, A. Yarovoy, and D. Caratelli, "Super-shaped dielectric resonator antennas," in *Proceedings of the IEEE Antennas and Propagation Society International Symposium*, pp. 1–4, June 2009.
- [4] M. Simeoni, R. Cicchetti, A. Yarovoy, and D. Caratelli, "Circularly polarized supershaped dielectric resonator antennas for indoor ultra wide band applications," in *Proceedings of the IEEE International Symposium on Antennas and Propagation Society*, pp. 1–4, July 2010.
- [5] D. M. Pozar, Microwave Engineering, John Wiley & Sons, New York, NY, USA, 2012.
- [6] K. M. Luk and K. W. Leung, Eds., Dielectric Resonant Antenna, Research Studies Press, 2003.
- [7] J.-I. Moon and S.-O. Park, "Dielectric resonator antenna for dual-band PCS/IMT-2000," *Electronics Letters*, vol. 36, no. 12, pp. 1002–1003, 2000.

- [8] J. F. Legier, P. Kennis, S. Toutain, and J. Citerne, "Resonant frequencies of rectangular dlekctric resonators," *IEEE Transactions on Microwave Theory and Techniques*, vol. 28, no. 9, pp. 1031–1034, 1980.
- [9] R. K. Mongia, A. Ittibipoon, and M. Cuhaci, "Low profile dielectric resonator antennas using a very high permittivity material," *Electronics Letters*, vol. 30, no. 17, pp. 1362–1363, 1994.
- [10] K.-L. Wong, N.-C. Chen, and H.-T. Chen, "Analysis of a Hemispherical dielectric resonator antenna with an airgap," *IEEE Microwave and Guided Wave Letters*, vol. 3, no. 10, pp. 355– 357, 1993.
- [11] K. W. Leung, X. S. Fang, Y. M. Pan, E. H. Lim, K. M. Luk, and H. P. Chan, "Dual-function radiating glass for antennas and light covers—part II: dual-band glass dielectric resonator antennas," *IEEE Transactions on Antennas and Propagation*, vol. 61, no. 2, pp. 587–597, 2013.
- [12] A. Petosa, A. Ittipiboon, and M. Cuhaci, "Array of circular-polarised cross dielectric resonator antennas," *Electronics Letters*, vol. 32, no. 19, pp. 1742–1743, 1996.
- [13] M. Akbari, S. Gupta, R. Movahedinia, S. Zarbakhsh, and A. R. Sebak, "Bandwidth enhancement of 4×4 subarrays circularly polarized rectangular dielectric resonator antenna by sequential feeding network," in *Proceedings of the 10th European Conference on Antennas and Propagation (EuCAP '16)*, pp. 1–4, Davos, Switzerland, April 2016.
- [14] M. W. McAllister, S. A. Long, and G. L. Conway, "Rectangular dielectric resonator antenna," in *Proceedings of the International Symposium Digest—Antennas and Propagation*, vol. 21, pp. 696– 699, May 1983.
- [15] K. W. Leung, K. M. Luk, K. Y. A. Lai, and D. Lin, "Theory and experiment of a coaxial probe fed hemispherical dielectric resonator antenna," *IEEE Transactions on Antennas and Propagation*, vol. 41, no. 10, pp. 1390–1398, 1993.
- [16] R. A. Kranenburg and S. A. Long, "Microstrip transmission line excitation of dielectric resonator antennas," *Electronics Letters*, vol. 24, no. 18, pp. 1156–1157, 1988.
- [17] L.-N. Zhang, S.-S. Zhong, and S.-Q. Xu, "Broadband U-shaped dielectric resonator antenna with elliptical patch feed," *Electronics Letters*, vol. 44, no. 16, pp. 947–949, 2008.
- [18] R. A. Kranenburg, S. A. Long, and J. T. Williams, "Coplanar waveguide excitation of dielectric resonator antennas," *IEEE Transactions on Antennas and Propagation*, vol. 39, no. 1, pp. 119–122, 1991.
- [19] B. Ghosh, K. Ghosh, and C. S. Panda, "Coplanar waveguide feed to the hemispherical DRA," *IEEE Transactions on Antennas and Propagation*, vol. 57, no. 5, pp. 1566–1570, 2009.
- [20] K.-W. Leung, K.-M. Luk, K. Y. A. Lai, and D. Lin, "Theory and experiment of an aperture-coupled hemispherical dielectric resonator antenna," *IEEE Transactions on Antennas and Propagation*, vol. 43, no. 11, pp. 1192–1198, 1995.
- [21] Y. M. Pan and S. Y. Zheng, "A low-profile stacked dielectric resonator antenna with high-gain and wide bandwidth," *IEEE Antennas and Wireless Propagation Letters*, vol. 15, pp. 68–71, 2016.
- [22] A. A. Kishk and W. Huang, "Use of electric and magnetic conductors to reduce the DRA size," in *Proceedings of the IEEE International Workshop on Antenna Technology: Small and Smart Antennas Metamaterials and Applications (iWAT '07)*, pp. 143–146, IEEE, Cambridge, UK, March 2007.
- [23] M. T. K. Tam and R. D. Murch, "Half volume dielectric resonator antenna designs," *Electronics Letters*, vol. 33, no. 23, pp. 1914–1916, 1997.

- [24] A. A. Kishk and W. Huang, "Size-reduction method for dielectric-resonator antennas," *IEEE Antennas and Propagation Magazine*, vol. 53, no. 2, pp. 26–38, 2011.
- [25] Nasimuddin and K. P. Esselle, "Antennas with dielectric resonators and surface mounted short horns for high gain and large bandwidth," *IET Microwaves, Antennas and Propagation*, vol. 1, no. 3, pp. 723–728, 2007.
- [26] T. A. Denidni, Y. Coulibaly, and H. Boutayeb, "Hybrid dielectric resonator antenna with circular mushroom-like structure for gain improvement," *IEEE Transactions on Antennas and Prop*agation, vol. 57, no. 4, pp. 1043–1049, 2009.
- [27] R. Cicchetti, A. Faraone, E. Miozzi, R. Ravanelli, and O. Testa, "A high-gain mushroom-shaped dielectric resonator antenna for wideband wireless applications," *IEEE Transactions on Antennas* and Propagation, vol. 64, no. 7, pp. 2848–2861, 2016.
- [28] A. Petosa, S. Thirakoune, and A. Ittipiboon, "Higher-order modes in rectangular DRAs for gain enhancement," in Proceedings of the 13th International Symposium on Antenna Technology and Applied Electromagnetics and the Canadian Radio Sciences Meeting (ANTEM/URSI '09), pp. 1–4, February 2009.
- [29] L. Zhong, J. S. Hong, and H. C. Zhou, "A novel patternreconfigurable cylindrical dielectric resonator antenna with enhanced gain," *IEEE Antennas and Wireless Propagation Let*ters, vol. 15, pp. 1253–1256, 2016.
- [30] M. Mrnka and Z. Raida, "Enhanced-gain dielectric resonator antenna based on the combination of higher-order modes," *IEEE Antennas and Wireless Propagation Letters*, vol. 15, pp. 710–713, 2016.
- [31] G. Drossos, Z. Wu, and L. E. Davis, "Circular polarised cylindrical dielectric resonator antenna," *Electronics Letters*, vol. 32, no. 4, pp. 281–283, 1996.
- [32] K. W. Leung, W. C. Wong, K. M. Luk, and E. K. N. Yung, "Circular-polarised dielectric resonator antenna excited by dual conformal strips," *Electronics Letters*, vol. 36, no. 6, pp. 484–486, 2000.
- [33] M. T. K. Tam and R. D. Murch, "Circularly polarized circular sector dielectric resonator antenna," *IEEE Transactions on Antennas and Propagation*, vol. 48, no. 1, pp. 126–128, 2000.
- [34] M. B. Oliver, Y. M. M. Antar, R. K. Mongia, and A. Ittipiboon, "Circularly polarised rectangular dielectric resonator antenna," *Electronics Letters*, vol. 31, no. 6, pp. 418–419, 1995.
- [35] K. P. Esselle, "Circularly polarised higher-order rectangular dielectric-resonator antenna," *Electronics Letters*, vol. 32, no. 3, pp. 150–151, 1996.
- [36] S. Fakhte, H. Oraizi, and R. Karimian, "A novel low-cost circularly polarized rotated stacked dielectric resonator antenna," *IEEE Antennas and Wireless Propagation Letters*, vol. 13, pp. 722– 725, 2014.
- [37] M. Zou and J. Pan, "Wide dual-band circularly polarized stacked rectangular dielectric resonator antenna," *IEEE Anten*nas and Wireless Propagation Letters, vol. 15, pp. 1140–1143, 2015.
- [38] G. Almpanis, C. Fumeaux, and R. Vahldieck, "Offset cross-slot-coupled dielectric resonator antenna for circular polarization," IEEE Microwave and Wireless Components Letters, vol. 16, no. 8, pp. 461–463, 2006.
- [39] A. Laisné, R. Gillard, and G. Piton, "Circularly polarised dielectric resonator antenna with metallic strip," *Electronics Letters*, vol. 38, no. 3, pp. 106–107, 2002.
- [40] K. W. Leung, W. C. Wong, and H. K. Ng, "Circularly polarized slot-coupled dielectric resonator antenna with a parasitic patch," *IEEE Antennas and Wireless Propagation Letters*, vol. 1, no. 1, pp. 57–59, 2002.

- [41] B. Li and K. W. Leung, "Strip-fed rectangular dielectric resonator antennas with/without a parasitic patch," *IEEE Transactions on Antennas and Propagation*, vol. 53, no. 7, pp. 2200–2207, 2005.
- [42] R. Chair, S. L. S. Yang, A. A. Kishk, K. F. Lee, and K. M. Luk, "Aperture fed wideband circularly polarized rectangular stair shaped dielectric resonator antenna," *IEEE Transactions on Antennas and Propagation*, vol. 54, no. 4, pp. 1350–1352, 2006.
- [43] R. Chair, A. A. Kish, and K. F. Lee, "Wideband stair-shaped dielectric resonator antennas," *IET Microwaves, Antennas and Propagation*, vol. 1, no. 2, pp. 299–305, 2007.
- [44] W. Huang and A. A. Kishk, "Compact dielectric resonator antenna for microwave breast cancer detection," *IET Microwaves, Antennas and Propagation*, vol. 3, no. 4, pp. 638–644, 2009.
- [45] P. Gupta, D. Guha, and C. Kumar, "Dielectric resonator working as feed as well as antenna: new concept for dual-mode dual-band improved design," *IEEE Transactions on Antennas and Propagation*, vol. 64, no. 4, pp. 1497–1502, 2016.
- [46] R. Chair, A. A. Kishk, and K. F. Lee, "Experimental investigation for wideband perforated dielectric resonator antenna," *Electronics Letters*, vol. 42, no. 3, pp. 137–139, 2006.
- [47] T. A. Denidni and Z. Weng, "Rectangular dielectric resonator antenna for ultrawideband applications," *Electronics Letters*, vol. 45, no. 24, pp. 1210–1212, 2009.
- [48] M. Khalily, M. K. A. Rahim, and A. A. Kishk, "Bandwidth enhancement and radiation characteristics improvement of rectangular dielectric resonator antenna," *IEEE Antennas and Wireless Propagation Letters*, vol. 10, pp. 393–395, 2011.
- [49] Z. Fan and Y. M. M. Antar, "Slot-coupled DR antenna for dual-frequency operation," *IEEE Transactions on Antennas and Propagation*, vol. 45, no. 2, pp. 306–308, 1997.
- [50] S. Dhar, R. Ghatak, B. Gupta, and D. R. Poddar, "A wideband Minkowski fractal dielectric resonator antenna," *IEEE Transactions on Antennas and Propagation*, vol. 61, no. 6, pp. 2895–2903, 2013.
- [51] B. Mukherjee, P. Patel, and J. Mukherjee, "A novel cup-shaped inverted hemispherical dielectric resonator antenna for wideband applications," *IEEE Antennas and Wireless Propagation Letters*, vol. 12, pp. 1240–1243, 2013.
- [52] K. W. Leung, W. C. Wong, K. M. Luk, and E. K. N. Yung, "Annular slot-coupled dielectric resonator antenna," *Electronics Letters*, vol. 34, no. 13, pp. 1275–1277, 1998.
- [53] K. W. Leung and C. K. Leung, "Wideband dielectric resonator antenna excited by cavity-backed circular aperture with microstrip tuning fork," *Electronics Letters*, vol. 39, no. 14, pp. 1033–1035, 2003.
- [54] H. Y. Lam and K. W. Leung, "Analysis of U-slot-excited dielectric resonator antennas with a backing cavity," *IEE Proceedings—Microwaves, Antennas and Propagation*, vol. 153, no. 5, pp. 480–482, 2006.
- [55] A. Perron, T. A. Denidni, and A.-R. Sebak, "High-gain hybrid dielectric resonator antenna for millimeter-wave applications: design and implementation," *IEEE Transactions on Antennas* and Propagation, vol. 57, no. 10, pp. 2882–2892, 2009.
- [56] D. Guha, Y. M. M. Antar, A. Ittipiboon, A. Petosa, and D. Lee, "Improved design guidelines for the ultra wideband monopoledielectric resonator antenna," *IEEE Antennas and Wireless Propagation Letters*, vol. 5, no. 1, pp. 373–376, 2006.

- [57] D. Guha, B. Gupta, and Y. M. M. Antar, "Hybrid monopole-DRAs using hemispherical/conical-shaped dielectric ring resonators: improved ultrawideband designs," *IEEE Transactions* on Antennas and Propagation, vol. 60, no. 1, pp. 393–398, 2012.
- [58] Y. Gao, A. P. Popov, B. L. Ooi, and M. S. Leong, "Experimental study of wideband hybrid dielectric resonator antenna on small ground plane," *Electronics Letters*, vol. 42, no. 13, pp. 731–733, 2006.
- [59] Y.-F. Lin, H.-M. Chen, and C.-H. Lin, "Compact dual-band hybrid dielectric resonator antenna with radiating slot," *IEEE Antennas and Wireless Propagation Letters*, vol. 8, pp. 6–9, 2009.
- [60] E. Erfani, T. Denidni, S. Tatu, and M. Niroo-Jazi, "A broadband and high gain millimeter-wave hybrid dielectric resonator antenna," in *Proceedings of the 17th International Symposium* on Antenna Technology and Applied Electromagnetics (ANTEM '16), pp. 1–2, IEEE, Montreal, Canada, July 2016.
- [61] Q. Lai, C. Fumeaux, W. Hong, and R. Vahldieck, "60 GHz aperture-coupled dielectric resonator antennas fed by a half-mode substrate integrated waveguide," *IEEE Transactions on Antennas and Propagation*, vol. 58, no. 6, pp. 1856–1864, 2010.
- [62] Y.-M. Pan, K. W. Leung, and K.-M. Luk, "Design of the millimeter-wave rectangular dielectric resonator antenna using a higher-order mode," *IEEE Transactions on Antennas and Propagation*, vol. 59, no. 8, pp. 2780–2788, 2011.
- [63] Y. Coulibaly, M. Nedil, I. Ben Mabrouk, L. Talbi, and T. A. Denidni, "High gain rectangular dielectric resonator for broadband millimeter-waves underground communications," in *Proceedings of the 24th Canadian Conference on Electrical and Computer Engineering (CCECE '11)*, pp. 001088–001091, IEEE, Ontario, Canada, May 2011.
- [64] Y. Coulibaly, M. Nedil, L. Talbi, and T. A. Denidni, "Design of high gain and broadband antennas at 60 GHz for underground communications systems," *International Journal of Antennas* and Propagation, vol. 2012, Article ID 386846, 7 pages, 2012.
- [65] M. J. Al-Hasan, T. A. Denidni, and A. R. Sebak, "Millimeter-wave EBG-based aperture-coupled dielectric resonator antenna," *IEEE Transactions on Antennas and Propagation*, vol. 61, no. 8, pp. 4354–4357, 2013.
- [66] R. Karimian, A. Kesavan, M. Nedil, and T. A. Denidni, "Low mutual coupling 60-GHz MIMO antenna system with frequency selective surface wall," *IEEE Antennas and Wireless Propagation Letters*, 2016.
- [67] P. V. Bijumon, Y. M. M. Antar, A. P. Freundorfer, and M. Sayer, "Integrated dielectric resonator antennas for system on-chip applications," in *Proceedings of the International Conference on Microelectronics (ICM '07)*, pp. 275–278, IEEE, Cairo, Egypt, December 2007.
- [68] P. V. Bijumon, Y. M. M. Antar, A. P. Freundorfer, and M. Sayer, "Dielectric resonator antenna on silicon substrate for system on-chip applications," *IEEE Transactions on Antennas and Propagation*, vol. 56, no. 11, pp. 3404–3410, 2008.
- [69] M.-R. Nezhad-Ahmadi, M. Fakharzadeh, B. Biglarbegian, and S. Safavi-Naeini, "High-efficiency on-chip dielectric resonator antenna for mm-wave transceivers," *IEEE Transactions on Antennas and Propagation*, vol. 58, no. 10, pp. 3388–3392, 2010.
- [70] D. Hou, Y.-Z. Xiong, W.-L. Goh, S. Hu, W. Hong, and M. Madihian, "130-GHz on-chip meander slot antennas with stacked dielectric resonators in standard CMOS technology," *IEEE Transactions on Antennas and Propagation*, vol. 60, no. 9, pp. 4102–4109, 2012.

- [71] L. Ohlsson, T. Bryllert, C. Gustafson et al., "Slot-coupled millimeter-wave dielectric resonator antenna for highefficiency monolithic integration," *IEEE Transactions on Antennas and Propagation*, vol. 61, no. 4, pp. 1599–1607, 2013.
- [72] X.-D. Deng, Y. Li, C. Liu, W. Wu, and Y.-Z. Xiong, "340 GHz On-Chip 3-D antenna with 10 dBi Gain and 80% radiation efficiency," *IEEE Transactions on Terahertz Science and Technology*, vol. 5, no. 4, pp. 619–627, 2015.
- [73] M. O. Sallam, M. Serry, S. Sedky et al., "Micromachined onchip dielectric resonator antenna operating at 60 GHz," *IEEE Transactions on Antennas and Propagation*, vol. 63, no. 8, pp. 3410–3416, 2015.

Hindawi Publishing Corporation International Journal of Antennas and Propagation Volume 2016, Article ID 8536058, 7 pages http://dx.doi.org/10.1155/2016/8536058

#### Research Article

## A Multiband Proximity-Coupled-Fed Flexible Microstrip Antenna for Wireless Systems

# Giovanni Andrea Casula,¹ Paolo Maxia,¹ Giorgio Montisci,¹ Giuseppe Valente,² Giuseppe Mazzarella,¹ and Tonino Pisanu²

<sup>1</sup>Dipartimento di Ingegneria Elettrica ed Elettronica, Università di Cagliari, Piazza D'Armi, 09123 Cagliari, Italy <sup>2</sup>Osservatorio Astronomico di Cagliari, Cagliari, Italy

Correspondence should be addressed to Giuseppe Mazzarella; mazzarella@diee.unica.it

Received 4 August 2016; Accepted 18 September 2016

Academic Editor: Renato Cicchetti

Copyright © 2016 Giovanni Andrea Casula et al. This is an open access article distributed under the Creative Commons Attribution License, which permits unrestricted use, distribution, and reproduction in any medium, provided the original work is properly cited.

A multiband printed microstrip antenna for wireless communications is presented. The antenna is fed by a proximity-coupled microstrip line, and it is printed on a flexible substrate. The antenna has been designed using a general-purpose 3D computer-aided design software (CAD), CST Microwave Studio, and then realized. The comparison between simulated and measured results shows that the proposed antenna can be used for wireless communications for WLAN systems, covering both the WLAN S-band (2.45 GHz) and C-band (5.2 GHz), and the Wi-Max 3.5 GHz band, with satisfactory input matching and broadside radiation pattern. Moreover, it has a compact size, is very easy to realize, and presents a discrete out-of-band rejection, without requiring the use of stop-band filters. The proposed structure can be used also as a conformal antenna, and its frequency response and radiated field are satisfactory for curvatures up to 65°.

#### 1. Introduction

In modern wireless systems, different bands of the frequency spectrum are used to fulfil the high data rate required in the communications, and the antennas of these communication systems must operate in different frequency bands (multiband antennas).

Microstrip patch antennas have found many applications in wireless communication systems, because of their light weight, low profile, low cost, high performance, and compact size, besides an easy design, fabrication, and integration into frontend circuits [1–4]. As a matter of fact, planar antennas are a very common choice for Universal Mobile Telephone Systems (UMTS), Synthetic Aperture Radars (SAR), and Radio-Frequency Identification (RFID) systems [5–7].

The use of multiband antennas is the best choice, because it reduces the numbers of antennas to be mounted in the communication system and can allow satisfying the requirements of different wireless communication systems, which can share the same multiband antenna, such as Wireless Local Area Network (WLAN) and IEEE 802.16 Worldwide

Interoperability for Microwave Access (WiMAX), with a substantial saving of space, cost, and complexity realization of the wireless system itself. Therefore, several different multiband WLAN planar antennas have been proposed in recent years [8–12], showing either a multiband or a tuneable behavior. In particular, a dipole printed on a thin, low-permittivity dielectric substrate and having high operational bandwidth and low radiated signal distortion has been proposed in [9]. It is particularly suitable for multiprotocol WLAN, WiMAX, and UWB wireless communications, and, thanks to a reduced parasitic coupling with the radio frequency circuitry, also in communication systems and radio base stations and, in general, for all the emerging applications of the wireless technology.

In the last years, flexible technologies are becoming very popular in a number of wireless applications such as health monitoring systems and flexible displays and sensors [13], because of the many advantages offered by the antennas fabricated on these flexible substrates. As a matter of fact, if compared with traditional planar antennas fabricated on rigid materials, they offer light weight, small thickness, low

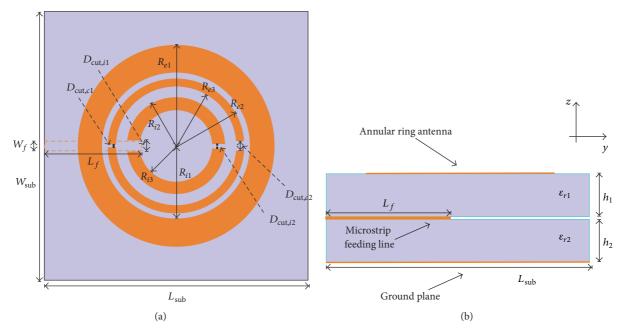


FIGURE 1: Antenna layout. (a) Top view; (b) side view.  $L_{\text{sub}} = W_{\text{sub}} = 40 \text{ mm}, W_f = 1.41 \text{ mm}, L_f = 14.75 \text{ mm}, h_1 = h_2 = 0.5 \text{ mm}, R_{e1} = 15.22 \text{ mm}, R_{i1} = 11.22 \text{ mm}, R_{e2} = 10.27 \text{ mm}, R_{i2} = 9.24 \text{ mm}, R_{e3} = 7.41 \text{ mm}, R_{i3} = 5.675 \text{ mm}, D_{\text{cut},c1} = 0.25 \text{ mm}, D_{\text{cut},c2} = 1.25 \text{ mm}, D_{\text{cut},i1} = 1.5 \text{ mm}, and D_{\text{cut},i2} = 0.5 \text{ mm}.$ 

profile [13], and an easy mounting over conformal surfaces. Flexible antennas can be designed on textile substrates [14], paper [15], PET [16], Kapton, adhesive-layer substrates, and so on [17]. However, on the other hand, these substrates can be severely affected by the environmental conditions. For example, paper and textile substrates are likely subjected to discontinuities and fluids absorption, PET and paper have relatively high losses, and paper is very sensitive to humidity and is not robust to bending and rolling.

In this work, we present a multiband printed antenna, working both in the S and in the C frequency bands (2.45 GHz, 3.5 GHz, and 5.2 GHz), which meets the requirements of different wireless communication standards, such as IEEE 802.11, HiperLan, and Bluetooth [18]. We decide to use a flexible but robust dielectric substrate (ARLON AD250 with 0.5 mm thickness), in order to limit the effect of the environment over the antenna performance. The use of different and cheaper dielectric substrates such as paper, or PET, is possible, of course, but it probably will lead to a nonnegligible decrease of the robustness of the final antenna.

In the design of planar antennas, the most common feeding techniques are the microstrip-fed [8, 9] and the coplanar waveguide- (CPW-) fed [10–12]. The most serious disadvantage of microstrip antennas is certainly their very small bandwidth, and a large number of attempts have been made to increase the bandwidth of printed antennas beyond the typical values of a few percent [19]. The most straightforward way of doing this is to use a thicker substrate, but it is difficult to achieve more than about 4-5% bandwidth in this manner, before the imaginary part of the input impedance becomes too large, causing matching problems [20, 21]. As an alternative, parasitic elements can be inserted

to obtain a double resonance response, or an appropriate matching network can be designed to improve the bandwidth of a patch on a thick dielectric substrate [22].

Since we need a flexible structure, the antenna substrate must be thin and flexible, and therefore, in this work, we choose an alternative method to enhance the bandwidth of a microstrip antenna, which consists of a microstrip feed line proximity-coupled to a patch antenna printed on a dielectric substrate, which lies above the feeding line [23, 24]. This proximity-coupled feeding technique is also referred to in the literature as "electromagnetically coupling."

The geometry of the proximity-coupled annular ring antenna proposed in this paper is shown in Figure 1. The microstrip feed line is printed on the bottom substrate, while the annular concentric rings are printed on the upper substrate, bonded to the feed substrate. The feed line is centered with respect to the rings, and its length, measured from the edge of the dielectric substrate, is equal to  $L_f$ . In general, the two substrates may be of different thickness and permittivity, but in our case both substrates are equal (ARLON AD250 with 0.5 mm thickness).

Differently from [23], in order to match each annular ring to the coupled microstrip feeding line, we did not use any shunt tuning stub, but we add two symmetrical cuts on each ring (see Figure 1), as described in the following section. The working frequency band of the antenna is determined by both the impedance bandwidth (the bandwidth over which the antenna remains matched to the feed-line to some specified level, which is typically determined by the frequency range in which the SII has a module less than  $-10\,\mathrm{dB}$ ) and the radiated field bandwidth (the bandwidth over which the far field pattern remains satisfactory). In our case, the far

field pattern bandwidth is larger than the input impedance bandwidth, which is the most critical point. Although the antenna bandwidth is not very large (about 1.5–2%, due to the thin substrate used to obtain a flexible antenna), due to the chosen dielectric substrate (which is thin and flexible), the proposed structure can be used also as a conformal antenna and is very robust with respect to flexibility, since it has been bended with different curvatures, and the simulations show a very stable frequency response, and a satisfactory radiated field, for curvatures up to 65°.

The designed antenna, due to its bandwidth characteristics, can be suitable for applications related to the Vehicle-to-Vehicle (V2V) Communication Systems, employed to provide safety warnings and traffic information, such as the Wireless Access in Vehicular Environments (WAVE)/Dedicated Short Range Communication (DSRC) based Intelligent Transportation System (ITS) [25, 26] and also for short range communications devices employed in V2V and in vehicle-to-roadside (V2R) communications units [27]. As a matter of fact, the operating bandwidth required for these systems is very limited (from 20 to 80 MHz around the operating frequency of 5.8 GHz) [25, 26].

The proposed structure is very compact, flexible, and easy to realize and has a very cheap production cost. Moreover, it radiates a broadside pattern, is characterized by a good matching within the WLAN frequencies (both S-Band and C-Band), and Wi-Max frequency, and presents a satisfactory out-of-band rejection, which allows avoiding undesired interferences, making it particularly suitable for modern wireless systems. The antenna has been designed using a general-purpose 3D computer-aided design software (CAD), CST Microwave Studio, and then realized and characterized, with a good agreement between measured and simulated data.

#### 2. Design of Multiband Annular Ring Patch Antenna

The antenna geometry consists of three concentric annular rings printed on a top dielectric layer, fed by a proximity-coupled microstrip line, printed on the bottom dielectric substrate, which is attached to a metallic ground plane, as shown in Figure 1. The substrate used is a flexible Arlon AR250, with a thickness of  $h=0.5\,\mathrm{mm}$ , relative permittivity  $\varepsilon_r=2.5$ , and  $\tan\delta=0.0018$ . The antenna size is  $40\,\mathrm{mm}\times40\,\mathrm{mm}$ , and it is very compact.

The width  $W_f$  of the microstrip line has been chosen equal to 1.41 mm, which corresponds to an input impedance of 50 Ohm. The length of the feeding line has been optimised to get a satisfactory input matching of the complete antenna.

For each of the three working frequencies (2.45 GHz, 3.5 GHz, and 5.2 GHz), an annular ring has been designed, fed by a coupled microstrip line. The internal radius of the ring mostly influences the ring's resonant frequency, whereas the outer radius mainly influences the ring's input impedance, with a little effect also on the resonant frequency. In order to match the annular ring with the microstrip line, we inserted two symmetrical cuts in correspondence with the feeding microstrip line. The depth of these cuts can be used to

modulate the input resistance of the antenna, with only a little effect on the imaginary part of the input impedance. In our case, the cuts have been inserted only in the two internal rings, whereas the external ring has no need to be cut.

We started designing the external annular ring, which must resonate at 2.45 GHz, obtaining an internal radius equal to  $R_{i1}=11.22$  mm and an external radius  $R_{e1}=15.22$  mm, with a length of the microstrip feeding line of  $L_f=14.75$  mm.

Then, taking the microstrip line length fixed at the value of  $L_f=14.75$  mm, we separately designed the central annular ring, resonating at 3.5 GHz, obtaining an internal radius equal to  $R_{i2}=9.24$  mm. The external radius has been chosen small enough to keep a distance of about 1 mm between the external and central ring, obtaining  $R_{e2}=10.27$  mm, so as to limit the coupling between these two rings. The matching between the feeding line and this central ring has been obtained by cutting the two sides of the ring symmetrically with respect to the feeding line and with a depth of  $D_{\mathrm{cut},c1}=0.25$  mm and  $D_{\mathrm{cut},c2}=1.25$  mm (see Figure 1).

The same procedure has been used to design the internal annular ring: taking the microstrip line length fixed at the value of  $L_f = 14.75$  mm, we separately designed the internal annular ring, resonating at 5.2 GHz, obtaining an internal radius equal to  $R_{i3} = 5.675$  mm and an external radius of  $R_{e3} =$ 7.41 mm. In this case, the resonant frequencies of the internal and central ring being far enough, we had no difficulties in the choice of the external radius. Also in this case, to improve the matching between the feeding line and the internal ring, we inserted two cuts in the two sides of the ring, symmetrically with respect to the feeding line, and with a depth of  $D_{\text{cut},i1}$ = 1.5 mm and  $D_{\text{cut},i2}$  = 0.5 mm (see Figure 1). Finally, we merged the three designed annular rings, obtaining the whole multiband antenna depicted in Figure 1. Thanks to the carried out design choice, as described above, the three rings are decoupled enough, and the frequency response of the whole antenna maintains the resonances and the bandwidth of each single ring, allowing obtaining a satisfactory multiband antenna, as we will show in the next section.

#### 3. Results

The annular ring antenna designed in Section 2 has been manufactured (see Figure 2) and characterized. In Figure 3, the comparison between the simulated and experimental reflection coefficient is shown, and the input matching is satisfactory, having three resonances in the required portions of S- and C-band for WLAN and Wi-Max applications (2.45 GHz, 3.5 GHz, and 5.2 GHz). The simulated and measured data are in good agreement, and the out-of-band rejection is satisfactory, especially considering that no stopband filters have been used in the antenna design. This behavior is mainly due to the relatively narrow frequency band of each annular ring which is part of the multiband antenna.

Figure 4 reports the frequency behavior of the realized gain  $G_R$  for the antenna shown in Figure 1 (evaluated by CST). The antenna gain has a peak value equal to 4.6 dB in the Sband and equal to 5.8 dB in the C-band. On the other hand, it

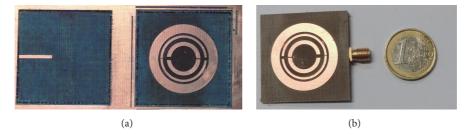


FIGURE 2: Photo of the designed antenna shown in Figure 1: (a) top and bottom layers; (b) assembled antenna.

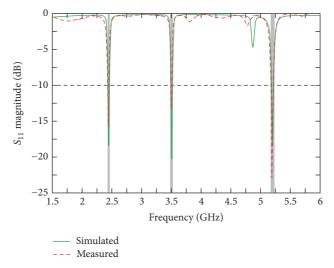


FIGURE 3: Frequency response of the designed antenna shown in Figure 1.

rapidly drops to less than 3 dB out of the working frequency band, confirming the very good out-of-band rejection of the proposed antenna, due to the small bandwidth of each annular ring, which works only for frequencies close to its resonant frequency.

In Figure 5, the simulated E- and H-Plane antenna radiation patterns are shown. The radiation pattern shows a broadside behavior within the design frequency bands (2.45 GHz, 3.5 GHz, and 5.2 GHz), with an F/B ratio greater than 10 dB, while it deteriorates very rapidly out of band, with both a bad SLL and front-to-back ratio. Therefore, the proposed structure can be successfully used as a multiband antenna for wireless communications.

In order to test the robustness of the proposed structure with respect to flexibility, in Figure 6 the frequency response of the antenna is shown for different values of the curvatures (from  $18^{\circ}$  to  $65^{\circ}$ ). The frequency response is very stable for all the tested bendings, with a maximum difference of  $\pm 10$  MHz with respect to the planar case reported in Figure 3, and the far field pattern remains broadside for all the working frequencies, with only a slight deterioration due to the bending of the radiating structure. The results in Figure 3 correspond to a bending towards the *y*-direction (see Figure 1(b)). Thanks to the structure symmetry, similar results, and therefore a similar robustness, can be obtained if the

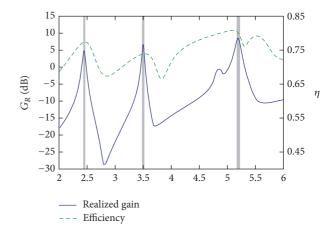


FIGURE 4: Realized gain and radiation efficiency of the designed antenna shown in Figure 1.

bendings are performed along the *x*-direction. These results confirm very good robustness of the proposed antenna, which can be successfully used also as a conformal antenna, with no modification on the geometry of the nonconformal (i.e., planar) structure, whose dimensions are reported in Figure 1.

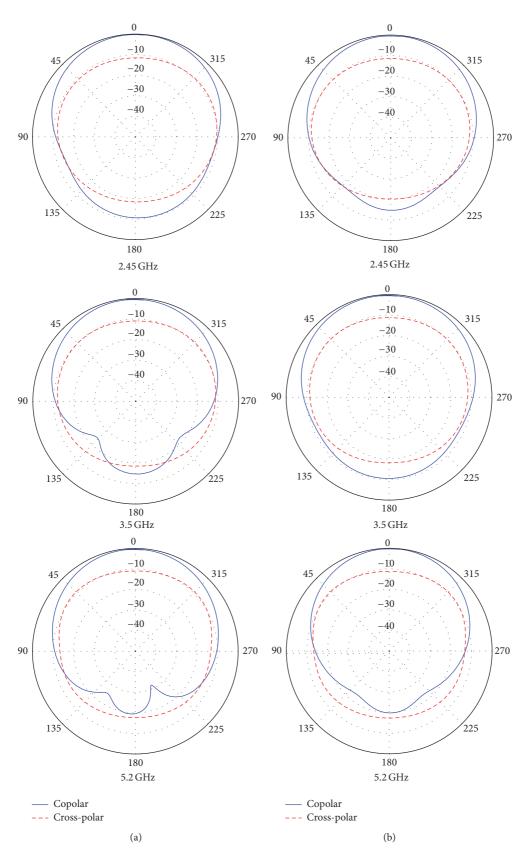


Figure 5: (a) E-Plane and (b) H-Plane radiation pattern of the designed antenna shown in Figure 1.

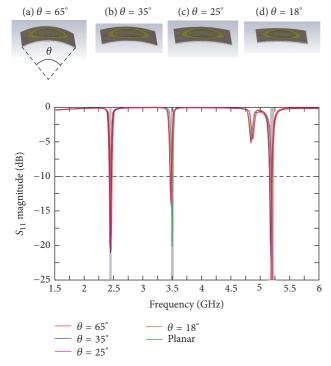


FIGURE 6: Frequency response of the designed antenna shown in Figure 1 for different curvature angles.

#### 4. Conclusion

In this work we present a multiband printed microstrip antenna for wireless communications, fed by a proximity-coupled microstrip line and printed on a flexible substrate, which covers both the WLAN frequencies (both S-Band at 2.45 GHz and C-Band at 5.2 GHz) and Wi-Max frequency at 3.5 GHz. The simulated and measured results are in very good agreement, showing a very good input matching, a broadside radiation pattern, and an excellent rejection out of its operating frequency band, without the use of stop-band filters, avoiding undesired interference. The antenna realized gain is above 4.6 dB within the working band and rapidly decreases in the out-of-band range. The proposed structure can be used also as a conformal antenna, and its frequency response and radiated field are satisfactory for curvatures up to 65°.

#### **Competing Interests**

The authors declare that there is no conflict of interests.

#### References

- [1] T. Huynh and K.-F. Lee, "Single-layer single-patch wideband microstrip antenna," *Electronics Letters*, vol. 31, no. 16, pp. 1310–1312, 1995.
- [2] P. Callaghan and J. C. Batchelor, "Dual-band pin-patch antenna for Wi-Fi applications," *IEEE Antennas and Wireless Propaga*tion Letters, vol. 7, pp. 757–760, 2008.

- [3] Y. J. Cho, Y. S. Shin, S. H. Hwang, and S.-O. Park, "A wideband internal antenna with dual monopole radiation elements," *IEEE Antennas and Wireless Propagation Letters*, vol. 4, no. 1, pp. 381–384, 2005.
- [4] R. K. Joshi and A. R. Harish, "A modified bow-tie antenna for dual band applications," *IEEE Antennas and Wireless Propaga*tion Letters, vol. 6, pp. 468–471, 2007.
- [5] M. Rhee, "Universal mobile telecommunication system (UMTS)," in *Mobile Communication Systems and Security*, pp. 133–166, 2009.
- [6] R. Pokuls, J. Uher, and D. M. Pozar, "Microstrip antennas for SAR applications," *IEEE Transactions on Antennas and Propagation*, vol. 46, no. 9, pp. 1289–1296, 1998.
- [7] C.-Y. Sim and C.-J. Chi, "A slot loaded circularly polarized patch antenna for UHF RFID reader," *IEEE Transactions on Antennas and Propagation*, vol. 60, no. 10, pp. 4516–4521, 2012.
- [8] X. Q. Zhang, Y. C. Jiao, and W. H. Wang, "Compact wide triband slot antenna for WLAN/WiMAX applications," *Electronics Letters*, vol. 48, no. 2, pp. 64–65, 2012.
- [9] G. Cappelletti, D. Caratelli, R. Cicchetti, and M. Simeoni, "A low-profile printed drop-shaped dipole antenna for wideband wireless applications," *IEEE Transactions on Antennas and Propagation*, vol. 59, no. 10, pp. 3526–3535, 2011.
- [10] R. K. Raj, M. Joseph, C. K. Aanandan, K. Vasudevan, and P. Mohanan, "A new compact microstrip-fed dual-band coplanar antenna for WLAN applications," *IEEE Transactions on Antennas and Propagation*, vol. 54, no. 12, pp. 3755–3762, 2006.
- [11] P. Liu, Y. Zou, B. Xie, X. Liu, and B. Sun, "Compact CPW-fed tri-band printed antenna with meandering split-ring slot for WLAN/WiMAX applications," *IEEE Antennas and Wireless Propagation Letters*, vol. 11, pp. 1242–1244, 2012.
- [12] M. J. Hua, P. Wang, Y. Zheng, and S. L. Yuan, "Compact tri-band CPW-fed antenna for WLAN/WiMAX applications," *Electronics Letters*, vol. 49, no. 18, pp. 1118–1119, 2013.
- [13] H. R. Khaleel, H. M. Al-Rizzo, D. G. Rucker, and Y. Al-Naiemy, "Flexible printed monopole antennas for WLAN applications," in *Proceedings of the IEEE International Symposium on Antennas and Propagation (APSURSI '11)*, pp. 1334–1337, IEEE, Spokane, Wash, USA, July 2011.
- [14] P. Salonen, J. Kim, and Y. Rahmat-Sami, "Dual-band E-shaped patch wearable textile antenna," in *Proceedings of the IEEE Antennas and Propagation Society International Symposium*, pp. 466–469, Washington, DC, USA, July 2005.
- [15] D. E. Anagnostou, A. A. Gheethan, A. K. Amert, and K. W. Whites, "A direct-write printed antenna on paper-based organic substrate for flexible displays and WLAN applications," *Journal of Display Technology*, vol. 6, no. 11, pp. 558–564, 2010.
- [16] G. A. Casula, G. Montisci, and G. Mazzarella, "A wideband PET inkjet-printed antenna for UHF RFID," *IEEE Antennas and Wireless Propagation Letters*, vol. 12, pp. 1400–1403, 2013.
- [17] C. M. Lee, Y. Kim, Y. Kim, I. K. Kim, and C. W. Jung, "A flexible and transparent antenna on a polyamide substrate for laptop computers," *Microwave and Optical Technology Letters*, vol. 57, no. 5, pp. 1038–1042, 2015.
- [18] A. Doufexi, S. Armour, M. Butler et al., "A comparison of the HIPERLAN/2 and IEEE 802.11a wireless LAN standards," *IEEE Communications Magazine*, vol. 40, no. 5, pp. 172–180, 2002.
- [19] A. Henderson, J. R. James, and C. M. Hall, "Bandwidth extension techniques in printed conformal antennas," in *Proceedings of the Military Microwaves Conference*, pp. 329–334, Brighton, UK, June 1986.

- [20] E. Chang, S. A. Long, and W. F. Richards, "An experimental investigation of electrically thick rectangular microstrip antennas," *IEEE Transactions on Antennas and Propagation*, vol. 34, no. 6, pp. 767–772, 1986.
- [21] D. M. Pozar, "Considerations for millimeter wave printed antennas," *IEEE Transactions on Antennas and Propagation*, vol. 31, no. 5, pp. 740–747, 1983.
- [22] K. S. Fong, H. F. Pues, and M. J. Withers, "Wideband multilayer coaxial-fed microstrip antenna element," *Electronics Letters*, vol. 21, no. 11, pp. 497–499, 1985.
- [23] D. M. Pozar and B. Kaufman, "Increasing the bandwidth of a microstrip antenna by proximity coupling," *Electronics Letters*, vol. 23, no. 8, pp. 368–369, 1987.
- [24] H. G. Oltman and D. A. Huebner, "Electromagnetically coupled microstrip dipoles," *IEEE Transactions on Antennas and Propagation*, vol. 29, no. 1, pp. 151–157, 1981.
- [25] K.-C. Su, H.-M. Wu, W.-L. Chang, and Y.-H. Chou, "Vehicle-to-vehicle communication system through wi-fi network using android smartphone," in *Proceedings of the 1st International Conference on Connected Vehicles and Expo (ICCVE '12)*, pp. 191–196, Beijing, China, December 2012.
- [26] J. Imad, M. Nader, and Z. Liren, "Inter-vehicular communication systems, protocols and middleware," in *Proceedings of the IEEE 5th International Conference on Networking, Architecture* and Storage (NAS '10), Macau, July 2010.
- [27] W. Viriyasitavat and O. K. Tonguz, "Cars as roadside units: a cooperative solution," in *Proceedings of the 76th IEEE Vehicular Technology Conference (VTC Fall '12)*, Québec City, Canada, September 2012.

Hindawi Publishing Corporation International Journal of Antennas and Propagation Volume 2016, Article ID 7439403, 9 pages http://dx.doi.org/10.1155/2016/7439403

#### Research Article

# On-Body Characterization of Planar Differential Antennas for Multiple, Wide, and Narrow Bands

### Luigi Vallozzi, Domenico Pepe, 2,3 Thijs Castel, Hendrik Rogier, and Domenico Zito 2,4

Correspondence should be addressed to Domenico Zito; domenico.zito@tyndall.ie

Received 2 February 2016; Revised 2 June 2016; Accepted 26 June 2016

Academic Editor: Antonio Faraone

Copyright © 2016 Luigi Vallozzi et al. This is an open access article distributed under the Creative Commons Attribution License, which permits unrestricted use, distribution, and reproduction in any medium, provided the original work is properly cited.

This paper reports the results of the on-body experimental tests of a set of four planar differential antennas, originated by design variations of radiating elements with the same shape and characterized by the potential for covering wide and narrow bands. All the antenna designs have been implemented on low-cost FR4 substrate and characterized experimentally through on-body measurements. The results show the impact of the proximity to the human body on antenna performance and the opportunities in terms of potential coverage of wide and narrow bands for future ad hoc designs and implementations through wearable substrates targeting on-body and off-body communication and sensing applications.

#### 1. Introduction

UWB radar for contactless detection of respiratory rate of human beings [1-4] is an active research area requiring innovative transceiver and antenna developments [5, 6]. A novel planar differential antenna was proposed recently by our research group [7]. This antenna was designed to meet the design constrains, electromagnetic performance, and physical integration, required by the ultrawideband (UWB) pulse radar sensor operating approximately in the frequency band from 3 to 5 GHz [2-4]. The proximity between the radiating elements of the proposed differential antenna has allowed achieving a significant bandwidth enhancement. In addition to original differential antenna development, we also investigated some design variations with the objective of showing how these reflect on the antenna performance, showing that the antennas originating from radiating elements with the same shape can be potentially adopted through an agile design strategy to cover wide and narrow bands of interest for a number of wireless applications, communication, and sensing, as a consequence of variations in size and orientation

of the radiating elements with respect to the original planar differential antenna [8].

Numerous studies were carried out about the effects of human body on performance of planar antennas. Concerning nondifferential antennas, many contributions reported the effects on S-parameters and gain patterns, like in [9, 10]. Considering differentially fed antennas, in [11], the in-body near-field radiation pattern of an on-body antenna was characterized. In other studies, implantable antennas were considered, like in [12, 13], where the in-body radiation patterns and S-parameters were investigated. However, to the authors' knowledge, the experimental characterization of differential antennas on human body, in terms of off-body far-field radiation patterns, which is proposed in the present paper, has received no attention yet in existing literature.

Fully differential transceivers are less prone to commonmode noise and interferers; thereby differential antennas could play a significant role in future networks and communications, especially considering the massive amount of devices envisaged for the Internet of Things era [14, 15] that

<sup>&</sup>lt;sup>1</sup>Department of Information Technology, Ghent University-iMinds, Technologiepark Zwijnaarde 15, 9052 Gent, Belgium

<sup>&</sup>lt;sup>2</sup>Tyndall National Institute, Lee Maltings, Dyke Parade, Cork T12 R5CP, Ireland

<sup>&</sup>lt;sup>3</sup>DISMI, University of Modena and Reggio Emilia, Via Amendola 2, 42122 Reggio Emilia, Italy

<sup>&</sup>lt;sup>4</sup>School of Engineering, University College Cork, College Road, Cork T12 RXA9, Ireland

are supposed to operate in regions of frequency spectrum already crowded by existing applications and services.

In this paper, we report for the first time the results of the on-body experimental characterization of the variations of planar differential antenna design described in [8], resulting from measurements on a real human subject, which have not been reported in any of our previous publications. For reasons of space, the details and results of previous publication [8] will be not repeated here. Thereby, for the insights about the design, inherent properties, and free-space (in air) performances of the antennas, we invite the reader to inspect our previous work reported in [8]. In particular, in this work, here, we will show for the first time how the proximity to the human body affects the antenna performance and that the antennas, all originating from radiating elements with the same shape, can be potentially adopted in future ad hoc designs on flexible substrates or textile fabrics to cover multiple, wide, and narrow bands of interest for a number of wearable applications for both communication and sensing [16].

The paper is organized as follows. Section 2 reports the description of the antenna design variations and summarizes, for reasons of self-consistency, the main results obtained from the previous free-space tests, which provide the term of reference for design and performance. Section 3 reports the measurement results obtained from the tests on a real human body. Finally, in Section 4, the conclusions are drawn.

# 2. Planar Differential Antennas: Designs and Tests

Two different sets of planar differential antennas were designed on a low-cost FR4 substrate ( $\varepsilon_r = 4.4$ , dielectric thickness  $T = 1.6 \,\mathrm{mm}$ , copper thickness  $t = 35 \,\mu\mathrm{m}$ , and loss tangent tan  $\delta = 0.02$ ) for a complete characterization as stand-alone devices. The layout drawing of the first set of antennas, namely, folded planar differential antennas, is shown in Figure 1. The layout drawing of the second set of antennas, being antipodal planar differential antennas, is shown in Figure 2. At first glance, we observe that each radiating element of the antenna consists of a semicircle and a triangle that provides a smooth transition towards the input pins [7]. In particular, in the folded planar differential antenna, the two radiating elements are folded one aside the other. In particular, the design is characterized by the aperture angle of triangle  $\alpha$  and rotation angle  $\rho$  between the symmetry axes of the two radiating elements. The main features of this design approach are that it allows a compact design of both the transmitter and receiver antennas on the same board of the implemented radar sensor based on a system-on-a-chip radar transceiver, still maintaining good performance [2-4]. In the antipodal planar differential antenna, the two radiating elements are rotated by 180° one with respect to the others, so resulting in an antipodal position.

In the following subsections, we will summarize the results obtained for the experimental open-space tests. In

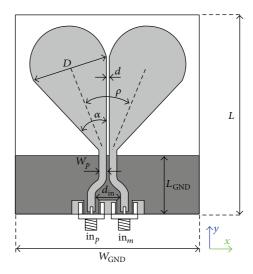


FIGURE 1: Layout drawing of the folded planar differential antennas. The top copper layer is in light grey and the bottom copper layer is in dark grey.

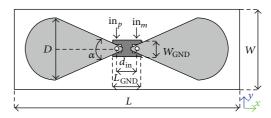


FIGURE 2: Layout drawing of the antipodal planar differential antennas. The top copper layer is in light grey and the bottom copper layer is in dark grey.

particular, we report the results of two antenna designs for each set, folded and antipodal, as follows:

- (A) Folded planar differential antenna with  $\rho = 45^{\circ}$  and D = 3 cm, as shown in Figure 1.
- (B) Folded planar differential antenna with  $\rho = 45^{\circ}$  and D = 4 cm, as shown in Figure 1.
- (C) Antipodal planar differential antennas with  $\rho = 180^{\circ}$  and D = 3 cm, as shown in Figure 2.
- (D) Antipodal planar differential antennas with  $\rho = 180^{\circ}$  and D = 4 cm, as shown in Figure 2.

All the antenna designs were carried out by means of the electromagnetic (EM) simulator Momentum by Keysight Technologies®, and characterized experimentally in anechoic chamber.

2.1. Folded Radiating Elements:  $\rho = 45^\circ$  and D = 3 cm. The physical implementation is shown in Figure 3. Distance d between the two sides of the antenna is equal to 1 mm. Diameter D is equal to 3 cm in order to resonate at the frequency of interest (i.e., roughly 3 GHz). The aperture angle of the triangle is  $\alpha = 45^\circ$ . The rotation angle of the two radiating elements is  $\rho = 45^\circ$ .

Table 1: Folded planar differential antenna sizing (D = 3 cm).

| D [cm] | α [deg] | $\rho$ [deg] | <i>d</i> [mm] | $W_p$ [mm] | $d_{\rm in}$ [cm] | $W_{\rm GND}$ [cm] | $L_{\mathrm{GND}}$ [cm] | <i>L</i> [cm] |
|--------|---------|--------------|---------------|------------|-------------------|--------------------|-------------------------|---------------|
| 3      | 45      | 45           | 1             | 3          | 1                 | 7.1                | 2.3                     | 7.9           |



FIGURE 3: Photograph of the physical implementation of the folded planar differential antenna ( $\rho = 45^{\circ}$ , D = 3 cm).

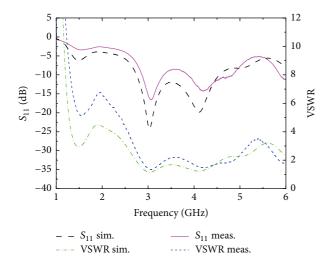


FIGURE 4: Measured and simulated  $S_{11}$  and VSWR versus frequency of the folded planar differential antenna ( $\rho = 45^{\circ}$ , D = 3 cm).

Two microstrip feeding lines were added in order to allow the connection of the antenna to a Vector Network Analyzer (VNA) by means of 2.92 mm connectors (horizontal) and carry out the experimental tests. Width of the microstrip line feeding paths  $(W_p)$  is equal to 3 mm in order to exhibit a characteristic impedance of  $Z_c = 50~\Omega$ . The distance between the two inputs of the antenna is equal to  $d_{\rm in} = 1~{\rm cm}$  to allow the placement of two adjacent connectors, as shown in Figure 1. The characteristic sizes of the UWB antenna are reported in Table 1. The simulated and measured  $S_{11}$  parameter and VSWR are reported in Figure 4. The measured  $S_{11}$  exhibits a magnitude lower than  $-10~{\rm dB}$  almost in the whole band of

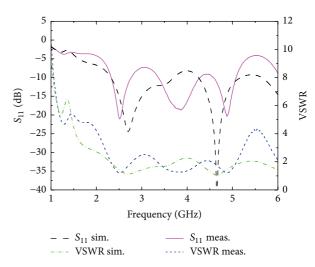


FIGURE 5: Measured and simulated  $S_{11}$  and VSWR as a function of frequency for the folded planar differential antenna ( $\rho = 45^{\circ}$ , D = 4 cm).

interest, roughly from 3 to 5 GHz [17, 18]. Figure 4 reports also the results for the voltage wave standing ratio (VSWR), which is lower than two almost in the whole band of interest.

2.2. Folded Radiating Elements:  $\rho = 45^{\circ}$  and D = 4 cm. Simulated and measured  $S_{11}$  parameter as a function of frequency of the antenna with folded radiating elements ( $\rho$ =  $45^{\circ}$  with D = 4 cm) are shown in Figure 5. All the other design parameters are unchanged with respect to the folded antenna with D = 3 cm. The measurements show  $S_{11}$  lower than approximately -7.5 dB from 2.4 to 5 GHz. In particular,  $S_{11}$  < -10 dB roughly from 2.3 to 2.7 GHz and from 3.3 to 5.1 GHz. Figure 5 reports also the measurement results for the VSWR which is lower than about 2 over the same bands reported above, for the measured antenna. As expected, the results confirm that the bandwidth, for this design variation with D = 4 cm, is extended roughly for about 0.5 GHz towards the lower frequencies with respect to the original design with D = 3 cm. This result shows that this design variation has the potential to be compatible with multiband operations for both industrial scientific medical (ISM) narrow band at 2.4 GHz [19, 20] and the lower portion of the UWB band from about 3 to 5 GHz [3].

2.3. Antipodal Radiating Elements:  $\rho=180^\circ$  and D=3 cm. The physical implementation of the antipodal planar differential antenna is shown in Figure 6. The design parameters are summarized in Table 2.  $S_{11}$  parameter and VSWR resulting from simulations and measurements are shown in Figure 7.  $|S_{11}|$  is lower than -10 dB in the frequency band from about 1.1 to 1.44 GHz. The antenna is thus compatible with operation

Table 2: Antipodal planar differential antenna sizing (D = 3 cm).

| D [cm] | α [deg] | $\rho$ [deg] | $d_{\rm in}$ [cm] | $W_{\rm GND}$ [cm] | $L_{\mathrm{GND}}$ [cm] | <i>W</i> [cm] | <i>L</i> [cm] |
|--------|---------|--------------|-------------------|--------------------|-------------------------|---------------|---------------|
| 3      | 45      | 180          | 1                 | 0.8                | 1.4                     | 4             | 11.2          |



FIGURE 6: Antipodal planar differential antenna: photograph of the physical implementation. The two 2.92 mm connectors (vertical) are soldered on the bottom plane.

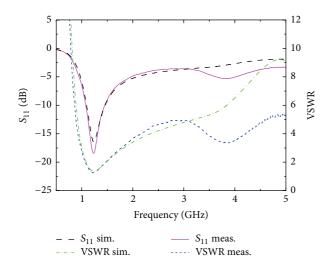


FIGURE 7: Measured and simulated  $S_{11}$  and VSWR as a function of frequency for the antipodal planar differential antenna ( $\rho = 180^{\circ}$ , D = 3 cm).

in 1.2 GHz lower L-band adopted by satellite applications for Global Positioning and Navigation Satellite Systems (GNSS) [21].

2.4. Antipodal Radiating Elements:  $\rho = 180^{\circ}$  and D = 4 cm. In this design, we have D = 4 cm, L = 14.6 cm, and W = 5 cm. All the other design parameters are unchanged with respect to those summarized for the previous case in Table 2.

 $S_{11}$  parameter and VSWR resulting from simulations and measurements are shown in Figure 8. We get  $|S_{11}| < -10 \,\mathrm{dB}$  in the frequency band from 0.8 to 1.06 GHz.

It is worth observing how the increase of diameter (D = 4 cm), with respect to the case with D = 3 cm, enables the potential coverage of the ISM band at 868 MHz [22, 23].

The discrepancies between measured and simulated  $S_{11}$ , for the discussed antenna variations, are the results of a number of factors influencing the impedance matching of the antenna prototype during measurements, which are not taken into account in the simulation model. Namely, the presence of SMA connectors and solders in the real prototype,

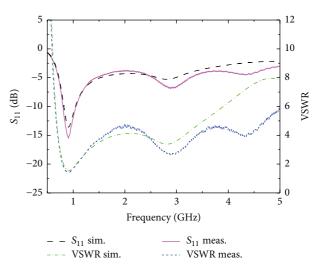


FIGURE 8: Measured and simulated  $S_{11}$  and VSWR as a function of frequency for the antipodal planar differential antenna ( $\rho = 180^{\circ}$ , D = 4 cm).

not accounting for in the simulation, can result in deviation of input impedances, with a consequent variation in measured S-parameters with respect to the simulated ones. Measurement cables, although accurately shielded during measurements, can also be partly responsible for such deviations, it is very difficult to completely eliminate coupling between them and the radiating elements. However, the discrepancies can be still considered more than acceptable.

#### 3. On-Body Characterization

All four variations of planar differential antennas summarized in the previous section were characterized through onbody experimental tests, in order to investigate the impact of the proximity to the human body on the antenna performance and explore their potentialities for future implementations through ad hoc designs on flexible substrates or textile fabrics [14] and exploitation in wearable applications [21].

The measurements were carried out in anechoic chamber, where the antennas under test were placed on the chest area of a real human subject, with fixed distance of 15 mm between the printed circuit board of the antenna and the body surface, achieved by means of a dielectric spacer placed between them. Each antenna was mounted on the spacer, and all together were placed on the chest of the human body. The radiating element of the antenna is on the opposite side of the interface with the spacer. *z*-axis is oriented away from and perpendicularly to the body surface, and *y*-axis is pointing upwards, as shown in Figures 9 and 10(a). The main physical and dielectric characteristics parameters of the antenna and spacer fabric are reported in Table 3.

| TABLE 3: Phy | rsical and ele | ectric parameters | of antenna and | d spacer. |
|--------------|----------------|-------------------|----------------|-----------|
|              |                |                   |                |           |

|                 | Dielectric layers |                                   | Conductive layers |                      |
|-----------------|-------------------|-----------------------------------|-------------------|----------------------|
|                 | Substrate         | Spacer                            | Conductive layers |                      |
|                 |                   | "3 mesh®"                         |                   |                      |
| Material        | FR4               | spacer<br>fabric–Müller<br>Textil | Material          | Copper               |
| T [mm]          | 1.6               | 15                                | t [μm]            | 35                   |
| $\varepsilon_r$ | 4.4               | ≈1.05                             | σ [S/m]           | $5.96 \times 10^{7}$ |
| $	an \delta$    | 0.02              | ≈0                                | 0 [0/111]         | 5.70 N 10            |

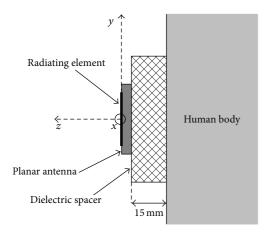


FIGURE 9: Cross section of planar antenna, dielectric spacer, and human body.

It is worth remarking that the purpose of the experimental on-body characterization was to test a realistic situation, that is, with the antenna placed on a real human body, where slight distance variations occur due to small body movements due to respiration and spacer compression. The scheme in Figure 9 is therefore a simple illustrative representation of the antenna placement on the body, not displaying the abovementioned realistic effects.

The reflection coefficient as a function of frequency and the differential gain pattern on azimuth plane (xz),  $G_d(\theta)$ were determined for all four antennas. The gain pattern was derived by measuring, by means of an Agilent PNAX network analyzer, transmission coefficient  $S_{d1}$  between the single output of a standard-gain horn and the differential terminals of the antenna under test, for different azimuth ( $\theta$ ) orientations, then rescaling the measured value by calibrating path loss, gain of the transmitting horn, and mismatch factors at both ends, in order to obtain the gain pattern. For all the measurements, particular care was taken to avoid as much possible interference and scattering as possible from measurement cables which, for this purpose, were covered by radiofrequency absorbing material. In addition, ferrite chokes were placed around the measurement cables in order to furtherly reduce scattering and undesired coupling with the antenna.

3.1. Folded Radiating Elements:  $\rho = 45^\circ$  and D = 3 cm. The measured reflection coefficient and azimuth gain pattern at f = 3 GHz, for the smaller antenna with folded radiating elements, on human body, are shown in Figures 11 and 12, respectively. One can see how the reflection coefficient, compared to the open-space measurements, is affected by small variations due to the proximity with human body. However, the reflection coefficient remains more than acceptable, being  $S_{11} < -10$  dB in the frequency band from 2.85 to 4.53 GHz.

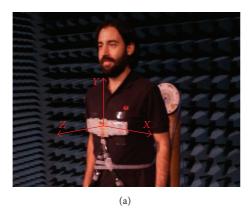
The measured differential gain pattern at  $f=3\,\mathrm{GHz}$  (i.e., about the lowest resonance frequency), shown in Figure 12, exhibits a main lobe in the half space oriented away from the human body (i.e.,  $-90^\circ < \theta < +90^\circ$ ). The maximum gain for  $\theta=0^\circ$  is about 4.14 dBi, which is increased by an amount of about 2.7 dB with respect to the open-space case, for which the maximum gain was about 1.43 dBi. It is worth noting that, in this case, the human body is acting as a reflector, producing an increase of the maximum gain and directivity. The backscattering gain is largely attenuated by the human body which absorbs most of the power radiated by the antenna.

Thereby, this antenna is also capable of operating when worn by a human body, for UWB off-body wireless communications in the lower portion of the UWB frequency spectrum (e.g., 3–5 GHz).

3.2. Folded Radiating Elements:  $\rho=45^\circ$  and D=4 cm. Figures 13 and 14 show the measured differential reflection coefficient and the azimuth gain pattern of the larger version of the antenna with folded elements (i.e., with D=4 cm). Similar to the folded antenna with D=3 cm, the reflection coefficient and consequently the VSWR undergo a slight variation due to the presence of the human body. In particular, we have  $S_{11}<-8.3$  dB and VSWR < 2.1 in the lower portion of the UWB band from 3 to 5 GHz, which indicates more than acceptable performance of this antenna when worn on human body. Moreover,  $S_{11}<-10$  dB in the bands from 2.3 to 2.7 GHz and from 3.3 to 5 GHz. Concerning the measured gain pattern of the on-body antenna shown in Figure 14, at f=2.5 GHz, this has a main lobe directed away from the body with a maximum of about 1.5 dBi in broadside direction.

The maximum gain is increased of about 3.5 dB when compared to open-space measurements, indicating reflection from the human body. This antenna variation, similar to the antenna with larger folded elements, is potentially suitable for on-body operation in UWB off-body communications in the lower UWB spectrum and 2.4 GHz ISM band.

3.3. Antipodal Radiating Elements:  $\rho=180^\circ$  and D=3 cm. The on-body measured reflection coefficient and gain pattern at f=1.2 GHz, compared to the open-space results, for the smaller antipodal antenna are shown in Figures 15 and 16, respectively. The reflection coefficient is affected by slight variations due to the proximity to the human body. In particular, -10 dB  $S_{11}$  band becomes slightly narrower, extending in the frequency band from 1.08 to 1.37 GHz, and the resonance frequency decreases by about 10 MHz to value of f=1.21 GHz.



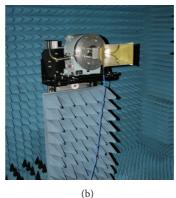


FIGURE 10: Photographs of the experimental setup. (a) Planar differential antenna placed on a spacer and then on the chest of the human body, along with the antenna reference system. (b) Standard-gain horn antenna.

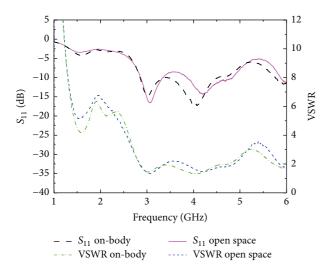


FIGURE 11: On-body measured  $S_{11}$  and VSWR versus frequency of the folded planar differential antenna with  $\rho=45^\circ$  and D=3 cm.

The gain pattern, shown in Figure 16, measured at f = 1.2 GHz, is prone to severe attenuation of the backscattering due to the human body and has a maximum value of about 0.5 dBi, that is slightly larger than value of -0.3 dBi obtained for the open-space case. Finally, in the on-body operation, this antenna remains capable of operating reliably in 1.2 GHz lower L-band for GNSS applications.

3.4. Antipodal Radiating Elements:  $\rho = 180^{\circ}$  and D = 4 cm. The experimental results for the bigger version of the planar differential antenna with antipodal elements (D = 4 cm) are shown in Figures 17 and 18.

The differential reflection coefficient, shown in Figure 17, indicates a resonance frequency of about 874 MHz, slightly decreased with respect to the open-space case, and  $S_{11} < -10~\rm dB$  (or VSWR < 1.92) in the band from 820 to 954 MHz, slightly narrower than the open-space band. The proximity to the human body worsens slightly the impedance matching

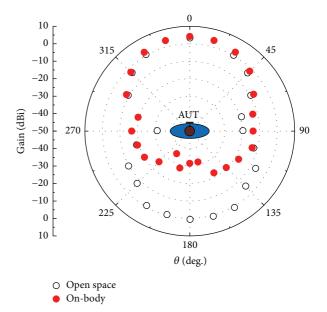


FIGURE 12: Measured differential gain pattern at f=3 GHz in the azimuth plane (xz) for the folded planar differential antenna ( $\rho=45^{\circ}, D=3$  cm).

performance with respect to the open-space measurements. In spite of all, the body-worn antenna is still capable of providing a good coverage of the 868 MHz ISM band.

As for the gain pattern in xz plane, Figure 18 shows that the gain pattern at  $f=868\,\mathrm{MHz}$  of the antenna worn on body is affected by a reduction of the maximum gain, which amounts to about  $-1\,\mathrm{dBi}$ ,  $2\,\mathrm{dB}$  lower than the value of about  $1\,\mathrm{dBi}$  in open space. Moreover, the backscattering of the gain pattern is, similar to all other antennas, severely attenuated by the human body. This antenna variation, in onbody operation, still exhibits the characteristic performance suitable for its potential usage in the Ultra High Frequency (UHF) band at 915 MHz for Radiofrequency Identification (RFID).

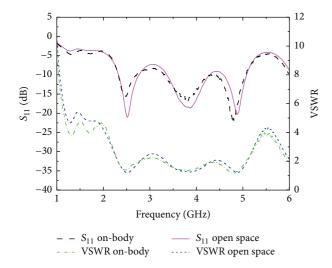


Figure 13: On-body measured  $S_{11}$  and VSWR versus frequency of the folded planar differential antenna with  $\rho=45^\circ$  and D=4 cm.

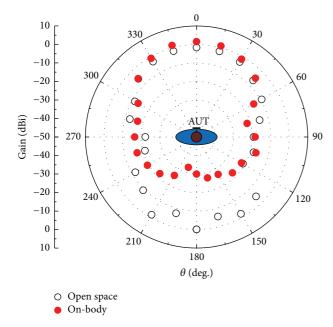


FIGURE 14: Measured differential gain pattern at  $f=2.5\,\mathrm{GHz}$  in azimuth plane (xz) for the folded planar differential antenna ( $\rho=45^\circ, D=4\,\mathrm{cm}$ ).

#### 4. Conclusions

Four different variations of planar differential antennas, for wide and narrow band applications, differing in dimensions and orientation of the radiating elements, were experimentally characterized when worn on the chest of a human body. Measurements were performed of the differential reflection coefficient and horizontal gain pattern of the antenna, with a distance of 15 mm between antenna and human body. Results were compared with those obtained with the antenna in open space and the following observations could be made.

Concerning the impact on the performance, the presence of the human body has a clear effect on reflection coefficient

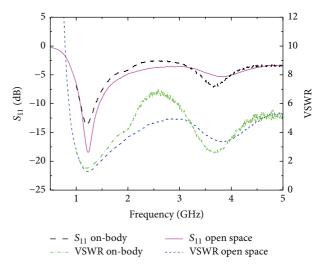


FIGURE 15: On-body measured  $S_{11}$  and VSWR versus frequency of the planar differential antenna with antipodal radiating elements ( $\rho = 180^{\circ}$ , D = 3 cm).

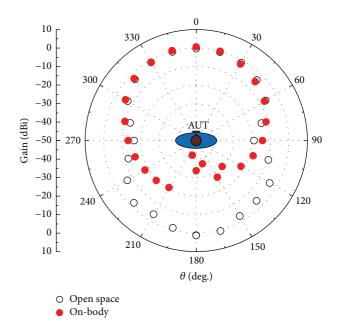


FIGURE 16: Measured differential gain pattern at  $f=1.2\,\mathrm{GHz}$  in azimuth plane (xz) for the antipodal planar differential antenna ( $\rho=180^\circ, D=3\,\mathrm{cm}$ ).

and gain patterns. In particular, as for the gain pattern, the proximity to the human body produces, for all antenna variations, a severe attenuation of the backscattering portion of the gain pattern, towards the back side of the wearer, due to absorption of the radiated power by the human body. Moreover, for 3 of the 4 antennas, the maximum gain measured on-body for the lowest resonance frequency, is affected by a small increase with respect to the open-space case, indicating that the human body acts as a reflector. For the larger ( $D=4\,\mathrm{cm}$ ) version of the antenna with antipodal elements only, the maximum gain results in a reduction of about 2 dB with respect to the open-space measurements.

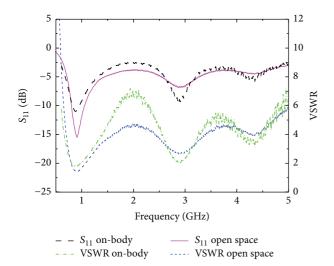


FIGURE 17: Measured and simulated  $S_{11}$  and VSWR versus frequency of the planar differential antenna with antipodal radiating elements ( $\rho = 180^{\circ}$ , D = 4 cm).

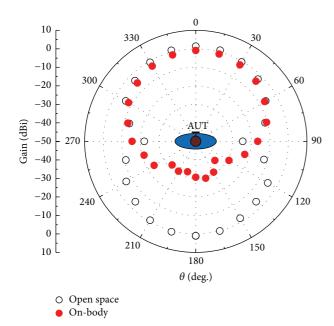


FIGURE 18: Measured differential gain pattern at  $f=0.868\,\mathrm{GHz}$  in azimuth plane (xz) for the folded planar differential antenna ( $\rho=45^\circ, D=4\,\mathrm{cm}$ ).

Concerning reflection coefficient, the presence of the human body results in small variations of the characteristics, with the most noticeable effect being a slight lowering of the resonance frequencies. The reflection coefficient performance remains more than acceptable for operation at the frequencies of interest.

In conclusion, the performance of all antennas remains more than acceptable when they are worn at 15 mm of distance from the chest area of a human body. This proves the potential for future wearable implementations of all considered prototypes, in particular for short range off-body communications, with applications such as monitoring of

vital signs or body area network personal communications. Moreover, the four antenna variations allow the coverage of several frequency bands of interests, such as the lower portion of the UWB from 3 to 5 GHz, the 868 MHz and 2.45 GHz ISM bands, the 1.2 GHz band (lower L-band) for the Global Positioning and Navigation Satellite System (GNSS), and the UHF band at 915 MHz for Radiofrequency Identification (RFID).

#### **Competing Interests**

The authors declare that there are no competing interests regarding the publication of this paper.

#### Acknowledgments

The authors are grateful to Keysight Technologies and Microlease for their generous donations of hardware equipment and software computer-aided design tools in support of the research activities carried out at the Marconi Lab, Tyndall National Institute. This work was supported in part by the Science Foundation Ireland under Grant SFI07/SK/I1258, in part by the Irish Research Council (IRC) under Grant R13485, and Higher Education Authority (HEA). This publication has emanated also from research supported in part by another research grant from SFI and is cofunded under the European Regional Development Fund under Grant no. 13/RC/2077.

#### References

- [1] P. Bernardi, R. Cicchetti, S. Pisa, E. Pittella, E. Piuzzi, and O. Testa, "Design, realization, and test of a UWB radar sensor for breath activity monitoring," *IEEE Sensors Journal*, vol. 14, no. 2, pp. 584–596, 2014.
- [2] D. Zito, D. Pepe, M. Mincica et al., "SoC CMOS UWB pulse radar sensor for contactless respiratory rate monitoring," *IEEE Transactions on Biomedical Circuits and Systems*, vol. 5, no. 6, pp. 503–510, 2011.
- [3] D. Zito and D. Pepe, "Planar differential antenna design and integration with pulse radar microchip sensor," *IEEE Sensors Journal*, vol. 14, no. 8, pp. 2477–2487, 2014.
- [4] D. Zito and D. Pepe, "Monitoring respiratory pattern in adult and infant via contactless detection of thorax and abdomen movements through SoC UWB pulse radar sensor," in Proceedings of the IEEE Topical Conference on Biomedical Wireless Technologies, Networks, and Sensing Systems (BioWireleSS '14), IEEE Radio Wireless Week (RWW '14), pp. 1–3, Newport Beach, Calif, USA, January 2014.
- [5] G. Cappelletti, D. Caratelli, R. Cicchetti, and M. Simeoni, "A low-profile printed drop-shaped dipole antenna for wideband wireless applications," *IEEE Transactions on Antennas and Propagation*, vol. 59, no. 10, pp. 3526–3535, 2011.
- [6] D. Zito and D. Pepe, "UWB pulse radio transceivers and antennas: considerations on design and implementation," in Proceedings of the 8th European Conference on Antennas and Propagation (EuCAP '14), pp. 1633–1637, The Hague, The Netherlands, April 2014.
- [7] D. Pepe, L. Vallozzi, H. Rogier, and D. Zito, "Planar differential antenna for short-range UWB pulse radar sensor," *IEEE Anten*nas and Wireless Propagation Letters, vol. 12, pp. 1527–1530, 2013.

- [8] D. Pepe, L. Vallozzi, H. Rogier, and D. Zito, "Design variations on planar differential antenna with potential for multiple, wide, and narrow band coverage," *International Journal of Antennas* and Propagation, vol. 2015, Article ID 478453, 13 pages, 2015.
- [9] L. Vallozzi, H. Rogier, and C. Hertleer, "Dual polarized textile patch antenna for integration into protective garments," *IEEE Antennas and Wireless Propagation Letters*, vol. 7, pp. 440–443, 2008.
- [10] T. Kellomäki, "On-body performance of a wearable single-layer RFID tag," *IEEE Antennas and Wireless Propagation Letters*, vol. 11, pp. 73–76, 2012.
- [11] X. Li, L. Zwirello, M. Jalilvand, and T. Zwick, "Design and near-field characterization of a planar on-body UWB slot-antenna for stroke detection," in *Proceedings of the IEEE International Workshop on Antenna Technology (iWAT '12)*, pp. 201–204, Tucson, Ariz, USA, March 2012.
- [12] H. Liu, X. Y. Liu, and Y. Fan, "A miniaturized differentially fed dual-band fractal antenna for in-body communications," in Proceedings of the 2015 IEEE MTT-S International Microwave Workshop Series on Advanced Materials and Processes for RF and THz Applications (IMWS-AMP), Microwave Workshop Series, pp. 1–3, Suzhou, China, July 2015.
- [13] A. Iftikhar, M. M. Masud, M. N. Rafiq, S. Asif, B. D. Braaten, and M. S. Khan, "Radiation performance and Specific Absorption Rate (SAR) analysis of a compact dual band balanced antenna," in *Proceedings of the IEEE International Conference on Elec*tro/Information Technology (EIT '15), pp. 672–675, Dekalb, Ill, USA, May 2015.
- [14] J. Lanza, L. Sánchez, L. Muñoz et al., "Large-scale mobile sensing enabled internet-of-things testbed for smart city services," *International Journal of Distributed Sensor Networks*, vol. 2015, Article ID 785061, 15 pages, 2015.
- [15] A. Zanella, N. Bui, A. Castellani, L. Vangelista, and M. Zorzi, "Internet of things for smart cities," *IEEE Internet of Things Journal*, vol. 1, no. 1, pp. 22–32, 2014.
- [16] C. Feránndez-Prades, H. Rogier, A. Collado, and M. M. Tentzeris, "Flexible substrate antennas," *International Journal of Antennas and Propagation*, vol. 2012, Article ID 746360, 2 pages, 2012.
- [17] F. Zito, D. Pepe, and D. Zito, "UWB CMOS monocycle pulse generator," *IEEE Transactions on Circuits and Systems. I. Regular Papers*, vol. 57, no. 10, pp. 2654–2664, 2010.
- [18] D. Pepe and D. Zito, "22.7-db gain-19.7-dbm ICP<sub>IdB</sub> UWB CMOS LNA," IEEE Transactions on Circuits and Systems II: Express Briefs, vol. 56, no. 9, pp. 689–693, 2009.
- [19] X. L. Quan, R. L. Li, Y. H. Cui, and M. M. Tentzeris, "Analysis and design of a compact dual-band directional antenna," *IEEE Antennas and Wireless Propagation Letters*, vol. 11, pp. 547–550, 2012.
- [20] C.-K. Wu, T.-F. Chien, C.-L. Yang, and C.-H. Luo, "Design of novel S-shaped quad-band antenna for MedRadio/WMTS/ISM implantable biotelemetry applications," *International Journal of Antennas and Propagation*, vol. 2012, Article ID 564092, 12 pages, 2012.
- [21] A. Dierck, A. H. Rogier, and F. A. Declercq, "A wearable active antenna for global positioning system and satellite phone," *IEEE Transactions on Antennas and Propagation*, vol. 61, no. 2, pp. 532–538, 2013.
- [22] T. Kaufmann, D. C. Ranasinghe, M. Zhou, and C. Fumeaux, "Wearable quarter-wave folded microstrip antenna for passive UHF RFID applications," *International Journal of Antennas and Propagation*, vol. 2013, Article ID 129839, 11 pages, 2013.

[23] F. Alimenti, M. Virili, G. Orecchini et al., "A new contactless assembly method for paper substrate antennas and UHF RFID chips," *IEEE Transactions on Microwave Theory and Techniques*, vol. 59, no. 3, pp. 627–637, 2011.

Hindawi Publishing Corporation International Journal of Antennas and Propagation Volume 2016, Article ID 9612987, 6 pages http://dx.doi.org/10.1155/2016/9612987

### Research Article

## **Band-Notched UWB Antenna with Switchable and Tunable Performance**

### Wei Wu, Yun-Bo Li, Rui-Yuan Wu, Chuan-Bo Shi, and Tie-Jun Cui

School of Information Science and Engineering, Southeast University, Nanjing 210096, China

Correspondence should be addressed to Tie-Jun Cui; tjcui@seu.edu.cn

Received 21 April 2016; Revised 19 June 2016; Accepted 23 June 2016

Academic Editor: Renato Cicchetti

Copyright © 2016 Wei Wu et al. This is an open access article distributed under the Creative Commons Attribution License, which permits unrestricted use, distribution, and reproduction in any medium, provided the original work is properly cited.

A band-notched UWB antenna is presented, which can switch between two notch bands and tune the central frequency simultaneously. It is the first time that the switchable and tunable behaviours are combined together in band-notched UWB antennas. In the band-notched structure, PIN diodes are used to switch the lower and upper frequency bands, while varactors could vary the central frequency of each notch band continuously. Measurement results show that the notch bands could switch between 4.2 GHz and 5.8 GHz when the state of varactors is fixed, and the ranges of tuning are 4.2–4.8 GHz and 5.8–6.5 GHz when the state of PIN diodes is ON and OFF, respectively.

### 1. Introduction

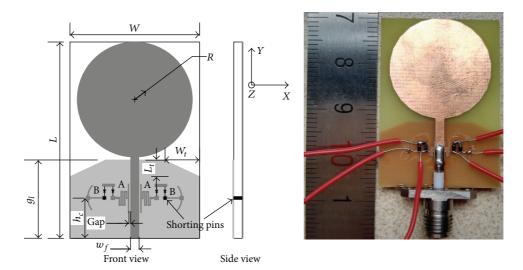
UWB communication (3.1–10.6 GHz) has attracted much attention in recent years owing to its high data rates, great channel capacity, and low power dissipation [1]. As a necessary component in the system, UWB antenna has been widely investigated. There are many shapes of the radiator, such as circle, rectangle, cup, and pyramid [2–5]. Besides, according to the relative position between the radiator and the ground, the UWB antenna could be classified into the coplanar waveguide (CPW) top-radiator-bottom-ground and stereoscopic structure [4–6].

Nevertheless, parts of UWB spectrum would overlap with other communication systems, such as WiMax (3.3–3.8 GHz), WLAN (5.15–5.85 GHz), or X-band satellite communication links (7.9–8.4 GHz) [7], which would cause electromagnetic interference. Generally, there are two ways to produce notch bands. One is adding stubs beside the feeding line or ground to produce notch bands [8–10], while the other is making slits in the feeding line or radiator [11, 12]. Of course, the combination of these two methods could produce multiple notch bands.

Afterwards, under the tendency of self-adaptive technologies and smart antennas, the concept of reconfiguration has been introduced into antennas, where PIN diodes and

varactors are common means to realize smart functions. As a specific term, the UWB antenna with reconfigurable notch bands has been observed recently. In general, these designs could be classified into two categories according to the function. One is to produce switchable notch bands with PIN diodes [7, 13, 14]. In fact, modifying the ON or OFF status of the diodes, the electrical path length of the surface currents changes and consequently the resonant processes responsible for the formation of the notch bands. Another category is using varactors to produce continuously changeable notch bands, so-called tunable notch bands [15, 16]. The capacitance of varactor varies continuously when the reverse bias voltage changes, leading to the resonance moving on the frequency spectrum. PIN diodes or varactors applied with stubs and slits could produce various band-notched UWB antennas.

In this paper, it is the first time that PIN diodes and varactors are combined together. The notch bands of the UWB antenna are not only switchable but also tunable. In the design, stubs with a pair of PIN diodes and varactors consist of band-notched structure. The ON and OFF states of PIN diodes are controlled by reverse bias voltages of 5 V and 0 V, which makes two notch bands (the lower and upper) switchable. Once the state of PIN diode is fixed, the continuously varying reverse voltage from 0 V to 15 V would make the notch band scannable in a certain range on the spectrum.



- Top metal
- Bottom metal
- Shorting pins

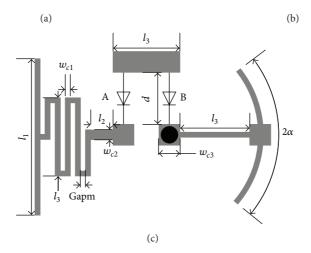


FIGURE 1: Geometry of the proposed switchable and tunable band-notched UWB antenna: (a) antenna structure, top view (left) and side view (right); (b) photo of fabricated prototype; (c) detailed band-notched structure.

Measurement results show that the notch band could be switched between 4.2 GHz and 5.8 GHz when reverse voltages on varactors are fixed at 0 V, and the tuning ranges are 4.2 GH–4.8 GHz and 5.8 GH–6.5 GHz under the ON and OFF states of PIN diodes.

### 2. Antenna Design

As is illustrated in Figures 1(a) and 1(b), the design is fabricated on a 1 mm thick FR4 ( $\varepsilon_r=4.3$ ;  $\tan\delta=0.002$ ) substrate, where the dimension is 26 mm  $\times$  36.6 mm. On the bottom layer, the ground with two cutting triangles for better impedance matching is printed. The band-notched structure, the feeding line, and the UWB circular monopole antenna are printed on the top layer. Among them, the band-notched structure is located beside the feed line. Detailed antenna parameters are listed in Table 1.

Figure 1(c) shows the detailed band-notched structure. The capital letters A and B appearing in Figure 1(c) refer to PIN diodes and varactors, respectively. In the PIN diodes the current will go through or it will be cut off, when the reverse bias voltage is 5 V or 0 V, which corresponds to the ON or OFF state. As for varactors, the capacitance will decrease from 2.37 pF to 0.46 pF when the reverse voltage increases from 0 V to 15 V. Besides, the meander line has been adopted to reduce the size of the inductance necessary for the excitation of the resonance process, while the shorting pins are used to suppress the high-order notch bands.

### 3. Study of the Notch Band Characteristic

In the design, varactors SMV1231-079LF and PIN diodes SMP1320-079LF which are all from Skyworks Solutions are applied. In the numerical simulation, the varactors and the

Table 1: Optimized parameters of the proposed antenna.

|           |      | Parameter |       |       |    |       |       |     |       |       |       |       |          |          |          |      |     |           |
|-----------|------|-----------|-------|-------|----|-------|-------|-----|-------|-------|-------|-------|----------|----------|----------|------|-----|-----------|
|           | L    | W         | $g_l$ | $h_c$ | R  | $W_t$ | $L_t$ | gap | $w_f$ | $l_1$ | $l_2$ | $l_3$ | $w_{c1}$ | $w_{c2}$ | $w_{c3}$ | gapm | d   | $2\alpha$ |
| Unit (mm) | 36.6 | 26        | 14    | 7.6   | 11 | 6     | 2.6   | 0.1 | 1.9   | 4.4   | 0.5   | 2     | 0.1      | 0.2      | 0.4      | 0.1  | 1.5 | 80        |

Table 2: Effective parameters of the circuits.

| Type        | Bias voltage (V) | C(pF) | $R(\Omega)$ | L(nH) |
|-------------|------------------|-------|-------------|-------|
|             | 0                | 2.37  | 1.65        | 0.7   |
| Varactor    | 8                | 0.54  | 0.09        | 0.7   |
|             | 15               | 0.46  | 0.005       | 0.7   |
| PIN diode   | 0 (OFF)          | 0.25  | 0.8         | 0.427 |
| r iiv diode | 5 (ON)           | 38.91 | 0.015       | 0.774 |

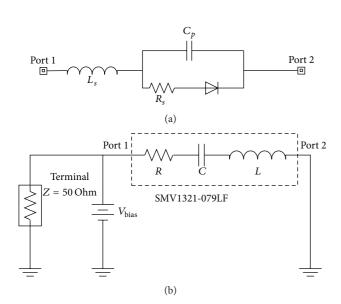


FIGURE 2: Extraction of effective parameters of the PIN diode and the varactor: (a) the spice model of the varactor; (b) circuit model of extraction, which is used to extract the effective circuit parameters of the varactor based on its spice model.

PIN diodes have been replaced, within the operating band, by equivalent circuits composed by a series RLC circuit. All the numerical simulations are conducted in HFSS 15. The exact circuit parameters are listed in Table 2, which are extracted from their spice model by using Advanced Design System 2009, as is shown in Figure 2. In the following simulation, the effective RLC circuits will represent the varactor and the PIN diode for simplicity.

The equivalent circuit of the band-notched structure is shown in Figure 3. The circuit consists of two seriesconnected impedances. One of the impedances  $R_{p1}+jX_{p1}$  or  $R_{p2}+jX_{p2}$  describes the effect of the PIN diode in the ON or OFF state, while the other is the variable impedance describing the electric behaviour of the varactor diode under changing reverse bias voltage. Besides, the rest RLC of the circuit produced by other notch band structures are also

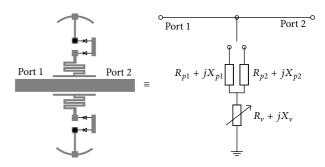


FIGURE 3: Equivalent circuit of the band-notched structure.

added into  $R_{\nu} + jX_{\nu}$  for simplicity. When the resonance of series circuit happens, signal will not transfer from port 1 to port 2 but will pass through the circuit to the ground, as if port 2 is shorted, and this is the reason that the notch band shows up on the UWB spectrum.

It is clear that the resonant frequency of the notch band will decrease when neither or both of the inductance and capacitance increase in the band-notched structure. Owing to the series connection of the elements forming the bandnotched structure depicted in Figure 3, the PIN diode acts like a switch at which the equivalent capacitance values ranging between 0.25 pF and 38.91 pF are associated, as is shown in Table 2. To put it in another way, in this design, ON state of PIN diodes and 0 V reverse bias voltage on varactors corresponds to the lowest resonance (series connection of 38.91 pF and 2.37 pF), while OFF state of PIN diodes and 15 V reverse bias voltage on varactors represents the highest resonance (series connection of 0.25 pF and 0.46 pF). That is, the PIN diode determines whether the resonance of notch band is in the lower or upper band, and varactors realize scanning in a range of spectrums once the state of PIN diode is fixed.

### 4. Results and Discussion

Figure 4 shows the distribution of the surface current on the feedline and the band-notched structure when the state of PIN diodes is ON and OFF, while the bias voltage is fixed at 0 V. It can be seen that, at band-notched frequencies, the energy is trapped in the notch band structure rather than passing through the feedline.

As is illustrated in Figure 5, a notch band shows up on the basis of UWB spectrum. The measurement of the reflection coefficient is obtained when PIN diodes work at ON or OFF state, while the reverse voltage on varactors is fixed at 0 V. It is clear that the resonant frequency of notch band is 4.2 GHz when PIN diodes are at ON state, while the central frequency is 5.8 GHz when PIN diodes are at OFF state. When the PIN

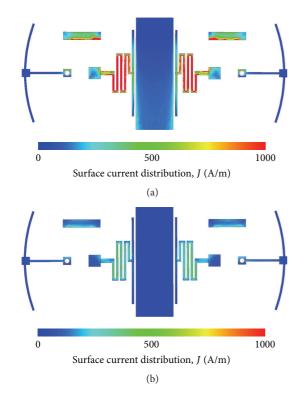


FIGURE 4: Distribution of the surface current on the feedline and the band-notched structure: (a) at 4.2 GHz when the state of PIN diodes is ON and bias voltage is 0 V; (b) at 5.8 GHz when the state of PIN diodes is OFF and bias voltage is 0 V.

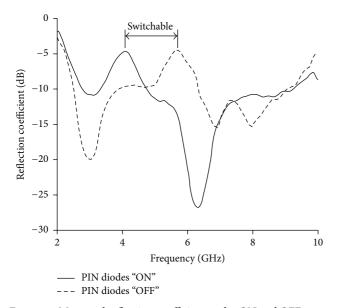


Figure 5: Measured reflection coefficient under ON and OFF states of PIN diode when the reverse voltage on varactors is fixed at 0 V.

diodes are ON, the electric length of resonance is relatively longer, which would lead to a lower resonant frequency.

Once the states of PIN diodes are fixed, the varying reverse voltage on varactors would produce a continuously changeable notch band. As demonstrated in Figure 6, when the bias voltage on varactors changes from 0 V to 15 V, the

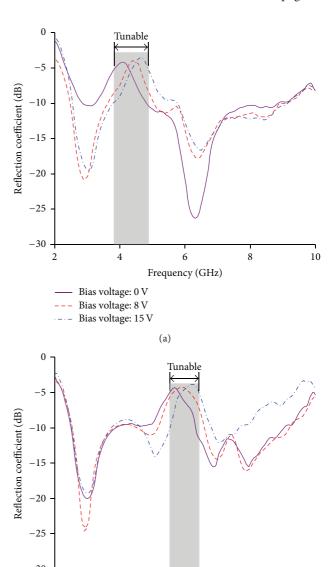


FIGURE 6: Measured reflection coefficient of the proposed reconfigurable band-notched UWB antenna with the reverse voltage on varactors varying from 0 V to 15 V: (a) the state of PIN diodes is ON; (b) the state of PIN diodes is OFF.

Bias voltage: 0 V Bias voltage: 8 V

Bias voltage: 15 V

6

Frequency (GHz)

10

central frequency of resonance varies continuously from 4.2 to 4.8 GHz and from 5.8 to 6.5 GHz under ON and OFF states of PIN diodes, respectively. The reason is that the capacitance of varactors ranges from 2.37 pF to 0.46 pF under 0 V–15 V reverse voltage, which yields the shifting resonance of notch bands.

Figures 5 and 6 together confirm the function of switchable and tunable band-notched UWB antenna, and the change of the notch band on spectrum fits the prediction

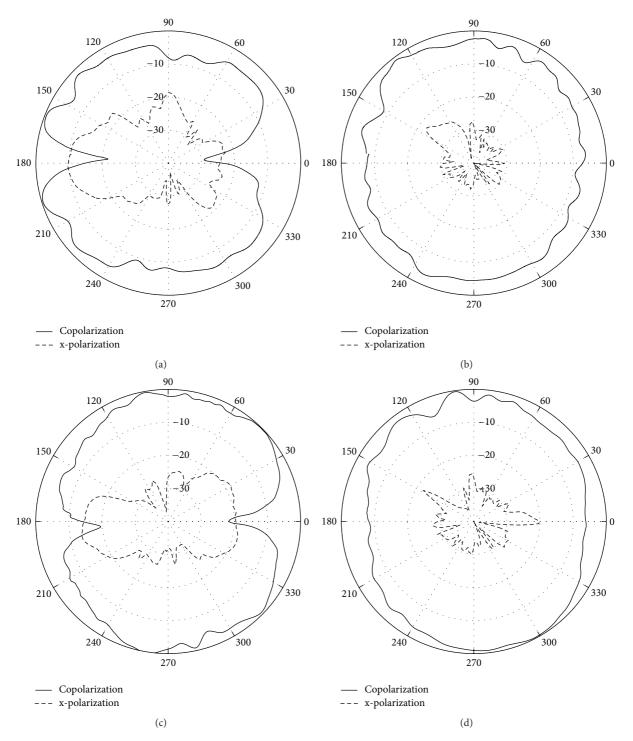


FIGURE 7: Measured normalized radiation patterns in YOZ plane and XOZ plane at two different frequencies: (a) YOZ plane at 4 GHz; (b) XOZ plane at 4 GHz; (c) YOZ plane at 8 GHz; (d) XOZ plane at 8 GHz.

of the equivalent circuit very well. That is to say, the PIN diodes work as a switch to choose the lower or upper notch frequency, and varactors produce the tunable performance. It should be noted that using the low loss varactors would improve the notch band performance. The normalized radiation patterns at 4 GHz and 8 GHz when the PIN diodes are

OFF and the bias voltage on varactors is 0 V are shown in Figure 7, which look like patterns of the monopole antenna: with 8-shape in y-z plane and omnidirectional performance in x-z plane. It is clear that the band-notched structure does not affect the omnidirectional radiation behaviour of UWB antenna in x-z plane (H-plane).

### 5. Conclusion

A novel UWB antenna with switchable and tunable notch bands has been presented. The ON and OFF states of PIN diodes can control the switch between lower and upper notch bands, while the reverse bias voltage on varactors can realize the tunable behaviours. Under the tendency of smart antennas and wearable devices, after combining with adaptive algorithm behind, the reconfigurable band-notched UWB antenna will fit more complicated circumstances.

### **Competing Interests**

The authors declare that they have no competing interests.

### **Authors' Contributions**

Wei Wu and Yun-Bo Li contributed equally to this work.

### Acknowledgments

This work was supported by the National Science Foundation of China (61571117, 61501112, 61501117, and 61522106) and the Scientific Research Foundation of Graduate School of Southeast University (YBJJ1435).

### References

- [1] J. H. Wang, Y. Z. Yin, and X. L. Liu, "Triple band-notched ultra-wideband antenna using a pair of novel symmetrical resonators," *IET Microwaves, Antennas and Propagation*, vol. 8, no. 14, pp. 1154–1160, 2014.
- [2] T. Li, H. Q. Zhai, L. Li, C. H. Liang, and Y. F. Han, "Compact UWB antenna with tunable band-notched characteristic based on microstrip open-loop resonator," *IEEE Antennas and Wireless Propagation Letters*, vol. 11, pp. 1584–1587, 2012.
- [3] A. Valizade, C. Ghobadi, J. Nourinia, and M. Ojaroudi, "A novel design of reconfigurable slot antenna with switchable band notch and multiresonance functions for UWB applications," *IEEE Antennas and Wireless Propagation Letters*, vol. 11, pp. 1166–1169, 2012.
- [4] S. A. Aghdam, "A Novel UWB monopole antenna with tunable notched behavior using varactor diode," *IEEE Antennas and Wireless Propagation Letters*, vol. 13, pp. 1243–1246, 2014.
- [5] Z. H. Hu, P. S. Hall, J. R. Kelly, and P. Gardner, "UWB pyramidal monopole antenna with wide tunable band-notched behaviour," *Electronics Letters*, vol. 46, no. 24, pp. 1588–1590, 2010.
- [6] Z.-H. Tu, W.-A. Li, and Q.-X. Chu, "Single-layer differential CPW-fed notch-band tapered-slot UWB antenna," *IEEE Anten*nas and Wireless Propagation Letters, vol. 13, pp. 1296–1299, 2014.
- [7] B. Badamchi, J. Nourinia, C. Ghobadi, and A. V. Shah-mirzadi, "Design of compact reconfigurable ultra-wideband slot antenna with switchable single/dual band notch functions," *IET Microwaves, Antennas and Propagation*, vol. 8, no. 8, pp. 541–548, 2014.
- [8] N. Wang and P. Gao, "A novel printed UWB and Bluetooth antenna with quad band-notched characteristics," in Proceedings of the International Workshop on Microwave and Millimeter

- Wave Circuits and System Technology (MMWCST '13), pp. 150–153, Chengdu, China, October 2013.
- [9] Y. F. Weng, S. W. Cheung, and T. I. Yuk, "Triple band-notched UWB antenna using meandered ground stubs," in *Proceedings* of the 6th Loughborough Antennas and Propagation Conference (LAPC '10), vol. 10, pp. 341–344, IEEE, Loughborough, UK, November 2010.
- [10] J. Wang, Y. Yin, T. Wang, and X. Liu, "Compact dual-band-notched UWB antenna with high notch-band-edge selectivity," *Microwave and Optical Technology Letters*, vol. 55, no. 10, pp. 2507–2513, 2013.
- [11] A. Foudazi, H. R. Hassani, and S. M. A. Nezhad, "Small UWB planar monopole antenna with added GPS/GSM/WLAN bands," *IEEE Transactions on Antennas and Propagation*, vol. 60, no. 6, pp. 2987–2992, 2012.
- [12] J. Xu, D. Shen, X. Zhang, and K. Wu, "A compact disc ultrawideband (UWB) antenna with quintuple band rejections," *IEEE Antennas and Wireless Propagation Letters*, vol. 11, pp. 1517–1520, 2012.
- [13] N. Tasouji, J. Nourinia, C. Ghobadi, and F. Tofigh, "A novel printed UWB slot antenna with reconfigurable band-notch characteristics," *IEEE Antennas and Wireless Propagation Letters*, vol. 12, pp. 922–925, 2013.
- [14] A. A. Kalteh, G. R. DadashZadeh, M. Naser-Moghadasi, and B. S. Virdee, "Ultra-wideband circular slot antenna with reconfigurable notch band function," *IET Microwaves, Antennas and Propagation*, vol. 6, no. 1, pp. 108–112, 2012.
- [15] L. Kurra, M. P. Abegaonkar, A. Basu, and S. K. Koul, "Switchable and tunable notch in ultra-wideband filter using electromagnetic bandgap structure," *IEEE Microwave and Wireless Com*ponents Letters, vol. 24, no. 12, pp. 839–841, 2014.
- [16] E. Antonino-Daviu, M. Cabedo-Fabrés, M. Ferrando-Bataller, and A. Vila-Jimenez, "Active UWB antenna with tunable bandnotched behaviour," *Electronics Letters*, vol. 43, no. 18, pp. 959– 960, 2007.

Hindawi Publishing Corporation International Journal of Antennas and Propagation Volume 2016, Article ID 2975425, 9 pages http://dx.doi.org/10.1155/2016/2975425

### Research Article

### A Wideband Antenna with Circular and Rectangular Shaped Slots for Mobile Phone Applications

## Wei-Hua Zong, <sup>1</sup> Xiao-Mei Yang, <sup>1</sup> Xia Xiao, <sup>1</sup> Shan-Dong Li, <sup>2</sup> Xiang-Yang Wei, <sup>3</sup> Zhe-Jun Jin, <sup>1</sup> and Xiao-Yun Qu<sup>4</sup>

Correspondence should be addressed to Wei-Hua Zong; weihuazong@126.com

Received 14 April 2016; Revised 16 June 2016; Accepted 22 June 2016

Academic Editor: Renato Cicchetti

Copyright © 2016 Wei-Hua Zong et al. This is an open access article distributed under the Creative Commons Attribution License, which permits unrestricted use, distribution, and reproduction in any medium, provided the original work is properly cited.

A wideband slot antenna for mobile phone applications is proposed. The antenna has two slots with open ends etched on the opposite edges of the ground plane. The main slot, of total length of 59 mm, is composed of a rectangle connected to a circle having radius of 5 mm. Another slot, having a rectangular shape with width of 2.8 mm and length of 26 mm, is employed to enhance the antenna bandwidth. The slots are fed by means of a rectangular monopole connected to a circular patch joined to a bent 50  $\Omega$  microstrip transmission line forming two right angles. To obtain a wideband impedance matching, the upper edge of the monopole and a part of the feeding line evolve along the top edge of the two slots. To reduce the antenna size, the upper part of the board above the slot (just 3 mm from the slot) is folded vertically to the ground plane. The measured bandwidth of the antenna is 0.698–1.10 GHz and 1.64–2.83 GHz covering LTE700/2300/2500, GSM850/900/1800/1900, and UMTS bands.

### 1. Introduction

Antennas for modern smart mobile phones are characterized by a low profile and multiple frequency bands. The widely used frequency bands for mobile communication include LTE700 (698–787 MHz), GSM850 (824–894 MHz), GSM900 (880–960 MHz), GSM1800 (1710–1880 MHz), GSM1900 (1850–1990 MHz), UMTS (1920–2170 MHz), LTE2300 (2305–2400 MHz), and LTE2500 (2500–2690 MHz). The conventional mobile phone antennas include three basic types of PIFAs (planar inverted-F antennas), printed monopole antennas, and printed slot antennas. With several limitations concerning the antenna size, it is not easy to design an antenna to cover the frequency bands 698–960 MHz and 1710–2690 MHz simultaneously. Several techniques based on conventional handset antennas, including the impedance matching circuit using lumped components [1–3], the

reconfigurable antenna using PIN diodes [4–7], and the tunable antenna using tunable capacitors [8], have been employed for the antenna design. These techniques involve lumped components or DC feeding system, which increase the complexity of the design and the realization cost.

In this paper, we address the design of a printed slot antenna for mobile phones. The most popularly used slot antennas adopt rectangular shape as the basic unit to form the desired shaped slot [9–14]. The antenna in [9] is composed of two open-ended slots cut at the same edge of the system ground plane. One of the slots has a rectangular shape and the other has an L shape. The bandwidth of the antenna is narrow and consequently only the frequency bands of the GSM850 and GSM900 are covered in the lower frequency band. The antenna in [10] consists of a C-shaped and an L-shaped slot occupying a 21  $\times$  45 mm² area on the ground plane. The slots in [9, 10] are both fed by 50  $\Omega$  microstrip

<sup>&</sup>lt;sup>1</sup>School of Electronics and Information, Qingdao University, Qingdao 266071, China

<sup>&</sup>lt;sup>2</sup>College of Physics and Key Laboratory of Photonics Materials and Technology in University of Shandong, Laboratory of Fiber Materials and Modern Textile, The Growing Base for State Key Laboratory, Qingdao University, Qingdao 266071, Shandong, China

<sup>&</sup>lt;sup>3</sup>RF Department, Goertek Inc., Qingdao 266071, China

<sup>&</sup>lt;sup>4</sup>No. 513 Institute, No. 5 Academy, China Aerospace Science and Technology Corporation, Yantai 264000, China

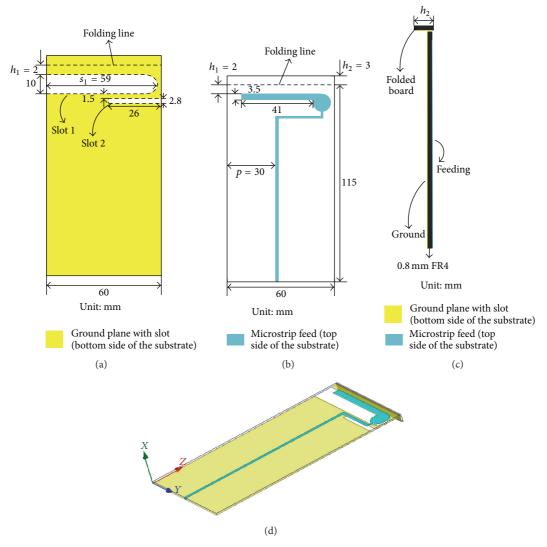


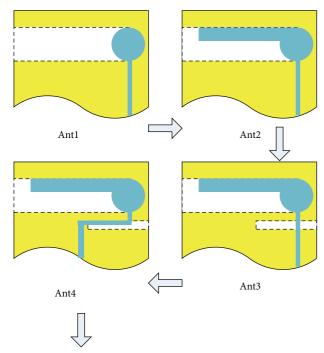
FIGURE 1: Configuration of the proposed antenna. (a) Bottom view. (b) Top view. (c) Side view. (d) 3D view.

line with straight shape. The slot antennas proposed in recent years employ suitable techniques for the excitation of the radiating slots [11–14]. Two monopoles connected to a 50  $\Omega$ microstrip line to feed two rectangular slots opened at the same edge of system board are proposed in [11]. L-shaped feeding structures are adopted to feed rectangular slots in [12, 13]. A simple printed monopole slot antenna and a Cshaped strip connected orthogonal to the bottom edge of the system ground plane are proposed in [12] for pentaband operation of a mobile handset. A simple printed monopole slot antenna with two parasitic shorted strips for pentaband wireless wide area network operation in a slim mobile phone is presented in [13], while in [14] a monopole with multiple branches and a parasitic ground strip with an L-shaped open slot are employed to realize an antenna for a multiband mobile handset.

A mobile antenna employing a circular radiating slot, having a frequency band ranging between 1.73 and 11 GHz, obtained by slightly modifying the UWB antenna presented

in [15], was proposed in [16]. A better performance is achieved by the antenna presented in [17], which, adopting an electromagnetic band gap (EBG) structure integrated in the ground plane, allows covering the frequency band of 1.53–11 GHz. Finally, inverted L-shaped slot and feeding structures have been employed in [18] to cover the 0.69–0.97 GHz and 2.3–3.32 GHz frequency bands.

In this paper, a novel slot antenna for mobile phone applications is presented. The antenna consists in a new version of the antenna presented in [18] featuring a smaller size and a wider bandwidth. The antenna is composed of two slots. The main slot, whose shape is a combination of a rectangle and of a circle, presents smaller width compared with the one in [18]. An additional slot having rectangular shape is employed to excite a resonance at the higher frequency band. The two slots are fed with a bent shape structure to obtain wideband impedance matching. The upper part of the board, at a distance of 3 mm above the slot, is folded vertically to the ground plane to reduce the antenna size. As a comparison



Proposed antenna (see Figure 1)

FIGURE 2: Design evolution.

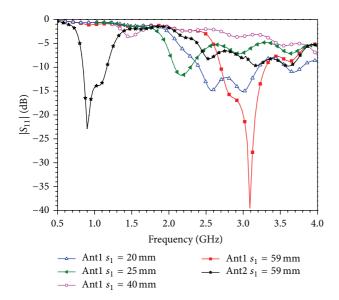


FIGURE 3: Frequency behavior of the parameter  $|S_{11}|$  versus the slot length  $s_1$  for Ant1 and Ant2.

in Table 1, the sizes and the bandwidths of the slot antennas available in the literature together with those proposed in the paper are reported.

### 2. Antenna Design

2.1. Antenna Configuration. The configuration of the proposed antenna is shown in Figure 1. The antenna is printed

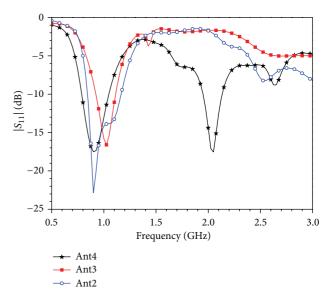


FIGURE 4: Frequency behavior of the parameter  $|S_{11}|$  of Ant4 compared with that of Ant3 and Ant2.

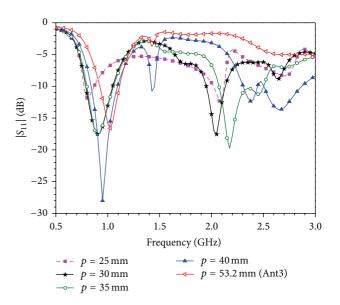


FIGURE 5: Frequency behavior of the parameter  $|S_{11}|$  versus the parameter p for Ant4.

on a 0.8 mm thick FR4 substrate with relative dielectric constant of 4.4, loss tangent of 0.02, and size of  $60 \times 115$  mm². Two open-ended slots, called slot 1 and slot 2, are etched at the opposite edges of the ground plane. Slot 1 with 10 mm width and total length of 59 mm is composed of a rectangle connected to a circle. Slot 2 has a rectangular shape with 2.8 mm width and 26 mm length. The two slots are excited by a rectangular monopole connected to a circular patch joined to a bent 50  $\Omega$  microstrip line. The circular patch and slot have the same radius of 5 mm, and the same center coordinates in the yz-plane. The footprints on the ground plane of the monopole and of the bent part of the feeding microstrip line are located within the slot regions (see Figure 2). The upper

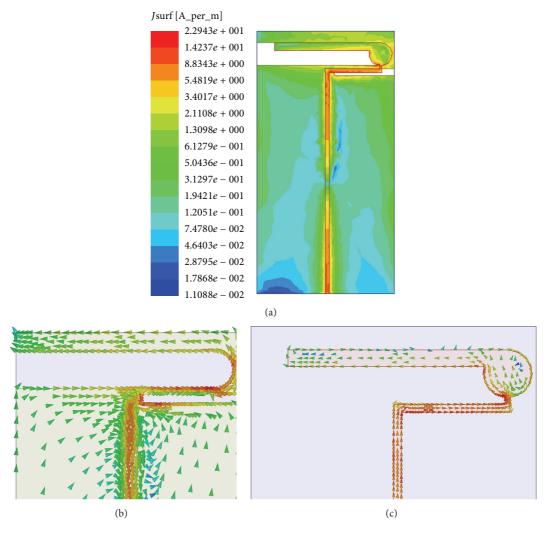


FIGURE 6: Simulated current distributions at 0.9 GHz. (a) Magnitudes of the surface current distributions on ground plane and top layer. (b) Vector representation on ground plane. (c) Vector representation on top layer.

TABLE 1: Comparison of the performance of the published slot antennas.

| Reference | PCB size (mm × mm) | Slot size (mm × mm) | Metal strip size (mm × mm) | Bandwidth (MHz)     |
|-----------|--------------------|---------------------|----------------------------|---------------------|
| [9]       | 40 × 100           | 15 × 40             | /                          | 822-962, 1670-2670  |
| [10]      | $45 \times 121$    | $21 \times 45$      | /                          | 778-1070, 1674-2741 |
| [11]      | $60 \times 110$    | $15 \times 51$      | /                          | 795–1035, 1700–2205 |
| [12]      | $60 \times 115$    | $15 \times 50$      | $10 \times 60$             | 750–1040, 1635–2485 |
| [13]      | $60 \times 115$    | $3.5 \times 40$     | $7 \times 60$              | 800-1300, 1710-2325 |
| [14]      | $60 \times 105$    | $15 \times 59$      | /                          | 660-1065, 1665-3000 |
| [18]      | $60 \times 115$    | $20 \times 59$      | /                          | 690-970, 2300-3320  |
| Proposed  | $60 \times 115$    | $14.3 \times 60$    | $3 \times 60$              | 698-1100, 1640-2830 |

part of the board, at a distance of 3 mm above the slot, is folded vertically to the ground plane to reduce the antenna size. The antenna has been designed following the design steps indicated in Figure 2 as Ant1, Ant2, Ant3, Ant4, and the proposed antenna.

2.2. Ant1 and Ant2 Analyses. Ant1 has a radiating slot whose geometry consists in an open-ended rectangle and

a closing semicircle. The slot is fed with a  $50\,\Omega$  microstrip line joined to a circular patch. Figure 3 shows the effect of slot length on  $|S_{11}|$  of Antl. The numerical simulations were performed using the full-wave commercial software Ansys High Frequency Structure Simulator (HFSS) based on the finite-element method. It is seen that Antl obtains a wide bandwidth in the upper frequency band with a slot length of  $s_1=20\,\mathrm{mm}$ . A longer slot results in lower resonance

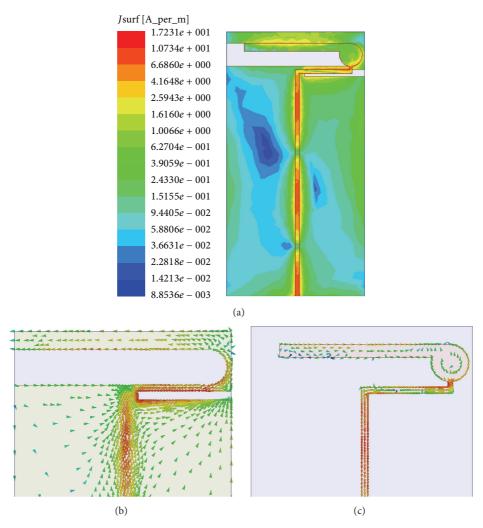


FIGURE 7: Simulated current distributions at 2 GHz. (a) Magnitudes of the surface current distributions on ground plane and top layer. (b) Vector representation on ground plane. (c) Vector representation on top layer.

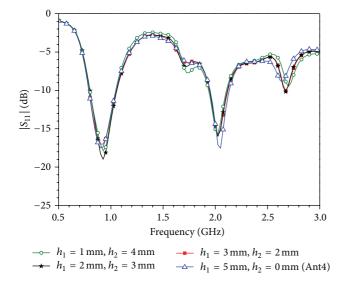


Figure 8: Frequency behavior of the parameter  $|S_{11}|$  of the proposed antenna versus the geometrical parameters  $h_1$  and  $h_2$ .

Table 2: Resonant frequencies and bandwidths of Ant1 and Ant2 for different values of the slot lengths  $s_1$ .

| Antenna | <i>s</i> <sub>1</sub> (mm) | Antenna first<br>resonant frequency<br>(GHz) | Bandwidth of<br>the first resonant<br>mode (GHz) |
|---------|----------------------------|--|--|
| Ant1    | 20                         | 2.6  | 2.2-4  |
| Ant1    | 25                         | 2.16   | 1.9-2.5  |
| Ant1    | 40                         | 1.48   | /  |
| Ant1    | 59                         | 0.95   | /  |
| Ant2    | 59                         | 0.9  | 0.82-1.23  |

but worse  $|S_{11}|$ . Table 2 gives the resonant frequencies and bandwidths of the first resonant modes for different values of the slot length  $s_1$ . The resonant frequency shifts to the lower frequencies and the bandwidth decreases as the parameter  $s_1$  increases. From Figure 3, it appears that, in the cases of

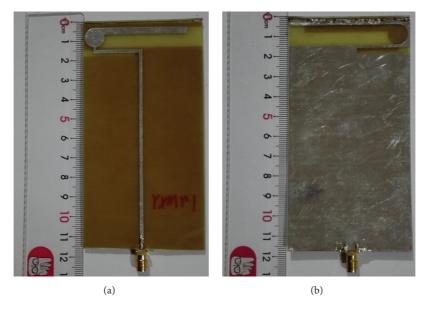


FIGURE 9: Photographs of the fabricated antenna. (a) Front view. (b) Back view.

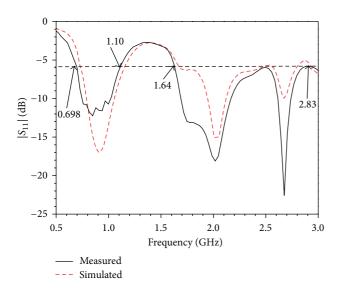


FIGURE 10: Frequency behavior of the parameter  $|S_{11}|$  of the proposed antenna.

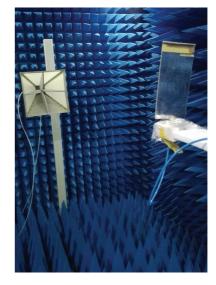


FIGURE 11: Antenna within the microwave anechoic chamber. The measurement setup adopted to measure the antenna radiation patterns can be observed.

 $s_1 = 40$  and 59 mm, the parameter  $|S_{11}|$  at the first resonant frequencies is worse than -6 dB.

To cover the lower band below 1 GHz, a long slot with a length of 59 mm is preferred. Impedance matching structure is required to reduce  $|S_{11}|$  of the first resonant mode. To this end, the feeding structure of Antl has been modified by adding a rectangular monopole to the end of the circular patch, giving rise to the antenna configuration identified as Ant2. In this design configuration the footprint of rectangular monopole falls inside the rectangular slot with its termination pointing toward the open end of the rectangular slot. In this way some current flow is excited around the slot realized on the ground plane. The optimized bandwidths for Ant2 are 0.82-1.23 GHz and 2.43-3.83 GHz. The left cutoff frequencies

for lower and upper bands are still too high to cover LTE700, GSM1800/1900, and UMTS. Thus, another slot (slot 2) having rectangular shape is added at Ant2 to adjust the bandwidth.

2.3. Ant3 Analysis and Ant4 Design. Ant3 is obtained by adding slot 2 directly below the main radiating slot of Ant2. Ant4 is finally obtained by moving the location of the microstrip line to the left side and bending it so that it results distributed along slot 2 (see Figure 2). Figure 4 shows the comparison of  $|S_{11}|$  of the three antennas. It is seen that Ant3 has worse  $|S_{11}|$  and narrower bandwidth than Ant2. The adoption of slot 2 worsens the antenna's matching. A

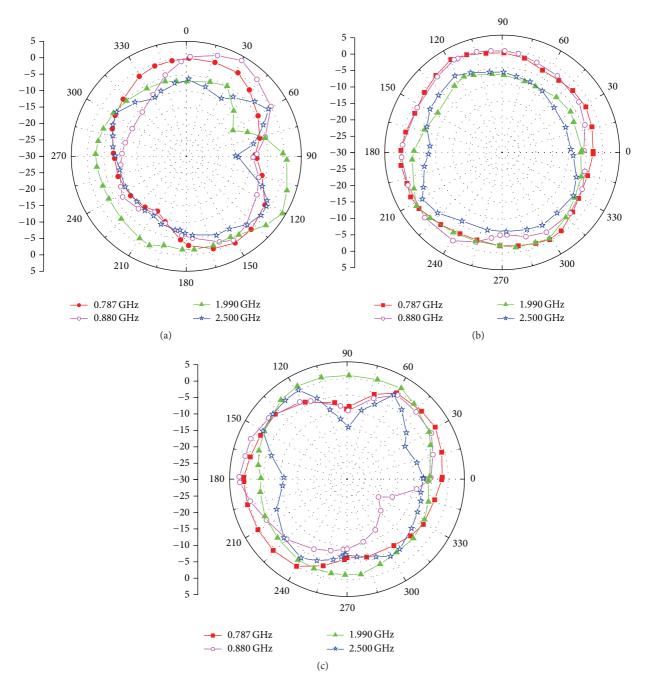


FIGURE 12: Measured radiation gain pattern (dBi). (a) xy-plane. (b) xz-plane. (c) yz-plane.

wider bandwidth and a frequency left-shifting are obtained simultaneously by a modification of the feeding microstrip location. The simulated -6 dB bandwidths of Ant4 cover the frequency bands 0.71–1.12 GHz and 1.70–2.73 GHz.

Figure 5 shows the effect of the feeding position p on the parameter  $|S_{11}|$ . It is seen that, by shifting the microstrip feeding line from the right corner ( $p = 53.2 \,\mathrm{mm}$ ) to the center of the board ( $p = 30 \,\mathrm{mm}$ ), the  $-6 \,\mathrm{dB}$  bands move to lower frequency. Moreover, a further shifting of the feeding line ( $p = 25 \,\mathrm{mm}$ ) results in a narrower bandwidth of the higher

frequency band. Therefore, p = 30 mm is chosen being the optimal value.

The surface currents excited at 0.9 GHz and 2 GHz on the metal surfaces of the monopole and of the ground plane are shown in Figures 6 and 7. From these figures it appears that on the monopole a significant level of surface current is excited at both frequencies, while the current flowing along the edges of slot 2 is for exciting a slot field useful to the compensation of the reactive component of the antenna input impedance with a consequent widening of the antenna bandwidth [19].

Finally, a higher surface current level is excited on the ground plane at the frequency of 0.9 GHz.

2.4. The Proposed Antenna Design. To reduce the antenna size, the upper part above the main slot is folded vertically to the board obtaining the final configuration of the proposed antenna. In order to determine the extension of the fold, identified by the parameter  $h_2$ , the frequency behavior of the parameter  $|S_{11}|$  has been investigated (see Figure 8). It is seen that folding the board has negligible effect on the antenna bandwidth. However, at frequencies around 2.5 GHz the parameter  $|S_{11}|$  becomes a little bit worse as the folded parameter  $h_2$  is increased. To balance the performances of size reduction and wide bandwidth,  $h_2 = 3$  mm and  $h_1 = 2$  mm are chosen.

### 3. Experiments and Discussion

The proposed antenna, whose prototype is shown in Figure 9, was fabricated and measured. The simulated and measured values of the parameter  $|S_{11}|$  are shown in Figure 10. The measurements were performed with an Agilent vector network analyzer N5224A in an ordinary laboratory without any microwave absorbers. As shown in Figure 10, there is a slight disagreement between measurement and simulation, which is mainly caused by the SMA connector adopted to excite the antenna. The measured bandwidths at  $-6\,\mathrm{dB}$  are in the frequency bands  $0.698-1.10\,\mathrm{GHz}$  and  $1.64-2.83\,\mathrm{GHz}$ , thus covering the LTE700/2300/2500, GSM850/900/1800/1900, and UMTS bands.

The radiation patterns were measured in a microwave anechoic chamber. The measurement environment is shown in Figure 11. Figure 12 shows the measured radiation pattern in the xy-, xz-, and yz-planes at 0.787, 0.88, 1.99, and 2.5 GHz. The patterns are omnidirectional in the xz-plane and nearomnidirectional in the xy-plane. The maximum gains at the four frequencies are 1.53, 2.91, 3.36, and 0.85 dBi, respectively. The antenna meets the directional requirement of mobile phones.

### 4. Conclusion

A low profile printed antenna formed by two slots and a suitable monopole used as exciter has been proposed. A circular shape has been adopted in the slot and in the feeding structures. To match the antenna, the feeding microstrip line has been folded keeping the folded sections parallel to the slots. The measurements performed on the antenna prototype confirm that the antenna is suitable to cover the LTE700/2300/2500, GSM850/900/1800/1900, and UMTS bands with near-omnidirectional radiation patterns. In conclusion, on the basis of the electrical characteristics, the small size and low profile, the antenna becomes suitable for smart phone applications.

### **Competing Interests**

The authors declare that they have no competing interests.

### Acknowledgments

This work was supported in part by the Natural Science Foundation of China (nos. 61501277 and 61307050) and Shandong Province Higher Educational Science and Technology Program (no. J14LN86).

### References

- [1] K.-L. Wong and P.-R. Wu, "Dual-wideband linear open slot antenna with two open ends for the LTE/WWAN smartphone," *Microwave and Optical Technology Letters*, vol. 57, no. 6, pp. 1269–1274, 2015.
- [2] K.-L. Wong and Y.-J. Li, "Low-profile open-slot antenna with three branch slots for triple-wideband LTE operation in the metal-framed smartphone," *Microwave and Optical Technology Letters*, vol. 57, no. 10, pp. 2231–2238, 2015.
- [3] J. Lee, Y. Liu, and H. Kim, "Mobile antenna using multiresonance feed structure for wideband operation," *IEEE Trans*actions on Antennas and Propagation, vol. 62, no. 11, pp. 5851– 5855, 2014.
- [4] S. W. Lee, H. S. Jung, and Y. J. Sung, "A reconfigurable antenna for LTE/WWAN mobile handset applications," *IEEE Antennas and Wireless Propagation Letters*, vol. 14, pp. 48–51, 2015.
- [5] C. Yoon, S.-G. Hwang, G.-C. Lee, W.-S. Kim, H.-C. Lee, and H.-D. Park, "A reconfigurable antenna using varactor diode for LTE MIMO applications," *Microwave and Optical Technology Letters*, vol. 55, no. 5, pp. 1141–1145, 2013.
- [6] S. W. Lee and Y. Sung, "Compact frequency reconfigurable antenna for LTE/WWAN mobile handset applications," *IEEE Transactions on Antennas and Propagation*, vol. 63, no. 10, pp. 4572–4577, 2015.
- [7] J. H. Lee and Y. Sung, "Reconfigurable hexa-band planar inverted-F antenna using a PIN diode for mobile handset," *Microwave and Optical Technology Letters*, vol. 55, no. 8, pp. 1926–1928, 2013.
- [8] S. M. Ali and K. Payandehjoo, "Tunable antenna techniques for compact handset applications," *IET Microwaves, Antennas and Propagation*, vol. 8, no. 6, pp. 401–408, 2014.
- [9] C.-I. Lin and K.-L. Wong, "Printed monopole slot antenna for internal multiband mobile phone antenna," *IEEE Transactions* on Antennas and Propagation, vol. 55, no. 12, pp. 3690–3697, 2007.
- [10] C.-H. Wu and K.-L. Wong, "Hexa-band internal printed slot antenna for mobile phone application," *Microwave and Optical Technology Letters*, vol. 50, no. 1, pp. 35–38, 2008.
- [11] S.-L. Zuo, Z.-Y. Zhang, and J.-J. Xie, "Design of dual-monopole slots antenna integrated with monopole strip for wireless wide area network mobile handset," *IET Microwaves, Antennas and Propagation*, vol. 8, no. 3, pp. 194–199, 2014.
- [12] K.-L. Wong, P.-W. Lin, and C.-H. Chang, "Simple printed monopole slot antenna for penta-band wireless wide area network operation in the mobile handset," *Microwave and Optical Technology Letters*, vol. 53, no. 6, pp. 1399–1404, 2011.
- [13] C.-H. Chang, W.-C. Wei, P.-J. Ma, and S.-Y. Huang, "Simple printed WWAN monopole slot antenna with parasitic shorted strips for slim mobile phone application," *Microwave and Optical Technology Letters*, vol. 55, no. 12, pp. 2835–2841, 2013.
- [14] C. Deng, Y. Li, Z. Zhang, and Z. Feng, "Planar printed multiresonant antenna for octa-band WWAN/LTE mobile handset," *IEEE Antennas and Wireless Propagation Letters*, vol. 14, pp. 1734–1737, 2015.

- [15] W.-S. Chen and C.-H. Lin, "A planar hybrid antenna for UWB application," *Microwave and Optical Technology Letters*, vol. 51, no. 5, pp. 1243–1246, 2009.
- [16] W.-H. Zong, X.-Y. Qu, Y.-X. Guo, and M.-X. Shao, "An ultrawideband antenna for mobile handset applications," *Advanced Materials Research*, vol. 383–390, pp. 4457–4460, 2012.
- [17] Z. Guo, H. Tian, X. Wang, Q. Luo, and Y. Ji, "Bandwidth enhancement of monopole UWB antenna with new slots and ebg structures," *IEEE Antennas and Wireless Propagation Letters*, vol. 12, pp. 1550–1553, 2013.
- [18] W. H. Zong, X. M. Yang, S. D Li, X. Y. Wei, and J. C. Hou, "Design and fabrication of a wideband slot antenna for Handset Applications," in *Proceedings of the IEEE International RF and Microwave Conference (RFM '15)*, Kuching, Malaysia, December 2015.
- [19] D. Caratelli, R. Cicchetti, G. Bit-Babik, and A. Faraone, "Circuit model and near-field behavior of a novel patch antenna for WWLAN applications," *Microwave and Optical Technology Letters*, vol. 49, no. 1, pp. 97–100, 2007.

Hindawi Publishing Corporation International Journal of Antennas and Propagation Volume 2016, Article ID 4791831, 7 pages http://dx.doi.org/10.1155/2016/4791831

### Research Article

### A Small Planar Antenna for 4G Mobile Phone Application

### Hu Jian-rong, Li Jiu-sheng, and Wu Di

Centre for THz Research, China Jiliang University, Hangzhou 310018, China

Correspondence should be addressed to Li Jiu-sheng; forever-li@126.com

Received 5 November 2015; Revised 26 February 2016; Accepted 2 March 2016

Academic Editor: Renato Cicchetti

Copyright © 2016 Hu Jian-rong et al. This is an open access article distributed under the Creative Commons Attribution License, which permits unrestricted use, distribution, and reproduction in any medium, provided the original work is properly cited.

The analysis and design of a small planar multiband antenna operating in the 4G frequency bands are presented. The numerical and experimental results demonstrated that the proposed antenna satisfies the requirement of 6 dB return loss for the impedance bandwidth of the LTE700/LTE2300/LTE2500 and WiMAX3500 bands. The gains at 750 MHz/2.3 GHz/2.6 GHz/3.5 GHz are 2.1 dBi/4.9 dBi/4.7 dBi/4.3 dBi, respectively. The measured radiation patterns verify the suitability of the antenna to be employed in mobile phones. The dimensions of the radiant patch are  $49 \times 10 \text{ mm}^2$ . The proposed antenna can be easily fabricated and customized to various 4G mobile phones as a compact internal antenna.

### 1. Introduction

With the rapid development of the fourth-generation (4G) mobile communication technologies, the mobile phone antennas have received substantial attention because of the wide applications made available in such systems [1-4]. In fact, these antennas, which are an important part of mobile phone terminals, affect the overall performance of these communication systems. The usual mobile phone antennas have been proved unable to meet the 4G wireless communication requirements of the multiband and broadband applications [5-7]. In the last few years, a variety of small Long Term Evolution (LTE) mobile phone antennas have become the hot topic of the communication industry research [8–11]. To address the difficulties of integrating antennas in 4G mobile phones, many efforts have been made to expand the performance of the antennas in the LTE bands [12-16]. However, these design solutions generally require large size or volumes, which may be not compatible with the new generation of mobile phone applications. Because of the extremely limited volume of a mobile terminal, it is very important to synthesize compact multifunctional and broadband antennas. In the near future, these consumer electronic devices will be capable of integrating multibands protocols (LTE, WiMAX, etc.) into one single communication system. Thus, the antenna for 4G mobile phones must be compact size and low profile.

In this paper, a multiband antenna for a 4G mobile terminal application is proposed. The antenna is made by means of compact multiresonator planar elements that occupy a size of  $49 \times 10 \times 1.6\,\mathrm{mm^3}$ . It covers multibands which include the LTE700 (698–787 MHz), LTE2300 (2305–2400 MHz), LTE2500 (2500–2690 MHz), and WiMAX3500 (3390–3600 MHz) operations. Good radiation characteristics within the operative antenna frequency band are obtained. Details of the proposed antenna design and of the related parametric analysis are presented and discussed in the next sections. With the attractive features described above, the proposed antenna is a promising candidate for wireless devices.

### 2. Antenna Configuration

The geometry of the proposed LTE-printed antenna is depicted in Figure 1. The antenna has a planar structure and a simple configuration consisting of two horizontal-U rings, a feed, a shorting line, and a ground plane. It is fed by a  $50~\Omega$  minicoaxial line connected between the feeding point (point A) of the driven monopole and the phone-display ground point (point B). The proposed antenna is fabricated on a commercially available FR4 substrate having thickness of 1.6 mm, relative permittivity of 4.4, and loss tangent of 0.024.

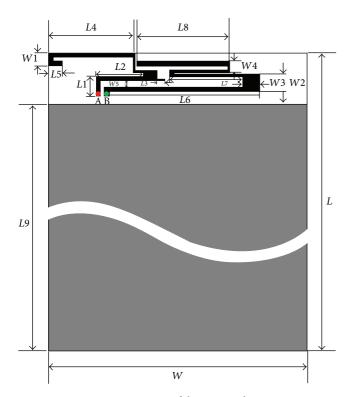


Figure 1: Geometries of the proposed antenna.

The system ground plane of the antenna has dimensions of  $108 \times 60 \text{ mm}^2$ . The area where the ground plane is not present has dimensions of about of  $49 \times 10 \text{ mm}^2$ . Thus, the size of this antenna is suitable for mobile phone applications.

The values of the design parameters shown in Figure 1 were evaluated by means of an extensive parametric analysis performed using the commercial software HFSS. After completing the optimization process the dimensions of the proposed antenna have been set as follows:  $L=120 \,\mathrm{mm}$ ,  $L1=4.5 \,\mathrm{mm}$ ,  $L2=11 \,\mathrm{mm}$ ,  $L3=2 \,\mathrm{mm}$ ,  $L4=20 \,\mathrm{mm}$ ,  $L5=3 \,\mathrm{mm}$ ,  $L6=34 \,\mathrm{mm}$ ,  $L7=16 \,\mathrm{mm}$ ,  $L8=20 \,\mathrm{mm}$ ,  $L9=108 \,\mathrm{mm}$ ,  $W=60 \,\mathrm{mm}$ ,  $W1=3 \,\mathrm{mm}$ ,  $W2=4 \,\mathrm{mm}$ ,  $W3=4 \,\mathrm{mm}$ ,  $W4=2.5 \,\mathrm{mm}$ , and  $W5=1.5 \,\mathrm{mm}$ . Based on the optimized design dimensions, a prototype of the proposed antenna depicted in Figure 2 was realized and tested.

### 3. Parameters Study

Figure 3 shows the frequency behavior of the antenna reflection coefficient for different lengths of the geometrical parameter L2 when the other parameters are kept constant to their optimized values. From Figure 3 it appears that the length L2 mainly controls the second antenna resonance frequency  $f_2$ . In particular, it is found that as the length L2 increases, the second resonance frequency  $f_2$  moves upward. From the figure, one can also see that the resonant frequency is of 2.6 GHz and the impedance bandwidth is 2.148~2.697 GHz, thus covering the LTE2300/LTE2500 frequency band, when the length L2 is of 11 mm. Therefore, the length of the parameter L2 is set to 11 mm.

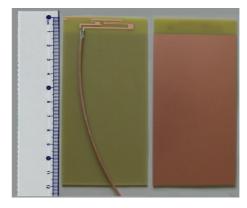


FIGURE 2: Photograph of the fabricated antenna with short feeding cable.

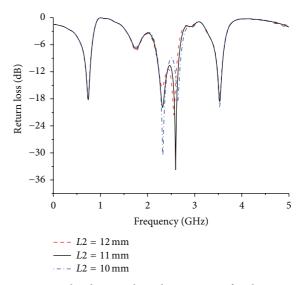


FIGURE 3: Simulated return loss characteristics for the proposed antenna for various values of *L*2.

Figure 4 illustrates the frequency behavior of the antenna reflection coefficient when the length of the parameter L7 varies from 15 mm to 17 mm when the other parameters are kept constant. From this figure it appears that the third resonance frequency  $f_3$  moves downward as the length of the parameter L7 is increased. The length of L7 mainly controls the third resonance frequency  $f_3$  for the 3.5 GHz WiMAX band. As is shown in Figure 4, when L7 is equal to 16 mm, the resonant frequency is of 3.53 GHz while the antenna bandwidth is in the frequency range 3.392~3.632 GHz. Therefore, the length of the parameter L7 is set to 16 mm so as to assure a resonance frequency at  $f_3$ .

A different behavior of the reflection coefficient with respect to the variation of the geometrical parameter L8 is observed in Figure 5. In fact, when this parameter increases from 18 mm to 22 mm, while maintaining the other structure parameters to the values of the optimized design, both the first resonance frequency  $f_1$  and the third resonance frequency  $f_3$  move downward. In particular, when L8 is of 20 mm, the first resonance frequency  $f_1$  and impedance

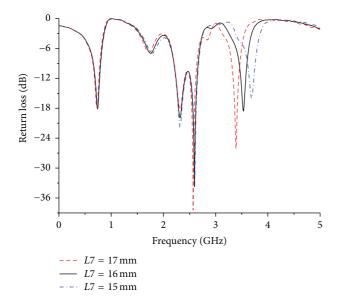


FIGURE 4: Simulated return loss characteristics for the proposed antenna for various values of *L*7.

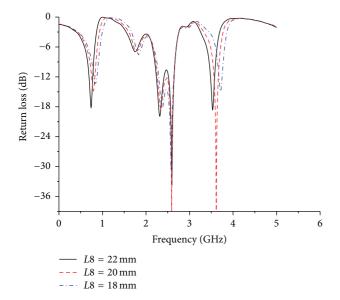
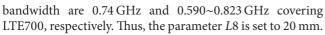


FIGURE 5: Simulated return loss characteristics for the proposed antenna for various values of *L*8.



Finally, in Figure 6 the simulated return loss of the proposed antenna for the different values of the widths W5 is shown. As in the other cases the other antenna geometrical parameters are kept constant. From Figure 6 it can be seen that both the first resonance frequency  $f_1$  and the third resonance frequency  $f_3$  move upward as the width W5 increases. In particular, when the width of W5 equals 1.5 mm, the first resonance frequency is 0.74 GHz and the impedance bandwidth defined by 6 dB return loss is  $0.590 \sim 0.823$  GHz, thus covering the LTE700 frequency band. At the same time, the third resonance frequency is 3.5 GHz and

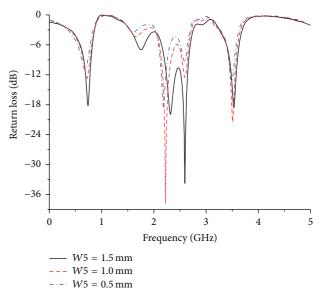


FIGURE 6: Simulated return loss characteristics for the proposed antenna for various values of *W*5.

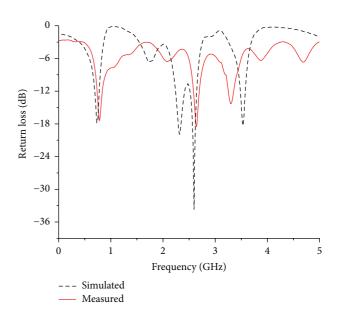


FIGURE 7: Simulated and measured return loss versus frequencies of the proposed antenna.

the impedance bandwidth is 210 MHz (3.39~3.60 GHz) at the 3.5 GHz WiMAX band. Therefore, the parameter W5 is chosen to be W5 = 1.5 mm.

### 4. Results and Discussions

An antenna prototype (see Figure 2) designed using the geometric parameters obtained by means of the parametric analysis presented above has been realized and measured. The proposed antenna has been measured using an Agilent PNA 8362B Network Analyzer in a frequency range from 45 to 5000 MHz. Figure 7 compares the frequency behavior of the simulated and measured return loss (reflection

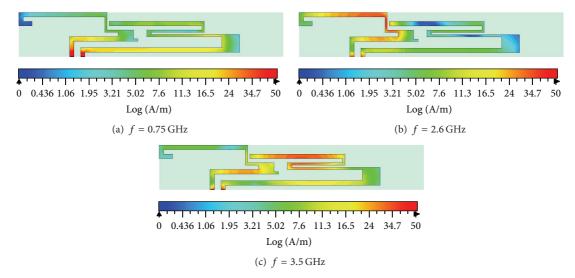


FIGURE 8: Surface current distributions on the radiating patch at (a) 0.75 GHz; (b) 2.6 GHz; and (c) 3.5 GHz.

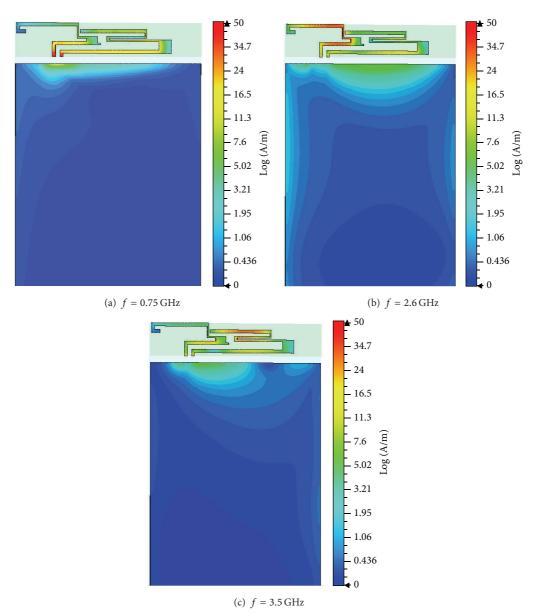


FIGURE 9: Surface current distributions on the proposed antenna at (a) 0.75 GHz; (b) 2.6 GHz; and (c) 3.5 GHz.

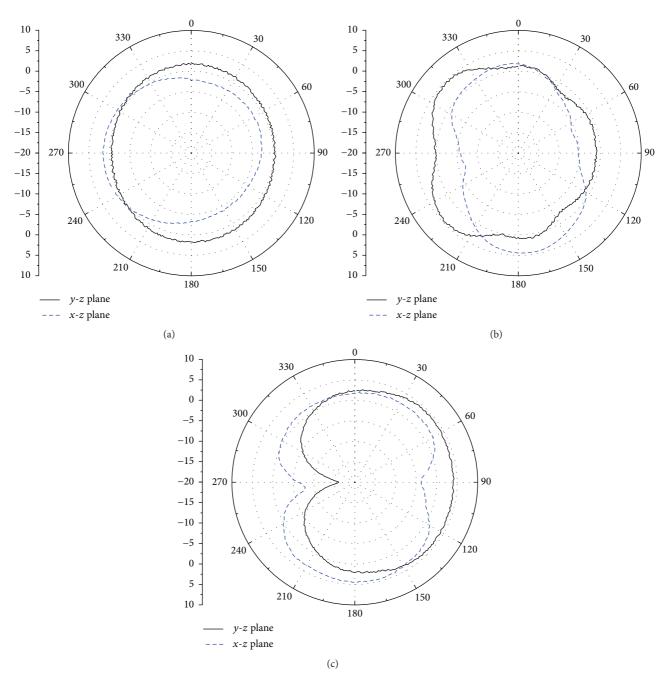


FIGURE 10: Measured radiation patterns of the proposed antenna for the LTE operation frequencies at (a) 0.75 GHz; (b) 2.6 GHz; and (c) 3.5 GHz.

coefficients) of the proposed antenna. All frequency bands are covered within the 6 dB of return loss, which is a widely used standard in the mobile phone antennas. The discrepancy observed between the computed and measured values of the reflection coefficient is due to the substrate and realization tolerances, as well as to the effect of the SMA connector and of the soldering points. When the antenna is carefully realized the measured impedance bandwidth is of 230 MHz (0.59 GHz~0.82 GHz, 32.6%) for the LTE 700 (698–787 MHz), of 550 MHz (2.15 GHz~2.70 GHz, 22.68%)

for the LTE2300 (2305–2400 MHz) and the LTE2500 (2500–2690 MHz), and of 230 MHz (3.40 GHz $\sim$ 3.63 GHz, 6.54%) for the 3.5 GHz WiMAX.

The numerical simulations were performed using the full-wave commercial software HFSS. This software was used to evaluate and verify the three resonant frequencies 0.75, 2.6, and 3.5 GHz, which mainly depend on the lengths of the different current paths along the two horizontal-U rings. Figures 8(a)–8(c) show the surface current density excited along the two horizontal-U rings antennas at the three

resonant frequencies 0.75, 2.6, and 3.5 GHz, respectively. In Figure 8(a), the lowest band surface current density distribution along the two input antenna ports at the resonant frequency of 0.75 GHz is shown. A larger surface current density flows along the first horizontal-U ring when the resonant frequency is 2.6 GHz as it is observed in Figure 8(b). However, larger surface current densities flow along the second horizontal-U ring when the resonant frequency is 3.5 GHz as is shown in Figure 8(c). Figures 9(a)-9(c) show the surface current density excited along the radiating patch and on the ground plane at the three resonant frequencies 0.75, 2.6, and 3.5 GHz, respectively. The emission phenomena take place along the U rings, at the patch corners, and at the substrate truncations where the conversion of surface waves into volume waves occurs [17]. In conclusion, the maximum amplitude of the surface current distribution excited on the antenna at the three resonant frequencies is located in different parts of the radiating structure.

Figure 10 shows the measured far-field radiation patterns in the E plane (x-z plane) and H plane (y-z plane). Figures 10(a)–10(c) show the radiation patterns at 0.75 GHz, 2.6 GHz, and 3.5 GHz, which are the resonance centre frequencies, respectively. That is to say, the proposed printed antenna covers three LTE bands and one WiMAX band. As evidenced by the radiation patterns it appears that the proposed antenna displays nearly omnidirectional radiation characteristics in the H plane, and monopole-like radiation pattern characteristics in the E plane at the considered frequencies. Moreover, since the planar radiating structure is realized on a single side printed circuit board is easy to manufacture.

### 5. Conclusions

A planar antenna for 4G mobile communication systems has been presented, realized, and tested experimentally. The obtained impedance bandwidth across the operating bands can reach about 356/413/237 MHz for the LTE bands and 210 MHz for the WiMAX band while the peak gains are about 2.1/4.7/4.3 dBi and 4.3 dBi, respectively. Good radiation characteristics across the operative bands have been also confirmed. The proposed antenna has a planar structure so it is easy to fabricate at low cost by printing it directly on the flexible printed circuit board of the mobile phone. Therefore, the proposed antenna meets the challenging requirements of the modern mobile phone communications.

### **Competing Interests**

The authors declare that they have no competing interests.

### Acknowledgments

The authors gratefully acknowledge the financial support from the Zhejiang Province Natural Science Fund under Grant no. LY15F050006 and National Natural Science Foundation of China under Grants nos. 61379024 and 61131005.

#### References

- [1] C.-H. Wu and K.-L. Wong, "Ultrawideband PIFA with a capacitive feed for penta-band folder-type mobile phone antenna," *IEEE Transactions on Antennas and Propagation*, vol. 57, no. 8, pp. 2461–2464, 2009.
- [2] H. S. Singh, M. Agarwal, G. K. Pandey, and M. K. Meshram, "A quad-band compact diversity antenna for GPS L1/Wi-Fi/ LTE2500/WiMAX/HIPERLAN1 applications," *IEEE Antennas and Wireless Propagation Letters*, vol. 13, pp. 249–252, 2014.
- [3] C. Y. D. Sim, K. R. Chen, and W. B. He, "A uniplanar printed antenna with an inverted L-shaped coupling feed for LTE/GSM/ DCS/PCS/UMTS operations," *International Journal of RF and Microwave Computer-Aided Engineering*, vol. 22, no. 5, pp. 610–618, 2012
- [4] M. E. de Cos, M. Mantash, A.-C. Tarot, and F. Las-Heras, "Dual-band coplanar waveguide-fed smiling monopole antenna for WiFi and 4G long-term evolution applications," *IET Microwaves, Antennas and Propagation*, vol. 7, no. 9, pp. 777–782, 2013.
- [5] J. Ilvonen, R. Valkonen, J. Holopainen, and V. Viikari, "Multi-band frequency reconfigurable 4G handset antenna with MIMO capability," *Progress in Electromagnetics Research*, vol. 148, pp. 233–243, 2014.
- [6] P. V. Naidu and A. Malhotra, "A small ACS-fed tri-band antenna employing C and L shaped radiating branches for LTE/WLAN/ WiMAX/ITU wireless communication applications," *Analog Integrated Circuits and Signal Processing*, vol. 85, no. 3, pp. 489–496, 2015.
- [7] J.-H. Lu and F.-C. Tsai, "Planar small-size LTE/WWAN tablet computer antenna with eight-band operation," *Journal of Electromagnetic Waves and Applications*, vol. 29, no. 8, pp. 1032– 1046, 2015.
- [8] X. Zhao, K. Kwon, and J. Choi, "MIMO antenna using resonance of ground planes for 4G mobile application," *Journal of Electromagnetic Engineering and Science*, vol. 13, no. 1, pp. 51–53, 2013.
- [9] S. Verma and P. Kumar, "Compact triple-band antenna for WiMAX and WLAN applications," *Electronics Letters*, vol. 50, no. 7, pp. 484–486, 2014.
- [10] Y. Li and W. Yu, "A miniaturized triple band monopole antenna for WLAN and WiMAX applications," *International Journal of Antennas and Propagation*, vol. 2015, Article ID 146780, 5 pages, 2015
- [11] A. M. Asghar, M. Malick, M. Karlsson, and A. Hussain, "A multi-wideband planar monopole antenna for 4G devices," *Microwave and Optical Technology Letters*, vol. 55, no. 3, pp. 589–593, 2013.
- [12] J. H. Lee and Y. Sung, "A simple penta-band reconfigurable antenna for mobile device applications," *Microwave and Optical Technology Letters*, vol. 56, no. 3, pp. 769–774, 2014.
- [13] C.-H. Chang and K.-L. Wong, "Printed λ/8-PIFA for pentaband WWAN operation in the mobile phone," *IEEE Transac*tions on Antennas and Propagation, vol. 57, no. 5, pp. 1373–1381, 2009
- [14] D. Kang and Y. Sung, "Compact hexaband PIFA antenna for mobile handset applications," *IEEE Antennas and Wireless Propagation Letters*, vol. 9, pp. 1127–1130, 2010.
- [15] A. Cabedo, J. Anguera, C. Picher, M. Ribó, and C. Puente, "Multiband handset antenna combining a PIFA, slots, and ground plane modes," *IEEE Transactions on Antennas and Propagation*, vol. 57, no. 9, pp. 2526–2533, 2009.

- [16] Y. K. Park and Y. Sung, "A reconfigurable antenna for quad-band mobile handset applications," *IEEE Transactions on Antennas and Propagation*, vol. 60, no. 6, pp. 3003–3006, 2012.
- [17] D. Caratelli, R. Cicchetti, G. Bit-Babik, and A. Faraone, "Circuit model and near-field behavior of a novel patch antenna for WWLAN applications," *Microwave and Optical Technology Letters*, vol. 49, no. 1, pp. 97–100, 2007.

Hindawi Publishing Corporation International Journal of Antennas and Propagation Volume 2016, Article ID 9071610, 8 pages http://dx.doi.org/10.1155/2016/9071610

### Research Article

# A Novel Dual-Band Circularly Polarized Rectangular Slot Antenna

### Biao Li, 1 Yang Ding, 2 and Ying-Zeng Yin 3

<sup>1</sup>CAST-Xi'an Institute of Space Radio Technology, Xi'an, Shaanxi 710100, China

Correspondence should be addressed to Biao Li; libiao504@163.com

Received 21 November 2015; Revised 9 March 2016; Accepted 7 April 2016

Academic Editor: Renato Cicchetti

Copyright © 2016 Biao Li et al. This is an open access article distributed under the Creative Commons Attribution License, which permits unrestricted use, distribution, and reproduction in any medium, provided the original work is properly cited.

A coplanar waveguide fed dual-band circularly polarized rectangular slot antenna is presented. The proposed antenna consists of a rectangular metal frame acting as a ground and an S-shaped monopole as a radiator. The spatial distribution of the surface current density is employed to demonstrate that the circular polarization is generated by the S-shaped monopole which controls the path of the surface currents. An antenna prototype, having overall dimension  $37 \times 37 \times 1 \,\mathrm{mm}^3$ , has been fabricated on FR4 substrate with dielectric constant 4.4. The proposed antenna achieves 10 dB return loss bandwidths and 3 dB axial ratio (AR) in the frequency bands 2.39–2.81 GHz and 5.42–5.92 GHz, respectively. Both these characteristics are suitable for WLAN and WiMAX applications.

### 1. Introduction

The rapid development in wireless communications with different standards has resulted in a huge demand for multiband antennas. Coplanar waveguide (CPW) fed slot antennas exhibit attractive features for multiband applications because of its favorable characteristics, such as wide bandwidth, light weight, low profile, less sensitivity to manufacturing tolerances, and easy integration with microwave integrated circuits. Circular polarization (CP) antennas have attracted much attention in the design of wireless systems since they are more effective in receiving and transmitting signals having arbitrary directions and polarizations. In addition, they can limit the multipath effect caused by walls and ground surfaces [1]. Moreover, the circular polarization provides better mobility and a field propagation less sensible to weather condition. Both these characteristics may prove useful in WLAN and WiMAX applications.

Several single-fed dual bands design solutions for the excitation of the circular polarization have been recently proposed in the literature [2–11]. Some of these solutions consist in the realization of an asymmetrical four-arm structure [7] or in spiral slots integrated in the ground plane [8]. A CPW-fed circular fractal slot antenna for dual-band

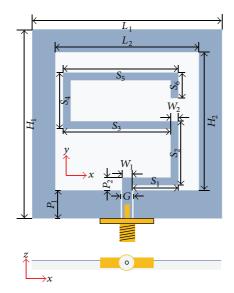
applications has been presented in [9]. However, only few designs of coplanar waveguide single-fed dual-frequency slot antennas for circular polarization have been reported in literature [9-11]. In any case, all the mentioned antennas have a complex structure. In this paper, a novel design of a CPWfed CP antenna with dual-band operation is introduced. The proposed antenna is formed by a rectangular metallic frame, acting as ground plane, inside which an S-shaped monopole is placed. The S-shaped monopole changes the path of the currents making the antenna more compact and suitable to excite a dual-band CP operation. The field vector composition, based on the surface current distribution flowing on the monopole and on the metal frame, is employed to explain the excitation of the dual-band CP operation. The antenna can find applications in wireless communication systems such as wireless routers and wireless access points. Details concerning the antenna design and experimental results are presented and discussed.

### 2. Antenna Configuration and Analysis

2.1. Configuration of the Proposed Antenna. Figure 1 shows the geometry and the photograph of the realized antenna.

<sup>&</sup>lt;sup>2</sup>AVIC-Xi'an Flight Automatic Control Research Institute, Xi'an, Shaanxi 710065, China

<sup>&</sup>lt;sup>3</sup>National Laboratory of Antennas and Microwave Technology, Xidian University, Xi'an, Shaanxi 710071, China



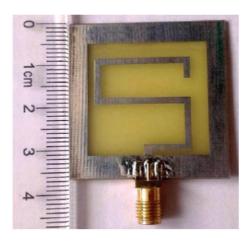


FIGURE 1: Geometry and photograph of the proposed antenna.

The antenna is printed on a low cost FR4 substrate having thickness 1 mm, dielectric constant 4.4, and loss tangent 0.02. The area of the antenna is  $L_1 \times H_1$ .  $L_2$  and  $H_2$  are the width and height of the rectangle slot. The S-shaped monopole, composed of 6 straight metal sections of width  $W_2$  and the lengths of  $S_1$ ,  $S_2$ ,  $S_3$ ,  $S_4$ ,  $S_5$ , and  $S_6$ , respectively, is fed by the coplanar waveguide. The CPW, designed for a 50  $\Omega$  characteristic impedance, consists of a stripline having width equal to 2 mm and a gap of 0.25 mm, respectively. The feed line is terminated with a standard SMA connector.

The full-wave commercial software Ansys HFSS has been adopted to determine the antenna performances. After completing the optimizing process the following antenna parameters were derived:  $L_1=37\,\mathrm{mm},\,H_1=37\,\mathrm{mm},\,L_2=28\,\mathrm{mm},\,H_2=27\,\mathrm{mm},\,P_1=5.5\,\mathrm{mm},\,P_2=2.5\,\mathrm{mm},\,G=2.5\,\mathrm{mm},\,W_1=2\,\mathrm{mm},\,W_2=1.5\,\mathrm{mm},\,S_1=9\,\mathrm{mm},\,S_2=12.5\,\mathrm{mm},\,S_3=21\,\mathrm{mm},\,S_4=11\,\mathrm{mm},\,S_5=22.5\,\mathrm{mm},\,\mathrm{and}\,S_6=5\,\mathrm{mm}.$  With these parameters an antenna with an impedance band in the frequency ranges 2.27–2.81 GHz and 4.94–6.08 GHz and with an axial ratio below 3 dB in the 2.39–2.98 GHz and 5.42–5.92 GHz frequency bands, respectively, is obtained. These features ensure the coverage of the frequency bands WLAN and WiMAX.

2.2. Antenna Evolution and Dual-Band Operation. Figure 2 illustrates the topological changes necessary to modify a straight monopole (Antenna Type I) into a more compact antenna having the desired dual-band characteristic (Antenna Type III), while Figure 3(a) shows the related  $S_{11}$  parameters.

In general, the length of monopole antenna is usually about a quarter-wavelength. Notice that the fundamental resonance frequency of Antenna Type I is of about 2.5 GHz, while the high-order resonant modes are employed to excite the circular polarization in the proposed S-shaped monopole

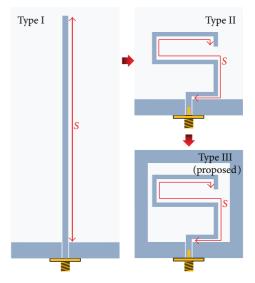


FIGURE 2: The evolution of the proposed antenna.

antenna (see Figures 8 and 9). When the antenna is operating at its resonant frequency, the imaginary part of its impedance becomes about zero. The simulated results of the input resistance and reactance of the three types of the antenna are shown in Figures 4(a) and 4(b). The surface currents of Antenna Type I have many null points due to the high-order modes, which will cause a deterioration of the radiation pattern. The current distribution along the S-shaped monopole (Antenna Types II and III) is different from that flowing on the straight monopole (Antenna Type I), exciting in this way a circularly polarized field whose AR, along the positive z-direction for Antenna Types II and III, are reported in Figure 3(b). By analyzing Figure 3 it can be observed that Antenna Type III is the one that presents the

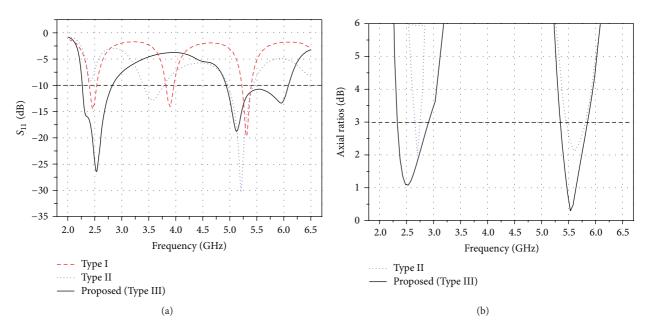


FIGURE 3: (a) The simulated  $S_{11}$  of Antenna Type I and Type II and the proposed antenna (Type III). (b) The simulated axial ratio of Antenna Type II and the proposed antenna (Type III).

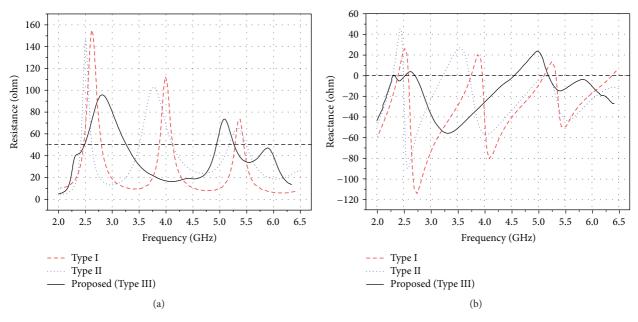


FIGURE 4: The simulated input (a) resistance and (b) reactance of Antenna Type I and Type II and the proposed antenna (Type III).

best performance and consequently is the one that has been realized. The excitation of the circular polarization and the effect of the ground parameters on the antenna performance will be discussed in the next sections.

2.3. Parametric Study. In order to investigate the effects of various parameters on the antenna performance, an extensive parametric analysis has been performed. To this purpose each antenna parameter was changed keeping the others to

a constant value. Unless specified, the fixed parameters were chosen so to coincide with those of the optimized design.

The length of each stub  $S_i$  ( $i=1\sim6$ ) of the S-shaped monopole is the key parameter of the antenna performance. As an illustration, the frequency behavior of the  $S_{11}$  parameters and that of the axial ratio computed along the positive z-direction, for different lengths of the parameters  $S_4$  and  $S_5$ , are shown in Figure 5.  $S_4+S_5$  is set to be a constant according to the evolution of Type I to Type II. There is no obvious frequency shift of  $S_{11}$ , but impedance matching is

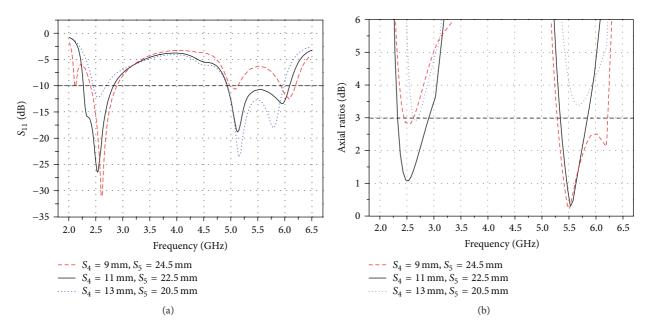


Figure 5: The simulated (a)  $S_{11}$  and (b) axial ratio for different  $S_4$  and  $S_5$  values of the proposed antenna (Type III).

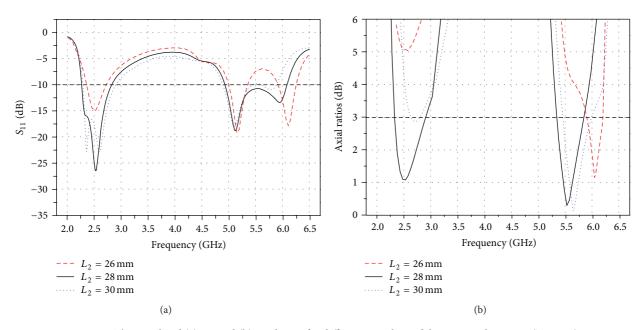


Figure 6: The simulated (a)  $S_{11}$  and (b) axial ratio for different  $L_2$  values of the proposed antenna (Type III).

deteriorated at the lower band and improved at the upper band as the length  $S_5$  decreases.  $S_4 = 11$  mm and  $S_5 = 22.5$  mm are the optimum design for the AR.

As mentioned above, the parameters of the rectangular slot  $(L_2, H_2)$ , which can be seen as a ground extension of Antenna Type II, can affect the impedance and AR bandwidth of the antenna. A parametric analysis is performed to evaluate the influence of these parameters on antenna characteristics. Figures 6 and 7 show the frequency behavior of the  $S_{11}$  parameters and AR along the positive z-direction for different values of the antenna geometrical parameters

 $L_2$  and  $H_2$ . It can be seen that  $L_2$  and  $H_2$ , which affect the impedance matching of the antenna, have a great effect on AR at the lower frequency but less effect at the upper frequency. According to these simulation results  $L_2 = 28$  mm and  $H_2 = 27$  mm are chosen as the optimal value.

2.4. Circular Polarization Analysis. To excite the circular polarization, the antenna must radiate fields of equal magnitude that are orthogonal in space and in time. In order to illustrate how the circular polarization is achieved, the simulated surface currents distributions at 2.5 GHz and 5.75 GHz,

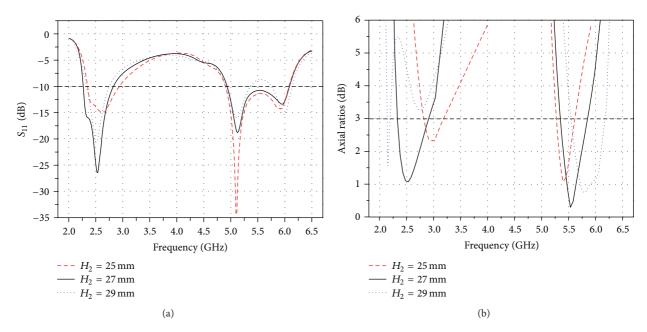


FIGURE 7: The simulated (a)  $S_{11}$  and (b) axial ratio for different  $H_2$  values of the proposed antenna (Type III).

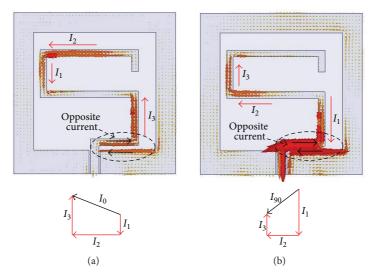


FIGURE 8: Simulated surface currents distributions at orthogonal phases (a) 0° and (b) 90° at 2.5 GHz of the proposed antenna.

when the phase of the exciting signal is  $0^{\circ}$  and  $90^{\circ}$ , are shown in Figures 8 and 9, respectively. The analysis based on the current vector composition employed in [11] is adopted to identify the polarization state of the radiated field. However, since the adjacent surface currents with the same intensity and opposite directions do not provide contribution to the far field, they are not taken into account. From the analysis of Figures 8 and 9 it is clear that the dominant radiating vectors on the antenna surface excite a right-hand polarized field along the positive z-direction at the considered frequencies of 2.5 GHz and 5.75 GHz.

### 3. Results and Discussion

An antenna prototype has been realized to verify the performances of the proposed antenna. The antenna has been analyzed using a full-wave commercial software (Ansys HFSS 15). The measures of the scattering parameters have been carried out by using a WILTRON37269A vector network analyzer, while those concerning the radiation patterns have been derived by means of a fully automated anechoic chamber.

The measured and simulated S-parameters results are depicted in Figure 10. The antenna presents a simulated

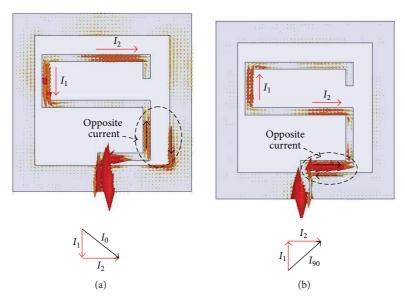


FIGURE 9: Simulated surface currents distributions at orthogonal phases (a) 0° and (b) 90° at 5.75 GHz of the proposed antenna.

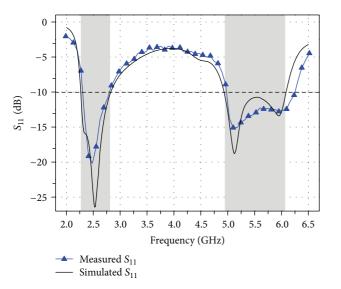


Figure 10: Measured and simulated  $S_{11}$  of the proposed antenna.

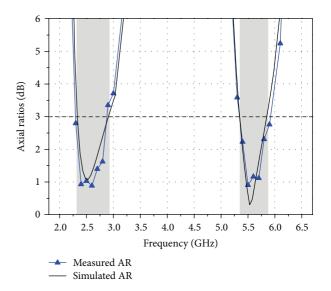


FIGURE 11: Measured and simulated axial ratio of the proposed antenna.

bandwidth ( $S_{11} \le -10 \,\mathrm{dB}$ ) of 21.3% (2.27–2.81 GHz) and 20.7% (4.94–6.08 GHz) and a measured bandwidth of 18.5% (2.31–2.78 GHz) and 22.6% (4.99–6.26 GHz) in the first and second operative band, respectively. The simulated and measured values of the axial ratio (AR < 3 dB) in the direction of maximum radiation (along the *z*-axis direction) are shown in Figure 11. From Figure 11 it appears that the proposed antenna exhibits excellent circular polarization. In particular, simulated axial ratio bandwidths of 21.9% (2.39–2.98 GHz) and 8.8% (5.42–5.92 GHz) and measured axial ratio bandwidths of 19.6% (2.30–2.80 GHz) and 8.8% (5.40–5.90 GHz) are observed in the figure. Finally, it can be observed that the numerical results concerning the operative bands of the proposed antenna are in good agreement with

the experimental measurements. Therefore, the operative bands of the antenna, that is, those where both the impedance and axial ratio requirements are satisfied simultaneously, are between 2.39 and 2.81 GHz and between 5.42 and 5.92 GHz, respectively.

Figure 12 shows the measured and simulated radiation pattern for XZ-plane and YZ-plane at 2.5 GHz and 5.75 GHz, respectively. From Figure 12 it appears that the proposed antenna radiates right-hand circular polarization (RHCP) in the positive z-direction and left-hand circular polarization (LHCP) in the negative z-direction. The level of the cross polarization along the main beam direction is lower than

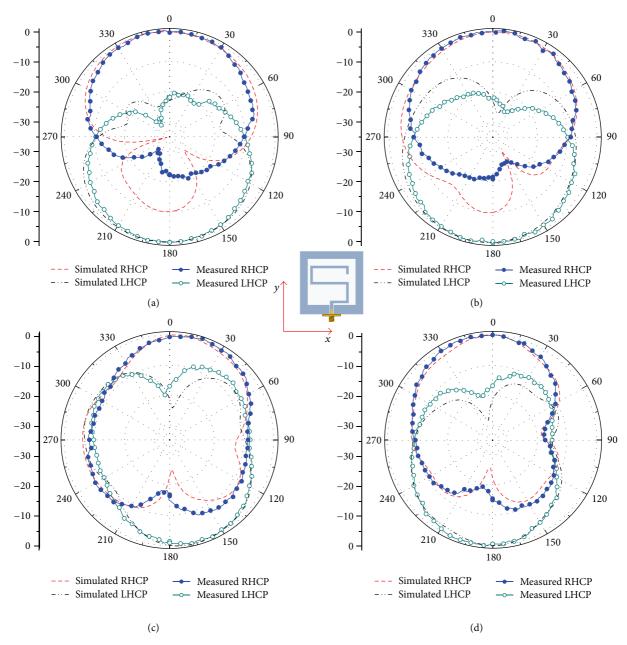


FIGURE 12: Measured and simulated radiation pattern of the proposed antenna. (a) XZ-plane at 2.5 GHz, (b) YZ-plane at 2.5 GHz, (c) XZ-plane at 5.75 GHz, and (d) YZ-plane at 5.75 GHz.

15 dB and 8 dB in the lower band and the higher band, respectively.

The gain of the proposed antenna is measured by using the comparison method. To this end the gain measurement was performed combining the vertical and horizontal field levels measured using a linearly polarized Standard Gain Antenna. Antenna gains of about 3.3 dBi, in the lower band, and of about 3.8 dBi, in the higher band, are observed along the z-direction (see Figure 13). The radiation efficiency using wheeler cap method [12] is also incorporated in Figure 13, which shows an average efficiency of 80% and 83% in the first and second bands, respectively.

### 4. Conclusion

A novel dual-band circularly polarized CPW-fed rectangular slot antenna has been presented. The vector composition of the surface current distribution has been employed to demonstrate that the S-shaped monopole is suitable to control the currents path so to excite the circular polarization. Finally, the experimental measurements performed on a prototype have shown that the proposed antenna achieves a 10 dB return loss in the frequency bands 2.31–2.78 GHz and 4.99–6.26 GHz, respectively, while it exhibits a 3 dB axial ratio in the frequency bands 2.30–2.80 GHz and 5.40–5.90 GHz.

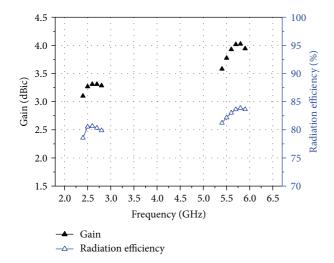


FIGURE 13: Measured gain and radiation efficiency of the proposed antenna.

Therefore, it appears as a good candidate for communications requiring circular polarizations in the WLAN and WiMAX frequency bands.

### **Competing Interests**

The authors declare that they have no competing interests.

### References

- [1] P. Bernardi, R. Cicchetti, and O. Testa, "An accurate UTD model for the analysis of complex indoor radio environments in microwave WLAN systems," *IEEE Transactions on Antennas and Propagation*, vol. 52, no. 6, pp. 1509–1520, 2004.
- [2] J. Yang, C.-H. Liang, and T. Wang, "Novel dual-band circularly polarized wideband antenna for WLAN and WiMAX," *Journal of Electromagnetic Waves and Applications*, vol. 26, no. 14-15, pp. 1881–1888, 2012.
- [3] P. Nayeri, K.-F. Lee, A. Z. Elsherbeni, and F. Yang, "Dual-band circularly polarized antennas using stacked patches with asymmetric U-slots," *IEEE Antennas and Wireless Propagation Letters*, vol. 10, pp. 492–495, 2011.
- [4] A. A. Heidari, M. Heyrani, and M. Nakhkash, "A dual-band circularly polarized stub loaded microstrip patch antenna for GPS applications," *Progress in Electromagnetics Research*, vol. 92, pp. 195–208, 2009.
- [5] M. Samsuzzaman, M. T. Islam, H. Arshad, J. S. Mandeep, and N. Misran, "Circularly polarized S band dual frequency square patch antenna using glass microfiber reinforced PTFE composite," *The Scientific World Journal*, vol. 2014, Article ID 345190, 10 pages, 2014.
- [6] T. S. Ooi, S. K. A. Rahim, and B. P. Koh, "2.45 GHz and 5.8 GHz compact dual-band circularly polarized patch antenna," *Journal* of *Electromagnetic Waves and Applications*, vol. 24, no. 11-12, pp. 1473–1482, 2010.
- [7] S. X. Ta and I. Park, "Dual-band operation of a circularly polarized four-arm curl antenna with asymmetric arm length," *International Journal of Antennas and Propagation*, vol. 2016, Article ID 3531089, 10 pages, 2016.

- [8] X. L. Bao and M. J. Ammann, "Monofilar spiral slot antenna for dual-frequency dual-sense circular polarization," *IEEE Transac*tions on Antennas and Propagation, vol. 59, no. 8, pp. 3061–3065, 2011.
- [9] D.-C. Chang, B.-H. Zeng, and J.-C. Liu, "CPW-fed circular fractal slot antenna design for dual-band applications," *IEEE Transactions on Antennas and Propagation*, vol. 56, no. 12, pp. 3630–3636, 2008.
- [10] C. H. Chen and E. K. N. Yung, "Dual-band dual-sense circularly-polarized CPW-fed slot antenna with two spiral slots loaded," *IEEE Transactions on Antennas and Propagation*, vol. 57, no. 6, pp. 1829–1833, 2009.
- [11] C.-H. Chen and E. K. N. Yung, "Dual-band circularly-polarized CPW-fed slot antenna with a small frequency ratio and wide bandwidths," *IEEE Transactions on Antennas and Propagation*, vol. 59, no. 4, pp. 1379–1384, 2011.
- [12] D. M. Pozar and B. Kaufman, "Comparison of three methods for the measurement of printed antenna efficiency," *IEEE Transactions on Antennas and Propagation*, vol. 36, no. 1, pp. 136–139, 1988.